MICROSTRUCTURE-SENSITIVE FATIGUE MODELING OF HEAT TREATED AND SHOT PEENED MARTENSITIC GEAR STEELS

A Dissertation
Presented to
The Academic Faculty

by

Rajesh Prasannavenkatesan

In Partial Fulfillment
of the Requirements for the Degree
Doctor of Philosophy in the
School of Mechanical Engineering

Georgia Institute of Technology
December 2009

MICROSTRUCTURE-SENSITIVE FATIGUE MODELING OF HEAT TREATED AND SHOT PEENED MARTENSITIC GEAR STEELS

Approved by:

Prof. David L. McDowell, Advisor
School of Mechanical Engineering
Georgia Institute of Technology

Prof. Min Zhou
School of Mechanical Engineering
Georgia Institute of Technology

Prof. Gregory B. Olson
Department of Materials Science and
Engineering
Northwestern University

Prof. Richard W. Neu
School of Mechanical Engineering
Georgia Institute of Technology

Prof. Kenneth Gall
School of Materials Science and
Engineering
Georgia Institute of Technology

Date Approved: 10/15/2009

To my late grandma Mrs. Lalitha

ACKNOWLEDGMENTS

TABLE OF CONTENTS

LIST OF TABLES

LIST OF FIGURES

SUMMARY

High strength secondary hardening lath martensitic steel is a strong candidate for high performance and reliable transmission systems in aircraft and automotives. The fatigue resistance of this material depends both on intrinsic microstructure attributes, such as fine scale (M_2C) precipitates, and extrinsic attributes such as nonmetallic primary inclusions. Additionally, the aforementioned attributes are affected by processing history. The objective of this research is to develop a computational framework to quantify the influence of both extrinsic (primary inclusions and residual stresses) and intrinsic (martensite laths and carbides) microstructure attributes on fatigue crack formation and the early stage of microstructurally small crack (MSC) growth that dominate high cycle fatigue (HCF) lifetime.

To model the fatigue response at various microstructure scales, a hierarchical approach is adopted. A simplified scheme is developed to simulate processing effects such as shot peening that is suitable to introduce representative residual stresses prior to conducting fatigue calculations. Novel strategies are developed to couple process route (residual stresses) and microstructure scale response for comprehensive analysis of fatigue potency at critical life-limiting primary inclusions in gear steels. Relevant microstructure-scale response descriptors that permit relative assessment of fatigue resistance are identified. Fatigue crack formation and early growth is highly heterogeneous at the grain scale. Hence, a scheme for physically-based constitutive models that is suitable to investigate crack formation and early growth in martensitic steel is introduced and implemented. An extreme value statistical/probabilistic framework to assess the influence of variability of

various microstructure attributes such as size and spatial distribution of primary inclusions on minimum fatigue crack formation life is devised. Understanding is sought regarding the relative role of microstructure attributes in the HCF process, thereby providing a basis to modify process route and/or composition to enhance fatigue resistance. Parametric studies are conducted to assess the effect of hot isostatic pressing and introduction of compliant coatings at debonded inclusion-matrix interface on enhancement of fatigue resistance.

A comprehensive set of 3D computational tools and algorithms for hierarchical microstructure-sensitive fatigue analysis of martensitic gear steels is developed as an outcome of this research; such tools and methodologies will lend quantitative and qualitative support to designing improved, fatigue-resistant materials and accelerating insertion of new or improved materials into service.

CHAPTER 1

INTRODUCTION

1.1 Introduction

Rising power density requirements in transmission gear applications demand significant technological innovation. In 2004, representative leaders of the gear industry, including members from the United States Army, Boeing, General Motors and John Deere, prepared the Gear Industry Vision to outline a way of addressing these needs, specifically defining strategic goals to be met by the year 2025 [1] . Among the stated objectives were ambitious goals for enhancing gear performance, calling for 25% increases in power density every 5 years as well as a 50% increase in power transfer efficiency. Such lofty aims will soon surpass the performance gains that can be obtained through gear redesign alone; success will ultimately depend on better gear materials. The Gear Industry Vision identifies clean steels that are heat treatable to ultra-high hardness levels (RC70+) as leading candidate materials, and the continuing development of such steels as a "key technological challenge" that must be addressed. Evidently, enhancing the fatigue resistance of the gear steels will be a major challenge to be addressed in order to accomplish long term goals.

Building on the design methodology demonstrated at Northwestern University [2], QuesTek Innovations LLC (Evanston, IL) has integrated modeling of process-structure-property-performance relations in several major design programs for over a decade, with emphasis on proprietary high performance alloys suited to advanced gears and bearings and stainless steels for landing gear applications. In developing the next generation high

strength steels, they utilized the system-based computational materials design approach [3]. Systems-based materials design focuses on the various interacting subsystems ultimately responsible for material performance. Drawing upon the existing knowledge base of various materials systems, targeted microstructures can be engineered for specific applications through the iterative feedback between theoretical modeling of these subsystem interactions and state-of-the-art analysis of prototype alloys.

While the methods and tools of parametric materials design are now well established and undergoing wide application under QuesTek's commercial design services, the broadening application of computational materials engineering in the materials-aware manufacturing context of both *Accelerated Insertion of Materials* (AIM) qualification and *Integrated Computational Materials Engineering* (ICME) concurrent engineering practices drives the demand for even higher fidelity integrated simulation and characterization tools. A new level of science-based modeling accuracy is now being achieved under the ONR/DARPA "D3D" Digital Structure consortium [4]. A suite of advanced 3D tomographic characterization tools is being used to calibrate and validate a set of high fidelity explicit 3D microstructure simulation tools spanning the hierarchy of microstructure scales. The QuesTek-led university consortium component of the D3D program focuses on design of fatigue and fracture resistant high strength steels. This program is integrated with other aspects of D3D, including visualization systems, statistical analysis of distributed microstructure, integration of an archival 3D microstructure "atlas" at the Naval Research Laboratory, and ultimate iSIGHT-based integration of the full toolset in both computational materials design and AIM qualification. The principal role of Georgia Institute of Technology, under the

supervision of Prof. McDowell, is to develop a suite of 3D process path and microstructure-sensitive fatigue modeling tools to understand and enhance the fatigue resistance of high strength martensitic steels.

1.2 Fatigue crack formation and growth

Fatigue is the process of progressive damage accumulation in engineering components subjected to repeated cyclic loading. The fatigue life is composed of two components; crack formation (nucleation and early growth) life and crack propagation life. Crack formation is further decomposed into crack nucleation or incubation, microstructurally small crack (MSC) growth and physically small crack (PSC) growth [5, 6]. In steels, crack formation (nucleation and early growth) accounts for a significant portion of fatigue life under high cycle fatigue (HCF) loading [7]. The crack formation and MSC growth stages depend on microstructure heterogeneities such as inclusions and grain boundaries [8-11]. Nonmetallic inclusions and pores often play an important role in limiting HCF life in high strength steels [12-17]. The mechanisms of crack formation from an inclusion involve either cracking of the inclusion or debonding of the inclusion/matrix interface, with the inclusion serving as a notch to concentrate cyclic plastic strain in the surrounding metal matrix [12, 18, 19]. Additionally, the presence of secondary precipitates (~3-100 nm) formed during heat treatment can influence the crack formation and small crack growth behavior in the vicinity of primary inclusions [20]. Residual stresses generated during processing play a critical role in dictating the service life by altering the mean stress in steel structures [21].

Microstructure attributes at different length scales (in the form of inclusions, and secondary precipitates) affect fatigue crack formation in martensitic steels [22-26]; however, computational models that correlate these attributes to variability in fatigue crack formation life have been very limited. Additionally, processing effects (for e.g., shot peening, carburization) play a crucial role in deciding the fatigue performance of martensitic steels. Since process variability results in microstructure variability, an integrated modeling strategy is imperative in predicting the expected fatigue life. Currently, no computational models are available to address the aforementioned challenge, and the objective of the proposed research is to utilize fully three-dimensional finite element approaches to devise methodologies that couple the effects of microstructure features and process routes in order to understand HCF response of martensitic steels. Fatigue crack formation in the HCF regime is highly heterogeneous at the grain (block) scale [10], and due to a hierarchy in microstruture of lath martensite at that scale it is impossible to develop an all-inclusive model coupling process effects and microstructure features at different scales; instead, a hierarchical approach will be more suitable and computationally efficient to investigate the process of crack formation and early growth in martensitic steels. It is important to study the overall cyclic stress-strain response and the plastic strain distribution for the local material heterogeneities during processing and service and to correlate these parameters with microstructure descriptors that permit assessment of relative fatigue resistance. This should facilitate the evaluation of variability in fatigue life with respect to the microstructure and process parameters and it should help in obtaining improved fatigue life estimates. Additionally, such a study (i) would be beneficial in designing the material microstructure to maximize fatigue

resistance and (ii) assist in devising improved process routes to extend the service life of components.

1.3 Plan of study

This work aims at developing 3D finite element based strategies to model HCF behavior of high strength martensitic gear steels. Specifically, attention is devoted towards formulating simplified algorithms to simulate effects of heat treatment and surface treatment on fatigue crack formation and early growth behavior at critical life-limiting attributes such as nonmetallic primary inclusions. More emphasis will be placed on using computational tools to facilitate comparison between microstructure attributes with the goal of design or specification of material microstructure. A hierarchical approach is undertaken while identifying relevant microstructure scales and developing suitable constitutive models to simulate the microstructure scale response in fatigue. The utility of the algorithms and material models are demonstrated through parametric studies considering idealized inclusion geometries. Based on the knowledge gained through such studies, modified process routes that enhance fatigue resistance are computationally investigated.

In Chapter 2, a brief summary of the microstructure and processing details of the lath martensitic steels is presented. Furthermore, salient observations from the experimental bending fatigue studies performed by Tiemens [27] is reported. In Chapter 3, a computational strategy to characterize the fatigue crack formation potency at subsurface primary inclusions in carburized and shot peened martensitic gear steels is developed and demonstrated. A simplified scheme to induce compressive residual stresses mimicking

the shot peening process is developed which is suitable to initialize residual stresses prior to conducting fatigue calculations. Parametric studies are performed to investigate the transition of critical crack formation site to subsurface inclusions in the presence of residual stresses as observed in experiments. In Chapter 4, a 3D FE based methodology to investigate relaxation of compressive residual stresses is presented. Using a three-dimensional crystal plasticity model for cyclic deformation of lath martensitic steel, a simplified scheme is adopted to simulate the effects of shot peening to induce initial compressive residual stresses. The model is utilized to investigate the subsequent cyclic relaxation of compressive residual stresses in shot peened lath martensitic gear steel in the HCF regime. Chapter 5 presents a strategy to model the sensitivity of fatigue resistance of secondary hardening martensitic gear steels to variability in extrinsic inhomogeneities such as primary inclusions, and pores, coupled with intrinsic microstructure variability such as variation in polycrystalline matrix grain orientation. A simplified approach is developed to quantify the variability of fatigue indicator parameters (FIPs) in the matrix at nonmetallic inclusions and pores in lath martensitic gear steels using a three-dimensional crystal plasticity constitutive model. In Chapter 6, a 3D dislocation density based crystal plasticity constitutive model is developed that is suitable to investigate the effects of sub-micron scale M_2C precipitates on fatigue resistance of martensitic gear steels. The model is utilized to couple intrinsic variability arising due to variation in polycrystalline matrix grain orientation and M_2C precipitate volume fraction with extrinsic variability due to size and spacing of primary inclusions. A statistical framework to estimate the minimum life for crack formation is adopted. In Chapter 7, the capabilities of an elastic interphase material adhered to the inclusion

6

surface to alter the FIP in the matrix is computationally explored. By varying the elastic stiffness of the encapsulating interphase, the stresses and cyclic plastic strains are examined in the matrix in the proximity of a partially debonded inclusion, a worst case scenario for formation. In Chapter 8, a three-dimensional finite element based framework to assess the effect of hot isostatic pressing (HIPping) on void closure at partially debonded nonmetallic primary inclusion in high strength martensitic gear steels is developed. The effect of HIPping on fatigue crack formation potency at nonmetallic primary inclusion is evaluated. Chapter 9 summarizes the research outcomes and their relevance to computational design of fatigue resistant martensitic steels. Finally, recommendations are made for future research efforts.

CHAPTER 2

BACKGROUND

This chapter summarizes the microstructure and processing details of the secondary hardening martensitic steel used as a model material to develop fatigue modeling tools. Furthermore, a brief summary of the experimental bending fatigue studies performed by Tiemens [27] is reported. The experimental efforts and observations motivate certain aspects of the development of microstructure-sensitive fatigue models. The results and observations are utilized to develop suitable fatigue evaluation models and to support certain model predictions discussed in the subsequent chapters.

2.1 Secondary hardening steels

To address rising power density requirements, steels must exhibit superior hardness to resist localized contact and bending stresses while at the same time sustain adequate toughness for sufficient flaw tolerance. One family of steels that has demonstrated the highest combination of strength and toughness is high-alloy secondary hardening martensitic steels [28, 29]. Secondary hardening steels get their name from a secondary hardening response exhibited by these alloys when aged at Stage IV (450-600°C) tempering temperatures. This hardening behavior arises from the formation of fine alloy carbide dispersions that replace coarse cementite particles during tempering. Because these alloy carbides are stable at higher temperatures, secondary hardening steels were first utilized as tool steels in order to maintain hardness at elevated temperatures, a phenomenon called "hot-hardness" or "red-hardness". The superior combination of strength and toughness afforded through the fine alloy carbide dispersion was then

utilized in high-strength high toughness structural steels, leading to commercial alloys such as Aermet100 and AF1410. It is this same optimized combination of strength and toughness that makes secondary hardening alloys well suited for high power density gear applications.

2.2 System structure

The systems flow block diagram, or Olson diagram, of secondary hardening steels is shown in Fig. 2.1. The two primary performance objectives are the limiting failure modes, namely, bending fatigue and sliding/rolling contact fatigue. Bending fatigue is observed to be the limiting failure mode when attempting to achieve elevated power densities in transmission gear applications. In addition to optimizing the hardness and toughness of the steel, the fatigue resistance is enhanced through surface treatments and stabilizing the strengthening dispersions. Ultimately, a hard and wear resistant carburized case with a high toughness core is achieved, suitable for high power density applications.

Once the actual gear is manufactured from the raw material through cast ingot, direct casting, or powder metallurgy, it is typically heat treated to harden the surface through processes such as carburization. Carburization treatment consists of solutionizing to an austenitic state to dissolve primary carbides and enhance carbon solubility. The gear is quenched following carburization and subsequently subjected to cryogenic treatment to achieve complete martensitic transformation. Tempering treatments are then performed to achieve secondary hardening through precipitation of alloy carbides (M_2C). Shot peening is employed to impart beneficial compressive residual stresses to enhance fatigue

resistance. Surface finishing such as honing, grinding, and burnishing is performed to get rid of stress elevating asperities.

2.3 Matrix

2.3.1. Microstructure

The base microstructure of Ni-Co secondary hardening steels typically consists of a tempered lath martensite matrix, with Ni and Co in solid solution. The lath structure is formed upon quenching the FCC austenite phase through a diffusionless shear transformation, resulting in highly dislocated substructure due to accommodation of the transformation strains [23, 30]. The fine structure of lath martensite combined with high dislocation density provides excellent combination of strength and toughness.

Suspended in solid solution within the lath martensite microstructure are both the Ni and Co alloying additions. Ni is a common alloying elements utilized in steels to enhance toughness [20, 31, 32]. Co addition enables precipitation of finer, stable and more efficient M_2C carbides and maximizes secondary hardening response. It is noted that given sufficient tempering time, the coarse cementite particles are dissolved during secondary hardening as finer alloy carbides are precipitated. In order to resist grain coarsening during high temperature heat treatments, fine submicron secondary dispersions are often introduced to pin grain boundaries. Small additions of Ti are frequently added to form TiC and TiN; these grain refining precipitates can serve as sites for microvoid formation during fracture [33].
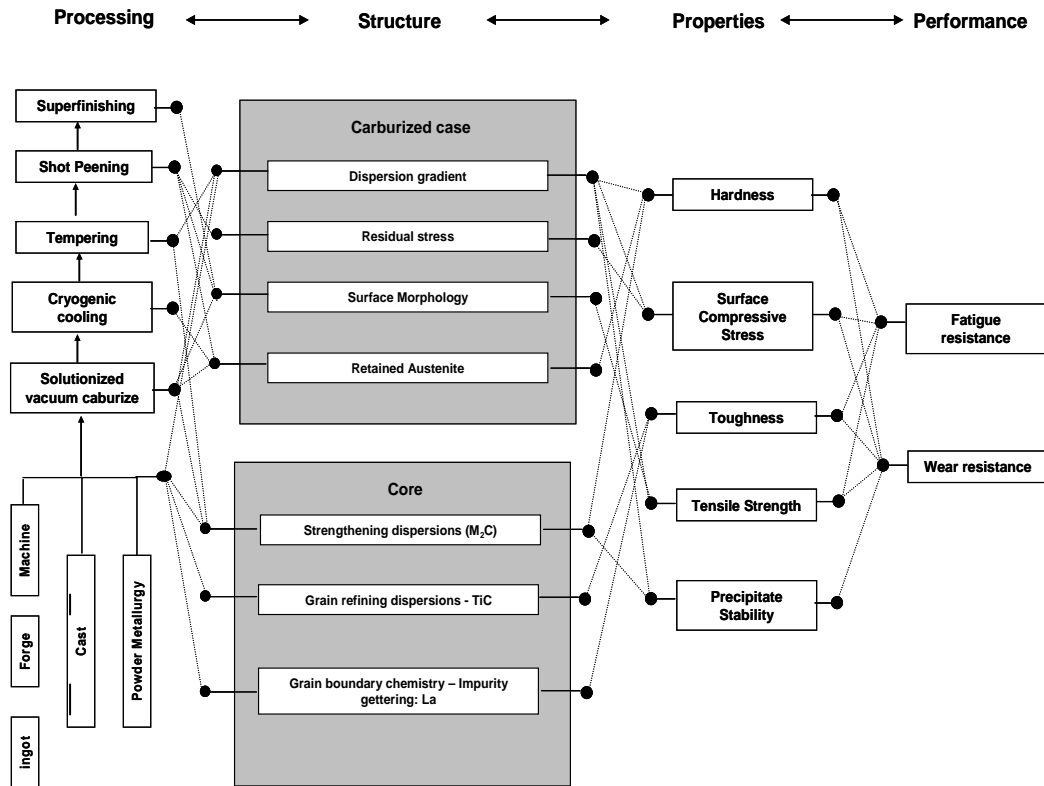
Figure 2.1: Olson diagram of high power density gear applications.

2.3.2 M_2C carbide precipitation and strengthening

Secondary hardening steels garner most of their strength through a fine dispersion of alloy carbides. The level of precipitation strengthening achieved is highly dependent on the interaction mechanism between a gliding dislocation and a precipitate. When precipitates are small and coherent with the surrounding matrix, dislocations are able to cut into and shear the precipitate given sufficient driving force. Depending on the particular system, the resistance to particle shearing and the associated strengthening is due to several mechanisms, including coherency strains between precipitates and matrix (coherency strengthening), disruption of atomic ordering within precipitates (order strengthening) and additional surface area created from particle shearing (chemical

strengthening). With all of these strengthening mechanisms, larger particles provide more resistance to shearing than smaller ones, resulting in the general strengthening behavior for particle shearing illustrated in Figure 2.2 [34].
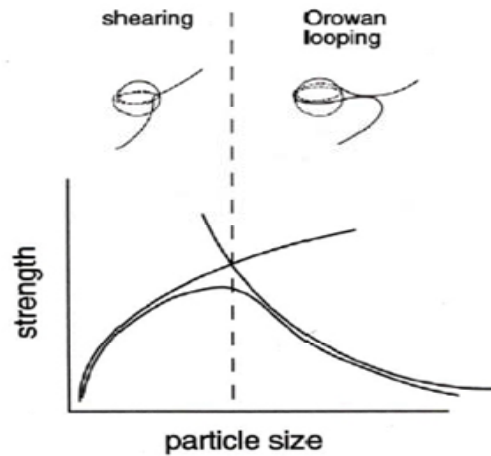
Figure. 2.2. Schematic representation of precipitation strengthening of particle size at constant volume fraction.

With continued growth, precipitates become increasingly difficult to shear due to their larger size as well as loss of coherency with the surrounding matrix. Eventually particles become non-shearable and gliding dislocations must bow around the particles. The Orowan bypass regime than dominates where a gliding dislocation must bow completely around a particle until touching to form a contained loop, thereby allowing the remaining reconnected dislocation segment to continue gliding. Unlike particle shearing, Orowan bypass resistance is governed by interparticle spacing; increasing the number of obstacles impedes dislocation motion. For a given particle volume fraction, fewer larger precipitates are less efficient Orowan strengtheners than a larger number of smaller precipitates. The particle size dependence for strengthening through particle shearing and by particle bypass results in the maximum precipitation strengthening occurring at the

transition between these two mechanisms, as also shown schematically in Figure 2.2. Optimization of precipitation strengthening thus requires the refinement of the utilized precipitate strengthening dispersion to a sufficiently fine size scale.

Ni-Co secondary hardening steels achieve very fine dispersions of alloy carbides in part due to their large Co alloying additions. As previously discussed, the added temper resistance provided by the Co allows for increased heterogeneous nucleation sites for alloy carbides. By easing nucleation, the driving force for precipitates is increased resulting in finer precipitate dispersions. Additionally, the type of carbide utilized in precipitation also plays a vital role. Carbides capable of maintaining high coherency with BCC Fe are able to precipitate at a much finer size scale. These carbides correspond to close packed structures, namely the FCC MC carbide (M=Nb, Ta, Ti, V) and HCP M_2C carbide (M=Fe, Cr, Mo, W) [35].

The precipitate dispersions of choice in Ni-Co secondary hardening steels are M_2C alloy carbides, where strong carbide forming elements (M) include Cr, Mo, V and W. Although metastable, M_2C carbides exhibit the strongest driving force for precipitation from martensite as well as display the aforementioned coherency with the BCC tempered martensite matrix, resulting in the ability to form exceedingly fine strengthening dispersions. The transition between particle shearing and particle bypass marking the point of maximum precipitation strengthening has been shown to occur at an M_2C precipitate diameters of about 3 nm. In order to reach dispersions on such a fine size scale, the thermodynamic driving force and kinetics for precipitation are controlled through alloying to compose mixed alloy carbides of $(Cr, Mo, V, W)_2C$. Due to the increased stability of Mo_2C over Cr_2C, Mo increases the precipitation driving force when

13

substituted for Cr but is ultimately limited for solidification segregation considerations. Small additions of V and W also greatly increase the driving force for M_2C precipitation; however both are also constrained due to limited solubility in FCC Fe.

2.4 Current alloys

A family of ultra-high strength, secondary hardening carburized steels were chosen as the candidate materials to address high power density gear applications due to their optimized combination of strength and toughness. Using the systems-based materials design approach, the first prototypes of these alloys were developed by John Wise at Northwestern University [34], successfully achieving case hardness of 69 HRC. These prototypes were further developed and commercialized as GearMet® C69 and C67 by QuesTek Innovations in Evanston, IL. Designed for maximized case hardness, this alloy has proven to be superior to M50 bearing steel in NTN ball-on-rod rolling contact fatigue (RCF) screening tests and superior to X53 gear steel in full gear test by NASA Glenn [36]. Subsequently, QuesTek developed additional secondary-hardening steel, for conventional gear steel surface hardness levels (58-61 HRC) with a harder and flaw-resistant core. Termed GearMet® C61 steel, this alloy has successfully been implemented in racing applications at reduced gear widths with limited impact on performance. This research will focus on developing a microstructure-sensitive FE modeling approach to evaluate the fatigue resistance of the C61 class of secondary hardening steels.

2.5. Experimental investigation of fatigue failure in martensitic steel

The material of investigation in this work is GearMet® C61 alloy gear steel (referred to as C61 steel) [36] with the composition listed in Table 2.1 [27]. Heat treatment of this steel involves carburization at either 950°C, 1000°C or 1050°C followed by cryogenic treatment in a liquid nitrogen bath to obtain complete martensitic transformation at the surface. This is followed by tempering at 482°C for 15 hours to achieve the desired case strength. Shot peening is a standard dual peening employed in GM power trains and is performed by the Metal Improvement Company at their Romulus, MI facility. Dual peening consists first of a high-intensity application of peening media to maximize and deepen compressive residual stress at the target surface, followed by a less-intense saturation of softer media intended to smooth out asperities and to raise the compressive stress at the near surface. The measured variation in compressive residual stress with depth is shown in Figure 2.3, and the experimentally measured Vickers microhardness variation with depth is shown in Figure 2.4.

Table 2.1. *Composition of C61 martensitic steel (wt %).*

	Co	Cr	Ni	Mo	V	C	B	La	Ti	Fe
C61	18	3.5	9.5	1.1	0.08	0.16	0.001- 0.003	0.01- 0.03	0.01- 0.03	Bal

To assess the bending fatigue performance of secondary hardening ultra-hard steels, single tooth bending fatigue tests on GearMet C61 spur gear were conducted at the GM Powertrain Gear Center in Wixom, MI. The use of standard GM performance validation techniques is important as it allows for comparison with existing unpublished data as well as incorporates relevant gear manufacturing processes that ultimately affect material

performance. Additionally, the utilization of such accepted practices to demonstrate the performance of perceived "nontraditional" gear steels provides a visible and practical example to industry on the merits of such materials and the design methodology.
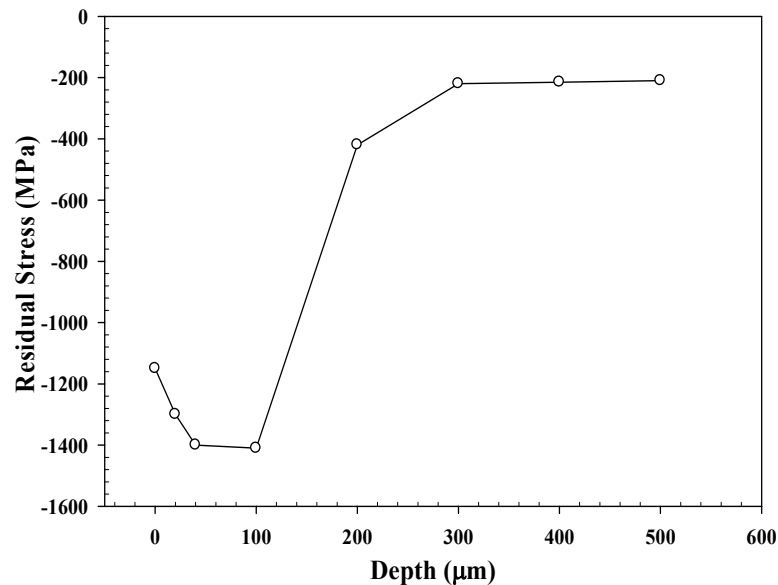
Figure 2.3. *Measured variation of compressive residual stress with depth after shot peening.*

With the increase of case depth, the carbon content decreases, as does the microhardness. As measured by X-ray diffraction, initial compressive residual stress exists after shot peening within a thickness of 0.5 mm in the surface layer and reaches a maximum value of -1400 MPa at a depth of around 75 to 100 μm. The S-N curve for different surface conditions of C61 spur gear is shown in Figure 2.5. Shot peening was observed to enhance fatigue performance substantially when compared with as-heat treated specimens.
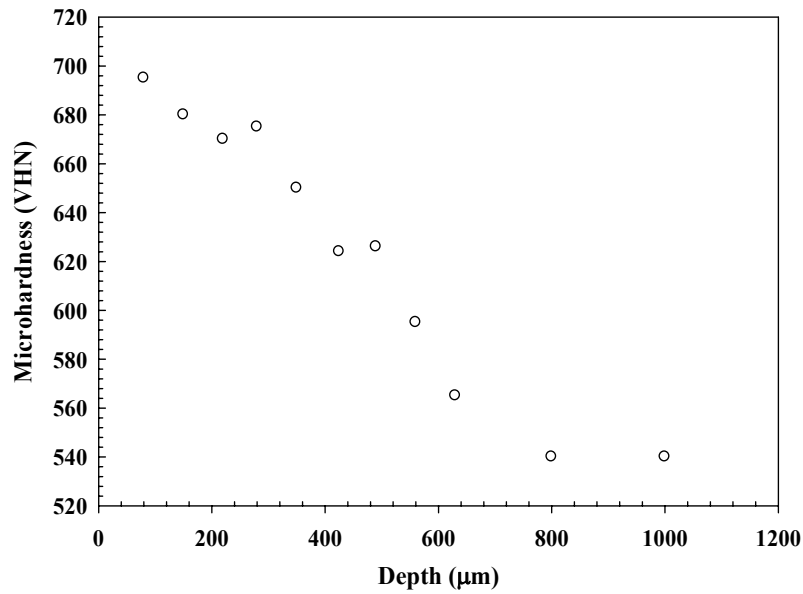
Figure 2.4. *Measured variation of Vickers microhardness after heat treatment (carburization and tempering) with depth.*
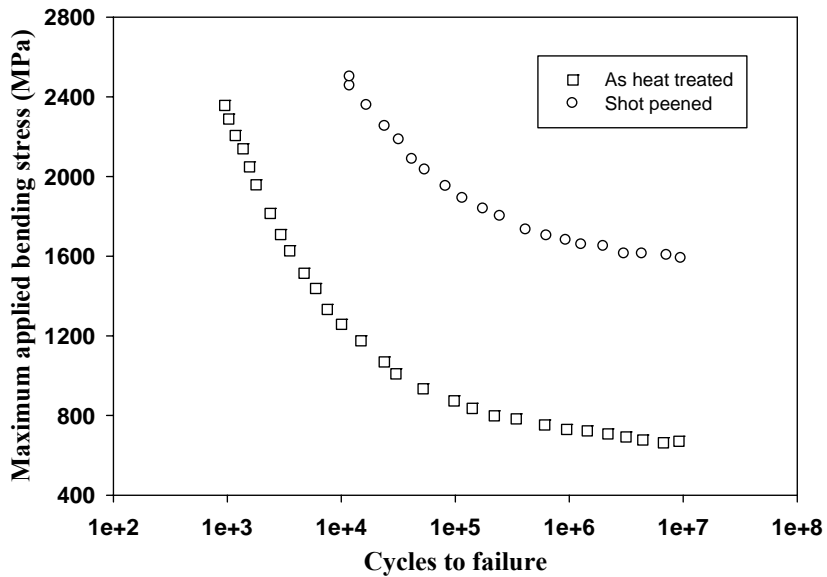
Figure 2.5. *Stress-life curves for different surface condition of C61 spur gear.*

A common life-limiting failure mode observed in the bending fatigue tests was inclusion initiated cracks. On the fracture surface, the "fisheye" morphology was observed to radiate outward from each failure-initiating subsurface inclusion. The cracks

were observed to originate at subsurface inclusions at a depth of 100-300 μm below the surface. Two classes of inclusions were observed as verified qualitatively by energy dispersive spectroscopy (EDS): Alumina (Al_2O_3) inclusions in shot peened C61 spur gears and lanthanum oxy-sulfide (La_2O_2S) inclusions in shot peened C61 and C67 spur gears. The switch from Al_2O_3 to La_2O_2S inclusions is a direct result of La additions to C61 (0.003 wt%) alloys to specifically getter impurities.
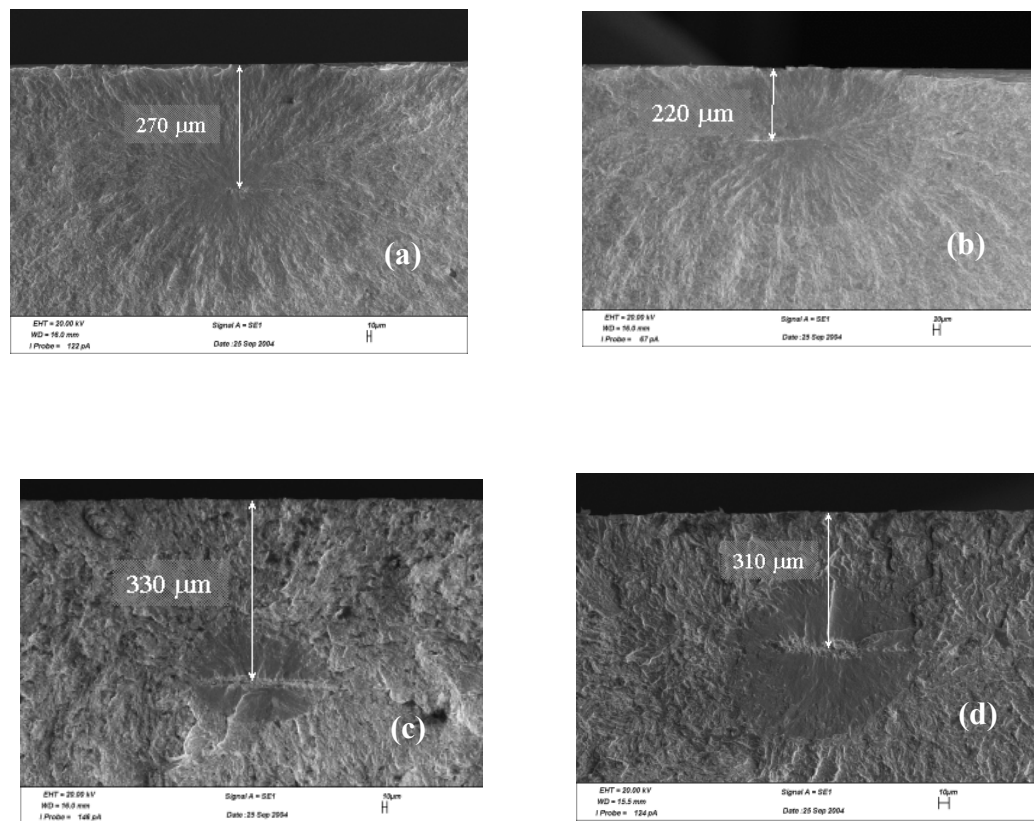
Figure 2.6. *Measured depth of subsurface fatigue crack formation at nonmetallic inclusions in different grades of lath martensitic steels. (a) C61, (b) C61, (c) C69, and (d) C69.*

Figures 2.6 a-d shows the measured depth of subsurface fatigue crack formation in different grades of shot peened martensitic steels. Figures 2.7 and 2.8 show SEM micrographs of both classes of inclusions, as seen on the tooth fracture surfaces, as well as the corresponding mating fracture surfaces of the failed spur gear. Both Al_2O_3 and La_2O_2S inclusions were composed of clusters of individual particles aligned along the hot working direction of the billets from which the gears were manufactured. Individual inclusion particles composing Al_2O_3 and La_2O_2S cluster were all between 1-10 μm in diameter. The cluster morphology was very different between Al_2O_3 and La_2O_2S. Al_2O_3 clusters (see Figure 2.7) were generally composed of only a couple individual inclusion particles tightly concentrated along a single line. In contrast, La_2O_2S clusters were composed of numerous particles and had a much larger cluster width. Experimental investigations revealed La_2O_2S to be most severe with regard to limiting fatigue performance. All La_2O_2S inclusions which caused failure occurred at much shallower depths where the compressive residual stress values were near their maximum values. In contrast, Al_2O_3 inclusions were only observed to form fatigue cracks at depths where compressive residual stress levels reduced by 75%. Although the overall size of the inclusion clusters was not significantly different for Al_2O_3 and La_2O_2S inclusions, the nature of the individual particles within them did show significant differences. As shown in Figure 2.8, La_2O_2S particles are located on both mating fracture surfaces with individual particles primarily de-cohering from the opposing fracture surface leaving behind a concavity. It is unclear if numerous clustered particles are in fact separate or the fractured remnants of a larger particle, and some single particles did show signs of

fracture, such as the annotated particle 4 in Figure 2.8. Al_2O_3 particles, in contrast, were primarily located and tightly bonded on only one mating fracture surface, displaying de-cohesion from the opposing surface with no discernable signs of particle fracture. The size and spatial distributions of the inclusions affect the fatigue crack formation potency and it is of prime importance to discern the relative potency of different inclusion types considering the intrinsic and extrinsic factors that affect the fatigue performance. This research will develop the means to perform the aforementioned investigations that will contribute towards designing fatigue-resistant microstructure and devising modified process routes to enhance the fatigue performance.
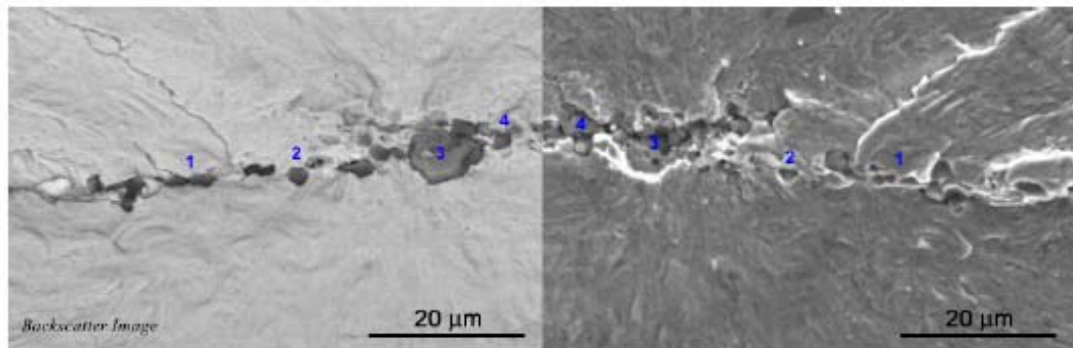
Figure 2.7. *Backscatter SEM image of crack initiation zone showing characteristic Al₂O₃ inclusion sizes, cluster and debonding of inclusion-matrix interfaces.*
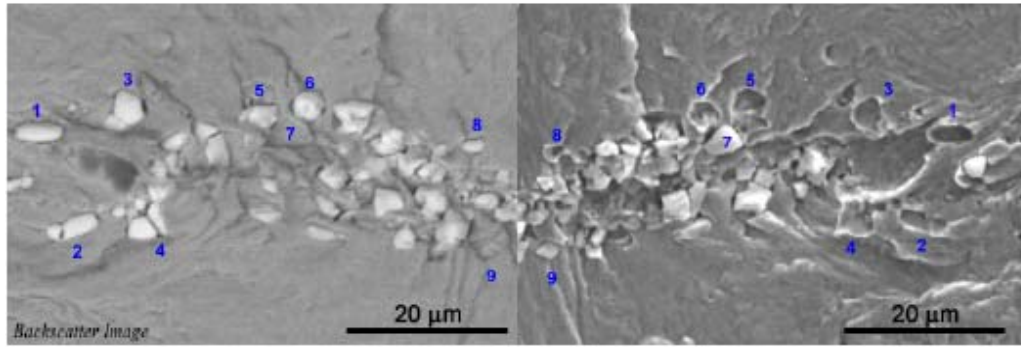
Figure 2.8. Backscatter SEM image of crack initiation zone showing characteristic lanthanum oxy-sulfide inclusion sizes, cluster , debonding of inclusion-matrix interfaces and cracking of inclusions.

Chapter 3

MODELING EFFECTS OF PROCESS ROUTE ON FATIGUE

CRACK FORMATION POTENCY AT PRIMARY INCLUSIONS

In this chapter a computational strategy is developed to characterize the fatigue crack formation potency at subsurface primary inclusions in carburized and shot peened martensitic gear steels. Experimental investigation revealed minimum fatigue strength to be controlled by subsurface fatigue crack formation at inclusion clusters under cyclic bending. An algorithm is presented to simulate residual stress distribution induced through the shot peening process following carburization and tempering. A methodology is developed to analyze potency of fatigue crack formation at subsurface inclusions. Rate-independent 3-D finite element analyses are performed to evaluate plastic deformation during processing and service at room temperature. The specimen is subjected to reversed bending stress cycles with R = 0.05, representative of loading on a gear tooth. The matrix is modeled as an elastic-plastic material with pure nonlinear kinematic hardening. The inclusions are modeled as isotropic, linear elastic. Idealized inclusion geometries (ellipsoidal) are considered to facilitate parametric study of the fatigue crack formation potency at various subsurface depths. Three distinct types of second-phase particles (perfectly bonded, partially debonded, and cracked) are analyzed. Parametric studies are conducted to quantify the effects of inclusion size, orientation and clustering on subsurface crack formation in the HCF or very high cycle fatigue (VHCF) regimes. The nonlocal average value of the maximum plastic shear strain amplitude and Fatemi-Socie (FS) parameter calculated in the proximity of the inclusions is considered as the fatigue

indicator parameters (FIP) for fatigue crack formation and microstructurally small crack growth. The simulations indicate a strong propensity for crack formation at subsurface depths in agreement with experiments in which fatigue cracks formed at inclusion clusters, still in the compressive residual stress field. It is observed that the gradients from the surface of residual stress distribution, bending stress, and carburized material properties all play a pivotal role in fatigue crack formation at subsurface primary inclusions. The fatigue potency of inclusion clusters is greatly increased by prior interfacial damage during processing. Additionally, systematic parametric studies are conducted to investigate the spatial interaction of inclusions with the objective of framing a methodology to estimate the critical inclusion spacing for minimal interaction in fatigue. Furthermore, parametric studies are performed to explore the effect of variation of orientation of ellipsoidal inclusions in a cluster with respect to loading axis and free surface on fatigue crack formation potency. The primary aim is to identify the least damaging orientation, thereby provide basis for efforts to pursue modified process routes to achieve enhanced fatigue performance.

3.1. Introduction

Due to the highly localized nature of the bending stresses in gear teeth with maxima at the surface, the most pertinent processing parameters for bending fatigue relate to various surface treatments. Of particular interest in this research is the residual stress fields induced through the shot peening process. Shot peening is perhaps the most widely used mechanical treatment to modify the surface state of metallic materials, and it is often used for the specific purpose of improving the fatigue resistance. Compressive residual

stresses of high magnitudes are induced at and near the surface layer of the specimen during shot peening by virtue of constrained plastic deformation. Such treatment benefits fatigue resistance of the gear [37]. Extensive experimental observations have been reported, elaborating on the advantages of heat treatments including carburization and surface treatment such as shot peening with regard to improving fatigue resistance of steel components [38-42]. The fact that the bending fatigue strength of steel gear teeth is increased considerably by carburizing and shot peening has been widely utilized in industry [43-49].

3.2. Survey of modeling approaches

3.2.1. Simulation of shot peening process

Residual stresses are an inescapable consequence of manufacturing and fabrication processes, with magnitudes that can be a high proportion of the yield strength. Additionally, residual stresses are induced intentionally through heat and surface treatments to enhance fatigue resistance, as discussed in the previous section. In the absence of residual stresses induced by shot peening, cracks tend to form at the surface of the specimen during fatigue [50-52]. With carburization and shot peening, crack formation is observed to shift from the surface toward the subsurface of the carburized gears [27]; this is primarily due to the presence of high compressive residual stress and comparatively high hardness at the surface. It is well known that crack formation in the subsurface occurs preferentially at nonmetallic inclusions and other inhomogeneities. Such second phase particles often serve as fatigue crack formation sites in a variety of metallic materials [5, 12, 14, 53-55]. Extensive experimental observations have been reported earlier on similar subsurface crack formation [13, 56-61].

Modeling shot peening is a challenging task. The process of shot peening involves bombarding the surface of the component with small spherical shots made of hardened cast-steel, conditioned cut-wire, glass, or ceramic beads at a relatively high impingement velocity (40–70 m/s). The major focus of such modeling has been devoted to predicting the residual stress pattern which can be utilized to optimize the actual shot peening process. Empirical models based on experimental data have been suggested by a few authors [62, 63] to predict the residual stress distribution following shot peening. The earliest effort to model shot peening was undertaken by Shaw and De Salvo [64], where they performed quasi-static analyses of single and twin shots on plastic strain distribution. Similar approaches were undertaken by many authors [65, 66] to understand the effect of a single shot on the stress and strain distribution at the specimen's surface. The dynamic modeling of a single shot was initially conducted by Johnson [67] and Iida [68]. With the advent of high performance computing facilities in addition to the availability of multiple commercial FE codes, dynamic 2-D and 3-D FE simulations of shot peening have been successful in predicting the residual stress distribution in a variety of metallic materials [69-75].

Although much progress has been made with regard to modeling surface treatments, detailed FE studies of fatigue crack formation and small crack growth behavior in such processed materials have been very limited. This is due to the vast disparity in the scales between the specimen dimensions (> 1mm) at which process parameters are framed and the underlying microstructure attributes such as nonmetallic inclusions (~5 μm) that dictate the HCF performance of the gear steels. The microstructure has even lower characteristic scales ranging from several nanometers to the order of 1 μm. Due to the

highly localized nature of fatigue crack formation occurring at fatigue critical 'hot spots' within the material, it is computationally prohibitive to perform fully coupled analysis of process routes and fatigue crack formation in martensitic steels. The microstructure hierarchy exhibited by lath martensite microstructure, in addition to the presence of submicron size carbides, demands a robust hierarchical computational framework to couple the extrinsic and intrinsic factors influencing the fatigue resistance of lath martensitic steels.

3.2.2. Review of approaches to couple process routes and fatigue life prediction

Historically, relatively simple macroscopic fatigue parameters have been used in stress-based criteria for HCF, with constants and parametric forms specialized to each alloy system [10]. The resulting idealizations based on pure metals, both experimentally and theoretically, tend to support the empirical Coffin-Manson power law relation [76] for the number of cycles to fatigue crack formation and growth in the MSC regime. However, fatigue at the microstructure scale is a complex, evolutionary process with stages of formation and growth that depend on the hierarchical morphology of phases and grains, as well as on the presence of primary nonmetallic inclusions in high strength steels. Additionally, it is critical to understand the role of residual stresses developed during processing in the vicinity of primary inclusions.

Toyada et al. [13] performed a series of rotating-bending fatigue tests on shot peened Cr-Mo steels and estimated the influence of the inclusions on the fatigue strength, employing the projected $\sqrt{area}$ approach suggested by Murakami and Endo [14], with necessary modifications to incorporate the residual stress effects. They showed that there exists a critical inclusion size that initiates subsurface failure within the specimen. Linear

elastic fracture mechanics (LEFM) based approaches to fatigue resistance typically assume an initial crack with size determined by inclusion size, regardless of the mode of crack formation or the condition of inclusion matrix interfaces. In this case, crack arrest is posed to occur if either the apparent LEFM ΔK is less than the small crack threshold value, ΔK_{th}, or if the crack driving force, ΔK, reduces as the crack grows from the inclusion or due to development of roughness and/or plasticity induced closure to levels below the long crack ΔK_{th}. Hence, the effects of inclusion size and subsurface depths are considered in the context of LEFM ΔK and concept of threshold ΔK_{th}. The semi-empirical Murakami and Endo model has successfully predicted upper and lower bounds on service lives for specimens containing inclusions.

The LEFM approach has been widely applied for the bending fatigue analysis of carburized components and steels [77-79]. Kim and co-workers [77] studied the effect of residual stress near the surface on the fatigue life using LEFM. The influence of residual stress on fatigue life was quantified by analyzing the change in stress intensity factor due to residual stress. Sharma and co-workers [78] presented a detailed study of various factors influencing K_{1c} of case steels including alloying elements, retained austenite and carbon content. Lin et al. [79] investigated the general methodology of bending fatigue life prediction using strain life and fracture mechanics approaches for SAE 8620 steel. Both approaches were reported to compare reasonably well with experimental data on fatigue life, although the strain life approach proved to be more conservative in its predictions. The life prediction models employed in these previous numerical and analytical studies are insufficient to understand the detailed mechanistic and microstructure-related causes of crack formation at nonmetallic inclusions or to compare

more detailed scenarios in terms of inclusion type, interface condition, and so forth. Furthermore, the influence of the damage state of the second phase particles on fatigue crack formation would be essential to devise methods to mitigate such phenomena. In order to develop models for fatigue crack formation at inclusions, detailed and accurate information regarding the local deformation and stress conditions in the proximity of inclusions is imperative.

Mackaldener and co-workers [80] developed a two-dimensional plane strain gear tooth FE model and studied the stress state history at every point within the tooth during a single contact load cycle. The residual stress induced through case hardening was simulated by applying a thermal load cycle and the McDiarmid critical plane approach [81] was employed to project the fatigue crack formation at various depths, with necessary modifications to incorporate shot peening effects. They reported that development of tensile residual stresses due to case hardening led to high risk of fatigue crack formation in the interior of the tooth. Although their method was computationally effective and considered various aspects of surface treatment in the macroscopic analysis, it was not able to describe the root cause for crack formation occurring beneath the surface region where the residual stresses are still compressive and it may not be sufficient to describe the role of microstructural inhomogenieties and interfacial damage conditions of inclusions in such failure scenarios. Borbeley et al. [82] attempted to study the cause for subsurface failures initiating from pores in AZ91 magnesium alloys through 3D FE simulations. The results of local stresses and plastic strains in the vicinity of the pores showed that critically sized pores present just beneath the surface have maximum tendency to form fatigue cracks. Melander and Gustavsson [18] performed 2-D FE based

investigation of short cracks growing from nonmetallic inclusions in AISI 51200 martensitic bearing steel under the influence of thermal residual stresses generated during heat treatment. The thermal stresses were introduced by virtue of CTE mismatch between the inclusion and the steel matrix and fatigue calculations were performed by introducing stationary cracks in the vicinity of primary inclusions. The crack driving force was measured in terms of cyclic crack tip opening displacement. The authors reported that the crack driving force was significantly reduced by increasing the thermal misfit between matrix and inclusions. Furthermore, the crack driving force in the vicinity of a pore was observed to be significantly higher than that in the vicinity of a hard intact alumina inclusion. Although the aforementioned findings are relevant to understanding the effect of thermal residual stresses on fatigue crack formation, the FE framework is an over-simplification of the complex transformation process that occurs during heat treatment.

Clearly, residual stresses play a pivotal role in influencing fatigue crack formation and early MSC propagation within the material. Significant portion of the service life is consumed in fatigue crack formation and MSC growth on the order of the nonmetallic inclusions in HCF [16]. Considerable effort has been made to accurately model the residual stresses and thereby to understand their influence on the service life of the component [83-90]. When analyzing the fatigue failure initiating at nonmetallic primary inclusions, it is essential to consider the effects of damaged particles or inclusions and their influence on fatigue crack formation [5, 18, 19, 91-93].

The aim of the present study is to quantify the potency for fatigue crack formation from damaged subsurface inclusions using FIPs in carburized and shot peened gear steels. Detailed FE analyses of the failure scenarios described above has been very

limited. This work presents initial efforts to develop a 3D modeling strategy for estimating fatigue potency of martensitic gear steels with Al_2O_3 inclusions. A new algorithm is presented to account for representative residual stresses induced via plastic deformation due to shot peening. Case hardening (carburization and tempering) is considered by varying the material properties from surface to core. To determine quantitative relationships between local cyclic plastic strains and far-field loading, representative 3D finite element meshes are constructed which contain inclusions surrounded by carburized matrix. Cracked and debonded inclusions are considered, consistent with experimental findings as reported in Chapter 2. Nonlocal average values of plastic shear strain range [19, 92, 93] and the Fatemi-Socie parameter [94] are considered as the FIPs. The fatigue crack formation potency at various case depths is compared with experimental findings. Additionally, a methodology is presented to estimate the critical inclusion spacing to achieve negligible interaction in fatigue. Furthermore, effect of orientation of inclusions in a cluster with respect to loading axis and free surface is systematically investigated with the intention of identifying the desirable orientation for enhanced fatigue resistance. All simulations were performed using ABAQUS [95] .

3.3. Characterization of mechanical properties of matrix and inclusions

Three-dimensional FE analyses were performed to understand the mechanisms of fatigue crack formation and early growth within the tempered martensite matrix. Detailed description of heat treatment, surface treatment and composition of the material is presented by Tiemens [27]. The inclusions were assumed to be isotropic, linear elastic

30
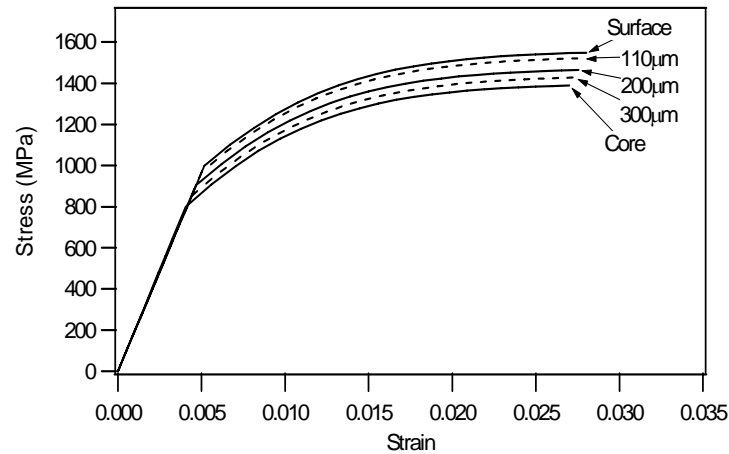
Figure 3.1. *Simulated monotonic tension stress-strain behaviors as a function of depth from surface. Depth of core is 1.2 mm below surface.*

with Young's modulus E = 400 GPa and Poisson's ratio $\nu = 0.2$. The matrix was modeled as a rate-independent elastic-plastic material with a nonlinear kinematic hardening law cast in a hardening minus dynamic recovery format. After carburization, the variation of carbon content from the surface to core has significant influence on local mechanical properties of the material. Elastic modulus, yield strength and work hardening rate depend on carbon content. Donzella et al. [96] and Pedersen et al. [97] presented an empirical relation between yield strength and micro-hardness for case hardened steel. Elghazal et al. [98] and Vincent et al. [99] presented a novel technique to characterize the local elasto-plastic properties of surface hardened steels through nano-indentation measurements and surface hardness profile. Considering the experimental observations and applying the empirical relations to the micro-hardness values presented in Figure 2.4, the material parameters of martensitic gear steel were obtained for FE

31

analyses. Figure 3.1 shows the corresponding simulated monotonic tension stress-strain curves at various depths for the material considered[*].

3.4. Elasto-plastic framework

The rate-independent plasticity model with kinematic hardening for the matrix employs the simple Mises yield surface

$$F = f(\underset{\sim}{\sigma} - \underset{\sim}{\chi}) - \sigma_y^2 \tag{3.1}$$

with $F = 0$ during plastic flow, and

$$f(\underset{\sim}{\sigma} - \underset{\sim}{\chi}) = \frac{3}{2}(\underset{\sim}{S} - \underset{\sim}{\chi}') : (\underset{\sim}{S} - \underset{\sim}{\chi}') = \frac{3}{2}(S_{ij} - \chi'_{ij})(S_{ij} - \chi'_{ij}) \tag{3.2}$$

Here, $\underset{\sim}{S}$ is the deviatoric stress tensor, $\underset{\sim}{\sigma}$ is the stress tensor, $\underset{\sim}{\chi}$ is the back stress tensor and $\underset{\sim}{\chi}'$ is its deviatoric component. The uniaxial cyclic yield strength is defined by σ_y.

The associative plastic flow rule is given by

$$\dot{\underset{\sim}{\varepsilon}}^p = \sqrt{\frac{3}{2}} \dot{\bar{\varepsilon}}^p \frac{\partial F}{\partial \underset{\sim}{\sigma}} \left\| \frac{\partial F}{\partial \underset{\sim}{\sigma}} \right\|^{-1} = \sqrt{\frac{3}{2}} \dot{\bar{\varepsilon}}^p \underset{\sim}{N} = \sqrt{\frac{3}{2}} \dot{\bar{\varepsilon}}^p \frac{\underset{\sim}{S} - \underset{\sim}{\chi}'}{\left\| \underset{\sim}{S} - \underset{\sim}{\chi}' \right\|} \tag{3.3}$$

---

[*] While estimating the cyclic yield strength of the case layer, the material was assumed to significantly soften (~35%) in fatigue ([100] Boller C, Seeger T. Materials Data for Cyclic Loading, Part B: Low Alloy Steels. New York: Elsevier, 1987). However, such as assumption was not validated with experiments for the lath martensitic steel modeled in this study. It is noted that based on the hardness values reported in Figure 2.4 the corresponding yield strength will be considerably higher. Hence, the simulations conducted in this Chapter are primarily intended to present the algorithm and framework to conduct fatigue analyses considering the effects of compressive residual stresses.

where $\dot{\varepsilon}^p$ the plastic strain rate tensor and $\dot{\bar{\varepsilon}}^p$ is the equivalent plastic strain rate, defined by

$$\dot{\bar{\varepsilon}}^p = \sqrt{\frac{2}{3}\dot{\varepsilon}^p : \dot{\varepsilon}^p} \qquad (3.4)$$

The evolution equation for the back stress tensor $\underset{\sim}{\chi}$ is expressed as [101]

$$\dot{\underset{\sim}{\chi}} = \frac{c}{\sigma_y}\left(\underset{\sim}{\sigma} - \underset{\sim}{\chi}\right)\dot{\bar{\varepsilon}}^p - r\underset{\sim}{\chi}\dot{\bar{\varepsilon}}^p \qquad (3.5)$$

where c and r are material parameters. Here, c is the initial kinematic hardening modulus and r determines the rate of dynamic recovery of the back stress with increasing plastic deformation. Isotropic hardening is neglected in view of the desire to simulate cyclically stable response in parametric studies with pure kinematic hardening.

The elastic response is given by

$$\underset{\sim}{\sigma} = \underset{\approx}{C} : \underset{\sim}{\varepsilon}^e \qquad (3.6)$$

where $\underset{\sim}{\varepsilon}^e$ denotes the elastic strain tensor, and $\underset{\approx}{C}$ is the isotropic elastic stiffness tensor. It is assumed that room temperature response is modeled, so temperature and rate effects are neglected.

3.4.1. Relations in connection with the return mapping scheme

To estimate the increment in the hydrostatic part of the back stress we re-write Equation (3.5) in the incremental form as shown below,

$$d\underset{\sim}{\chi} = \frac{c}{\sigma_y}\left(\underset{\sim}{\sigma} - \underset{\sim}{\chi}\right)d\bar{\varepsilon}^p - r\underset{\sim}{\chi}d\bar{\varepsilon}^p \tag{3.7}$$

Principal components in Equation (3.7) can be written as,

$$d\chi_{i\bar{i}} = \frac{c}{\sigma_y}\left(\sigma_{i\bar{i}} - \chi_{i\bar{i}}\right)d\bar{\varepsilon}^p - r\chi_{i\bar{i}}d\bar{\varepsilon}^p \tag{3.8}$$

The bar over indices indicates no summation. The incremental hydrostatic part of the back stress tensor is obtained from Equation (3.8),

$$d\chi^h = \frac{c}{\sigma_y}\left(\sigma^h - \chi^h\right)d\bar{\varepsilon}^p - r\chi^h d\bar{\varepsilon}^p \tag{3.9}$$

where $\sigma^h = \dfrac{\sigma_{ii}}{3}$ and $\chi^h = \dfrac{\chi_{ii}}{3}$

The back stress tensor is additively decomposed into its deviatoric and hydrostatic parts, i.e.,

$$d\chi_{ij} = d\chi'_{ij} + d\chi^h \delta_{ij} \tag{3.10}$$

Applying Equation (3.7), Equation (3.10) can be re-written as,

$$d\chi'_{ij} = \frac{c}{\sigma_y}\left(\sigma_{ij} - \chi_{ij}\right)d\bar{\varepsilon}^p - r\chi_{ij}d\bar{\varepsilon}^p - d\chi^h \delta_{ij} \tag{3.11}$$

Inserting Equation (3.9) into Equation (3.11) we obtain,

$$d\chi'_{ij} = \frac{c}{\sigma_y}\left(S_{ij} - \chi'_{ij}\right)d\bar{\varepsilon}^p - r\chi'_{ij}d\bar{\varepsilon}^p \tag{3.12}$$

3.4.2. Backward Euler discretization

If we consider the interval from a state n to $n+1$, the fully implicit backward Euler method allows Equations (3.1) to (3.6) to be discretized as follows [102]

$$\varepsilon_{n+1} = \varepsilon^e_{n+1} + \varepsilon^p_{n+1} \tag{3.13}$$

$$\varepsilon^p_{n+1} = \varepsilon^p_n + \Delta\varepsilon^p_{n+1} \tag{3.14}$$

$$\sigma_{n+1} = \underset{\sim}{C} : \left(\varepsilon_{n+1} - \varepsilon^p_{n+1}\right) \tag{3.15}$$

$$\Delta\varepsilon^p_{n+1} = \sqrt{\frac{3}{2}}\Delta\lambda_{n+1}\underset{\sim}{N}_{n+1} \quad (\lambda\text{ - plastic multiplier}) \tag{3.16}$$

$$\underset{\sim}{N}_{n+1} = \sqrt{\frac{3}{2}}\frac{\underset{\sim}{S}_{n+1} - \underset{\sim}{\chi}'_{n+1}}{\overline{\sigma}_{n+1}} \tag{3.17}$$

$$F_{n+1} = \frac{3}{2}\left(\underset{\sim}{S}_{n+1} - \underset{\sim}{\chi}'_{n+1}\right):\left(\underset{\sim}{S}_{n+1} - \underset{\sim}{\chi}'_{n+1}\right) - \sigma^2_y \tag{3.18}$$

$$\underset{\sim}{\chi}_{n+1} = \underset{\sim}{\chi}_n + \frac{c}{\sigma_y}(\underset{\sim}{\sigma}_{n+1} - \underset{\sim}{\chi}_{n+1})d\overline{\varepsilon}^p - r\underset{\sim}{\chi}_{n+1}d\overline{\varepsilon}^p \tag{3.19}$$

3.4.3. Nonlinear scalar equations

Given the constitutive variables at n and the total strain increment $\Delta\varepsilon_{n+1}$, we need to obtain σ_{n+1}, satisfying the discretized relations given in Equations (3.13)-(3.19). To solve

for σ_{n+1} we perform return mapping, which consists of elastic predictor and plastic corrector. The elastic predictor stress is given by

$$\sigma_{n+1}^* = \underset{\approx}{C} : \left(\varepsilon_{n+1} - \varepsilon_n^p \right) \tag{3.20}$$

The yield condition is then checked using the yield function

$$F_{n+1}^* = \frac{3}{2} \left(\underset{\sim}{S}_{n+1}^* - \underset{\sim}{\chi}_n' \right) : \left(\underset{\sim}{S}_{n+1}^* - \underset{\sim}{\chi}_n' \right) - \sigma_y^2 \tag{3.21}$$

If $F_{n+1}^* \leq 0$, σ_{n+1}^* is accepted as σ_{n+1}. If $F_{n+1}^* > 0$, σ_{n+1}^* is brought on the yield surface

$F_{n+1} = 0$ as follows :

Substituting Equations (3.14) and (3.20) into Equation (3.15) gives

$$\sigma_{n+1} = \sigma_{n+1}^* - \underset{\approx}{C} : \Delta\varepsilon_{n+1}^p \tag{3.22}$$

where $\underset{\approx}{C} : \Delta\varepsilon_{n+1}^p$ is the plastic corrector. Taking the deviatoric part of the above relation

and noting that $\underset{\approx}{C} : \Delta\varepsilon_{n+1}^p = 2G\Delta\varepsilon_{n+1}^p$ (G -shear modulus) we obtain

$$\underset{\sim}{S}_{n+1} - \underset{\sim}{\chi}_{n+1}' = \underset{\sim}{S}_{n+1}^* - 2G\Delta\varepsilon_{n+1}^p - \underset{\sim}{\chi}_{n+1}' \tag{3.23}$$

To evaluate $\underset{\sim}{\chi}_{n+1}'$ we use Equation (3.12) and perform implicit integration, i.e.,

$$\underset{\sim}{\chi}_{n+1}' - \underset{\sim}{\chi}_n' = \frac{c}{\sigma_y} \left(\underset{\sim}{S}_{n+1} - \underset{\sim}{\chi}_{n+1}' \right) \Delta\lambda_{n+1} - r\Delta\lambda_{n+1}\underset{\sim}{\chi}_{n+1}' \tag{3.24}$$

where $\Delta\lambda_{n+1} = d\bar{\varepsilon}^p_{n+1}$. Simplifying Equation (3.24) we obtain,

$$\chi'_{n+1} = \frac{\chi'_{n+1} + \dfrac{c}{\sigma_y}\left(S_{n+1}\right)\Delta\lambda_{n+1}}{\left(1 + \Delta\lambda_{n+1}\left(\dfrac{c}{\sigma_y} + r\right)\right)}$$ (3.25)

Equation (3.25) can be rewritten as

$$\chi'_{n+1} = \Xi_{n+1}\left(\chi'_{n+1} + \frac{c}{\sigma_y}\left(S_{n+1}\right)\Delta\lambda_{n+1}\right)$$ (3.26)

where $\Xi_{n+1} = \dfrac{1}{\left(1 + \Delta\lambda_{n+1}\left(\dfrac{c}{\sigma_y} + r\right)\right)}$

Similarily, the hydrostatic part of the back stress tensor can be obtained using Equation (3.9), i.e.,

$$\chi^h_{n+1} = \Xi_{n+1}\left(\chi^h_n + \frac{c}{\sigma_y}\left(\sigma^h_{n+1}\right)\Delta\lambda_{n+1}\right)$$ (3.27)

In Equation (3.22), $\Delta\varepsilon^p_{n+1}$ is eliminated using Equations (3.16) and (3.17), i.e.,

$$S_{n+1} - \chi'_{n+1} = S^*_{n+1} - 3G\Delta\lambda_{n+1}\left(\frac{S_{n+1} - \chi'_{n+1}}{\bar{\sigma}_{n+1}}\right) - \chi'_{n+1}$$ (3.28)

Equation (3.28) can be simplified using Equation (3.25) to obtain

$$S_{n+1} - \chi'_{n+1} = \frac{\left(S^*_{n+1} - \Xi_{n+1}\left(\chi'_n + \frac{c}{\sigma_y}(S_{n+1})\Delta\lambda_{n+1}\right)\right)\bar{\sigma}_{n+1}}{\bar{\sigma}_{n+1} + 3G\Delta\lambda_{n+1}} \tag{3.29}$$

In the absence of isotropic hardening the following relation holds,

$$\bar{\sigma}_{n+1} = \sigma_y \tag{3.30}$$

Substituting Equations (3.29) and (3.30) into Equation (3.19) we obtain the final form for equivalent plastic strain increment, i.e.,

$$\Delta\lambda_{n+1}^{(k+1)} = \frac{\sqrt{\frac{3}{2}\left[S^*_{n+1} - \Xi_{n+1}\left(\chi'_n + \frac{c}{\sigma_y}(S_{n+1})\Delta\lambda_{n+1}^{(k)}\right)\right]:\left[S^*_{n+1} - \Xi_{n+1}\left(\chi'_n + \frac{c}{\sigma_y}(S_{n+1})\Delta\lambda_{n+1}^{(k)}\right)\right]} - \sigma_y}{3G} \tag{3.31}$$

Equation (3.31) is solved using method of successive substitution to obtain $\Delta\lambda_{n+1}$. A flow chart is presented in Figure 3.2 elaborating on the numerical scheme employed to obtain $\Delta\lambda_{n+1}$. In Equation (3.31) the superscript k and $k+1$ correspond the number of substitutions in the method of successive substitution. A convergence criterion is set as shown in Equation (3.32).

$$\left| 1 - \frac{\Delta\lambda_{n+1}^{(k+1)}}{\Delta\lambda_{n+1}^{(k)}} \right| \leq 10^{-5} \tag{3.32}$$
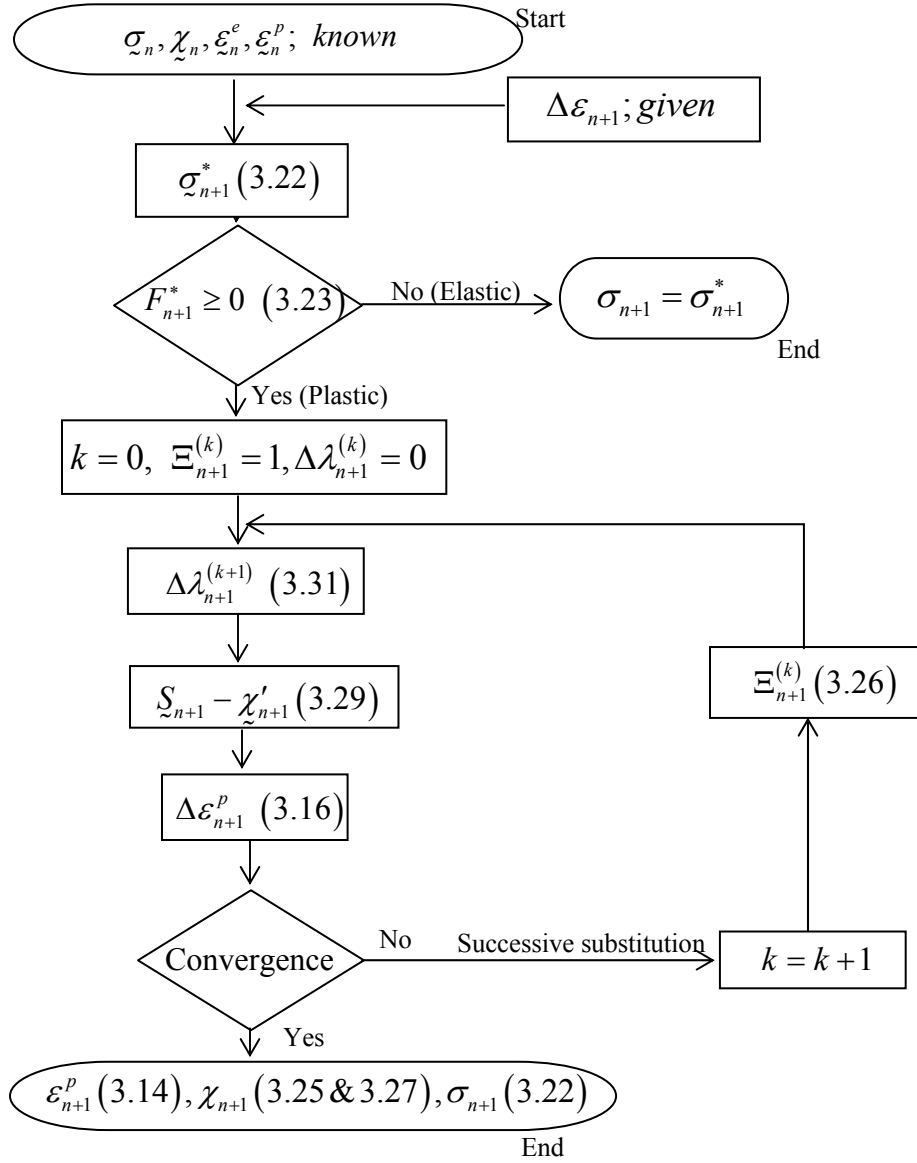
Figure 3.2 *Flow diagram for radial return mapping scheme with successive substitution.*
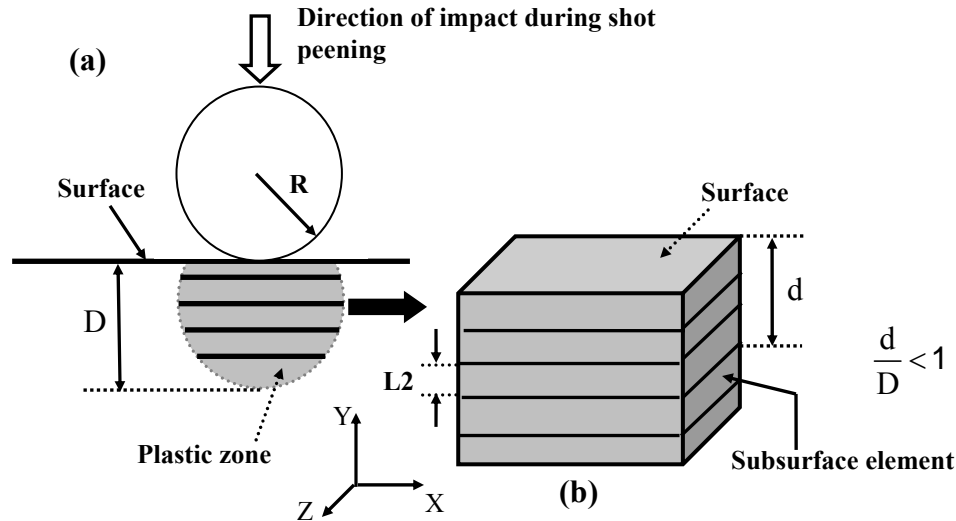
Figure 3.3. *(a) A schematic showing a metallic ball impacting the specimen surface during shot peening, causing constrained plastic deformation to a depth D below surface, and (b) an equivalent volume element of the plastic zone divided into several subsurface elements, each corresponding to a depth d below the surface where shot peening and fatigue simulations are performed.*

3.5. Imposition of residual stress: modeling the effect of shot peening process

During processing, heat treatment (carburization and tempering) and surface treatment (shot peening) introduce a compressive residual stress field near the surface. Comparatively, the residual stress introduced by carburization and tempering (-100 MPa to -300 MPa) is much lower than that introduced through shot peening, especially close to the surface layer of the specimen [27, 103]. A series of thermo-mechanical processes, such as diffusion, phase transformation, dynamic elastic-plastic deformation, and deformation-induced phase transformation are involved during carburization, tempering and shot peening. As a result, it is quite complex to simulate the evolution of residual stress based on the physical mechanisms. Although mechanism-based FE simulation of residual stress is effective for two-dimensional calculations, three-dimensional

simulations become computationally more demanding. Alternatively, a simplified scheme is followed to impose the measured residual stresses.

After carburization, the mechanical properties vary only with the depth. The bombardment of metallic balls on the specimen surface during shot peening gives rise to constrained and concentrated plastic deformation at and near the surface. Kobayashi and co-workers [104] reported that the shot peening process effectively induces equi-biaxial residual compressive stresses within the specimen by virtue of plastic deformation. It is reasonable to assume that the residual stress in the steel matrix at and near the surface layer after shot peening is also equi-biaxial. Figure 3.3a shows a schematic of the shot peening process and the region below the surface of depth D experiencing plastic deformation is denoted as the 'plastic zone'. Figure 3.3b shows an equivalent volume element of the plastic zone divided into multiple 'subsurface element', each corresponding to a depth d below surface. The dimensions of the 'subsurface element' are L1, L2, and L3 in directions X, Y, and Z, respectively. The residual elastic strains present within the deformed region are associated with compressive stresses; the self-equilibrating nature of the residual stresses results in development of tensile stress state deeper in the interior.
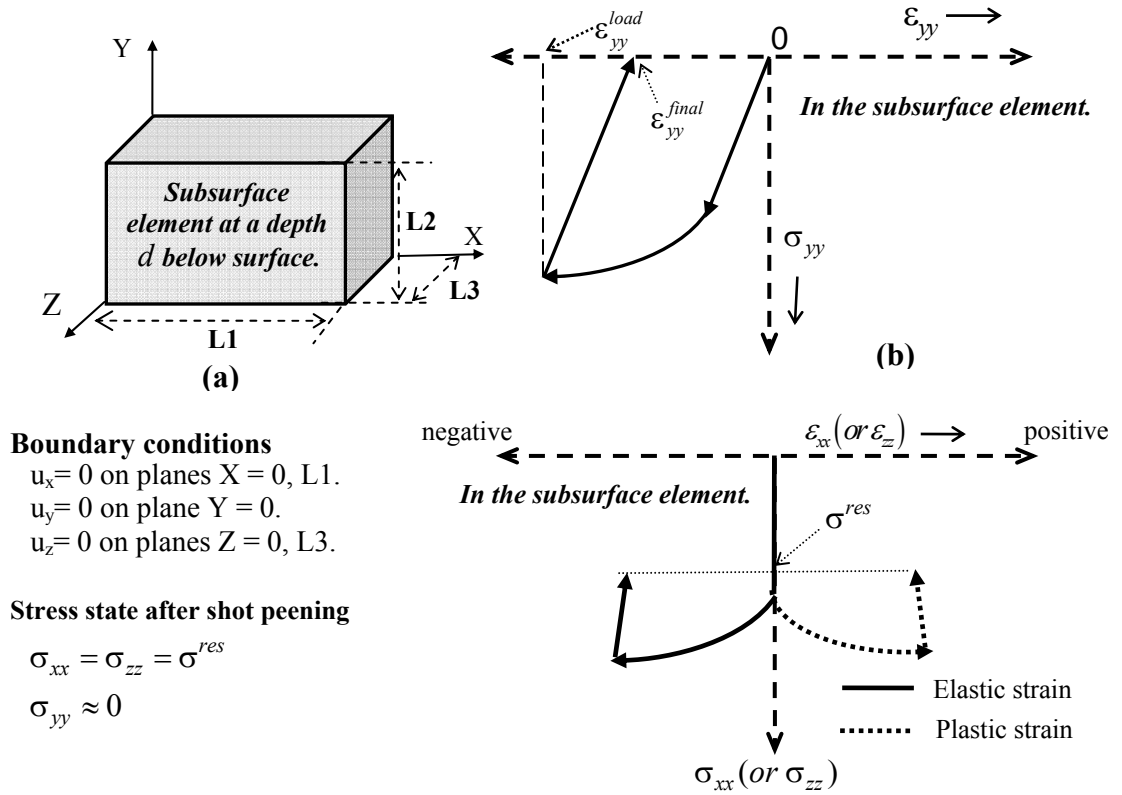
Figure 3.4. *Methodology to simulate shot peening process. (a) Schematic showing a subsurface element on which the strains are imposed, (b) σ_{yy} vs ε_{yy} response in the subsurface element during shot peening simulation, and (c) variation of elastic and plastic strain in X and Z directions in the subsurface element during shot peening.*

During shot peening all principal stresses remain compressive. With the aforementioned observations regarding shot peening, a methodology is developed to simulate compressive residual stresses within the material with the constraint that all normal components of the stress tensor remain compressive during shot peening in the surface coordinate system XYZ (Figure 3.4). The procedure is summarized as follows:

1. Consider a homogeneous matrix subsurface element of the specimen at a depth *d* below surface, initially without inclusions, as shown in Figure 3.4a. The carburized material properties corresponding to the depth *d* is assigned to the subsurface element.

2. Imposing the boundary conditions shown in Figure 3.4, the subsurface element is subjected to uniaxial compression in direction Y to strain levels calculated from the elastoplastic constitutive relations, in connection with the following step (ε_{yy}^{load} in Figure 3.4b). The total strain components (elastic plus plastic) in the X and Z directions are assumed as zero at each stage of the process, in accordance with overall constraints.

3. The compression is followed by unloading in direction Y (ε_{yy}^{final} in Figure 3.4b) to elastic strain levels that match the measured macroscopic residual stress distribution in the material as a function of depth (Figure 3.4c).

4. The resulting strain-time history is then applied as boundary conditions on the same subsurface element with embedded inclusions that are intact, debonded or cracked to assess the local residual stresses and strains in the vicinity of inclusions as initial conditions for subsequent fatigue simulations. This is repeated for each subsurface depth of interest.

In the above algorithm, a 'subsurface element' is a volume element representing the steel matrix with dimensions in μm (L1, L2, and L3 in Figure 3.4a). While considering the embedded inclusion of size δ, the dimensions of the subsurface element are chosen to be sufficiently large that the inclusion experiences negligible boundary interaction effects, i.e., $\dfrac{\delta}{L1}, \dfrac{\delta}{L2}$ and $\dfrac{\delta}{L3} \ll 1$ with L2<<D. The above methodology mimics the shot peening process, and is suitable for initializing residual stresses prior to conducting

fatigue calculations. The following direction convention holds for all subsequent 3-D calculations:

- Direction of impact (shot peening) – along Y direction

- Equibiaxial residual stress state – along X and Z directions

- Cyclic loading – along Z direction

In reality, the localized high strain rate deformation at and near the surface of the specimen during shot peening can result in cracking and debonding of inclusions. Plastic strains of very high magnitude at the point of impact during shot peening can alter the matrix microstructure (e.g., dislocation density) at the case layer. The plastic strain magnitudes vary with the depth from the free surface. Also, the local equivalent plastic strain magnitudes in the vicinity of debonded and cracked primary inclusions can be significantly higher (> 6 %) than that in the far-field and will be demonstrated later. Furthermore, formation of local free surface during decohesion of inclusion-matrix interface can result in significant softening of matrix encompassing the debonded inclusion. In this study, we pursue the strategy of simulating inclusions that are assumed to be already cracked or debonded at the beginning of the shot peening process as a means of assessing their influence on the local residual stress state and the fatigue crack formation potency at the inclusion.

3.6. Elasto-plastic relations relevant to imposing compressive residual stresses

The stress state at any subsurface depth *after* shot peening is given by (see Figure 3.4)

$$\sigma_{xx} = \sigma_{zz} = \sigma^{res}$$
$$\sigma_{yy} = 0$$
$$\tau_{xy} = \tau_{xz} = \tau_{yz} = 0 \tag{3.33}$$
$$\chi_{xy} = \chi_{xz} = \chi_{yz} = 0$$

During plastic deformation (shot peening), the following quantities and their differential increments always satisfy

$$\varepsilon_{xy}^p = \varepsilon_{xz}^p = \varepsilon_{yz}^p = 0 \qquad d\varepsilon_{xy}^p = d\varepsilon_{xz}^p = d\varepsilon_{yz}^p = 0$$
$$\varepsilon_{xx}^p + \varepsilon_{yy}^p + \varepsilon_{zz}^p = 0 \ \text{ and } \ d\varepsilon_{xx}^p + d\varepsilon_{yy}^p + d\varepsilon_{zz}^p = 0 \ \text{ (incompressibility)} \tag{3.34}$$
$$\varepsilon_{xx}^p = \varepsilon_{zz}^p = -\frac{1}{2}\varepsilon_{yy}^p \qquad d\varepsilon_{xx}^p = d\varepsilon_{zz}^p = -\frac{1}{2}d\varepsilon_{yy}^p$$

During the shot peening process the shear strain components are zero in the XYZ principal coordinate frame, i.e.,

$$\varepsilon_{xy} = \varepsilon_{yz} = \varepsilon_{zx} = 0 \tag{3.35}$$

Expanding the yield function in Equation (3.2) gives

$$F = \left[2(\sigma_{xx} - \chi_{xx}) - (\sigma_{yy} - \chi_{yy}) - (\sigma_{zz} - \chi_{zz}) \right]^2 + \left[2(\sigma_{zz} - \chi_{zz}) - (\sigma_{xx} - \chi_{xx}) - (\sigma_{yy} - \chi_{yy}) \right]^2 + \tag{3.36}$$
$$\left[2(\sigma_{yy} - \chi_{yy}) - (\sigma_{xx} - \chi_{xx}) - (\sigma_{zz} - \chi_{zz}) \right]^2 - 6\sigma_y^2 = 0$$

Due to equi-biaxial deformation, the following relationships hold during the entire process of shot peening:

$$\sigma_{xx} - \chi_{xx} = \sigma_{zz} - \chi_{zz}$$
$$S_{xx} - \chi'_{xx} = S_{zz} - \chi'_{zz} \tag{3.37}$$
$$\varepsilon_{xx}^p = \varepsilon_{zz}^p, \quad \dot{\varepsilon}_{xx}^p = \dot{\varepsilon}_{zz}^p$$

45

Inserting Equation (3.37) into Equation (3.36) the yield function reduces to

$$F = \left[\left(\sigma_{xx} - \chi_{xx} \right) - \left(\sigma_{yy} - \chi_{yy} \right) \right]^2 - \sigma_y^2 = 0 \tag{3.38}$$

Using the relation in Equation (3.9) the increment of equivalent plastic strain is given by,

$$d\bar{\varepsilon}^p = \left| d\varepsilon_{yy}^p \right| = 2 \left| d\varepsilon_{xx}^p \right| \tag{3.39}$$

Using the three-dimensional Hooke's law, the elastic and plastic strains at the end of shot peening process can be obtained by applying the boundary conditions shown in Figure 3.4, i.e.,

$$
\begin{aligned}
\varepsilon_{xx}^{e,final} &= \frac{\sigma^{res}}{E}\left(1-v\right) = -\varepsilon_{xx}^{p,final} \\
\varepsilon_{zz}^{e,final} &= \frac{\sigma^{res}}{E}\left(1-v\right) = -\varepsilon_{zz}^{p,final} \\
\varepsilon_{yy}^{e,final} &= \frac{-v}{E}\left(2\sigma^{res}\right)
\end{aligned}
\tag{3.40}
$$

Here, the superscript '*final*' corresponds to final strain state at the end of shot peening. Coupling Equations (3.34), (3.39), and (3.40), the final strain component along direction Y after unloading can be obtained as

$$\varepsilon_{yy}^{final} = \frac{-v}{E}\left(2\sigma^{res}\right) + 2\varepsilon_{xx}^{e,final} \tag{3.41}$$

In order to obtain the peak uniaxial compressive strain to be imposed along direction Y $\left(\varepsilon_{yy}^{load}\right)$ to induce the target residual stress level, the above equations coupled with the nonlinear kinematic hardening relation described in Equation (3.5) are solved numerically. We employ the method of successive substitution (see Section 3.4) along with an interval-halving scheme to iteratively solve the set of equations. Additionally, a closed form solution to estimate the compressive strains is derived in [105]. We do note that, a closed form solution is not possible for more complex elasto-plastic constitutive relations. For example, while considering isotropic hardening a numerical scheme such as the approach illustrated in this work will be more useful.

3.7. Modeling fatigue crack formation under cyclic loading
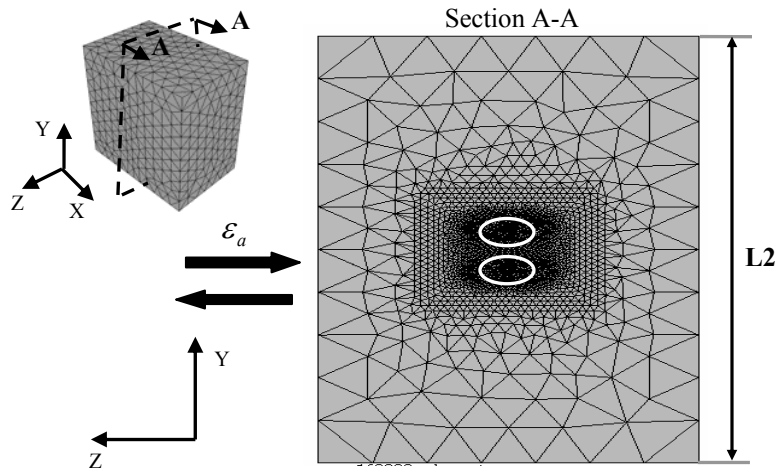
Figure 3.5. *Cross-section of FE mesh through the center of inclusion with refinement close to the inclusion.*

Three-dimensional FE simulations were performed to quantify FIPs at depths 75μm to 300 μm below the surface. Idealized shape inclusions (ellipsoidal and spherical) were used

to pursue parametric computational study of FIPs to evaluate relative potency of subsurface crack formation. Figure 3.5 shows a cross-section of a 3-D FE mesh with closely spaced inclusions. A fine mesh is employed close to the inclusion(s) for detailed investigation of inelastic deformation and stress state in the proximity of the inclusions. All simulations were performed using 4-node 3D tetrahedral elements (C3D4) in ABAQUS. Reduced integration is employed.

It was assumed that the inclusion sizes are small compared to the overall specimen dimensions and hence the gradient of applied stress and residual stress over an inclusion is negligible. With this assumption, the stress state is imposed at discrete depths within each subsurface inclusion-matrix volume element and the stresses and plastic strains around the inclusion(s) are examined. Figure 3.6 shows the variation of peak applied uniaxial compressive strain ε_{yy}^{load} and the strain after unloading ε_{yy}^{final} with depth for the martensitic gear steel during the shot peening simulation. The residual stress simulation is followed by three cycles of strain-controlled loading with $R_\varepsilon = 0.05$ (applied strain ratio). Since the remote loading is within the elastic limit, R_ε is effectively R_σ. Figure 3.7 shows a plot of peak applied strain during cyclic bending and its variation with depth. FIPs for crack formation are calculated over the third load cycle. Two FIPs, namely the nonlocal average maximum shear plastic strain range, $\Delta\gamma_{max}^{p*}$, and Fatemi-Socie (FS) parameter, $\Delta\Gamma$, are considered. The latter parameter also includes limited consideration for small crack propagation [106]. The FS parameter considers the effect of the maximum normal stress, σ_n^{max}, perpendicular to the plane of maximum cyclic plastic shear strain, and has proven to be a very effective correlative parameter for multiaxial fatigue [107]. It has been generalized by McDowell [6] and Shenoy et al. [108] to form the basis for microstructure-

48

sensitive small crack growth laws (microstructural fracture mechanics), with the latter study using computational micromechanics to compute the FS parameter. Several successful experimental correlations have been obtained on fatigue lives of different metallic materials using the FS critical plane approach (cf. [109-115]). The FS parameter is defined by

$$\Delta\Gamma = \frac{\Delta\gamma^{p*}}{2}\left(1 + K\frac{\sigma_n^{max*}}{\sigma_y}\right) \tag{3.42}$$

where, $K = 0.6$ is a material parameter that is assigned a value used for 1045 steel [94]. The superscript '*' denotes a nonlocal average value described later.
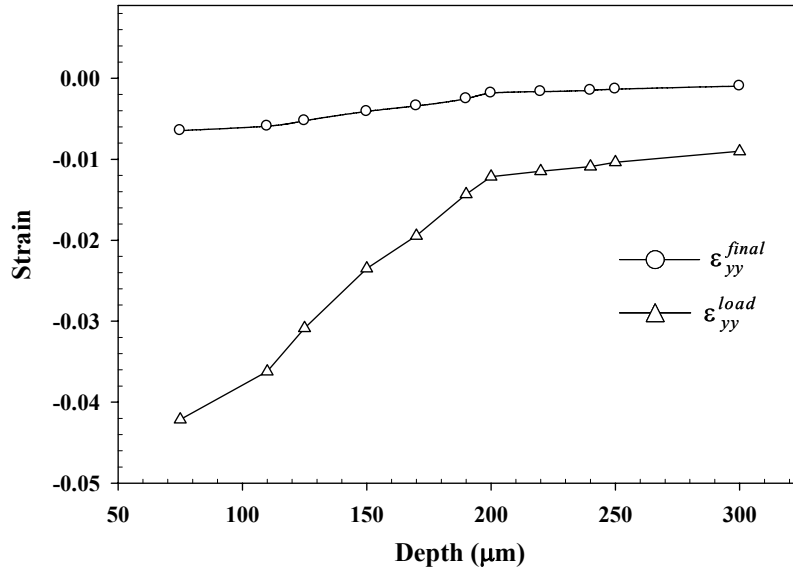
Figure 3.6. *Variation of the peak compressive strain $\left(\varepsilon_{yy}^{load}\right)$ and the strain after unloading $\left(\varepsilon_{yy}^{final}\right)$ along direction Y during shot peening simulation with depth.*

The cyclic plastic shear strain amplitude in the matrix is essential to the evaluation of potency of inclusions with regard to fatigue crack formation. In local FE analyses, the micronotch root maximum plastic shear strain amplitude is mesh-sensitive; it is therefore necessary to introduce a nonlocal volume averaging procedure over integration points in

the mesh to (i) effectively remove mesh dependence and also (ii) to accord with the physical process zone for crack formation (typically on the order of a micron). Motivated by earlier work [19, 92], the maximum plastic shear strain amplitude is averaged over a volume of 1 μm^3 (unit cube), which corresponds to 9.5% of the inclusion volume (for inclusion of minimum size), and is selected as that volume at the notch root that maximizes the the nonlocal plastic shear strain amplitude. We employ this nonlocal volume $\left(V_\delta = 1 \ \mu m^3\right)$ for all the cases examined in this parametric computational study. Naturally, such a small volume is considered in terms of evaluating the probability to form a crack, and larger domains would be necessary to consider propagation resistance.
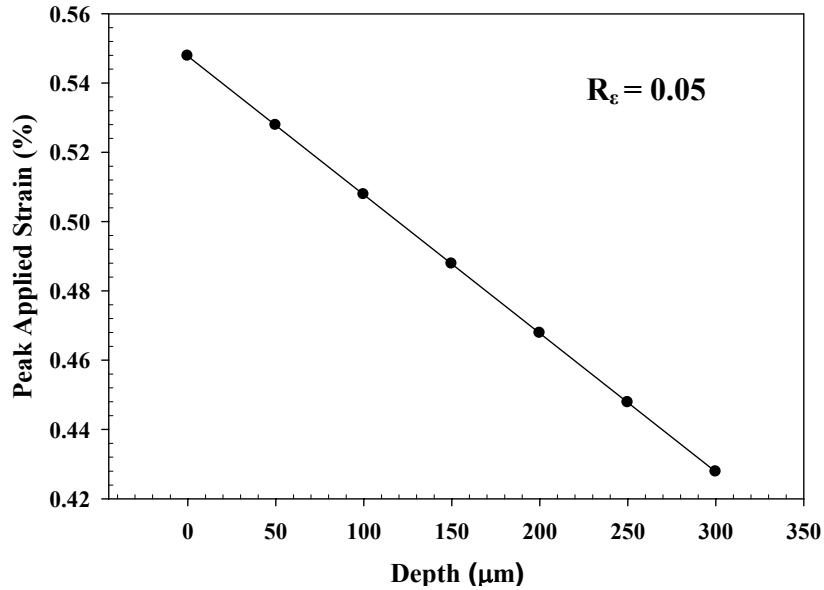
Figure 3.7. *Peak applied strain* $\left(\varepsilon_{zz}\right)$ *as a function of depth (bending) during cyclic loading.*

At every integration point lying within the nonlocal averaging region, we compute the plastic shear strain γ_θ^p on the plane-θ by projecting onto it the plastic strain tensor ε_{ij}^p at each integration point, i.e.,

$$\frac{\gamma_\theta^p}{2} = n_i \varepsilon_{ij}^p t_j \qquad \theta = 1 \ldots N \tag{3.43}$$

where n_i and t_j are the unit normal and tangent vectors, respectively, on the plane-θ, and N is the number of discrete planes. Discrete set of tangent vectors are screened on any given plane-θ to estimate the plastic shear strain. The nonlocal average plastic shear strain is then calculated by averaging over the volume V_δ of the nonlocal region, i.e.,

$$\gamma_\theta^{p*} = \frac{1}{V_\delta} \int_{V_\delta} \gamma_\theta^p dV \tag{3.44}$$

The nonlocal cyclic plastic shear strain range for every plane is calculated over the third load cycle of the simulation. The nonlocal maximum cyclic plastic shear strain range, is defined by

$$\Delta\gamma_{max}^{p*} = \max_\theta \left(\Delta\gamma_\theta^{p*} \right) \tag{3.45}$$

Once the critical plane and nonlocal maximum plastic shear strain range are determined, $\Delta\Gamma$ is calculated using Equation (3.42) at every integration point on the critical plane (determined by $\Delta\gamma_{max}^{p*}$) and a volume average is performed in the nonlocal region similar to Equation (3.44); this effectively results in a nonlocal FS parameter. A simple local form of Coffin-Manson law can be used to correlate the number of cycles for formation of fatigue cracks with each choice of FIP [10, 93] .

3.8. Results: effect of residual stresses

3.8.1. Cracked inclusion analyses

Cracked ellipsoidal inclusions, embedded in the elastoplastic matrix, were subjected to residual compressive stresses from simulated shot peening followed by three cycles of loading (strain controlled). Simulations were also performed with intact particles and results showed negligibly small FIPs for all case depths below the surface in this case. Similar observations were reported by Gall and co-workers [19] for A356 aluminum alloy. This may be due to the fact that the peak applied bending stress is below the elastic limit of C61 gear steel ($\leq 0.8\,\sigma_{ys}$). Also, localization of stresses and plastic strains in the matrix around intact particles are not as intense as those observed near damaged particles. In addition to the aforementioned observations, it is important to note that fatigue crack formation in the HCF regime is highly heterogeneous at the grain scale [10]. Investigation of the potency of intact particles to form fatigue cracks while operating close to the fatigue limit of the specimen demands rigorous scale-dependent and discrete dislocation plasticity simulations and the J_2 plasticity assumption may not be sufficient to capture such failure scenarios. Accordingly, this ideal case study focuses on cracks forming at damaged particles such as cracked and partially debonded inclusions where substantial cyclic plastic strains are predicted using a J_2 plasticity assumption.

Figure 3.8 illustrates the three-dimensional boundary conditions and orientation of a cracked particle with respect to the loading direction and the surface. It is assumed that inclusions tend to crack when the major axis of the ellipsoidal particle is oriented parallel to the loading direction. Table 3.1 summarizes the list of cases considered while analyzing the effect of cracked particle on fatigue crack formation in the matrix at

subsurface depths. In Tables 3.1 and 3.2, 2a and 2b represent the major and minor axis dimensions of the ellipsoidal inclusion, respectively; 2c and 2d represent that of the neighboring inclusion. L represents the longitudinal spacing between the inclusions, chosen to be 1μm in this limited parametric study. More detailed investigation of the effect of inclusion spacing will be presented later. For convenience, all cases and results presented in the subsequent sections will be addressed with the 'case pointer' listed in Table 3.1. Figure 3.9a shows the equivalent plastic strain contour plot around the cracked inclusions located at 250μm below surface, at the end of the third loading cycle for case R1, for example.
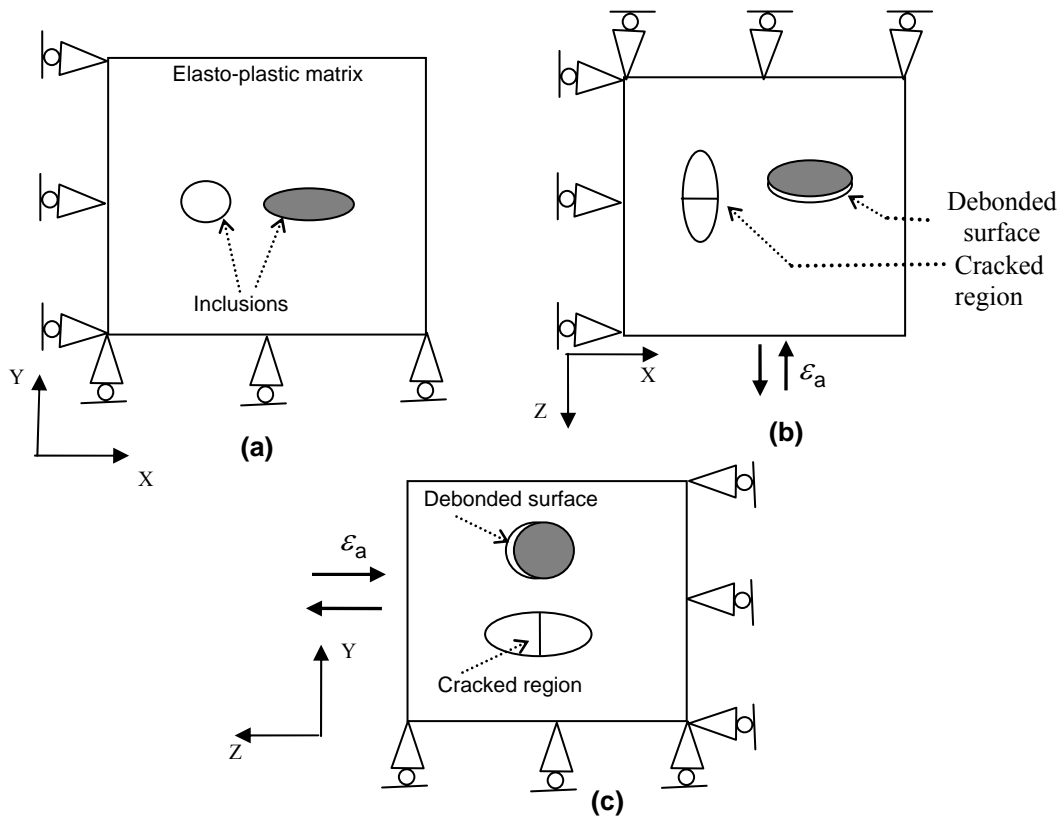
Figure 3.8. *Cross-sectional views of the 3-D section with embedded inclusion showing the debonded and cracked surfaces, boundary conditions, and cyclic loading direction in bending. Views across (a) XY, (b) XZ, and (c) YZ cutting planes through the center of the inclusion.*

Table 3.1. *List of cases analyzed in the study of cracked inclusions.*

Case pointer	No of inclusions	Shape of inclusion	2a	2b	2c	2d	L
P1	1	Ellipsoidal	5	2	-	-	-
Q1	2	Ellipsoidal	5	2	5	2	1
R1	2	Ellipsoidal	5	2	10	4	1

(all dimensions in μm)

Plastic strain intensification is observed to occur in the matrix at the intersection of the cracked particle with the matrix. The severity of stresses and cyclic plastic strain localization was observed to depend on the size of the inclusion and inclusion spacing. Evidently, the highest values of stresses and plastic strains were observed in case R1 as compared to case P1 and Q1 in the vicinity of cracked particle. Stress intensification arising due to interaction of inclusions could magnify the FIPs relative to the case of a single inclusion. A detailed investigation of the effect of particle shape, alignment, spacing and configuration on local stress distribution under cyclic loading can be found elsewhere [116].

Figure 3.10 shows the variation of the $\Delta\gamma^{p*}_{\max}/2$ and $\Delta\Gamma$ with depth for case P1. Interestingly, the maximum value of these FIPs occurs at a depth of about 250 μm below surface, which falls within the depth range observed in experiments for C61 gear steels. Also, observing the values close to the surface, it can be seen that the FIPs are negligibly small at depths between 75 to 150 μm, even though the applied strain amplitude is higher close to the surface. Shot peening suppresses the FIPs at the surface and shifts the critical

crack formation site to subsurface depths. The critical depth shows strong dependence on residual stress distribution, applied load and property gradients. Presence of other inhomogeneities such as pores and soft inclusions (sulfide particles) could alter the favorable site for crack formation depending on the intensity of localization around such inclusions.
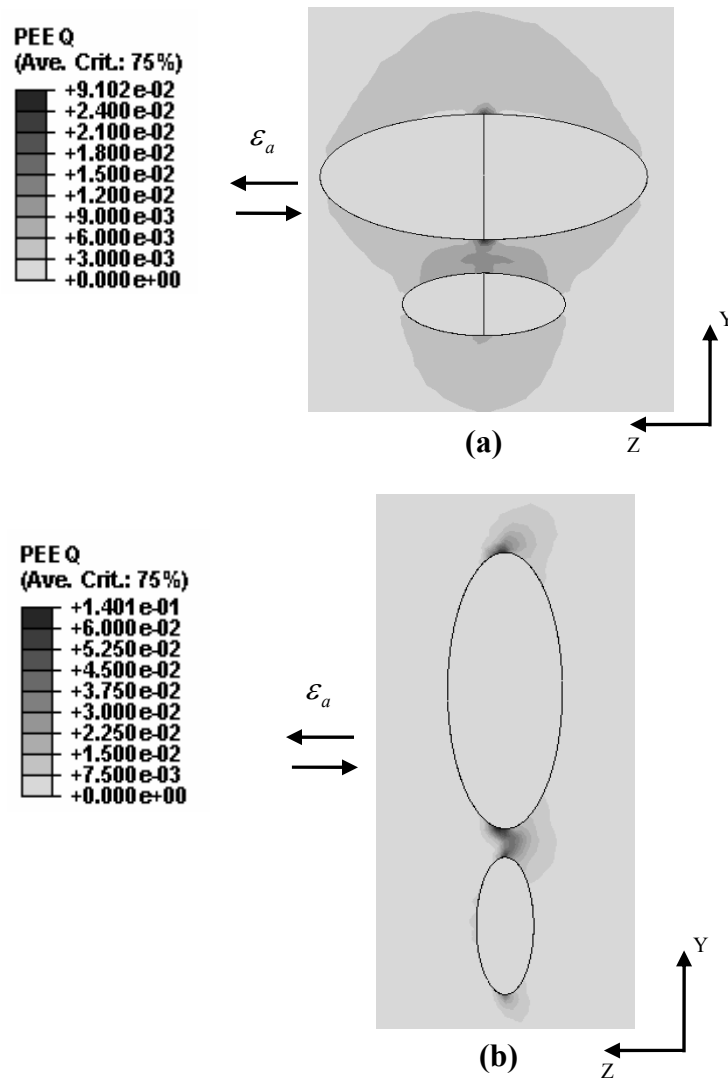
Figure 3.9. Contour plot of the equivalent plastic strain at the end of third loading cycle at a depth of 250μm below surface: (a) case R1 and (b) case E1.
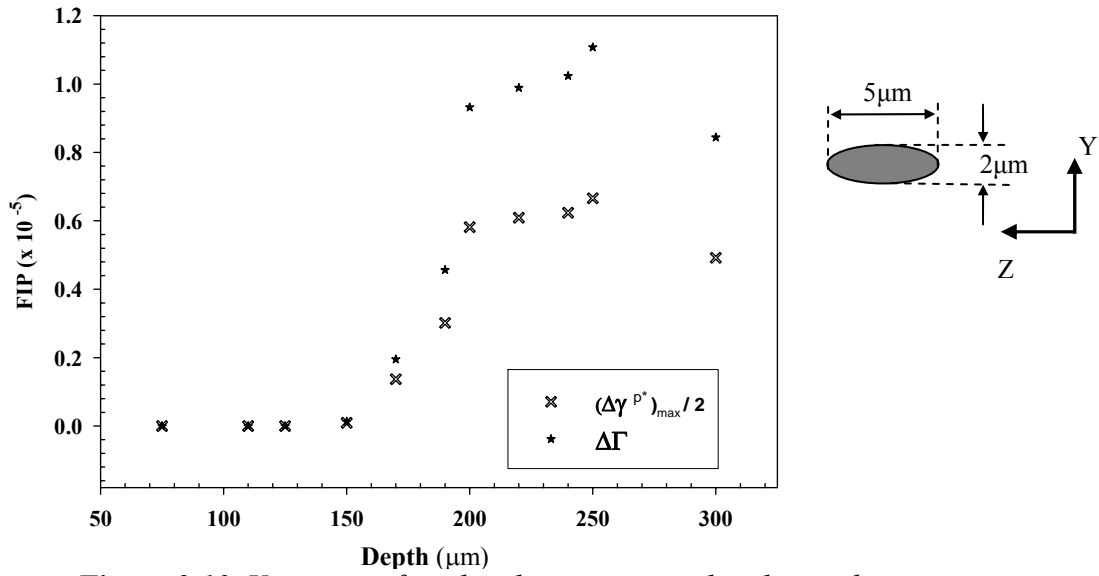
Figure 3.10. *Variation of nonlocal maximum cyclic plastic shear strain amplitude and FS parameter with depth for case P1.*
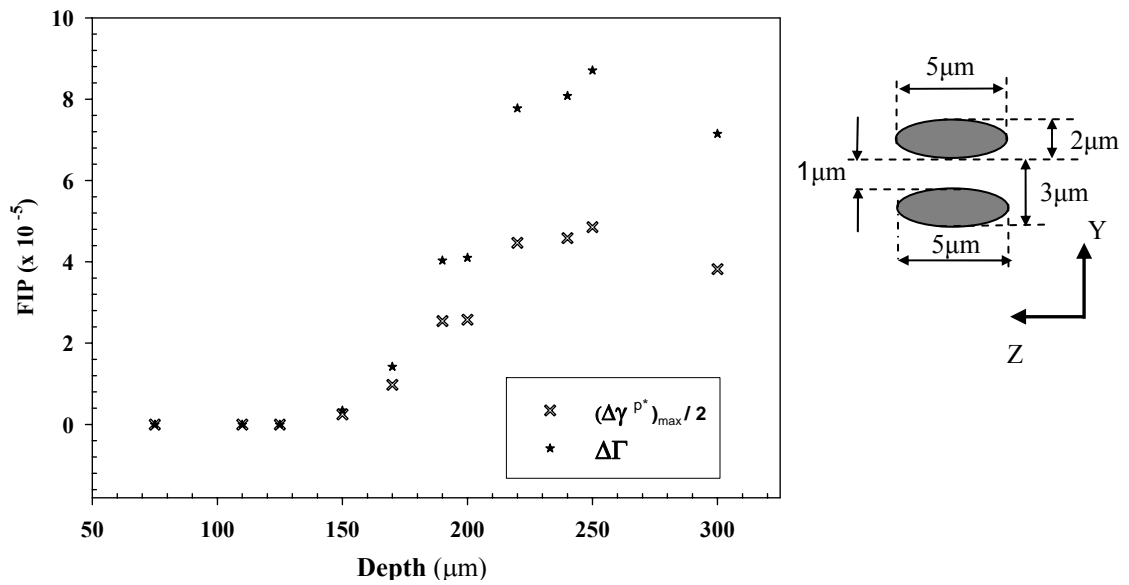
Figure 3.11. *Variation of nonlocal maximum cyclic plastic shear strain amplitude and FS parameter with depth for case Q1.*
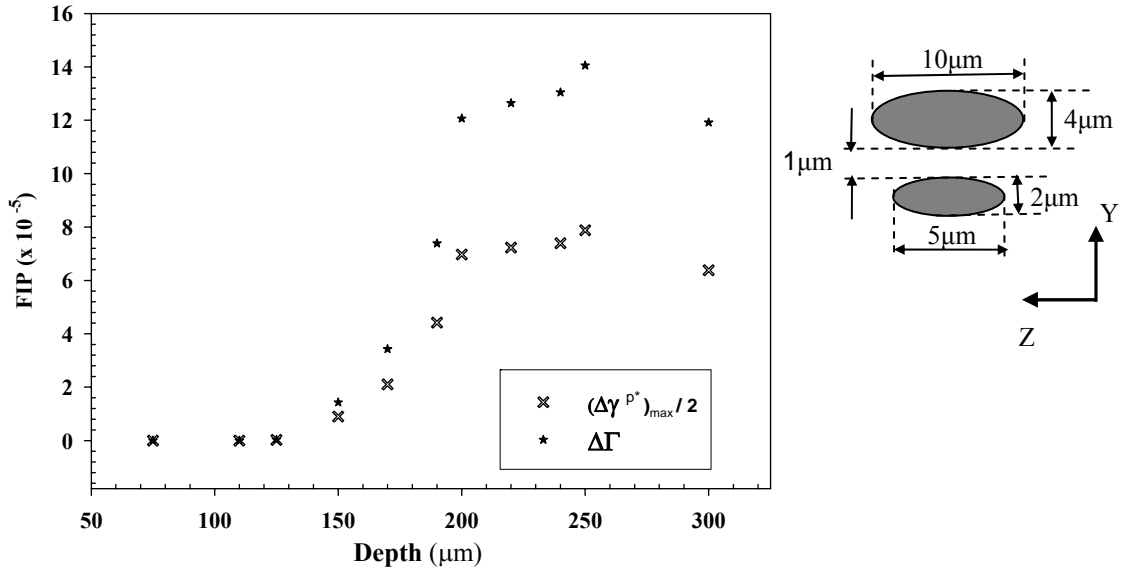
Figure 3.12. *Variation of nonlocal maximum cyclic plastic shear strain amplitude and FS parameter with depth for case R1.*

The nonlocal maximum plastic shear strain amplitude and FS parameter were also calculated for cases with two closely spaced cracked inclusions (case Q1and R1); results are shown in Figure 3.11 and Figure 3.12, respectively. The trends were similar to that of the single cracked inclusion (case P1), but the values are an order of magnitude higher due to size and interaction of inclusions. Increase in FIPs with increase of inclusion size (case R1 compared to case Q1) supports the observation reported by Toyoda and co-workers [13] relating the inclusion size to fatigue strength. Also, the sensitivity of fatigue crack formation life to the size and number of particles (clustering) is most pronounced at lower stress levels than at stress levels above macroscopic yielding [93]. Several other factors in addition to the inclusion size and spacing affect the HCF crack formation life including the shape and orientation of the inclusion [5, 91, 116]. However, detailed

investigation of all the factors influencing subsurface fatigue crack formation in shot peened C61 steel is beyond the scope of this limited parametric study.

3.8.2. Partially debonded inclusion analyses

Three-dimensional FE analyses were performed involving partially debonded inclusions (ellipsoidal) embedded in an elasto-plastic matrix. McDowell et al. [5] showed for A356-T6 Al alloy that partially debonded inclusions offer the most conservative scenario among various damaged particles for assessment of fatigue potency. Figure 3.13 describes the convention followed to represent ellipsoidal inclusion orientation in XY plane, denoted by φ. More detailed study exploring the effect of varying the orientation of inclusions in a cluster will be presented later. In all cases, the ellipsoidal inclusions were aligned such that the major axis of the inclusion was perpendicular to the loading direction. Figure 3.8 shows cross section views of the 3-D domain, elaborating on the boundary conditions, loading direction, and debonded surface of the inclusions considered in the parametric study.

The inclusion-matrix volume element was subjected to similar loading conditions as described in cracked inclusion analyses. Table 3.2 summarizes the different cases of a partially debonded inclusion analyzed in the parametric study. All the cases presented in the following plots and discussion will be addressed with the 'case pointer' listed in Table 3.2. Figure 3.9b shows the equivalent plastic strain contour plot for case E1 at the end of the third loading cycle, for example. Intensified plastic strains at the intersection of the debonded and bonded surfaces of the matrix (debond termination) can be observed from the contour plot. The intensification is due to the crack-like nature of the tip of the

58

debond seam coupled with the constraint and contact of embedded inclusions. It was mentioned by Gall et al. [5, 19] that high stresses around cracked inclusions will invariably facilitate debonding at the particle matrix interface. It was also shown that once a cracked particle begins to debond, the local plastic strains are intensified in the matrix with the same order of magnitude as a crack-free but partially debonded inclusion. Similar to cracked inclusion analyses, the severity of stress and plastic strain localization was influenced by particle size and spacing. Evidently, the magnitudes of plastic strains and stresses in the matrix encompassing the partially deboned alumina inclusion were highest in cases D1 and E1 compared to all other cases listed in Table 3.2.

Table 3.2 *List of cases analyzed in the study of partially debonded inclusions.*

Case Pointer	# of Inclusions	Shape of inclusion	2a	2b	2c	2d	L	φ_1	φ_2
A1	1	Ellipsoidal	5	2	-	-	-	0°	-
B1	2	Ellipsoidal	5	2	5	2	1	0°	0°
C1	2	Ellipsoidal	5	2	5	2	1	90°	90°
D1	2	Ellipsoidal	5	2	10	4	1	0°	0°
E1	2	Ellipsoidal	5	2	10	4	1	90°	90°

(φ_1 and φ_2 represent the orientation of inclusion 1 and inclusion 2, respectively)
(all dimensions in μm)
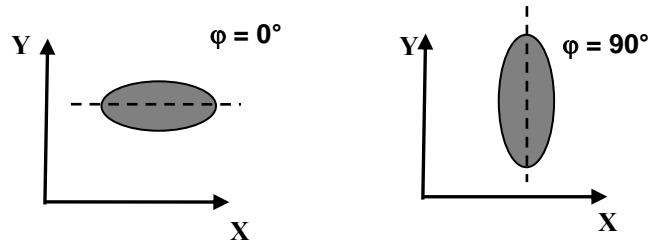
Figure 3.13. *Convention followed to represent the orientation of inclusion. Angle φ is measured with respect to X axis (loading axis along Z direction).*
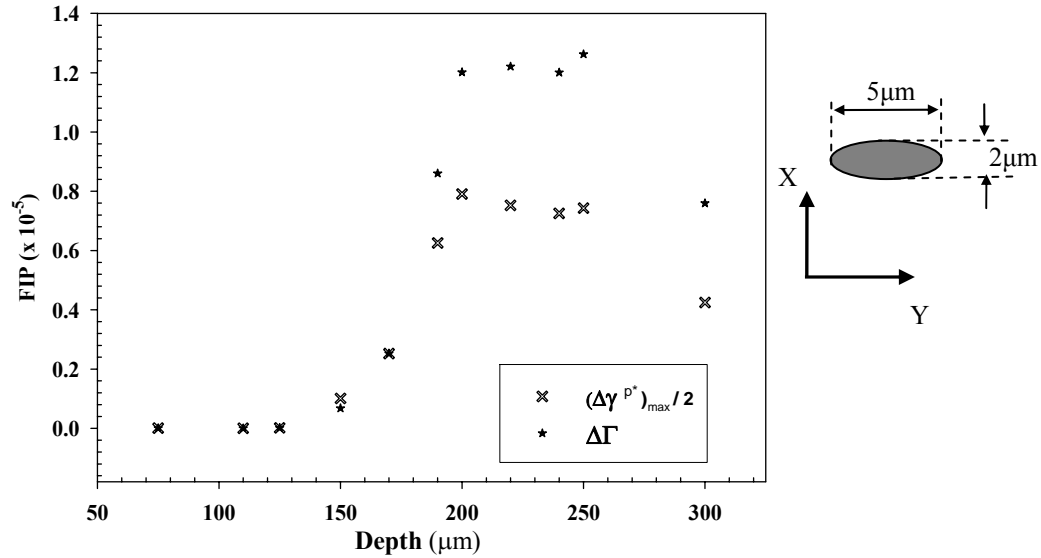
Figure 3.14. *Variation of nonlocal maximum cyclic plastic shear strain amplitude and FS parameter with depth for case A1.*
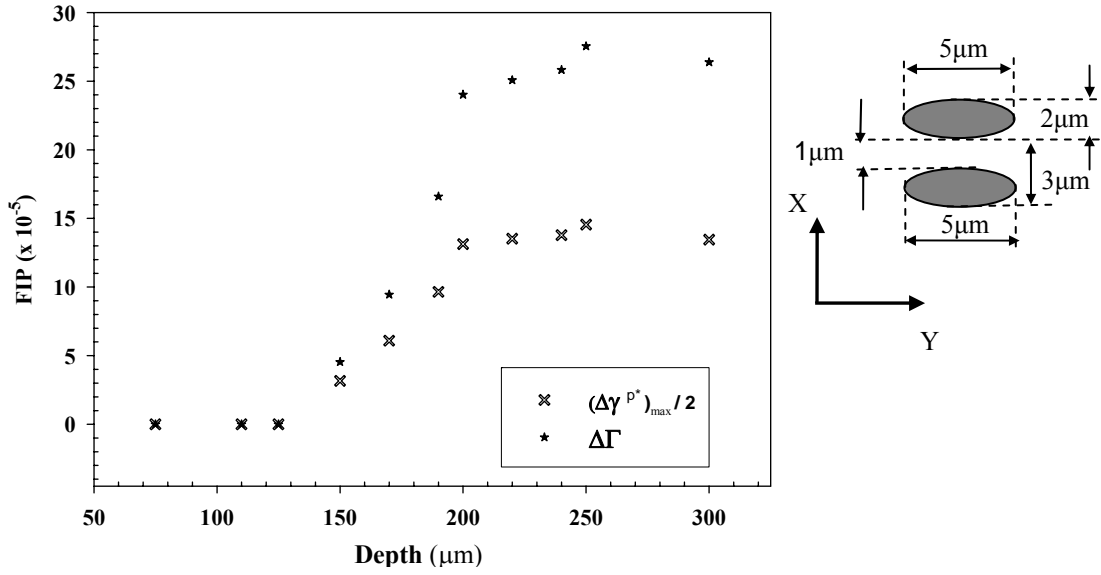
Figure 3.15. *Variation of nonlocal maximum cyclic plastic shear strain amplitude and FS parameter with depth for case B1.*
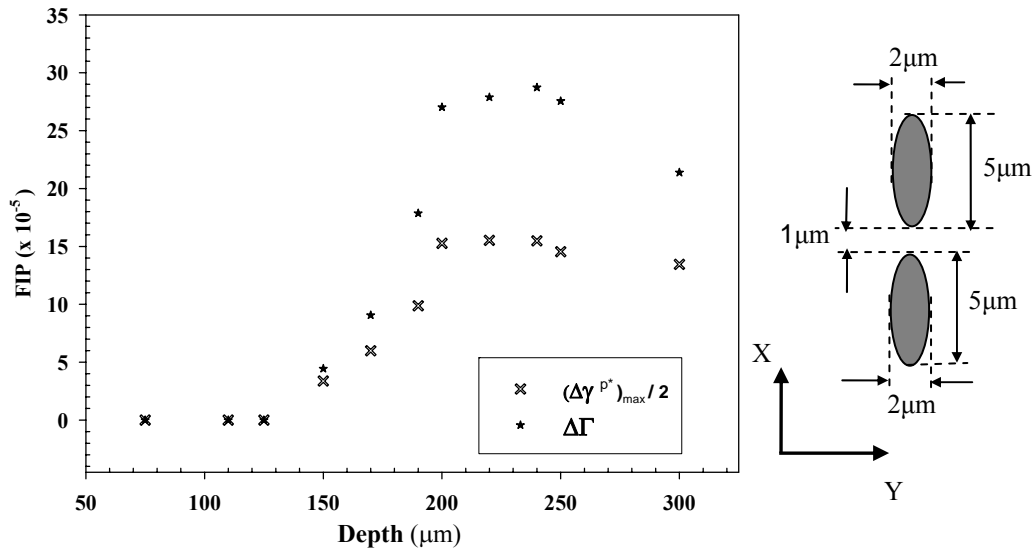
Figure 3.16. *Variation of nonlocal maximum cyclic plastic shear strain amplitude and FS parameter with depth for case C1.*

61
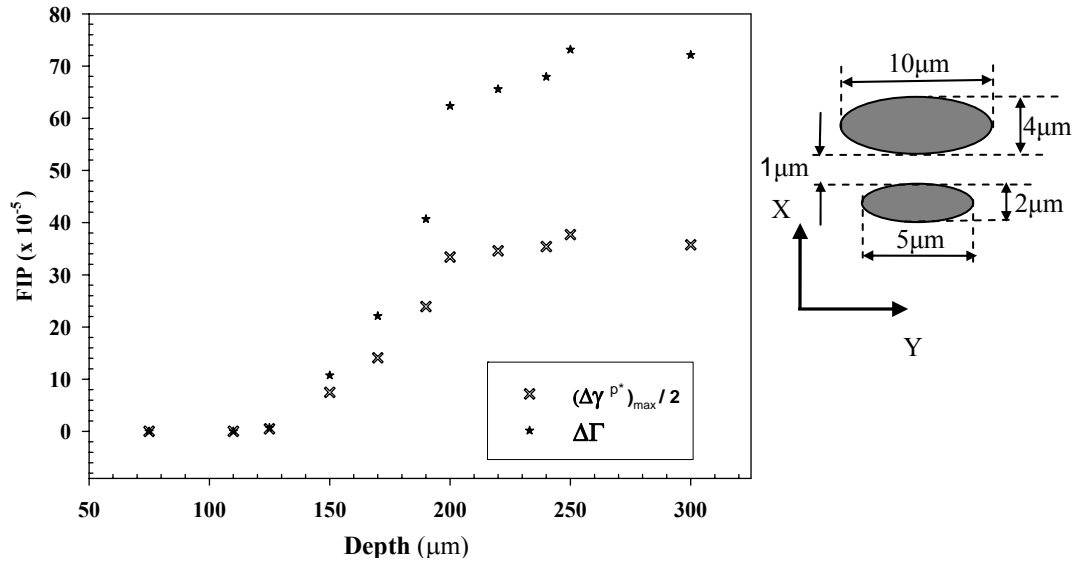
Figure 3.17. *Variation of nonlocal maximum cyclic plastic shear strain amplitude and FS parameter with depth for case D1.*
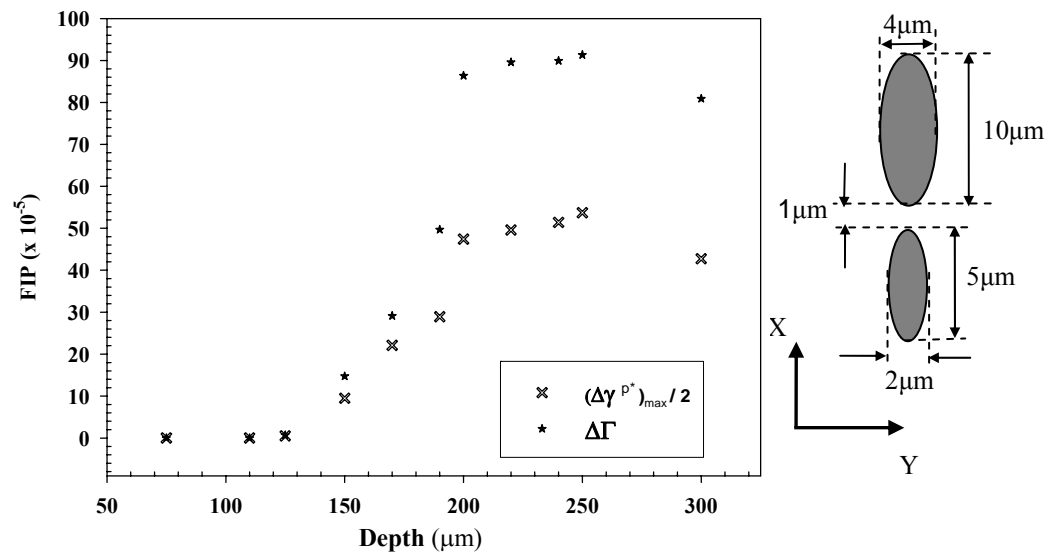
Figure 3.18. *Variation of nonlocal maximum cyclic plastic shear strain amplitude and FS parameter with depth for case E1.*

Figure 3.14 shows the variation of nonlocal maximum plastic shear strain amplitude and nonlocal FS parameter with depth for the case A1. Similar to the results obtained in the cracked inclusion analyses, the critical depth for fatigue crack formation trends towards 250 μm. The debonded inclusion was observed to facilitate higher plastic strains under monotonic loading, which in turn leads to higher local stress states. Consequently, reversed yielding occurs more readily near debonded inclusions. Consistent results were obtained for all the cases listed in Table 3.2 (see Figures 3.14-3.18) where the predicted critical depth for subsurface fatigue crack formation was in accordance with experimental observation. Size and spacing of partially debonded inclusions are observed to play a significant role in fatigue crack formation potency at subsurface depths. Case E1 is observed to be most detrimental under cyclic loading among all cases analyzed in this parametric study. This is due to the presence of a large partially debonded inclusion coupled with intensification arising due to interaction with neighboring inclusion. The variations arising due to spatial alignment of individual inclusion in a cluster (comparing case D1 and case E1) will be addressed later. The predictions and observations reported in this parametric study emphasize the importance of the inclusion-matrix interface character on fatigue crack formation potency. Comparing the single cracked particle results (case P1) in Figure 3.10 and single partially debonded inclusion results (case A1) in Figure 3.14, where the inclusion size is equal, the FIPs are relatively higher in the presence of partially debonded inclusions. Similar observations can be made by comparing different cases of partially debonded and cracked inclusions with equal size and spacing; it is evident that a cracked inclusion does not localize plastic strains and stresses in the matrix as severely as the partially debonded inclusion.

The choice of ellipsoidal inclusion in this parametric study facilitates assessment of the effect of individual inclusion alignment in a cluster with respect to loading direction on fatigue crack formation. Although partially debonded inclusions were aligned such that the major axis of the ellipsoid was perpendicular to loading direction, some disparity in the FIPs arises by varying the relative alignment of individual inclusions in the XY plane. The differences were significant between case D1 (Figure 3.17) and case E1 (Figure 3.18). The FIPs are relatively higher at subsurface depths for case E1. Since the plastic strain localization is most severe at the inclusion notch root for an ellipsoidal particle, the magnitudes of FIPs are expected be relatively higher when the inclusions are aligned such that the major axis of individual inclusion coincides (as in case E1). Comparing cases B1 and C1 as shown in Figures 3.15 and 3.16, the difference in the magnitudes of FIPs are relatively small. This observation suggests that the effect of relative spatial alignment of individual inclusion in a cluster on fatigue crack formation is more pronounced in presence of large inclusion ($\geq 10\mu m$). The disparity in fatigue response arising due to variations in spatial arrangement of inclusions in a cluster is a major contributor to the scatter in HCF lives observed in experiments. It is also evident from cases D1, E1 and R1 that the presence of large inclusions has more detrimental effect under cyclic loading. This is widely acknowledged from the perspective of initial flaw size, treating the inclusion as a crack starter for application of fracture mechanics.

3.8.3. Investigation of the residual stress fields in the proximity of primary inclusions

It is informative to study the distribution of residual stress fields in the vicinity of primary inclusion at the selected case depths below the surface. Figures 3.19, 3.20 and

3.21 show the nonlocal average values of residual stress fields in the proximity intact, cracked and partially debonded particle, respectively. For comparison, the far field residual stresses are plotted along with the local fields. The residual stresses are estimated at the end of the shot peening process. The residual stresses along X and Z directions are denoted as RS11 and RS33, respectively. The nonlocal averaging region corresponds to the fatigue critical zone demonstrating highest FIPs described in Sections 3.8.1 and 3.8.2. The results of the cracked particle correspond to case P1 in Table 3.1 and that of the partially debonded inclusion correspond to case A1 in Table 3.2. The intact particle is the same as case A1 with completely bonded surface.
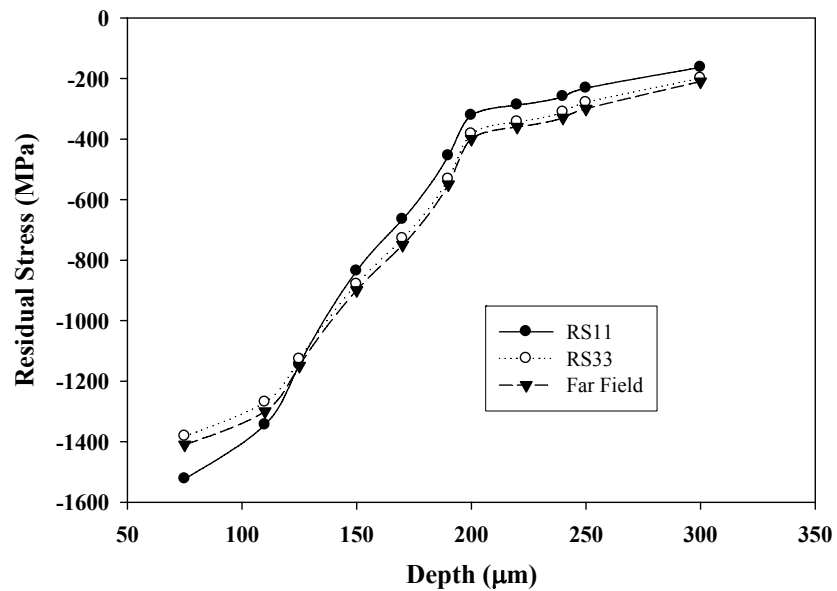
Figure 3.19. *Residual stress distribution around single intact ellipsoidal inclusion (RS11=σ_{xx} and RS33= σ_{zz}).*
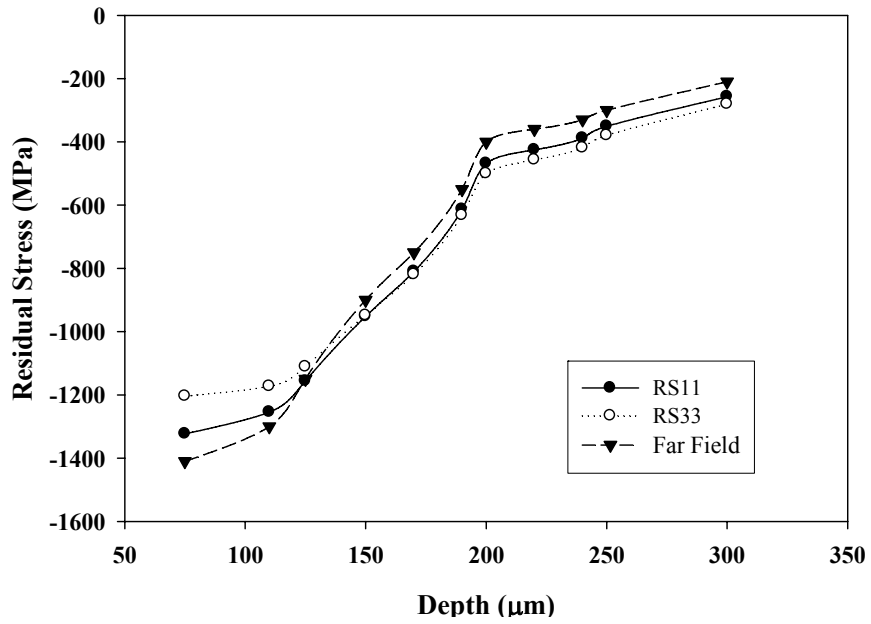
Figure 3.20. *Residual stress distribution around single cracked ellipsoidal inclusion (RS11=σ_{xx} and RS33= σ_{zz}).*
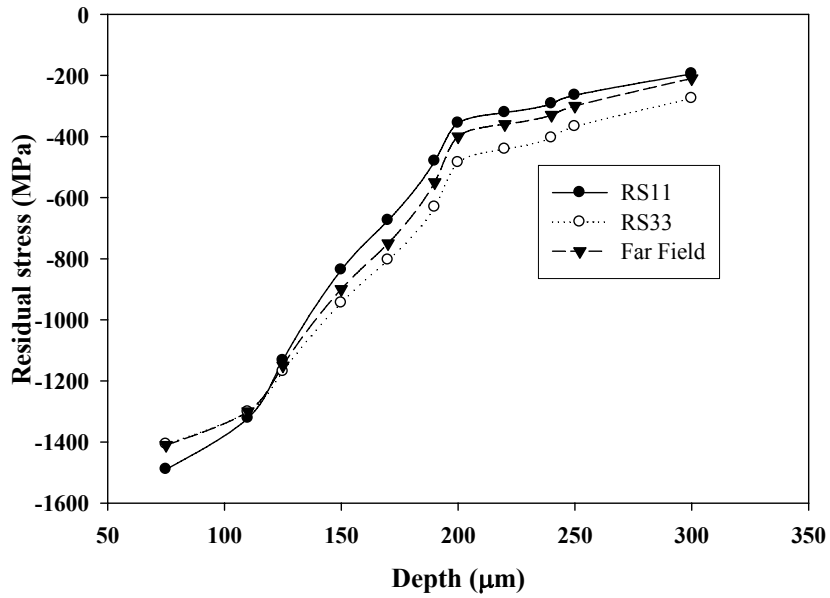
Figure 3.21. *Residual stress distribution around single partially debonded ellipsoidal inclusion (RS11=σ_{xx} and RS33= $\boldsymbol{\sigma_{zz}}$).*

66

The modest variation in the residual stress magnitude between the far field and the near inclusion zone is due to property mismatch, coupled with the constraint and contact of the embedded inclusion. Furthermore, comparing the local residual stress magnitude between the cracked, debonded, and intact particle, the differences are not significant. Evidently, high magnitudes of compressive residual stress around debonded or cracked particle at depths 75 to 100 μm would oppose interface separation during fatigue cycling. Consequently, plastic strain intensification is suppressed during cyclic loading, leading to negligibly small FIPs at those depths as observed in Figures 3.10-3.12, 3.14-3.18. It is well known that high compressive residual stresses suppress crack formation and growth potency in fatigue. The FS parameter utilized in this study accounts for such local stress effects while estimating the fatigue potency at primary inclusions. At depths of 200 μm and below, low magnitude of near inclusion residual stresses superimposed with the applied tensile stress during cyclic bending permits relatively larger interfacial separation. This leads to higher FIPs at subsurface depths of 200 μm and below.

3.8.4. Fatigue crack formation potency in the absence of compressive residual stresses

To illustrate the effect of residual stresses, variation of $\Delta\Gamma$ with depth for case A1 (single partially debonded ellipsoidal inclusion) simulated without compressive residual stresses is shown in Figure 3.22, for example. Gradients in elasto-plastic properties and applied bending stress were considered. The simulation result corresponds to an unpeened material. Evidently, the potency for fatigue crack formation is highest close to the surface where the applied bending stress is the highest. Comparing the magnitudes of $\Delta\Gamma$ in Figures 3.14 and 3.22, we observe substantial reduction in FIP at depths of 75 to

180 μm. At depths of 200 μm and below, however, the FIPs are comparable. This result supports the observation that shot peening suppresses crack formation potency at the surface and shifts the critical site for crack formation to subsurface inclusions.
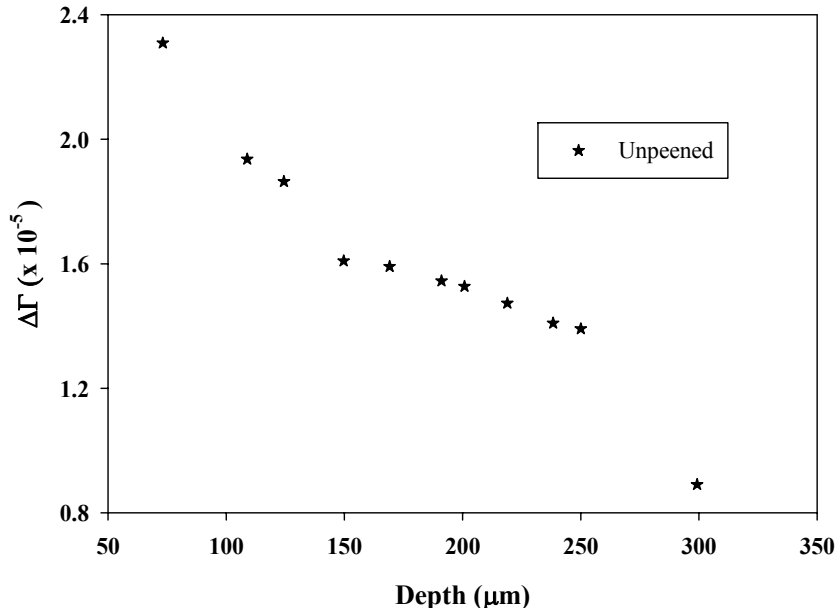
Figure 3.22. Variation of nonlocal FS parameter with depth for case A1 without compressive residual stresses.

3.9. Estimation of critical spacing between inclusions for minimal interaction in fatigue

The parametric studies involving compressive residual stresses substantiated the importance of inclusion interaction in fatigue. Understanding the severity of interaction of inclusions and devising process routes to achieve minimal interaction would significantly enhance the service life of the components. Here, we conduct systematic parametric study involving two inclusions to understand the effect of inclusion interaction. For simplicity, residual stresses are neglected. Case E1 (see Table 3.2) is

modeled to investigate the effect of inclusion spacing. The objective of this study is to estimate the critical spacing between inclusions that demonstrates negligible interaction. The spacing between the inclusions, L, is varied from 1 μm to 8 μm and the nonlocal FIPs are evaluated over the third loading cycle in the proximity of the largest inclusion. Additionally, simulations are performed involving single large isolated inclusion; in this case $L = \infty$. Simulations are conducted for several remote applied strain ranges (ε_r).
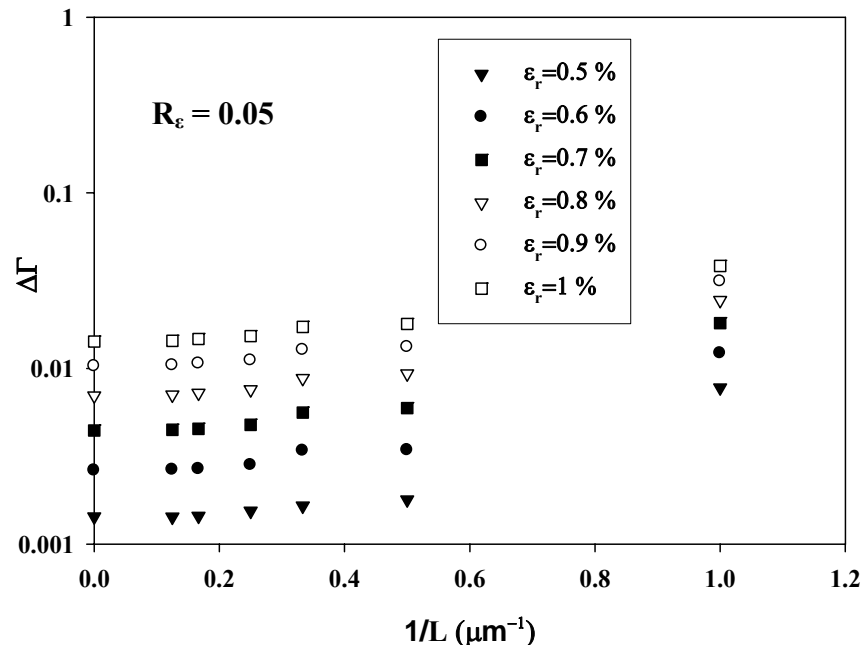
Figure 3.23. *Variation of ΔΓ (log scale) with longitudinal spacing between the inclusions.*

Figure 3.23 shows the variation in nonlocal FIP with inclusion spacing for several applied strain ranges. Interestingly, we observe a drastic reduction in FIP for L > 1μm. Evidently, as the spacing between the inclusions is increased the FIP converges to the value of the order of single isolated inclusion. Also, there is a nonlinear dependence of FIP on inclusion spacing with increasing applied strain amplitude. Based on the results the critical spacing between the inclusions (L_{cr}) that demonstrates negligible inclusion

interaction is approximately 8 μm. If D_{inc} denotes the largest dimension of the inclusion

which in this case is about 10 μm, then L_{cr} is on the order of D_{inc} $\left(or \ \dfrac{L_{cr}}{D_{inc}} \sim 1 \right)$.

3.10. Effect of orientation of ellipsoidal inclusions on fatigue resistance

Clusters of primary inclusions are often observed on fracture surface (e.g., Figure 2.6). During manufacturing such as primary forging the inclusions tend to get aligned along the forging (flow) direction. This results in variation (or anisotropy) in fatigue response with applied loading direction and is a significant contributor to scatter in HCF lives [117, 118]. However, it is possible to leverage such preferential alignment of inclusions to enhance the fatigue resistance. Identifying the least damaging orientation of the inclusions in a cluster with respect to the loading axis and the free surface and devising modified process routes to achieve desirable orientation could significantly enhance the fatigue resistance. The orientation of inclusions depends on the deformation processing history and is potentially controllable. Due to highly localized nature of the fatigue crack formation process such investigations are feasible through computational modeling.

Here, we attempt to model the effect of orientation of inclusions in a cluster on fatigue resistance of martensitic steels. The objective is to identify the least damaging orientation in fatigue. A schematic illustrating the convention followed to represent the orientation of an ellipsoidal inclusion in 3D space with respect to loading axis is shown in Figure 3.24. In Figure 3.24, θ represents the zenith angle, and ϕ represents the azimuth angle. The normal to the free surface is parallel to Y-axis and the cyclic loading direction

is parallel to the Z-axis. In this study, θ and ϕ are varied from 0° to 90° independently in the increments of 45° resulting in seven different orientations.
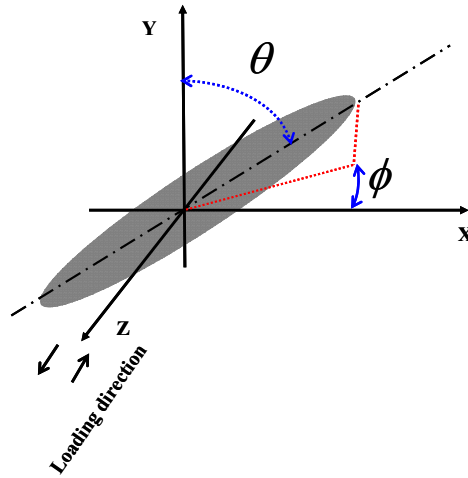
Figure 3.24. *Convention followed to represent the orientation of inclusion in 3D space. θ is the zenith angle measured between the Y-axis and the major axis of the inclusion. ϕ is the azimuth angle on the X-Z plane. Normal to the free surface is parallel to the Y-axis. Cyclic loading direction is parallel to Z-axis.*

Three-dimensional FE mesh comprising of seven closely spaced ellipsoidal inclusions of equal size are constructed using ABAQUS script [95]. Dimensions of the major and minor axis of the ellipsoidal particle are 5 μm and 2 μm, respectively. A schematic of the simulated inclusion cluster is shown in Figure 3.25 elaborating on the spacing between the inclusions which is consistent for all the orientations investigated in this study. For the case of $\theta = 90°$ and $\phi = 90°$, the spatial arrangement of the inclusions in the cluster were chosen such that the inclusions experience minimal shielding effect [119] during cyclic loading. Figures 3.26a-d illustrates four different orientations of the inclusion cluster with respect to the loading axis, for example. Figure 3.26d shows the spatial arrangement of inclusions chosen for $\theta = 90°$ and $\phi = 90°$ orientation. The edge to edge spacing between the inclusions when projected onto the XY plane is same as that shown

in Figure 3.25. The dimensions of the inclusion-matrix volume element are chosen such that the inclusions experience negligible boundary interactions. Elasto-plastic properties corresponding to a depth of 75 μm below surface was assigned to the matrix. Residual stresses are not considered. Intact inclusions are considered since specifying the debonding inclusion-matrix interface for various orientations is tedious. The inclusion-matrix volume element is subjected to three cycles of loading with remote applied strain range of 1.5% and $R_\varepsilon = 0.0$. Nonlocal average value of the FIP is computed over the third loading cycle. The averaging volume is selected as that volume in the proximity of the inclusion that maximizes the nonlocal FIP.
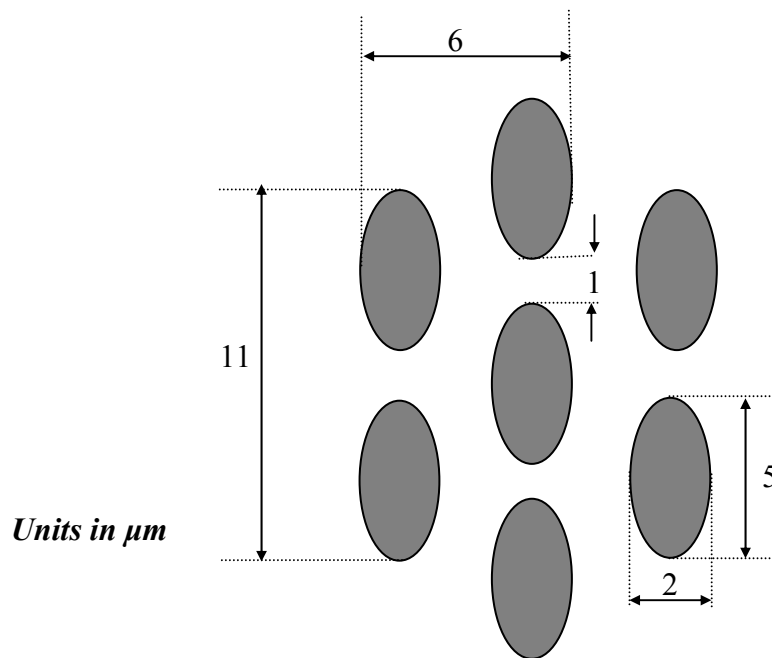
Figure 3.25. Schematic showing the size of the inclusions and the spacing between them in a cluster.
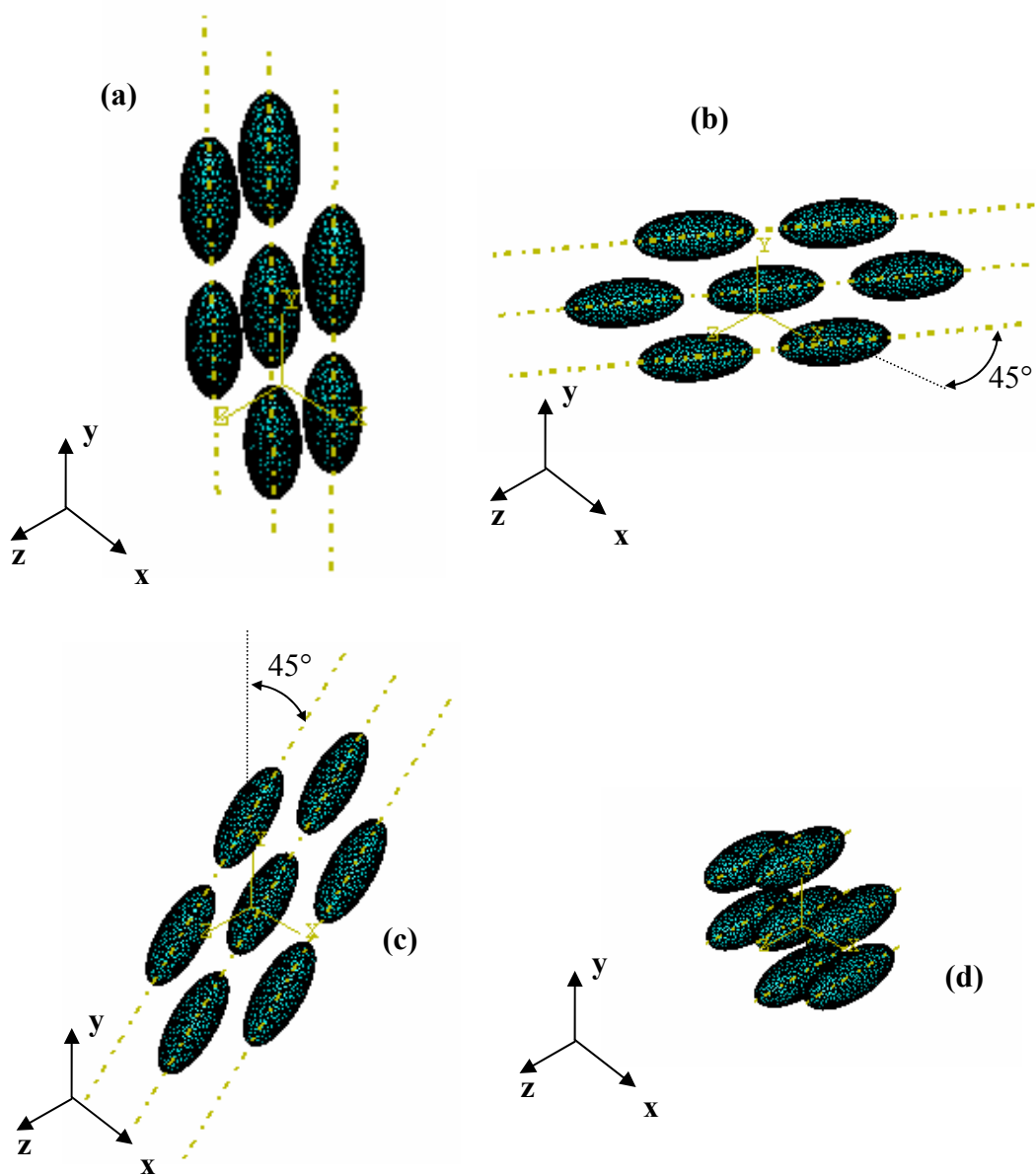
Figure 3.26. *Three different orientations of inclusion cluster with respect to loading direction and free surface shown for the purpose of illustration (a)* $\theta = 0°, \phi = 0°$, *(b)* $\theta = 90°, \phi = 45°$ *(c)* $\theta = 45°, \phi = 90°$, *and (d)* $\theta = 90°, \phi = 90°$. *Cyclic loading is in Z-direction.*
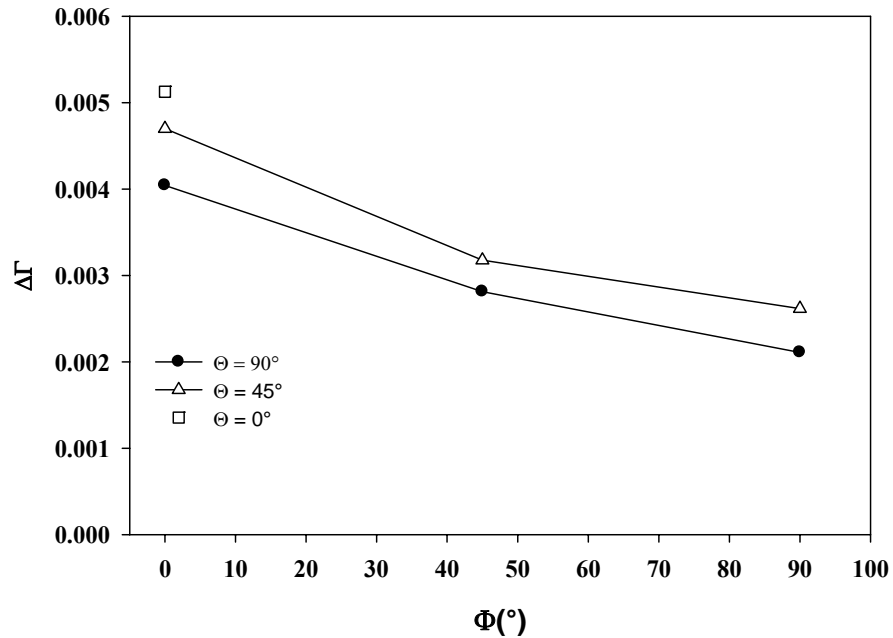
Figure 3.27. *Variation of nonlocal FIP with 3D orientation of inclusion with respect to loading axis and free surface.*

Figure 3.27 shows the variation in nonlocal FIP with the orientation of inclusions. Interestingly, ellipsoidal inclusions with major axis oriented perpendicular to the loading axis $\left(\theta = 0°, \phi = 0°\right)$ demonstrate the worst case scenario for fatigue crack formation and inclusions with major axis oriented parallel to loading axis $\left(\theta = 90°, \phi = 90°\right)$ were the least damaging in fatigue. At least 10% difference in the FIP is observed between the two extreme orientations which could project to a significant difference in the fatigue life. This difference can also be justified through the projected $\sqrt{area}$ approach [53]. An ellipsoidal inclusion with major axis aligned parallel to the loading axis would exhibit minimum projected area, leading to longer fatigue life. The aforementioned observation of anisotropy in fatigue response arising due to variation in orientation of second phase particles has supporting experimental evidence in literature (cf. Ott and Mughrabi [117],

and Mughrabi et al.[120]). They considered elongated raft-like γ' precipitate (life-limiting feature) morphologies in addition to the usual cuboidal structure in Ni-base superalloy. Two types of elongated precipitates were considered, one with its long axis oriented perpendicular to the loading axis and the other with its long axis aligned with the loading axis. It was observed that the fatigue life was highest for the microstructure with the elongated precipitates aligned with the loading direction and was lowest for the case for which elongated precipitates were aligned perpendicular to the loading direction. For microstructures with cuboidal precipitates aligned perpendicular to loading direction, it was easier for the fatigue crack to find a contiguous path normal to loading direction. On the other hand, for the microstructure with precipitates aligned parallel to the loading direction, the precipitates acted as obstacles to deflect the crack; in this case, the crack propagation rate was considerably reduced for this microstructure, leading to a longer fatigue life.

3.11. Summary and conclusions

Finite element modeling can be used to study the effects of microstructure attributes on the fatigue performance. Parametric studies of the type undertaken in this work can facilitate exploration of the effects of variation of single features of microstructure holding other features fixed, which is generally not possible in experimental studies. Simple computational algorithms developed here such as the methodology to simulate shot peening and the procedure to explore its effect on fatigue crack formation at subsurface primary inclusions can aid in design of fatigue resistant material systems. The critical contributions and findings of this work are summarized below:

1)   A new algorithm is presented to simulate residual stress distribution arising from the shot peening process that is suitable for initializing residual stresses prior to conducting both 2-D and 3-D finite element based fatigue calculations.

2)   An integrated methodology is developed to analyze the fatigue indicator parameters at three-dimensional subsurface inclusions in carburized and shot peened gear steels under the influence of compressive residual stresses. The methodology was applied to predict the favorable site for fatigue crack formation in a martensitic gear steel. The simulation results indicate a strong propensity for crack formation at the subsurface at depths in accordance with experiments [27] . This work has been submitted to archival journals as part of my thesis research and has appeared in 2009 [121].

3)   Under the given external loading, material model, and the selected fatigue crack formation criterion, partially debonded inclusions were most severe with regard to fatigue crack formation.

 4)   The subsurface fatigue crack formation potency depends on the size and clustering of inclusions. Interaction of inclusions in a cluster was observed to magnify the FIPs. Based on the analyses conducted on spatial interaction of inclusion, it was concluded that the minimum spacing between inclusions to achieve negligible interaction in fatigue was of the order of the largest dimension of the inclusion.

5)   Fatigue response depends on the orientation of the inclusions with respect loading axis. It was observed that ellipsoidal inclusions whose major axis was aligned perpendicular to the loading axis were most severe with regard to fatigue crack formation. On the other hand, ellipsoidal inclusions with major axis oriented parallel to loading axis were least damaging (highly desirable).

Chapter 4

POLYCRYSTAL PLASTICITY MODELING OF CYCLIC RESIDUAL STRESS RELAXATION IN SHOT PEENED MARTENSITIC STEEL

In this Chapter, a FE based methodology to investigate relaxation of compressive residual stresses is presented. Using a three-dimensional crystal plasticity model for cyclic deformation of lath martensitic steel, a simplified scheme is adopted to simulate the effects of shot peening on inducing initial compressive residual stresses. The model is utilized to investigate the subsequent cyclic relaxation of compressive residual stresses in shot peened lath martensitic gear steel in the HCF regime. A strategy is identified to model both shot peening and cyclic loading processes for polycrystalline ensembles. Relaxation of the residual stress field during cyclic bending is analyzed for strain ratios $R_\varepsilon = 0$ and -1 for multiple realizations of polycrystalline microstructure. Cyclic microplasticity in favorably oriented martensite grains (blocks) is the primary driver for the relaxation of residual stresses in HCF. For the case of $R_\varepsilon = -1$, cyclic plasticity occurs throughout the microstructure (macroplasticity) during the first complete loading cycle, resulting in substantial relaxation of compressive residual stresses at the surface and certain subsurface depths. The initial magnitude of residual stress is observed to influence the degree (percentage) of relaxation. The necessity of describing the differential yielding among grains of the model to capture the experimentally observed trends of residual stress relaxation is noteworthy.

4.1 Introduction

It is well known that mechanical surface treatments, such as deep rolling, shot peening and laser shock peening, can significantly improve the fatigue behavior of highly-stressed metallic components, as discussed in earlier chapters. These stresses enhance the service life of the component by resisting fatigue crack formation and growth on and near the surface of the specimen. The residual stresses can relax significantly due to subsequent mechanical and/or thermal loading even under normal operating conditions. Measurements and effects of residual stresses have proven difficult to interpret in relation to influence on fatigue life. To a large extent, this uncertainty arises from the limitations associated with the surface measurements of residual stresses through the depth of the shot peened layer. There is also a lack of knowledge of the effect of fatigue cycling on such stresses since it is difficult to measure residual stress changes during cycling. Computational modeling such as finite element analysis offers a convenient platform to investigate the effects of process history (including residual stresses) on fatigue resistance of components. There is considerable interest in developing improved fatigue life prediction models that incorporate residual stress effects [37, 122, 123].

Extensive experimental studies have been performed to understand the relaxation of compressive residual stresses induced through shot peening [124-127]. Accordingly, the relaxation during fatigue cycling can be divided into two stages: abrupt relaxation during the first cycle and gradual change in the following cycles [128]. It is conventionally held that residual stress relaxation due to mechanical loading occurs when the superposition of applied stress and residual stress exceeds the macroscopic yield strength of the material. Also, decrease in the yield strength with increase in temperature can promote residual

stress relaxation. During service, cyclic hardening or softening due to repeated loading can alter the residual stress distribution [129]. The present work explores how short-range microplastic deformation during cyclic loading promotes relaxation of residual stresses at remote stress amplitudes well below the yield strength of the material which is typical of HCF loading conditions. Almer et al. [130] pointed out that microstresses within grains relax rapidly during fatigue while macroscopic stress relaxes less rapidly; this can significantly influence fatigue crack formation and growth behavior in HCF.

Several dynamic 2-D and 3-D FE simulations of shot peening have been successful developed to predict the residual stress distribution in a variety of metallic materials [69, 70, 72, 74, 75]. However, it is tedious to conduct such dynamic FE simulations using polycrystal plasticity models. This is due to the vast disparity between the specimen scale (>1 mm) where the process parameters are framed and the underlying microstructure such as the lath martensite grains (<10 μm). Furthermore, the microstructure hierarchy exhibited by lath martensite at the grain scale aggravates the issue of computational efficiency. We overcome this issue by adopting a simplified multiscale modeling approach to simulate the shot peening effects and cyclic stress relaxation.

Modeling efforts to investigate the shot peened residual stress relaxation have been very limited. Jhansale and Topper [131] proposed a logarithmic relationship between mean stress relaxation and the number of cycles. The relationship was suitable to model relaxation of residual stress *after* the first loading cycle [132]; however, the first loading cycle can result in significant relaxation of residual stress fields. In an effort to model residual stress relaxation, Smith et al. [133] and Zhuang and Halford [127] conducted FE analyses using different material models. However, they used empirical relations to

model peening-induced residual stress distributions. Meguid et al. [88] devised a dynamic FE methodology to simulate shot peening process through bombardment of metallic balls on the target specimen surface and investigated the residual stress relaxation due to overloads during cyclic loading in AISI 4340 steel. Although, the methodology is suitable to examine the relaxation when the remote applied stress is of the order of macroscopic yield strength, it is insufficient for low strain amplitudes for which relaxation is primarily due to heterogeneous microplasticity in favorably oriented grains. There have been no computational studies utilizing crystal plasticity constitutive model to investigate the cyclic relaxation of residual stresses in shot peened materials.

4.2 Lath martensite microstructure

The lath martensite structure is composed of fine "packets" or groups of laths with almost the same habit plane, and "blocks" which contain a group of laths with the same orientation, as shown schematically in Figure 4.1 [134-138] . A prior austenite grain is divided into several martensite packets that are further subdivided by blocks, forming a hierarchical structure. It is also observed that blocks are further divided by sub-blocks (variants) with interlath misorientation less than 10°. The packet and block sizes are observed to depend on the prior austenite grain size and considerable efforts have been made to refine prior austenite grain size to achieve high strength and wear resistance. Morito et al. [136] explored the dependence of packet size and block width on prior austenite grain size in Fe-0.2C-Mn steel. Lath martensite formed during the carburization process tends to have BCT crystal structure, which has limited ductility. Tempering of steels is performed to achieve the desired case strength and enhance ductility after

carburization. The heat treatment process results in precipitation of iron carbides and alloy carbides of submicron size which act as strengthening agents by pinning dislocations. During the process of tempering, the tetragonality of martensite is reduced and the resulting lath martensite is close to BCC structure [139]. Since both the block and packet boundaries are high angle boundaries, they are expected to act as barriers of moving dislocations during deformation of the lath martensite structure. However, in early studies on the strength of the lath martensite, the packet size measured on optical micrographs was often taken as the effective grain size for a Hall–Petch type analysis of the martensite strength [20, 23, 140]. This is because martensite blocks cannot always been revealed clearly in optical microscopy, and more importantly the blocks are planar structure (plate-like) and a precise measurement of block width requires information about the inclination of block boundary planes with respect to the observation surface, which is impossible to obtain with optical microscopy. However, recent work by Morito and co-workers demonstrated block size to be a key structural parameter when analyzing the strength-structure relationship of lath martensite [141].

Based on the aforementioned observations, the following assumptions are made:

1. Tempered lath martensite has BCC crystal structure with 48 slip systems [142].

2. A block of lath martensite within a prior austenite grain constitutes a single grain for purposes of assigning orientation distribution of grains in polycrystal plasticity.

3. A random orientation distribution of grains is assigned.
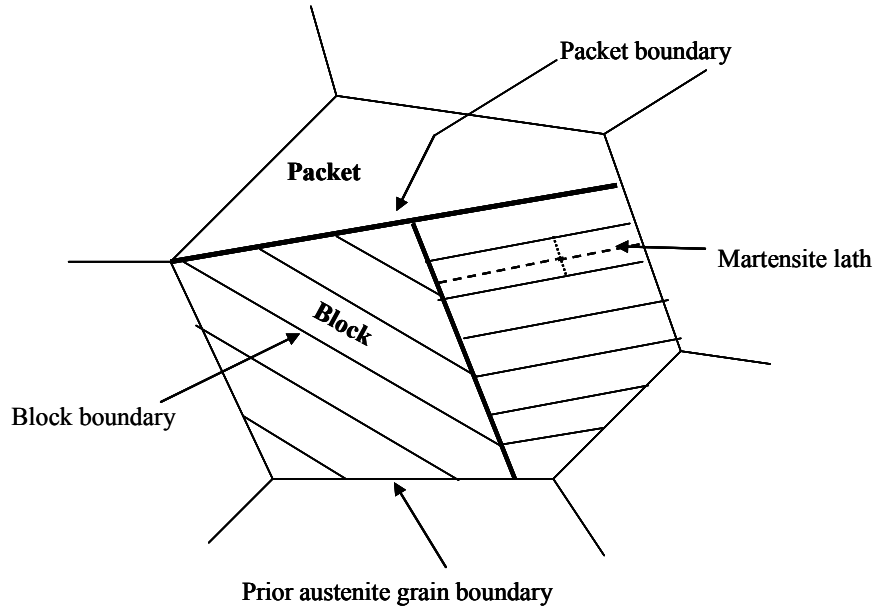
Figure 4.1. *Hierarchical lath martensite microstructure.*

4.3. Crystal plasticity framework

The crystal plasticity algorithm with the numerical implementation applied here is described elsewhere [143, 144], and is an extension of the fully implicit technique discussed in [145]. In the algorithm, the kinematics of crystal plasticity [146] are employed with the multiplicative decomposition given by

$$\underset{\sim}{F} = \underset{\sim}{F}^{e} \cdot \underset{\sim}{F}^{p} \tag{4.1}$$

where $\underset{\sim}{F}$ is the total deformation gradient, $\underset{\sim}{F}^{e}$ is the elastic deformation gradient representing elastic stretch and rigid rotation, and $\underset{\sim}{F}^{p}$ is the plastic deformation gradient that describes the collective effect of dislocation glide along crystallographic planes relative to the fixed lattice in the reference configuration.

The kinetics of dislocation glide is formulated by the relationships between the resolved shear stress and the shearing rate along the slip system. The plastic shearing rate ($\dot{\gamma}^\alpha$) on the αth slip system is assumed to follow the power law form

$$\dot{\gamma}^\alpha = \dot{\gamma}_0 \left| \frac{\tau^\alpha - \chi^\alpha}{g^\alpha} \right|^m \text{sgn}\left(\tau^\alpha - \chi^\alpha\right) \tag{4.2}$$

In Equation (4.2), $\dot{\gamma}_0^\alpha$ is a reference shearing rate, m is the flow exponent (or inverse strain-rate sensitivity exponent), g^α is a reference shear stress, χ^α is the back stress on the αth slip system, and the resolved shear stress is given by $\tau^\alpha = \underset{\sim}{\sigma} : \left(\underset{\sim}{s}^\alpha \otimes \underset{\sim}{n}^\alpha\right)$, where $\underset{\sim}{\sigma}$ is the Cauchy stress tensor. The stress tensor is evaluated using linear elasticity in the intermediate configuration and then is pushed forward to the current configuration. A hardening minus dynamic recovery form is assumed for evolution of g^α [147], i.e.,

$$\dot{g}^\alpha = H \sum_{\beta=1}^{N} q^{\alpha\beta} \left| \dot{\gamma}^\beta \right| - Rg^\alpha \sum_{\beta=1}^{N} \left| \dot{\gamma}^\beta \right| \tag{4.3}$$

Here, H and R are the direct and dynamic recovery coefficients, respectively, and $q^{\alpha\beta} = h\left(\delta_{\alpha\beta} + lhr\left(1 - \delta_{\alpha\beta}\right)\right)$. In this work, $h = 1.1$ and $lhr = 1$. The back stress χ^α on each slip system evolves according to a nonlinear kinematic hardening rule of the Armstrong-Frederick type [148, 149], i.e., $\dot{\chi}^\alpha = A\dot{\gamma}^\alpha - A_d \chi^\alpha \left| \dot{\gamma}^\alpha \right|$, where A and A_d are the direct and dynamic recovery coefficients, respectively. In contrast to evolution of g^α, no

interactions are assumed among slip systems in evolution of χ^{α}; it is purely self-hardening in nature.
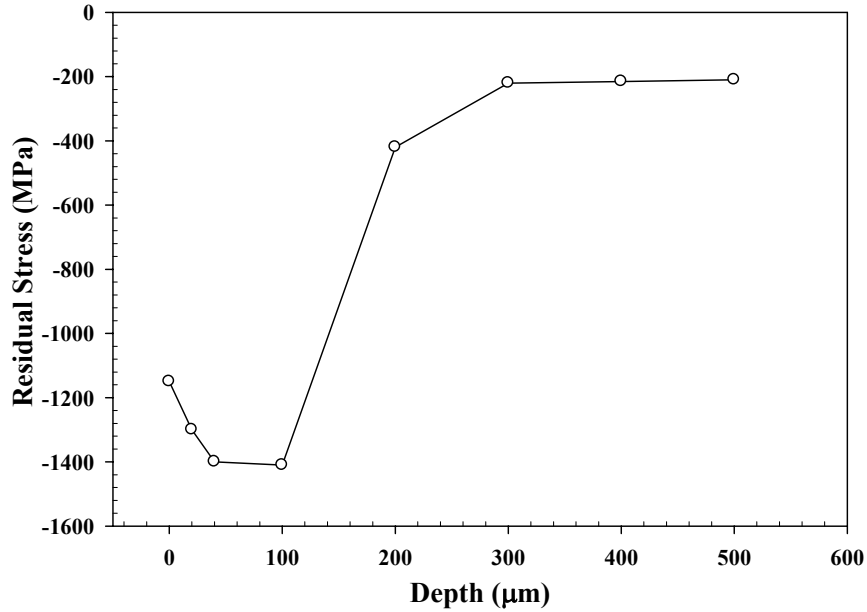
Figure 4.2. *Measured variation of residual stress* $\left(\sigma_{zz,0}^{res}, \sigma_{xx,0}^{res} \right)$ *with depth after shot peening.*

4.4 Simulating the effect of shot peening process: Inducing compressive residual stresses

The algorithm presented in Section 3.5 is used to induce compressive equi-biaxial residual stresses. The strains $\varepsilon_{yy,load}$ and $\varepsilon_{yy,final}$ (see Figure 3.4) are estimated iteratively using incremental polycrystal plasticity calibrated to the macroscopic stress-strain response of C61 steel. This is valid provided the ratio of subsurface layer depth *L2* (see Figure 3.4) to grain/block size is suitably large and the orientation distribution of grains is random. Such a scheme permits a computationally efficient means to perform three-

dimensional crystal plasticity simulations of residual stress relaxation. Material property gradients due to heat-treatments such as carburization are neglected in this study, although they play a secondary role in the actual problem; the effects of carburization are reflected to first order in the overall C61 gear stress stress-strain behavior to which the polycrystal plasticity model is calibrated.

4.5. Methodology

The experimentally measured variation in compressive residual stress with depth is shown in Figure 4.2. The crystal plasticity model is implemented as a User Material subroutine (UMAT) in ABAQUS. The elastic constants (C_{11}, C_{12}, C_{44}) for the martensite crystal are obtained from Ref. [150]. The reference shearing rate $\dot{\gamma}_o$ is set to 0.001 s^{-1}. The remaining material parameters in connection with Equations (4.1)-(4.3) are obtained by fitting the homogenized stress-strain response of a periodic representative volume element (RVE) comprised of 500 randomly oriented polycrystalline lath martensite grains to quasistatic room temperature experimental uniaxial tension stress-strain curves $\left(\dot{\varepsilon} \sim 10^{-3} s^{-1}\right)$ of lath martensitic steel. This is reasonable since we propose to study the relaxation of residual stresses during the initial few cycles following shot peening. Periodic boundary conditions were imposed on the RVE. Resulting material constants are listed in Table 4.1 and the simulated monotonic tensile stress-strain curve is shown in Figure 4.3.

Table 4.1. *Material parameters in the crystal plasticity constitutive model.*

C_{11} (GPa)	268
C_{12} (GPa)	110
C_{44} (GPa)	78
m	75
g_o^α (MPa)	705
H (MPa)	100
R	0.1
A (MPa)	100
A_d	10
$q^{\alpha\beta}$ (h , lhr)	1.1, 1
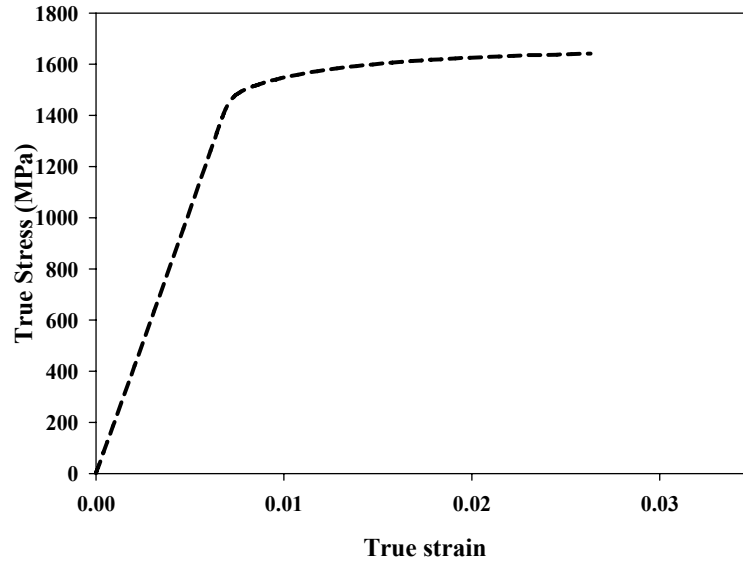
Figure 4.3. *Simulated monotonic tensile stress-strain response of the martensitic steel.*

In the relaxation simulations for each subsurface volume element, a polycrystalline subsurface volume element is cast as a three-dimensional FE mesh with 784 lath martensite grains, as shown in Figure 4.4. Each lath martensite grain (or block) is cubic

and is divided into eight three dimensional eight node brick elements (C3D8R). The size of individual lath martensite grain is 1.5 μm [141]. Although the FE model of polycrystalline microstructure may not be represent the realistic shape and size of individual lath martensite grains, it suffices for purposes of the intergranular interactions necessary for residual stress relaxation in the HCF regime. More detailed digital representations of microstructure may not provide additional useful information in this class of model in view of the lack of detailed consideration of the role of block and packet boundaries in slip transfer.
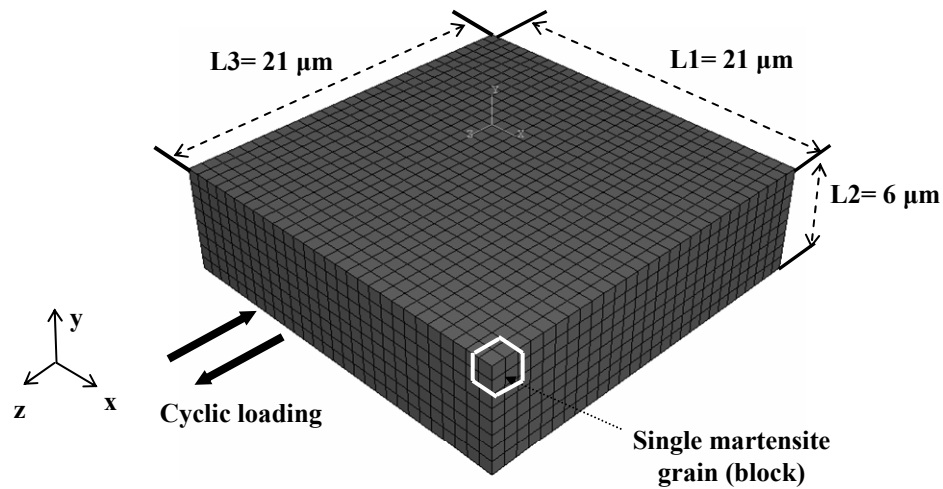
Figure 4.4. A typical finite element mesh of microstructure within a simulated subsurface volume element.

A polycrystalline volume element at each depth is subjected to shot peening followed by fifteen cycles of quasistatic strain-controlled cycling $\left(\dot{\varepsilon} \sim 10^{-3} s^{-1} \right)$. Accordingly, the measured initial residual stresses and the remote loading and boundary conditions corresponding to each subsurface depth are imposed. The applied cyclic bending strain range is shown in Figure 4.5 as a function of depth. Simulations were performed for two different strain ratios, R_ε = 0 and -1, corresponding to respective peak surface bending

strains of 0.55% and 0.275%. The following convention holds with regard to directions of shot peening followed by cyclic bending strain:

- Direction of impact (shot peening) – Y direction

- Equibiaxial initial residual stress state prior to cyclic loading – X and Z directions

- Cyclic bending stress – applied along Z direction

For purposes of comparison, the residual stresses are reported at the point $\varepsilon_{zz} = 0$ for each loading cycle.
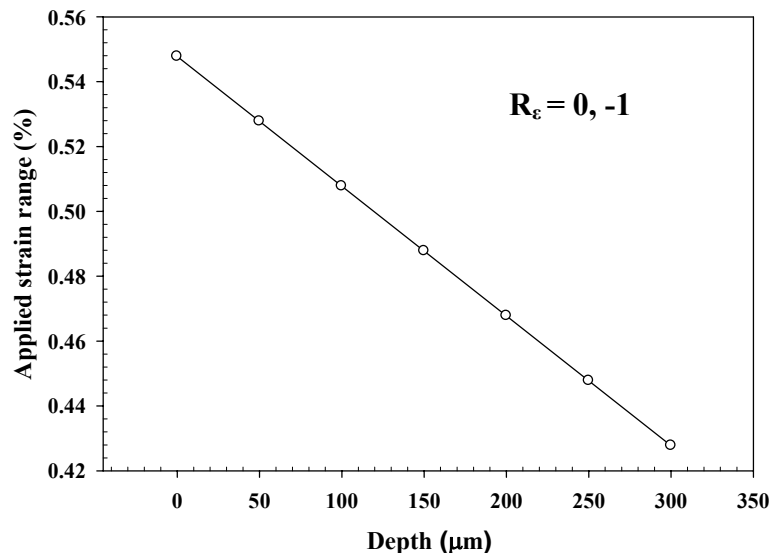
Figure 4.5. *Applied strain range as a function of depth during cyclic bending.*

4.6. Results

Figure 4.6 shows the relation between peak applied compressive strain during shot peening, $\varepsilon_{yy,load}$ and the strain after unloading, $\varepsilon_{yy,unload}$ from simulations. The maximum compressive stress occurs at a depth corresponding to the peak residual stress magnitude (75 μm) [151]. Multiple microstructure realizations of the subsurface volume elements were considered in estimating the shot peening strain levels required to match measured initial residual stress distribution, and the difference in the responses among realizations were negligible. This indicates that 784 grains are sufficient to consider the polycrystalline ensemble as a RVE for purposes of estimating residual stress. Depths considered in this study range up to 250 μm below the surface.
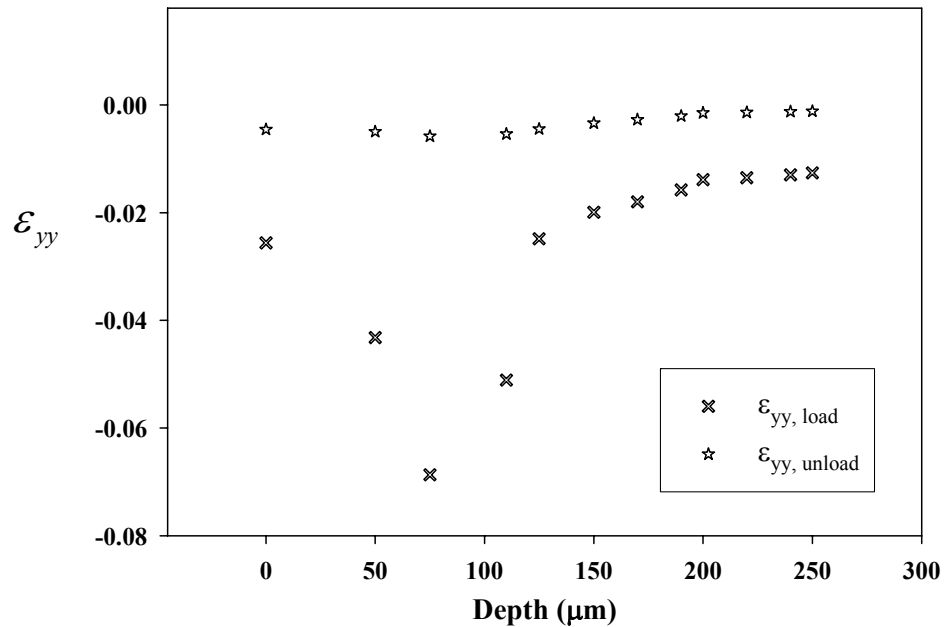
Figure 4.6. *Relation between the peak compressive strain* $\left(\varepsilon_{yy,load}\right)$ *and the strain after unloading* $\left(\varepsilon_{yy,unload}\right)$ *along surface normal direction Y during the shot peening simulation with depth.*
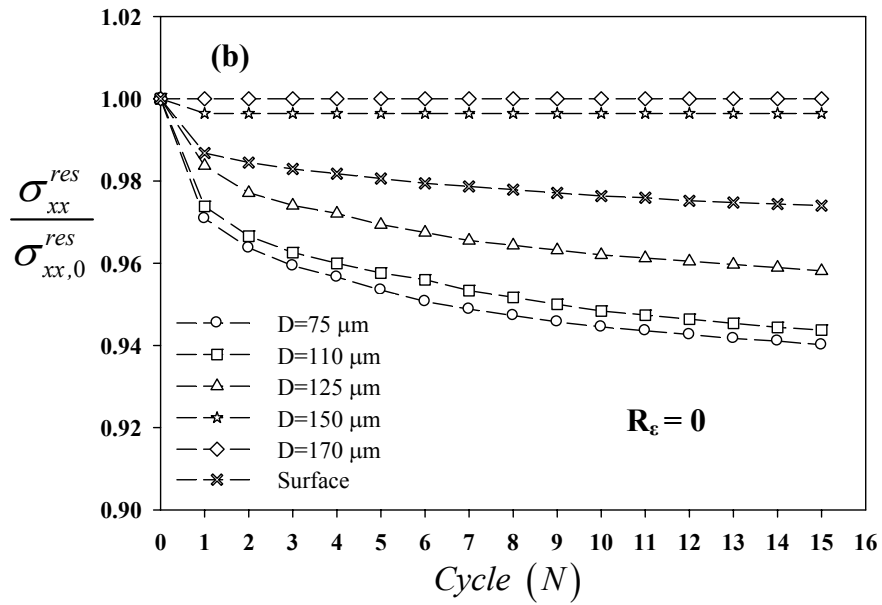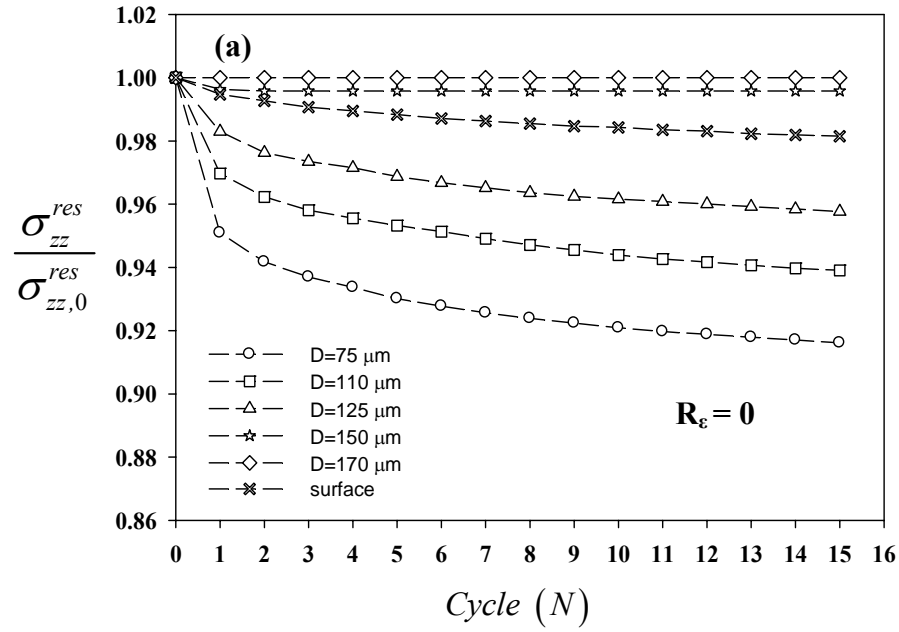
Figure 4.7. *Relaxation of residual stress components at different depths during cyclic bending (normalized by their respective initial values after shot peening) for $R_\varepsilon = 0$ case and for realization 1 along (a) Z direction and (b) X direction.*
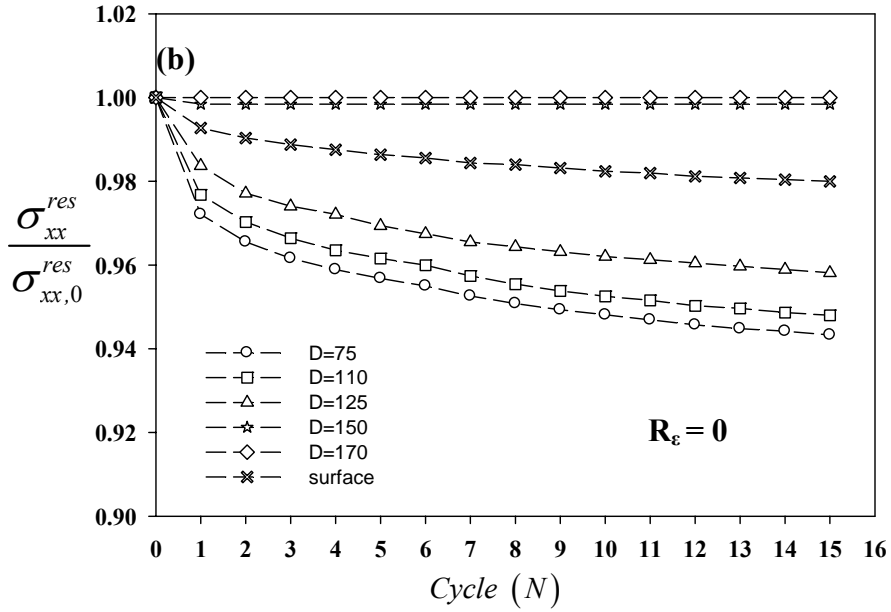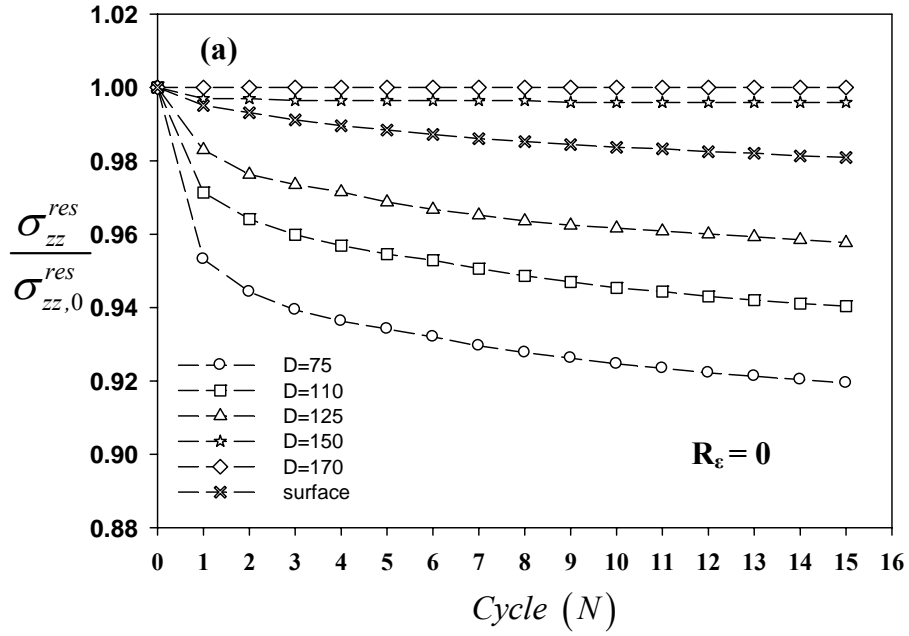
Figure 4.8. *Relaxation of residual stress components at different depths during cyclic bending (normalized by their respective initial values after shot peening) for $R_\varepsilon = 0$ case and for realization 2 along (a) Z direction and (b) X direction.*

The residual stresses introduced from shot peening simulation serve as initial conditions for subsequent cyclic loading which commences at $\varepsilon_{zz} = 0$. Figures 4.7a and 4.8a shows the variation of the normalized residual stress in the Z direction with number of cycles for R_ε = 0 for two different polycrystalline orientation distributions (realizations); the residual stresses are normalized by their respective initial values ($\sigma_{zz,0}^{res}$, see values in Figure 4.2) to illustrate the percentage reduction in the magnitude. A modest variation between different realizations is observed. Relatively significant relaxation occurs during the first loading cycle, followed by gradual relaxation with subsequent cycling; this is observed in experiments [124]. Maximum relaxation occurs at subsurface depths corresponding to the highest values of initial residual stress. Approximately 2% reduction (relaxation) in residual stress magnitude is observed at the surface and about 5% relaxation is observed at 75 μm below the surface after the first loading cycle even though the applied stress is highest at the surface during bending. The degree of relaxation depends on the initial magnitude of residual stress. Although the percentage relaxation is modest, it is still relevant to evaluating the fatigue crack formation potency since the distribution of slip within grains is heterogeneous [10, 152]. Detailed discussion on the significance of such a study will be presented later. Relaxation is not observed at depths below 170 μm. The residual stress in the lateral direction (X direction) exhibits similar relaxation trends, as shown in Figures 4.7b and 4.8b. Microplasticity occurring in favorably oriented grains promotes the relaxation of residual stress fields during fatigue cycling. Detailed investigation of the first cycle relaxation will be considered later. It is recognized that self-equilibrating nature of residual stresses will result in alteration of residual stress profile from surface to core after relaxation.

However, validating the stabilized residual stress profile requires supporting experimental evidence. Moreover, experimental estimation of the residual stress profile at regular interval in HCF is tedious.
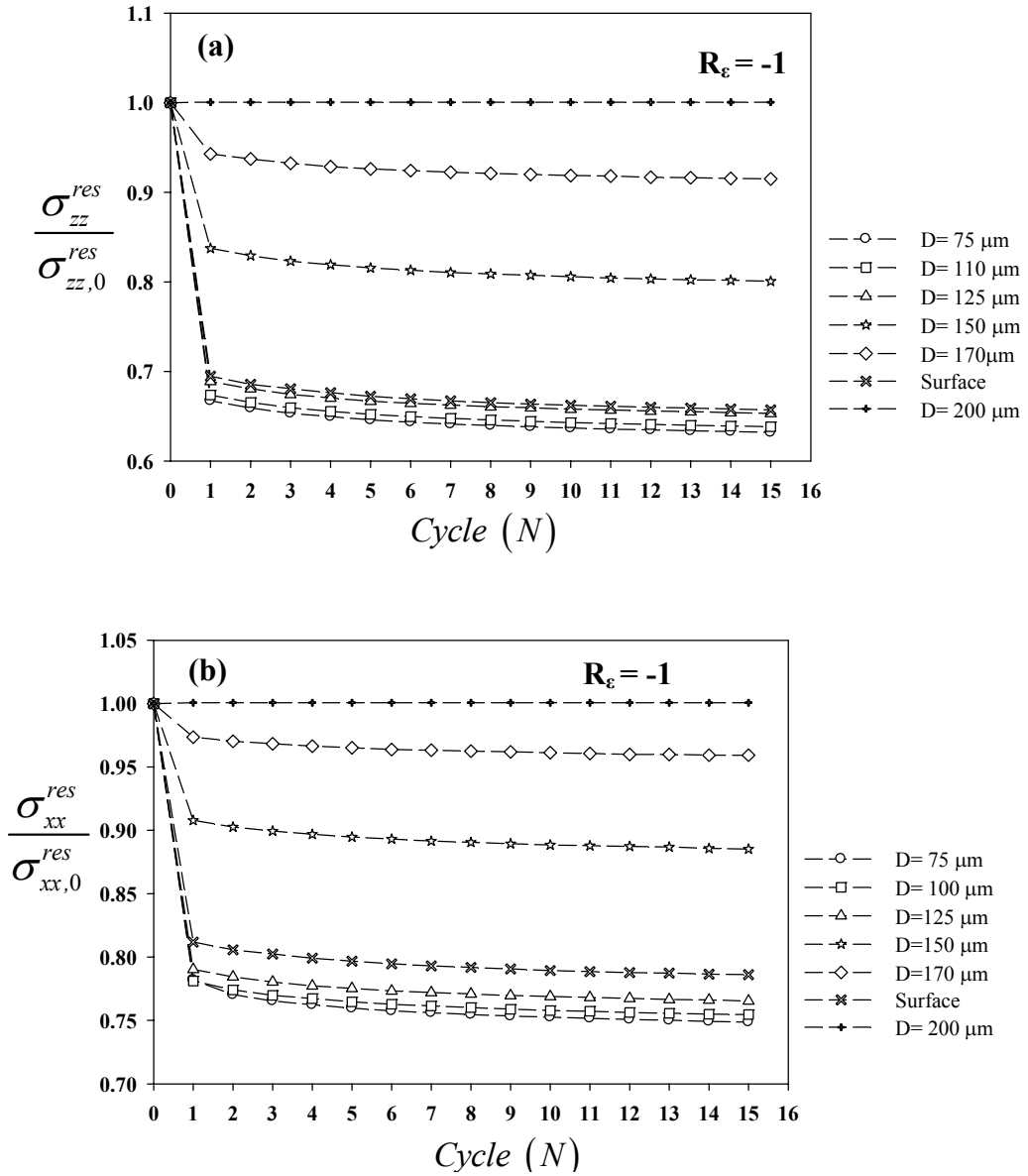
Figure 4.9. *Relaxation of residual stress components at different depths during cyclic bending (residual stresses are normalized by their respective initial values after shot peening) for $R_{\varepsilon} = -1$ case and realization 1 along (a) Z direction and (b) X direction.*
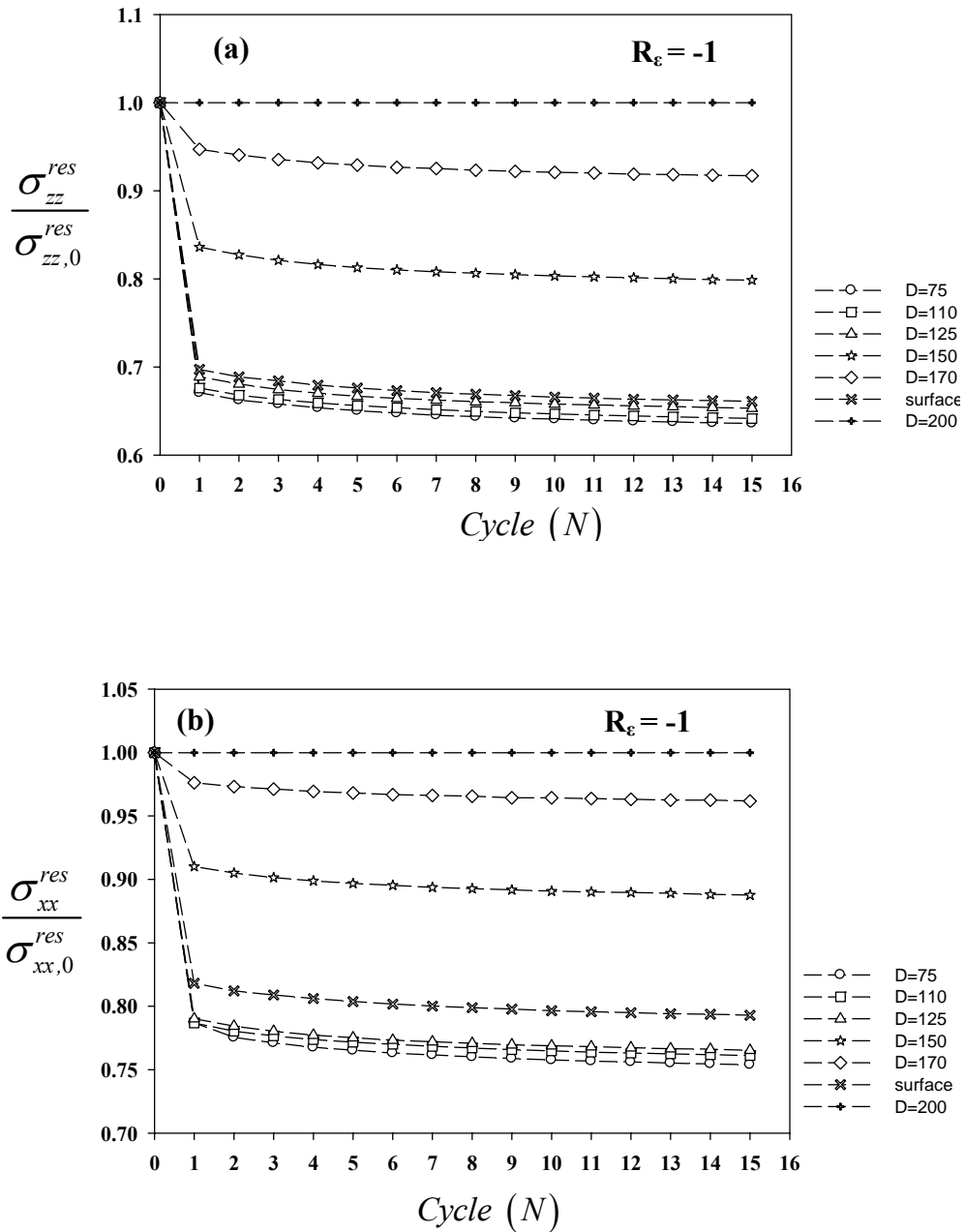
Figure 4.10. *Relaxation of residual stress components at different depths during cyclic bending (residual stresses are normalized by their respective initial values after shot peening) for $R_\varepsilon = -1$ case and realization 2 along (a) Z direction and (b) X direction.*

It is generally believed that relaxation less than 10% is negligible; however, such variations in residual stresses contribute to variability in fatigue crack formation and small crack growth at the grain scale. Fatigue crack formation could consume a

significant portion of service life under HCF loading [16] . Due to lack of sufficient experimental data, we attempt to investigate the salient points with regard to residual stress relaxation by plotting the variation in normalized residual stress values with fatigue cycling and subsequently draw potential implications.

In the case of $R_\varepsilon = -1$, for the same remote applied strain range, we observe substantial relaxation of residual stresses during the first loading cycle along X and Z directions, as shown in Figures 4.9 and 4.10; the results are shown for two different realizations. Approximately, 30% reduction in residual stress magnitude is observed during the first loading cycle at depths ranging from the surface to 125 μm. Relaxation beyond 200 μm depth is negligible. Maximum relaxation (~33%) is observed at 75 μm below the surface, similar to the $R_\varepsilon = 0$ case, indicating the dependence of relaxation on the initial residual stress magnitudes.

Figure 4.11 shows the σ_{zz} versus ε_{zz} response at different depths during the first loading cycle following shot peening for $R_\varepsilon = 0$ and -1, shedding light on relaxation of residual stress σ_{zz}. For $R_\varepsilon = 0$ at a depth of 75 μm below the surface, reverse yielding was observed during unloading. This is evident from the plot shown in Figure 4.11a. During tensile loading (loading sequence 1-2 in Figure 4.11a) the response is observed to be predominantly elastic; however, during unloading, the onset of macroplasticity is observed near the end of the cycle. This is illustrated in the enlarged inset of the stress-strain response shown in Figure 4.11a. At a depth of 170 μm, the stress-strain response is observed to be predominantly elastic without appreciable reduction of the residual stress magnitude. For $R_\varepsilon = -1$ at a depth of 75 μm below the surface, dramatic relaxation occurs during the first loading due to reverse macroscopic yielding occurring during
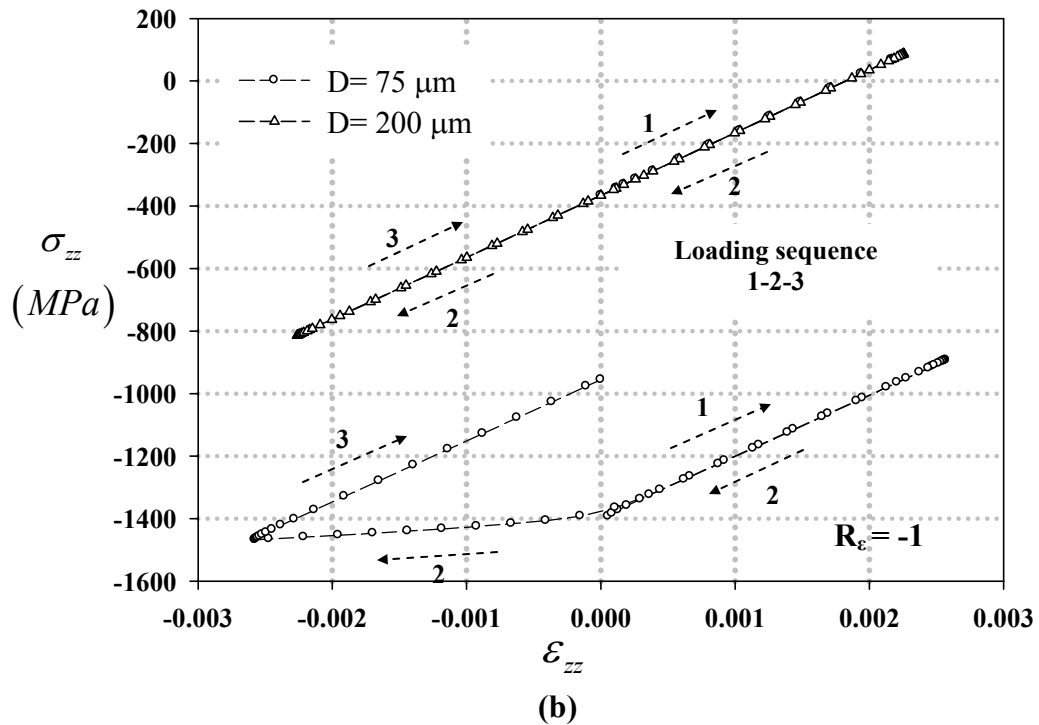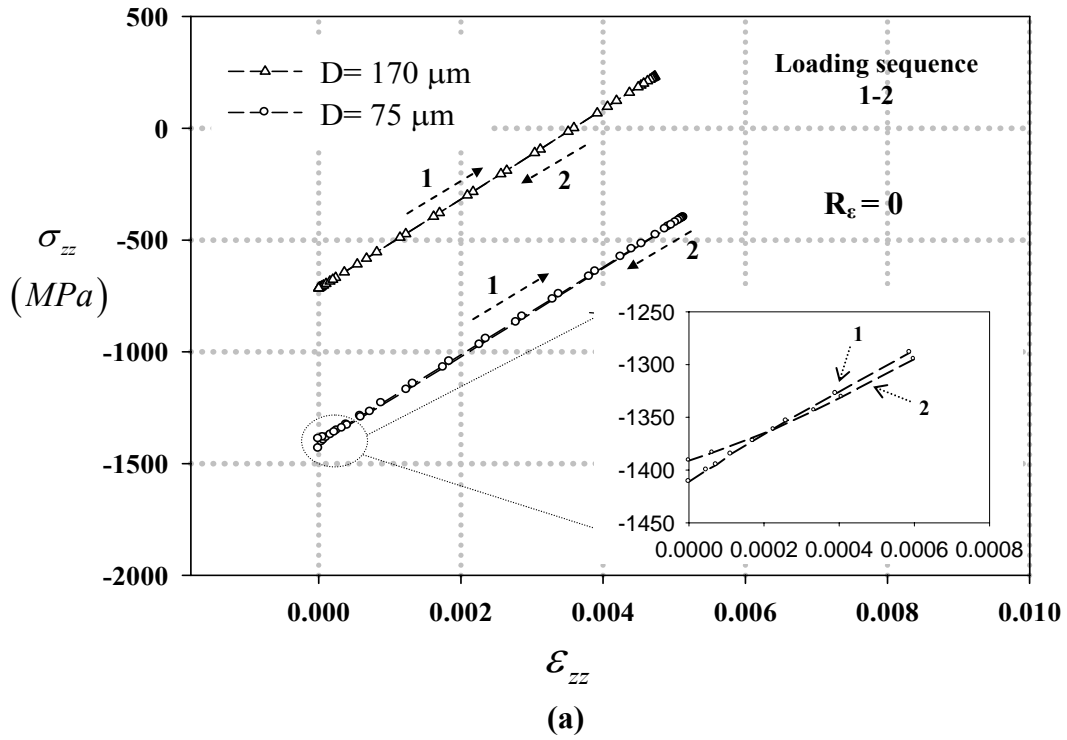
Figure 4.11. *Stress-strain response(realization 1) along cyclic bending stress direction (Z) at different subsurface depths during the first loading cycle following shot peening for (a) $R_\varepsilon = 0$ and (b) $R_\varepsilon = -1$.*

compressive half cycle, as shown in Figure 4.11b. Cyclic plasticity occurs throughout the microstructure, and subsequent unloading results in significant reduction of the residual stress magnitude, as illustrated in Figure 4.11b. Such reduction in residual stress magnitude is not observed at a depth of 200 μm below the surface as illustrated in Figure 4.11b.

4.7. Discussion

The distribution of localized cyclic plastic deformation in the microstructure (cyclic microplasticity) plays a key role in modeling HCF resistance. Unlike effective properties such as elastic stiffness, fatigue is manifested by extremal microstructure attributes that promote slip intensification. Cyclic microplasticity depends on numerous factors which include grain orientation, presence of inclusions, and processing effects (e.g., residual stresses). The modeling strategy pursued here facilitates a computational micromechanics investigation of variability in fatigue resistance due to microstructure variability [108, 153] that accounts for the influence of residual stress. For example, this framework can be utilized to evaluate the fatigue crack formation potency in the vicinity of primary inclusions that are of the order of the representative grain size. Since the process of HCF crack formation occurs through localized plastic deformation in the matrix near the inclusion, the strength of residual stress gradients at such fatigue critical "hot spots" may not be significant, such that the present algorithm is sufficient, provided the ratio of *L2* (see Figure3.4) to inclusion diameter is sufficiently large. Furthermore, the local R_ε in the vicinity of primary inclusions could significantly differ from the remote loading conditions [19]; this in turn can influence the local relaxation and redistribution of

residual stresses, and can contribute to variability in fatigue resistance. Additionally, this framework can be utilized to investigate surface to subsurface transition of sites for fatigue crack formation [154] in the presence of compressive residual stresses, accounting for relaxation of such beneficial residual stresses. The relaxation trends obtained through this computational study provide useful insight to support robust process route design. Although the percentage relaxation in residual stress for $R_\varepsilon = 0$ was small, a single compressive overload during a fatigue history can significantly reduce the beneficial compressive residual stress. This is evident from the results obtained for $R_\varepsilon = -1$ loading case. Compressive overloads can occur for many reasons such as human errors during maintenance, improper fixturing of components, component usage, etc. In addition, variable amplitude loading, operating environment, etc. can influence residual stress relaxation behavior.

An important point of the present study is that polycrystal plasticity is essential to capture the cyclic stress relaxation as the applied strain amplitude is decreased. Microplasticity occurs within favorably oriented grains well below the macroscopic yield strength, resulting in relaxation. Furthermore, since fatigue crack formation processes often start at the scale of grains, modeling the distribution of slip and residual stress relaxation is a significant aspect in the HCF regime.

4.8. Conclusions

A three-dimensional polycrystal plasticity model for cyclic deformation of lath martensitic gear steel is employed in a simplified scheme to simulate the effect of shot peening on residual stress distribution. The model was utilized to investigate the

relaxation of compressive residual stresses during cyclic bending in the HCF regime. Simulations were performed for two different applied bending strain ratios. The normalized trends of residual stress relaxation obtained through finite element simulations agree fairly well with experimental trends. Detailed investigation of the first cycle relaxation was performed. Residual stress relaxation in HCF is primarily attributed to the cyclic microplasticity occurring in favorably oriented grains. Furthermore, for R_ε = -1, extensive cyclic plasticity throughout the microstructure during the compression half cycle led to substantial relaxation in the first cycle. The initial magnitude of residual stress was observed to influence the degree of relaxation. Potential applications of the proposed computational framework were discussed, including the influence of residual stress on fatigue crack formation at primary inclusions. This work has been submitted as journal manuscript in 2009 and is in review [155].

Chapter 5

SIMULATED EXTREME VALUE FATIGUE SENSITIVITY TO INCLUSIONS AND PORES IN MARTENSITIC STEELS

This chapter presents a strategy to model the sensitivity of fatigue resistance of secondary hardening martensitic gear steels to variability in extrinsic inhomogeneities such as primary inclusions, and pores, coupled with intrinsic microstructure variability at scales on the order of block or grain size. A simplified approach is developed to quantify the variability in the FIPs in the matrix at nonmetallic inclusions and pores in lath martensitic gear steels using a three-dimensional crystal plasticity constitutive model. Several remote loading conditions are considered in the HCF regime relevant to applications. Idealized inhomogenieties (spherical) in the form of stiff (Al_2O_3), elastically compliant and plastically soft inclusions (La_2O_2S), and pores are systematically investigated. Relations between remote loading conditions and local plasticity are discussed as a function of stress amplitude and microstructure. The maximum plastic shear strain range is used in the modified form of Fatemi-Socie parameter evaluated at the grain scale as FIP. Multiple realizations of the polycrystal microstructure are considered to obtain a statistical distribution of this fatigue indicator parameter (FIP). The results are used to construct an extreme value Gumbel distribution of the FIPs for the selected microstructures. Subsequently, a computational micromechanics based minimum-life estimate that corresponds to 1% fatigue crack formation probability is calculated.

5.1. Introduction

Improved knowledge of critical life-limiting factors that govern the HCF response of lath martensitic gear steels will aid in design of new process routes to mitigate severity of damage during fatigue cycling. Of particular interest is the fatigue crack formation (nucleation plus early growth) at nonmetallic primary inclusions and pores in steel structures. HCF crack formation and microstructurally small crack growth is highly heterogeneous at the grain scale [10, 152, 156], and significant variability in fatigue response is realized in HCF. Much effort has been devoted to characterize the correlative relations in terms of statistical distributions of fatigue life or fatigue strength. Computational micromechanics schemes have been increasingly applied to gain more detailed understanding of HCF mechanisms and to shed light on the origins of scatter in HCF [108, 153, 157]. As pointed out by Ortiz [158] and McDowell [10, 159], computational micromechanics is still in a relatively early stage in addressing the nucleation of defects in crystals. Although formation of fatigue cracks is a tremendously complex, material-specific phenomenon, many aspects of fatigue of microstructures are amenable to relatively straightforward computation in order to gain insight into structure–property relations and to build more accurate, predictive engineering models for HCF.

Steels have highly complex microstructures. There are a myriad of interactions between steel chemistry and heat-treatment processing that combine to produce desirable microstructures and properties for specific applications. The presence of inhomogenieties in the form of nonmetallic inclusions and pores affect the longevity of steel components. Moreover, in multiphase steels in the transition regime from HCF to VHCF, there is a competition between crack formation at internal defects such as inclusions and soft

phases such as austenite [160]. Inclusions and pores are the most important microstructure attributes in establishing the extent of the statistical variation in the HCF life of high strength steels [161]. It is important to characterize the distributions of plastic strain measures in the neighborhood of the local material heterogeneities during processing and service and to correlate these measures with microstructure descriptors that permit assessment of relative fatigue resistance. Unlike effective properties such as elastic stiffness, fatigue is manifested by extremal microstructure attributes that promote slip intensification.

Several factors such as size, spacing, and spatial distribution of nonmetallic primary inclusions and orientation of grains contribute to the experimentally observed scatter in fatigue lives. Historically, fatigue damage occurring at nonmetallic inclusions and pores have been attributed to the extreme values of a single microstructure attribute (e.g., size of the inhomogenieties) [162-165]; however, there are several other factors such as residual stresses, matrix grain orientation in the vicinity of the inclusions, and interfacial damage (debonded or cracked inclusions) that contribute to minimum fatigue properties. Conventional extreme value statistical analyses rely on a sufficiently large number of costly and time-consuming experimental evaluations of fatigue failures [166]. Furthermore, assessment of individual factors such as the effects of spatial distribution of inclusions, process route (residual stresses), etc. on local inelastic response at fatigue critical inclusions is tedious to obtain from experiments. Both specimen scaling issues and measurement resolution are prohibitively problematic. Such issues are perhaps most effectively explored with computation [4, 167] as a means to leverage experiments.

In this work, the influence of variation in local polycrystalline matrix grain orientation on HCF crack formation at nonmetallic primary inclusions and pores is systematically investigated. We do note that pores are modeled as a limiting case of an elastically compliant inclusion; occurrence of pores is not a possibility in the secondary hardening martensitic steel investigated in the present study. Three-dimensional statistical volume elements (SVEs) with an idealized spherical inclusion or pore embedded in the polycrystalline steel matrix are subjected to several fatigue cycles with strain ratio $R_\varepsilon = 0$. Hard and soft inclusions (intact and partially debonded) and pores are considered. These SVEs are too small to be regarded as being statistically representative in terms of the distribution of localized plastic deformation. Hence, a number of SVE realizations or instantiations are necessary to build ensemble statistics. The target microstructure response (i.e., cyclic microplasticity) varies among each SVE realizations. A crystal plasticity framework described in Section 4.3 is utilized to model the microstructure-scale elastic-plastic response of high strength martensitic gear steel. Grain scale averaged values of the Fatemi-Socie (FS) parameter is used as FIP. Multiple realizations of the polycrystalline matrix grain orientation distribution are considered and the peak value of FIP from each realization is utilized to construct an extreme value Gumbel distribution [168]. Consequently, the Gumbel distribution is utilized to estimate 1% probability of fatigue crack formation at the grain scale. It is important to clarify that the terms "hard" and "soft" are used to describe the plastic compliance of the inhomogeneity and the terms "stiff" and "compliant" are used to describe the elastic compliance of the inhomogeneity. Hard inclusions are brittle. For example, La_2O_2S inclusions are elastically more compliant and plastically softer compared to Al_2O_3 inclusions as illustrated later.

5.2. Methodology

Statistical extremes of fatigue life distribution have been primarily based on extrapolation of large number of experimental data [169]. Furthermore, HCF crack formation and early growth depend mainly on a few key attributes (or set of attributes) such as the largest nonmetallic inclusion or the most favorably oriented grain for slip intensification. There is a significant scatter in the experimentally measured HCF life because attributes that govern minimum fatigue resistance lies in the tails of the *joint distributions* of attributes and responses, necessitating use of extreme value statistics. As pointed by Sasaki and co-workers [169], experimentally observed scatter in HCF is primarily due to formation and growth behavior of small cracks that cannot be adequately characterized through application of the traditional Paris crack growth law based on LEFM. The authors experimentally examined the effect of grain size on variability in fatigue crack formation and propagation lives in different metallic materials asserting the importance of characterizing different stages of fatigue crack formation and growth. Historically, the largest inclusion present in the fatigue critical regions was believed to govern the minimum fatigue life of the component, as summarized in the recent review by Atkinson [162]. However, the detrimental effects of a single large inclusion can be replicated by the interaction of relatively smaller inclusions closely spaced in a cluster. In addition to inclusion size, variation in the polycrystalline matrix grain size and orientation contribute to scatter in fatigue life [157, 170]. Such issues are perhaps more prominent in the HCF regime where cyclic microplasticity is confined to a low number density of fatigue critical "hot spots".

The present work focuses on characterizing the effect of variation in the polycrystalline matrix grain orientation in the vicinity of fatigue critical nonmetallic inclusions and pores on fatigue crack formation life of secondary hardening martensitic gear steel such as the C61 class of steel [36]. Experiments have revealed alumina (Al_2O_3) and lanthanum oxy-sulfide (La_2O_2S) inclusions to be the critical life-limiting attributes in C61 class of steels [27]. Here, we consider an idealized single spherical inclusion of diameter of 5 μm typical of the inclusion size observed on the fracture surface; Al_2O_3 inclusions are modeled as isotropic, linear elastic with Young's modulus, E=380 GPa, and Poisson's ratio, ν=0.2. Elastic properties of La_2O_2S [171] and yield strength [172] estimated from the hardness values were taken from the literature. Due to insufficient experimental data, La_2O_2S is modeled as an elastic-perfectly plastic material. The elastic properties of La_2O_2S are E=200 GPa and ν=0.23; the yield strength is estimated as 1.2 GPa. Two extreme interfacial conditions are considered, namely intact and partially debonded inclusion-matrix interfaces. In addition to the aforementioned inclusion types, we also model the effect of a spherical pore to evaluate the relative potency for fatigue crack formation. Table 5.1 lists the cases simulated in this study. For convenience, results for all cases presented in the subsequent sections will be identified with the 'case pointer' listed in Table 5.1.

Figure 5.1 shows different cross sectional views of the 3D domain, elaborating on the dimensions of FE domain with the boundary conditions, and uniaxial loading direction enforced in the simulations. Additionally, we impose a multipoint constraints that the nodes on the faces x=L and y=L (L=50 μm) have the same displacement in directions x and y, respectively, during fatigue cycling. The dimensions of each SVE are chosen to be

Table 5.1. *List of cases modeled to investigate the variability in fatigue resistance.*

Case pointer	Inhomogeneity	Interfacial condition
A	Al_2O_3	Intact
B	La_2O_2S	Intact
C	Pore	-
D	La_2O_2S	Partially debonded
E	Al_2O_3	Partially debonded

sufficiently large that the inclusion experiences negligible boundary interaction effects. We define a region, V_p, encompassing the inclusions and pores (see Figures 5.1a and b) in which the FIP is evaluated as an average value over each grain within the region. Such an approach is followed to locate the most favorably oriented grain undergoing cyclic microplasticity under the influence of the micronotch root stress field. Furthermore, a consistent FIP estimation procedure is necessary while investigating the fatigue response for different remote loading conditions. It is acknowledged that the grain adjacent to the inclusion or pore will experience peak stress (or strain) amplitude; however, since the size of individual grain $\left(\sim 2\mu m \right)$ is small relative to the size of the inhomogeneity$\left(5\mu m \right)$, the possibility that the second nearest neighbor is the most favorable site for crack formation cannot be completely ruled out. It is noted that the

distinction between "hard" and "soft" grain does not solely depend on the grain orientation but also on the neighboring grain orientations. Since random orientations are assigned to each grain in the present study, the aforementioned approach to estimate FIPs is justified.
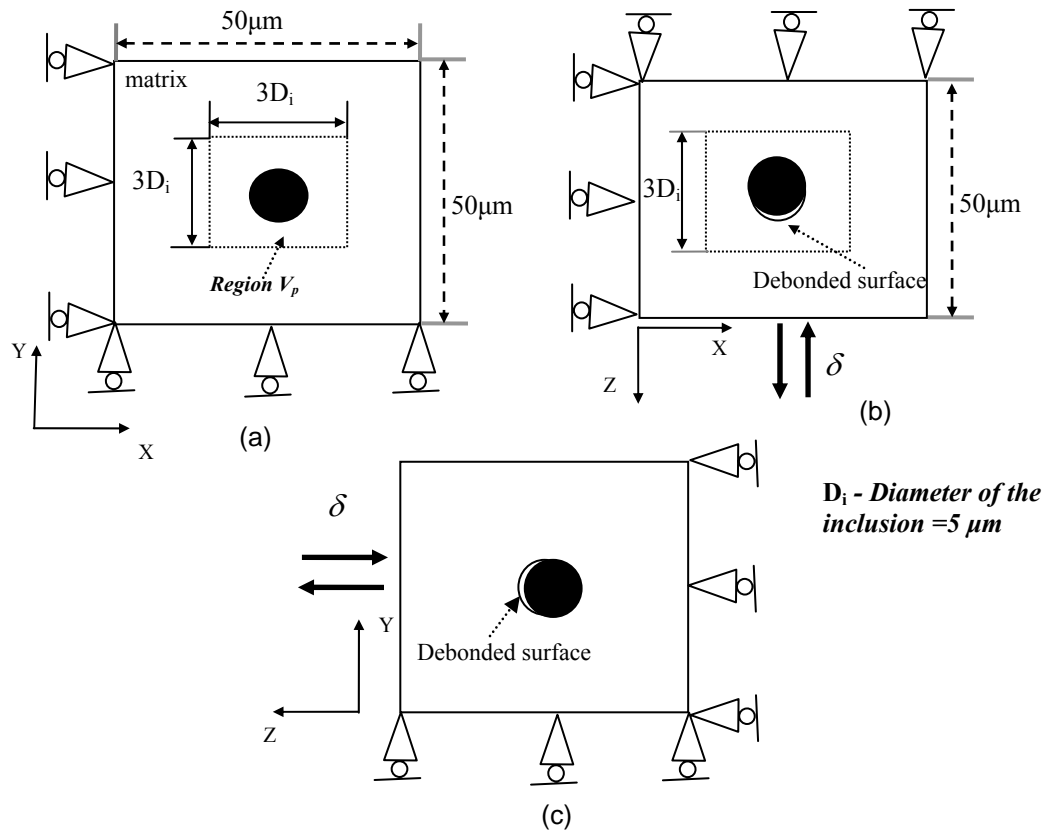
Figure 5.1. *Cross-sectional views of the 3-D section with embedded inclusion (or pore) elaborating on the debonded surface, boundary conditions for uniaxial loading and the direction of cyclic loading. Views across (a) XY, (b) XZ, and (c) YZ cutting planes through the center of the inclusion.*

Figure 5.2 shows a cross-section of a 3-D FE mesh. A fine mesh is employed close to the inclusion (element size about 0.5 μm), fanning out with a coarse mesh away from the inclusion for computational efficiency. The region of fine mesh corresponds to the

region V_p where each grain is comprised of several 3D four node tetrahedral elements. Reduced integration is employed. In the far field zone, more than one inclusion diameter away from the interface each finite element is assumed to represent a single lath martensite grain. Such an approach is adopted to enhance computational efficiency since 3D crystal plasticity simulations with 48 slip systems are computationally intensive. Furthermore, since the remote loading conditions are within the HCF regime for which cyclic microplasticity is confined to fatigue critical regions such as near the interface of nonmetallic inclusions, the aforementioned meshing strategy is acceptable.
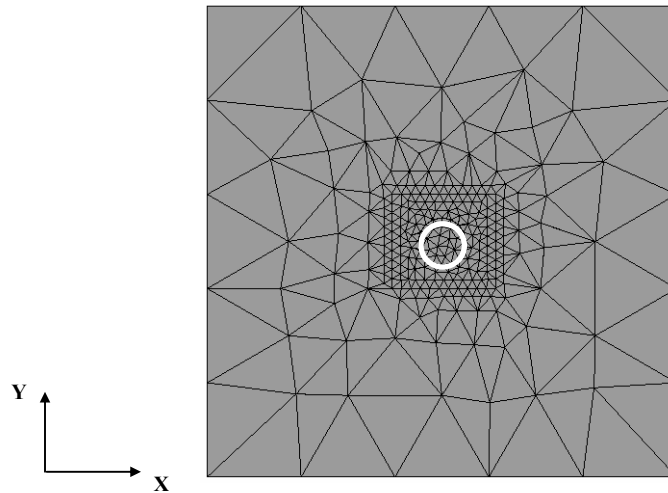
Figure 5.2. *Cross-section of the 3D FE mesh through the center of the inclusion, showing refinement close to the inclusion. Cyclic loading is in the Z direction.*

Although there are several sources of strengthening in secondary hardening lath martensitic steels such as precipitation strengthening, solid solution strengthening, dislocation strengthening, and grain boundary strengthening [27], contributions from the individual sources are not distinguished in the present study. To model strengthening processes occurring at submicron scales, suitable scale-dependent constitutive models are imperative; however, the evolution of slip resistance and back stress is captured in an

average sense through the crystal plasticity constitutive model in this case. Cyclic hardening occurs primarily due to large phase fraction of non-shearable M_2C precipitates serving as Orowan obstacles in the secondary hardening martensitic gear steels [27]. The material constants relevant to secondary hardening C61 gear steel is presented in Table 4.2. We may assert a nonlocal Coffin-Manson relation $\Delta\Gamma = \gamma'(N_i)^q$ with constants estimated as $\gamma' = 0.335$ and $q = -0.714$. N_i is the number of cycles to form a crack of length of the order of block size (~2 μm) in the vicinity of inclusions and pores. The

region V_p (see Figure 5.1) is comprised of 110 cubic lath martensite grains with each grain discretized into at least four 3D tetrahedral elements. The average element size is meshed to be 0.5 μm. This is achieved by constructing the FE mesh with inclusion and subsequently sub-dividing the matrix portion of FE mesh into several grains. The block size of tempered lath martensite is too small to experience significant stress gradients across the grain. Furthermore, the element size of 0.5 μm adopted in this study is a limiting value for application of continuum crystal plasticity. Hence, a mesh convergence study which varies the element size below this value may not conform to requirements of continuum approximation. Frictionless contact is assumed along debonded regions. A single FE mesh is sufficient for the present study since the variation in HCF response is achieved through assigning different random orientations to grains and modifying the inclusion material properties for each case investigated. In case C, the FE mesh corresponding to the inclusion is eliminated.

The ratio of peak remote applied uniaxial strain (ε_{max}) to the strain at macroscopic proportional limit $(\varepsilon_y \approx 0.7\%)$ is defined by $\zeta = \dfrac{\varepsilon_{max}}{\varepsilon_y}$. FIP distributions are computed for each case listed in Table 5.1 for several values of $\zeta (= 0.7, 0.85, 1)$ with $R_\varepsilon = 0$. A SVE representing a single realization of polycrystalline matrix grain orientation distribution is subjected to several quasistatic strain-controlled cycles $(\dot{\varepsilon} \sim 10^{-3} s^{-1})$ for a selected ζ and R_ε to obtain a stabilized FIP response and the peak value of the FIP, $(\Delta\Gamma_{max})_i$, is recorded for each of N instantiation, $i (= 1, 2, ... N)$. A sufficiently large number of realizations are necessary to construct a statistical ensemble. The distribution of $(\Delta\Gamma_{max})_i$ is used to construct an extreme value statistical distribution, as discussed in the next section.

5.3. Extreme value statistical framework and minimum life estimation

Murakami and co-workers [165, 173] were the first to apply statistics of extremes to predict the maximum inclusion size in a selected volume of steel. The main premise of extreme value theory is that when a fixed number of data points following a basic distribution are collected, the maximum and minimum of each of these sets also follow a distribution. The extreme value Gumbel distribution function of maxima obtained from a number of simulations is used in the present study to characterize the extreme value response with the form

$$G(z) = \exp\left(-\exp\left(-\left(\frac{z-\lambda}{\psi}\right)\right)\right) \qquad (5.1)$$

Here, $G(z)$ is the probability that the peak value of selected response or variable is not greater than z, and ψ and λ are the scale and location parameters, respectively. Recent investigation by Tiryakioglu [174] showed the Gumbel distribution function to be superior compared to other extreme value distribution functions in capturing size variability of critical defects in A356 castings.

If $z = \Delta\Gamma_{max}$, the cumulative probability of maximum FIP, $G(z_i)$, can be calculated via mean rank statistics by

$$G(z_i) = \frac{i}{N+1} = \exp\left(-\exp\left(-\frac{z_i-\lambda}{\psi}\right)\right) \qquad (5.2)$$

where z_i is the ith value of $(\Delta\Gamma_{max})_i$ which are classified, starting from the smallest, and ranked with $i = 1, 2, ...N$ according to

$$(\Delta\Gamma_{max})_1 \leq (\Delta\Gamma_{max})_2 \leq ... \leq (\Delta\Gamma_{max})_N \qquad (5.3)$$

Plotting $(\Delta\Gamma_{max})_i$ against $\varpi = -\ln\left(-\ln\left(G(z_i)\right)\right)$, and fitting a straight line we obtain the slope ψ and intercept on the vertical axis λ. Once λ and ψ are determined, employing the nonlocal Coffin-Manson relation discussed in Section 5.2, we obtain probability of fatigue crack formation at the scale of a grain as

$$P_{formation}(N_i) = 1 - \exp\left(-\exp\left(-\frac{\gamma'(N_i)^q - \lambda}{\psi}\right)\right) \tag{5.4}$$

This relation is used to estimate the minimum life for each case listed in Table 5.1.

5.4. Results
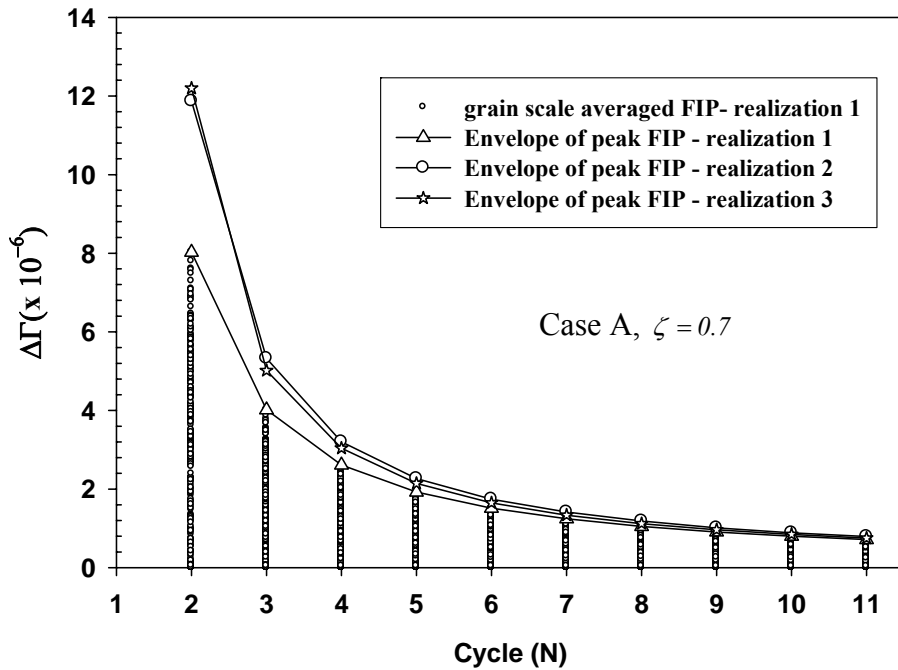
Figure 5.3. *Plot showing the variation of grain scale averaged FIP in the vicinity of primary inclusion for a selected polycrystal realization (realization 1) over several loading cycles and a plot of the envelope of peak FIP over several loading cycles for realizations 1, 2, and 3 for case A.*

Three-dimensional crystal plasticity simulations of SVEs comprising of single inclusion or pore embedded in a polycrystalline matrix were conducted for three values of $\zeta\,(= 0.7, 0.85, 1)$ and $R_\varepsilon = 0$. Twenty different realizations $(N = 20)$ of polycrystalline matrix grain orientations were considered to estimate the variability in the fatigue resistance for

each case listed in Table 5.1 and to construct the corresponding extreme value Gumbel distributions. Figure 5.3 shows the variation in the grain scale averaged (nonlocal) FIP for a single realization evaluated during each loading cycle for Case A and $\zeta = 0.7$, for example. The particular location of extreme value response (grain) in each case does not change with the loading cycles. Also shown in Figure 5.3 are the envelopes of peak FIP over each loading cycle for realizations 1, 2, and 3, illustrating the rapid reduction in the variability with loading cycles. Such behavior is observed even when the remote applied strain is within the elastic limit and is primarily attributed to the isotropic hardening occurring in the grains undergoing plasticity in the vicinity of inhomogeneities. Furthermore, constitutive models utilized in the computational methods such as FE analyses require stabilized local stress-strain response which occurs over several loading cycles depending on numerous factors such as remote loading conditions, operating temperature, etc. While considering cyclic softening, the corresponding FIP response inverts relative to cyclic hardening in that the FIP increases with loading cycles and stabilizes after several loading cycles.

The FIP distributions were observed to stabilize after 11 loading cycles for all the cases considered in this study. Hence, the extreme value of the FIP for each realization is obtained after 11 loading cycles and utilized to construct the corresponding Gumbel distribution. Although time-consuming, such a strategy is essential to model the HCF resistance of metallic materials using crystal plasticity. This is because FIPs estimated prior to stabilization may lead to inaccurate estimates of variability. For example, after three loading cycles, we observe significant variation in the peak values of FIPs between each realization, as shown in Figure 5.3. Furthermore, such estimation will lead to overly

conservative predictions of crack formation probabilities while employing extreme value statistics. In fact, more than 11 cycles would be desirable but are prohibitive for the present illustrative purposes.
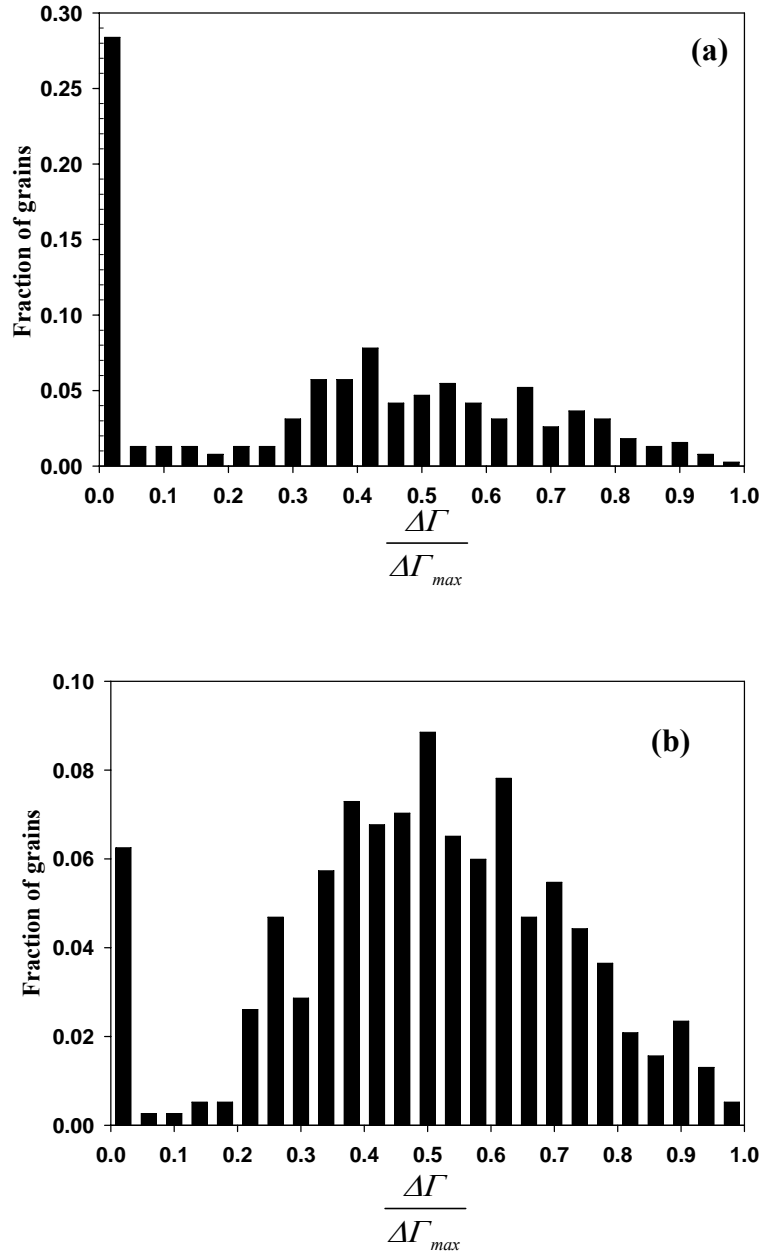
Figure 5.4. *Distribution of normalized FIP evaluated during 11th loading cycle for a single realization of polycrystalline microstructure (realization 1) for Case A: (a) $\zeta = 0.7 \left(\Delta \Gamma_{max} = 7.19 \times 10^{-7} \right)$, (b) $\zeta = 0.85 \left(\Delta \Gamma_{max} = 5.15 \times 10^{-6} \right)$, and (c) $\zeta = 1 \left(\Delta \Gamma_{max} = 1.39 \times 10^{-4} \right)$.*
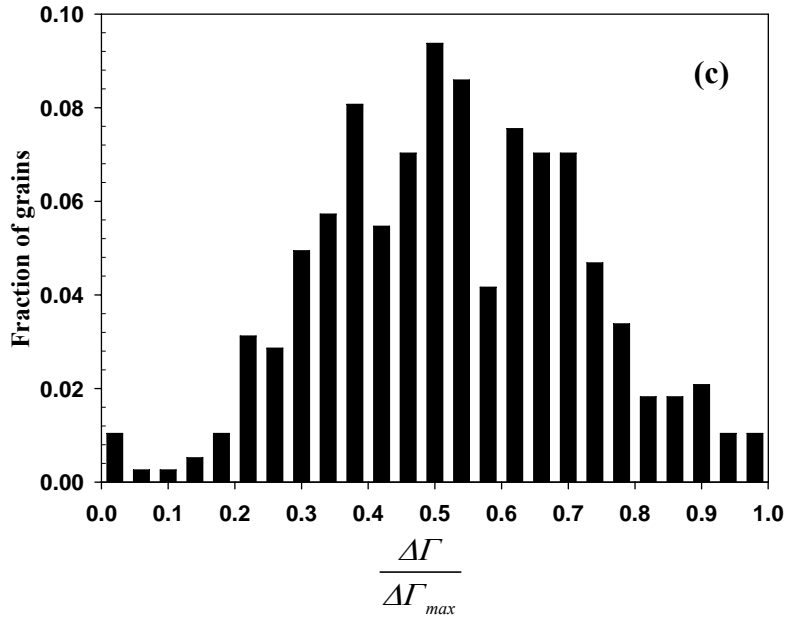
Figure 5.4. *Continued.*

It is instructive to consider the simulated distribution of the normalized nonlocal $\Delta\Gamma$ among grains plotted after eleven loading cycles for various ζ, as shown in Figures 5.4 (a)-(c). It is noted that only the results of Case A is plotted in Figure 5.4 for illustrative purposes. Comparatively, fewer grains experience cyclic plasticity at $\zeta = 0.7$. At macroscopic yielding $(\zeta = 1)$, in contrast, most grains undergo cyclic microplasticity. As the applied strain amplitude increases, slip heterogeneity decreases [148] and the shape of the distribution of $\Delta\Gamma$ shifts substantially. The tail of the distribution (maximum $\Delta\Gamma$) controls minimum fatigue crack formation life. This distribution of FIP can be used to project minimum crack formation life and its variability. Furthermore, as demonstrated by Shenoy et al. [108], such distributions can be utilized to predict the distribution of small cracks that form during fatigue of polycrystals, and are therefore useful for

developing relations of variability of fatigue properties as a function of microstructure and applied loading conditions.

Here, we consider 20 different realizations of the random polycrystalline matrix grain orientation distribution to characterize the variability in the fatigue resistance in the presence of inhomogenieties. The finite element mesh and grain size are the same for all realizations, with only the grain crystallographic orientation changed. For each case listed in Table 5.1, the peak value of FIP from each realization, $(\Delta\Gamma_{max})_i$ in Figure 5.4, is utilized to construct the extreme value Gumbel distribution for each value of ζ.
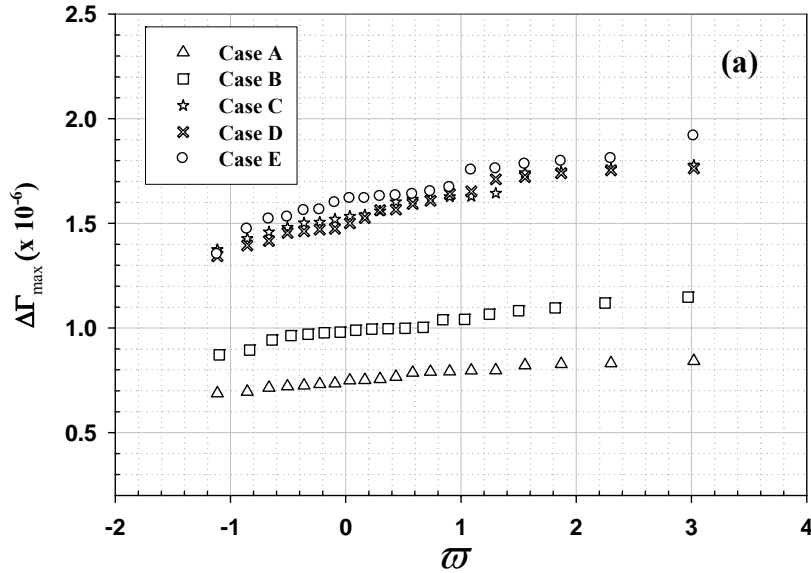
Figure 5.5. Extreme value FIP distribution (vs. $\varpi = -\ln\left(-\ln\left(G(z_i)\right)\right)$) as estimated over the grain size averaging volumes for (a) $\zeta = 0.7$, (b) $\zeta = 0.85$, and (c) $\zeta = 1$ after 11 loading cycles. The extreme value FIP was selected to be the FIP with highest magnitude among all the grains.
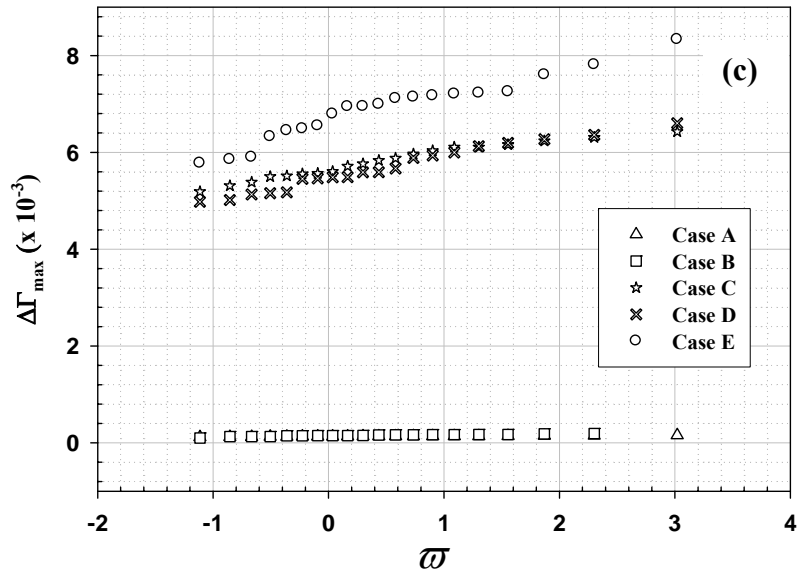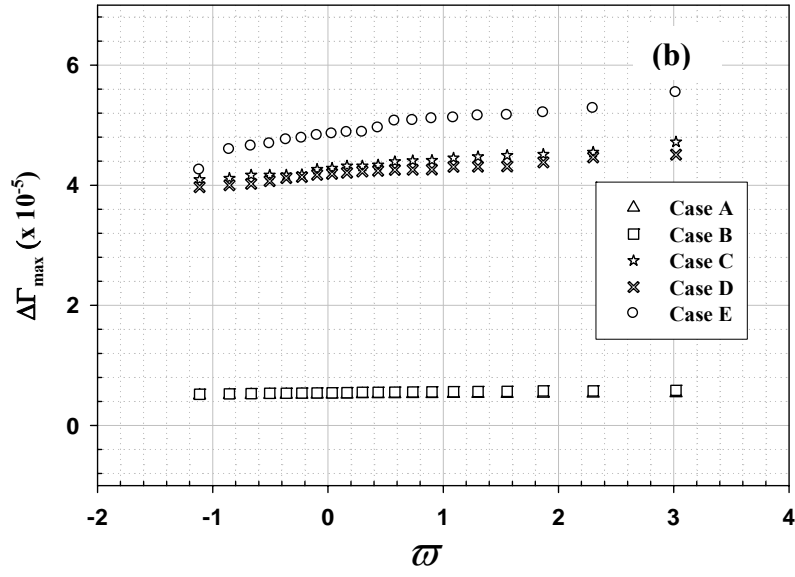
Figure 5.5. *Continued.*

Table 5.2. *The smallest and largest values of $\Delta\Gamma_{max}$ among realizations for each case investigated in this study.*

	$\zeta = 0.7$		$\zeta = 0.85$		$\zeta = 1$	
	$\left(\Delta\Gamma_{max}\right)_1$	$\left(\Delta\Gamma_{max}\right)_{20}$	$\left(\Delta\Gamma_{max}\right)_1$	$\left(\Delta\Gamma_{max}\right)_{20}$	$\left(\Delta\Gamma_{max}\right)_1$	$\left(\Delta\Gamma_{max}\right)_{20}$
Case A	6.88×10^{-7}	8.42×10^{-7}	5.01×10^{-6}	5.37×10^{-6}	1.18×10^{-4}	1.57×10^{-4}
Case B	8.72×10^{-7}	1.15×10^{-6}	5.18×10^{-6}	5.84×10^{-6}	0.97×10^{-4}	1.96×10^{-4}
Case C	1.37×10^{-6}	1.78×10^{-6}	4.09×10^{-5}	4.72×10^{-5}	5.19×10^{-3}	6.43×10^{-3}
Case D	1.34×10^{-6}	1.76×10^{-6}	3.96×10^{-5}	4.55×10^{-5}	4.98×10^{-3}	6.61×10^{-3}
Case E	1.35×10^{-6}	1.92×10^{-6}	4.25×10^{-5}	5.52×10^{-5}	5.78×10^{-3}	8.02×10^{-3}

Figures 5.5 (a)-(c) show the distribution of peak FIP from each realization for Cases A-E listed in Table 5.1 and for several remote loading strain levels $(\zeta = 0.7, 0.85, 1)$. The procedure outlined in Section 5.3 is used to construct the extreme value distribution $(\Delta\Gamma_{max} \, vs \, \varpi)$. For clarity, the smallest and the largest values of the extreme value of FIP for each case simulated in this study are reported in Table 5.2; the subscripts '1' and '20', denote the smallest and largest value of $\Delta\Gamma_{max}$ obtained from 20 different realizations, respectively. This distribution is utilized to obtain the scale (ψ) and location (λ) parameters, relevant to the Gumbel distribution by fitting a straight line and estimating the slope and the intercept on the vertical axis, as described in Section 5.3; resulting values of ψ and λ are reported in Table 5.3. Also listed in Table 5.3 are the values of goodness of fit (R^2). It can be seen from Table 5.3 that a reasonably good fit is obtained $(R^2 > 0.9)$ for the various extreme value FIP distributions. Recently, Przybyla and McDowell [157] showed that 25 different realizations of polycrystalline matrix orientations were sufficient to capture the scale and location parameters with reasonable

accuracy. Once λ and ψ are determined, it is relatively straightforward to estimate the

probability of fatigue crack formation employing Equation (5.4).

Table 5.3. *Values of λ, ψ, and R^2 for various cases modeled in this study.*

	$\zeta = 0.7$			$\zeta = 0.85$			$\zeta = 1$		
	ψ	λ	R^2	ψ	λ	R^2	ψ	λ	R^2
Case A	4.6×10^{-8}	7.4×10^{-7}	0.96	8.4×10^{-8}	5.2×10^{-6}	0.95	8.7×10^{-6}	1.3×10^{-4}	0.95
Case B	6.5×10^{-8}	9.8×10^{-7}	0.96	1.7×10^{-7}	5.4×10^{-6}	0.97	2.2×10^{-5}	1.4×10^{-4}	0.91
Case C	1.1×10^{-7}	1.5×10^{-6}	0.97	1.5×10^{-6}	4.3×10^{-5}	0.96	3.6×10^{-4}	5.6×10^{-3}	0.97
Case D	1.3×10^{-7}	1.5×10^{-6}	0.98	1.4×10^{-6}	4.2×10^{-5}	0.94	4.5×10^{-4}	5.4×10^{-3}	0.97
Case E	1.2×10^{-7}	1.6×10^{-6}	0.93	1.6×10^{-6}	6.2×10^{-5}	0.96	5.8×10^{-4}	6.6×10^{-3}	0.92
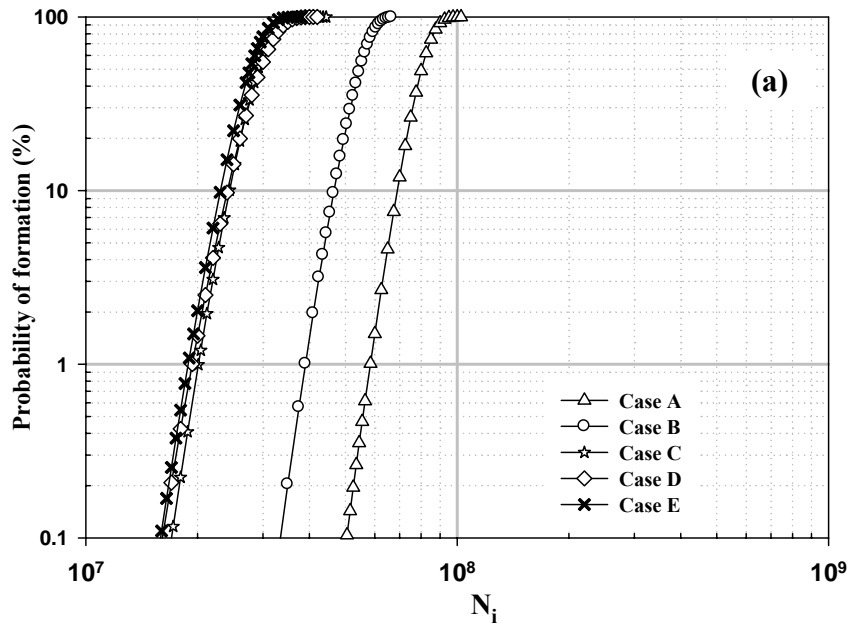
Figure 5.6. *Cumulative probability of fatigue crack formation versus the number of cycles to form a fatigue crack in secondary hardening martensitic steel for (a) $\zeta = 0.7$, (b) $\zeta = 0.85$, and (c) $\zeta = 1$.*
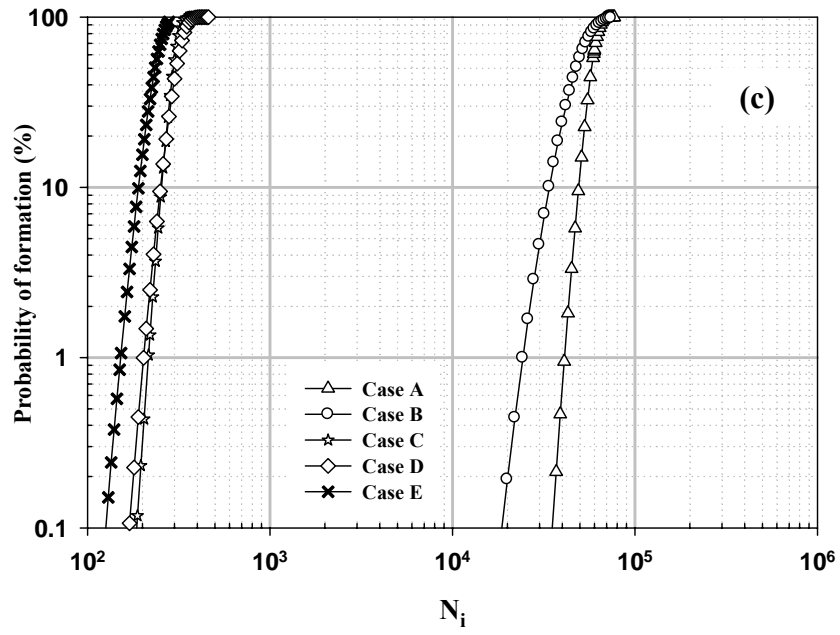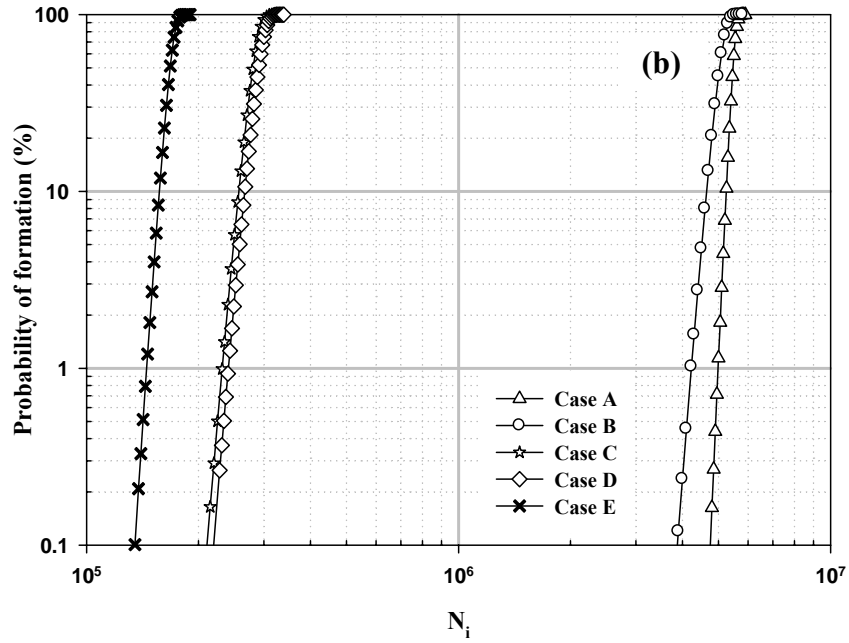
Figure 5.6. *Continued.*

120

Figures 5.6 (a)-(c) show the cumulative probability of fatigue crack formation against the estimated formation life for cases A-E. Partially debonded inclusions are observed to be most severe with regard to crack formation, as reported by McDowell et al. [5]; the severity is relatively more prominent at high strain amplitudes. Interestingly, comparing Cases A and B, soft and compliant intact inclusions demonstrate relatively higher local FIP in fatigue. This is believed to be due to relaxation of constraints at the compliant inclusion-matrix interface, permitting reverse plasticity during unloading and consequently altering the local R-ratio in the vicinity of nonmetallic inclusions. Such effects of reverse plasticity, elastic constraints, and local stress redistribution often make the transition from far-field cyclic conditions to local cyclic conditions non-trivial. In-depth investigation of the effect of local R-ratio can be found in Ref.[19].

As the elastic stiffness of the inclusion decreases, the extreme FIP reaches a limiting value comparable to that of a partially debonded inclusion, as demonstrated by the presence of the pore. A pore can be viewed as an extremely compliant inclusion. However, the presence of a pore creates a local free-surface effect which can lead to local softening in the matrix due to dislocation nucleation/annihilation. Similar local softening response is observed due to decohesion of inclusion-matrix interface [175]; however, formation and growth of voids at primary and secondary particles in fatigue and the resulting effect of softening on HCF resistance is still an active research topic. Additionally, it is realized that fatigue at the microstructure scale is a complex, heterogeneous evolutionary process with stages of formation and growth that depend on the hierarchy of microstructure features, and hence, does not conform to homogenization; this aspect introduces additional complexities with regard to developing suitable

constitutive models accounting for various aspects of mechanical response at different microstructure scales. Nevertheless, the application of crystal plasticity to capture the variability and the extreme scenario in HCF provides useful insights into structure-property relations that can be utilized to develop fatigue resistant material systems and will be discussed later.

Comparing Cases D and E, we observe that in the event of inclusion-matrix interface decohesion, hard elastic particles (Al_2O_3) are relatively more severe than compliant and soft inclusions (La_2O_2S) with regard to fatigue crack formation, although the disparity becomes more prominent with increasing ζ. The stiffness mismatch between the inclusion and matrix, coupled with stress intensification at the debond seam, leads to higher localized stresses and plastic strains in the vicinity of alumina particles. The elastic stiffness of lanthanum oxy-sulfide particle is comparable to that of the matrix with the yield strength being lower than the macroscopic yield strength of the encompassing polycrystal matrix, and hence results in relatively lower magnitudes of stress intensification. Apparently, debonding of inclusion-matrix interface increases the propensity of fatigue crack formation at the partially debonded interface. Contact constraint experienced due to partial decohesion of inclusion-matrix interface and the debond seam acting as a crack-like defect invariably results in peak stress intensification at the intersection of the debonded and bonded portions of the matrix, as observed through simple J_2 plasticity simulations; however, a grain situated adjacent to the debond seam may not always demonstrate minimum fatigue properties. Such an observation can be better understood by comparing the local maximum FIP obtained in Cases C, D, and E; a debond seam or contact constraint is absent in Case C (pore) and still the extreme

value FIP distributions and the minimum life estimates are comparable for all values of ζ investigated in the present study. It is necessary to clarify that we do not claim that fatigue cracks will not form in a grain adjacent to the debond seam; however, estimating the fatigue resistance by investigating the cyclic plasticity occurring in such specific locations may not always demonstrate the extreme scenario relevant to HCF resistance. Since the lath martensite grain (or block) size $(\sim 1 - 2\,\mu m)$ is relatively smaller than the size of the stress raiser $(5\,\mu m)$, the effect of micronotch root stress fields can span over several grains away from the stress raisers. The potency for crack formation does not solely depend on the individual grain orientation but also on the neighboring grain orientations. Hence, the possibility of the second nearest neighbor grain (with respect to the inclusion) demonstrating highest fatigue potency cannot be completely ruled out especially when assigning random orientations to each grain. Hence, the approach followed in this work in which we screen for maximum FIP in all the grains encompassing the inhomogeneity at a distance of the order of the size of the stress raiser is perhaps more reasonable. Furthermore, such an approach accounts for the process zone over which small cracks nucleate and grow under the influence of microstructure barriers such as the grain boundaries.
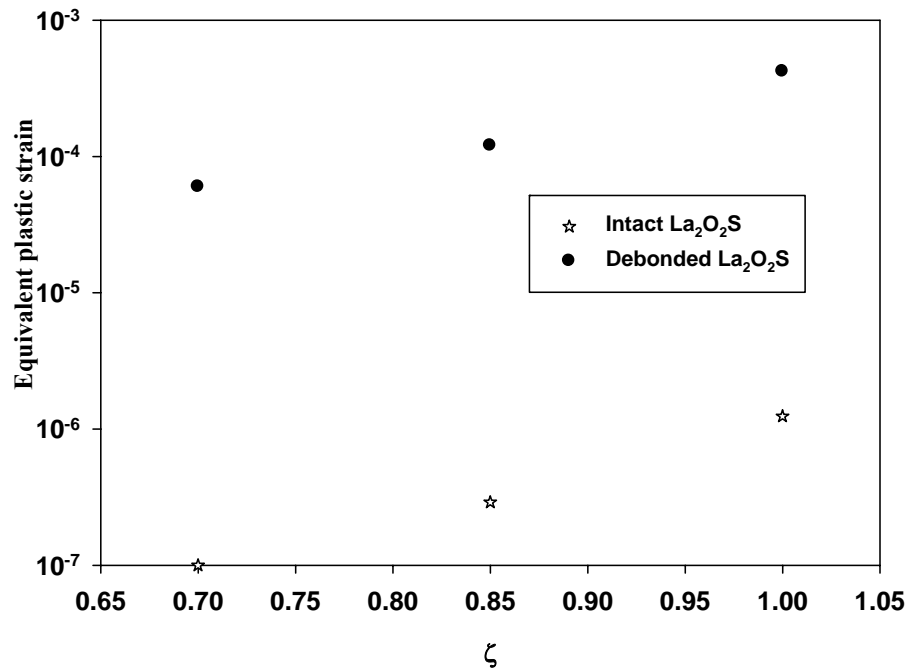
Figure 5.7. *Variation of equivalent plastic strain (volume average) in intact and debonded La$_2$O$_2$S inclusion with ζ computed at the end of 11th loading cycle for realization 1.*

It is important to investigate the role of plastic flow occurring in La$_2$O$_2$S inclusion in detail. Figure 5.7 shows the variation of equivalent plastic strain of intact and partially debonded La$_2$O$_2$S inclusion with ζ computed at the end of eleventh loading cycle for realization 1, for example. The equivalent plastic strain is estimate as a volume average within the La$_2$O$_2$S inclusion. In the case of intact particle, the volume average is performed over the elements within the inclusion lying at the inclusion-matrix interface. In the case the partially debonded particle, the volume average is performed over the finite elements within the inclusion lying at the debond seam (discontinuity). Evidently, the equivalent plastic strain is higher in partially debonded inclusion due to elevated stress levels at the debond seam. As stated earlier the plastic flow occurring within the La$_2$O$_2$S inclusion will reduce the severity of stress localization in the surrounding matrix;

this results in lower values of $\Delta\Gamma$ when compared to partially debonded Al_2O_3 inclusion (stiff and brittle particle). In the case of intact interface the equivalent plastic strains in La_2O_2S are negligibly small. In the absence of any discontinuity such as the debonded interface, the stress and plastic strain localization is primarily attributed to the modest property mismatch between the La_2O_2S inclusion and the matrix. However, the elastic compliance of La_2O_2S inclusions would permit reverse plasticity during unloading as described earlier. The aforementioned factor can be regarded as a second order effect which is more prominent at low stress concentration levels; this leads to relatively higher $\Delta\Gamma$ at intact La_2O_2S inclusion when compared to intact Al_2O_3 inclusion.

Figure 5.8 shows the variation in the minimum life estimate corresponding to 1% formation probability with normalized peak applied strain (ζ) for various cases listed in Table 5.1. Apparently, the disparity in the minimum-life estimate between intact and debonded particle is more prominent at high values of ζ. The local FIP estimated in the vicinity of the partially debonded inclusion and pore increases rapidly with increase in ζ [92], as shown in Table 5.4. Such a response is attributed to the discontinuity arising due to large interfacial separation at high values of ζ. Also, with an increase in the size of the inclusion, the disparity in the minimum life estimates could be more prominent even at low applied strain amplitude; however, such investigations are not performed in the present study.
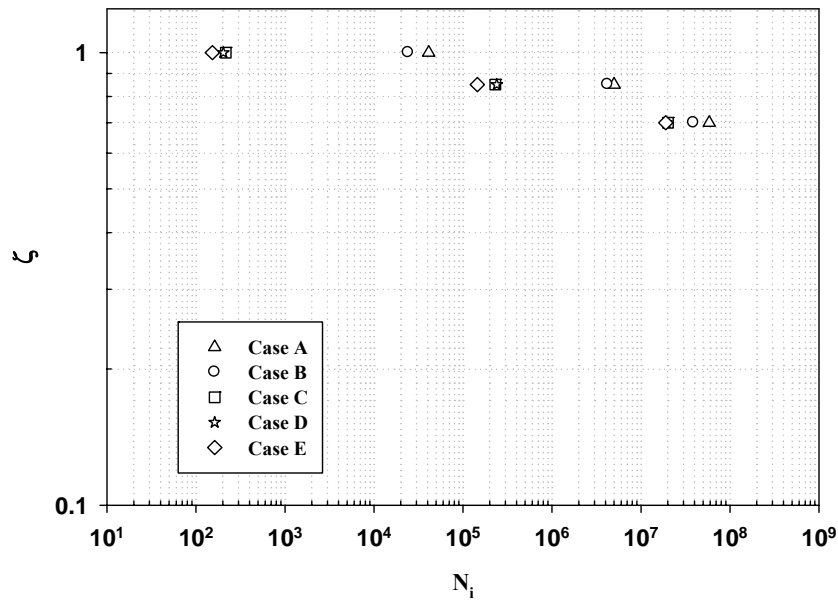
Figure 5.8. *Normalized peak applied strain (ζ) versus crack formation life for 1% probability of formation (minimum life) for different cases listed in Table 5.1.*

The present results confirm the necessity to account for attributes such as interfacial conditions for inclusions in minimum life estimates. Also, a single microstructure attribute may be inadequate to characterize minimum fatigue properties of the material. It is worth mentioning that in addition to accounting for interactions between the most favorably orientated grain and the local stress raisers, the effect of interaction among the grains is intrinsically accounted for while estimating the peak FIP. Recently, Przybyla and McDowell [157] considered the influence of crystallographic orientation relative to fatigue crack formation in the P/M Ni-base superalloy IN100. In this work, they developed a correlation function utilizing the grain Schmid factor marked by the extreme value response to identify which correlated grain types are most likely to exist at the locations of estimated extreme value response. Such an approach may not be necessary in the present study since the location of fatigue critical "hot spots" such as the grains in the proximity of nonmetallic inclusions or pores is known *a priori.* However, when

considering larger volumes with multiple potential hot-spots (e.g., inclusions) such an approach could be applied to consider correlations between different phases and/or grain orientation to quantify which correlations between second phase nonmetallic inclusions and specific grain orientations are most probable at the locations of extreme value response.

5.5. Discussion

While historically much work in modeling fatigue processes in metallic components focused on component life estimation, there is increasing interest in (i) designing microstructures with tailored resistance or (ii) components with microstructures that vary spatially in terms of composition and/or heat treatment to achieve location specific design. There is great financial and time pressure to compress overall material development and product design cycles, albeit retaining appropriate characterization of fatigue variability for the purpose of design for low probability of failure in HCF. Moreover, there is a need to better understand minimum fatigue life behavior of materials to address expensive and overly conservative early retirement of components.

There are several factors that contribute to variability in HCF. In this study we have attempted to address a few of them such as inclusion stiffness, interfacial conditions and variations in polycrystalline matrix grain orientation. The goal of this study was to develop a microstructure-sensitive extreme value assessment framework that includes the effects of several microstructure attributes that control HCF resistance of martensitic gear steels. There are practical limitations to modeling and simulation, of course. Incomplete understanding of failure mechanisms, regimes of dominance of each failure mode, and

127

uncertainty in associated models highlight the continuing importance of experiments in guiding modeling and simulation. Detailed modeling of heterogeneous cyclic plasticity (slip bands) and the crack formation process is still in its very early stages. Alternatively, systematic parametric studies such as the present study can be used as guidance in framing critical experiments that investigate key microstructure attributes controlling the minimum fatigue properties. Such an approach would result in significant cost savings and also accelerate the insertion of modified and new materials to service [4].

Constructing the extreme value distribution requires a significant number of simulations/experiments if they are to be considered statistically meaningful. Additionally, there are numerous factors that affect the fatigue response and an all-inclusive simulation strategy is almost impossible. However, a simplified approach such as design of experiments [116] using a macroscopic (J_2) plasticity model can be used to screen key microstructure features governing fatigue resistance before proceeding to apply intensive crystal plasticity calculations. However, microstructure-sensitive modeling using crystal plasticity simulations that focus on extreme statistics of potential sites for microplastic strain localization is essential to obtain meaningful estimates of minimum fatigue resistance. It is noted that fatigue is a cascade of processes of crack formation and growth that depends on the hierarchical morphology of phases and grains, as well as the presence of nonmetallic inclusions in high strength lath martensitic steels. Another critical aspect of HCF resistance, namely the growth of microstructurally small cracks out of the influence of the inclusion (or pore) micro notch root stress fields is not explicitly addressed in the present work; although the selected FIP (FS parameter) has limited consideration for small crack growth [107]. Formation and growth behavior of

small cracks is a significant contributor to variability in HCF [169]. Moreover, the issue of arrest of small cracks that form at isolated sites of cyclic plastic strain intensification is pertinent to the estimation of the fatigue limit. Typical fatigue experiments will not provide enough information to construct the extreme value distribution coupling effects of various microstructure attributes because such experiments consist of only a few data points at each stress/strain amplitude. In addition, experimentally, fatigue hot-spots are identified after failure and characterization of the sites of fatigue damage formation and their neighborhoods requires extensive resources, often involving destructive sectioning. We envision that this framework will be practically applied to simulations that are guided with limited experiments.

This study has reinforced the necessity to account for the effect of damaged inclusions while investigating the minimum fatigue resistance of martensitic gear steels. Inclusions can crack or debond either during processing such as shot peening or during service and subsequently can serve to promote fatigue crack formation. Inclusions are inevitable consequence of any processing. Addition of elements such as lanthanum or aluminum for scavenging purpose in order to remove the detrimental residual oxygen and sulfur content during processing results in formation of different inclusion types such as alumina and lanthanum oxy-sulfide. The present study, considering the effect of inclusion types (La_2O_2S and Al_2O_3) and interfacial conditions, can assist in the selection of appropriate alloying elements that could enhance minimum fatigue resistance. For example, debonded hard elastic inclusions demonstrated the worst case scenario with regard to crack formation and intact hard particles were least severe. Recently, Garrison [176] investigated the effect of manganese sulfide, lanthanum oxy-sulfide and titanium

carbo-sulfide on fracture toughness of AF1410 steel and reported that titanium carbo-sulfide demonstrated enhanced fracture toughness by virtue of superior interface strength and resistance to void nucleation. Similar studies on fatigue guided through simulations will be fruitful in developing fatigue resistant secondary hardening martensitic steels.

5.6 Conclusions

Computational simulations are employed to establish relations between remote loading conditions and microstructure-scale plasticity behavior by introducing the concept of FIPs to serve as computable response parameters that can facilitate comparisons of multiple microstructures via parametric studies. By identifying certain key microstructure attributes such as inclusion stiffness, interfacial conditions, polycrystalline matrix grain orientation, and remote loading conditions we have attempted to construct an extreme value statistical framework to estimate the minimum life for crack formation. The sole purpose of correlating with life was to rank order the severity of different attributes in fatigue and it is acknowledged that experimental data are essential to obtain actual fatigue lives. However, we assert that the degree of severity of different attributes can still be realized to be of the same order irrespective of the approach followed to estimate the crack formation life. Moreover, idealized cases were considered in the present study to facilitate parametric investigation. Certain key findings are summarized below.

1. While conducting crystal plasticity FE fatigue simulations, it is necessary to obtain a stabilized FIP response at fatigue critical "hot spots" by subjecting the

model to sufficient number of cycles. This is applicable even when the remote loading conditions are within the elastic limit and assists in avoiding overly conservative estimate of fatigue resistance. The number of cycles required to obtain stabilized FIP response depends on different factors: For example, while coupling the relaxation of residual stresses using the approach outlined in Chapter 4 with fatigue crack formation potency at primary inclusions or pores, the number of cycles required to obtain stabilized FIP response will depend on the initial residual stress magnitude, size and spatial distribution of inclusion, etc.

2. A single microstructure attribute such as the size of the inclusion may be inadequate to define minimum HCF response of high strength martensitic gear steels. As elaborated in this study, interfacial conditions such as presence of debonded inclusions are critical life-limiting factors that contribute towards defining minimum fatigue properties. The effect of variation in stiffness of inclusion is less significant when compared to interfacial conditions with regard to variability in fatigue response.

3. For the selected material model, inclusion size, inclusion stiffness, remote loading and interfacial conditions, partially debonded hard elastic inclusions (Al_2O_3) were the worst case scenario with regard to fatigue crack formation. An intact hard elastic inclusion demonstrated highest fatigue resistance. While considering intact inclusions, as the stiffness is reduced, the magnitude of the peak grain scale

averaged FIP response reaches a limiting value on the order of a debonded inclusion in high strength steels, as demonstrated by the case of the pore. This research work has been submitted as a journal manuscript in 2009 and is in review [177].

Chapter 6

MODELING EFFECTS OF INTRINSIC VARIABILITY ON EXTREME VALUE FATIGUE SENSITIVITY AT PRIMARY INCLUSIONS

In the previous Chapter, we used a crystal plasticity framework to model the extreme value fatigue sensitivity to inclusions and pores. However, the effects of various intrinsic sources of strengthening were not distinguished. As stated in Chapter 2, the abundance of submicron size alloy carbides operating as Orowan obstacles can significantly influence the work hardening behavior and the fatigue crack formation potency at primary inclusions. Furthermore, there is a significant gradient in the fine scale precipitate volume fraction from the surface to the core. Multiscale computational models linking the fatigue response at various microstructure scales in secondary hardening steels are very limited.

In this Chapter, we introduce a computational framework that is suitable to investigate the effects of submicron size precipitates and other intrinsic sources of strengthening on fatigue crack formation potency at primary inclusions. We demonstrate the linking of extrinsic (e.g., primary inclusions) and intrinsic (e.g., precipitate volume fraction, matrix grain orientation, etc.) microstructure variability to cyclic plasticity at the scale of the intrinsic microstructure of martensitic gear steel. A microstructure-based constitutive model for cyclic deformation of secondary hardening martensitic gear steel is developed and implemented. The matrix is modeled using a crystal viscoplasticity framework with dislocation density as an internal state variable. Using a homogenization scheme we

133

model the effects of several sources of strengthening, including Orowan strengthening due to fine scale non-shearable M_2C (M=Fe, Cr, Mo, W) precipitates, solid solution strengthening, dislocation, and grain boundary strengthening on initial slip resistance and work hardening. This model is capable of capturing several important features of secondary hardening gear steels, namely, (i) effects of fine scale precipitates on work hardening and on localized plastic strains, and (ii) crystallographic orientation dependence represented by the crystal plasticity model. The physically-based hardening laws are employed to evolve dislocation densities in the matrix in each slip system with consideration of dislocation interaction mechanisms. The fatigue resistance of a martensitic gear steel depends both on intrinsic microstructure attributes, such as fine scale precipitates, and extrinsic attributes such as nonmetallic primary inclusions. It is of prime importance to assess the effects of individual microstructure attributes on the minimum fatigue resistance.

We outline a philosophy to couple the variability in intrinsic microstructure attributes such as M_2C volume fraction and extrinsic microstructure attributes such as size and spacing of nonmetallic primary inclusion. Idealized inclusion geometries (ellipsoidal) are considered to study the fatigue crack formation potency in HCF regime. Relevant microstructure-scale FIPs are identified. Parametric studies are conducted to discern the effects of size and spatial distribution of partially debonded primary inclusions on fatigue resistance of martensitic gear steels. Several remote loading conditions are considered in the HCF regime relevant to applications. Multiple realizations of the polycrystal microstructure are considered to obtain a statistical distribution of the FIP. The results are used to construct extreme value statistical distributions for the selected microstructure

134

attributes. Subsequently, a computational micromechanics based minimum-life estimate is obtained.

6.1. Introduction

Although there have been several studies exploring the mechanical properties of high strength secondary hardening steels [178, 179], experimental studies characterizing the scatter in the HCF life of secondary hardening martensitic gear steels have been limited. Furthermore, developing microstructure-sensitive computational models to investigate the fatigue response of such steels is an active research topic. The abundance of grain boundaries and precipitates providing obstacles to dislocation motion during plastic deformation generally leads to enhanced strength in secondary hardening steels. This work presents initial efforts to develop a 3D modeling strategy to characterize the effects of intrinsic and extrinsic variability on minimum life of martensitic gear steels. The approach presented in this study is suitable to qualitatively and quantitatively discern the effects of various microstructure attributes that control the HCF response of gear steels; such methodologies will lend support to designing improved, fatigue-resistant materials.

6.2. Summary of processing of martensitic gear steel

The composition of C61 steel is listed in Table 1.1. Heat treatment of this secondary hardening steel involves carburization at either 950°C, 1000°C or 1050°C followed by cryogenic treatment in a liquid nitrogen bath to obtain complete martensitic transformation at the surface. This is followed by tempering (secondary hardening) at 482°C for 15 hours to achieve the desired case strength. Secondary hardening steels get

their name from a secondary hardening response exhibited by these alloys when aged at Stage IV (450-600°C) tempering temperatures. This hardening behavior arises from the formation of fine alloy carbide dispersions that replace coarse cementite particles during tempering. Secondary hardening steels derive most of their strength through the fine dispersion of alloy carbides. The level of precipitation strengthening achieved is highly dependent on the interaction mechanism between a glide dislocation and a precipitate. Detailed discussion of the precipitate strengthening mechanism is provided in Chapter 1. The gradient in carbon content induces a gradient in the M_2C volume fraction from the surface to the core, as shown in Figure 6.1.
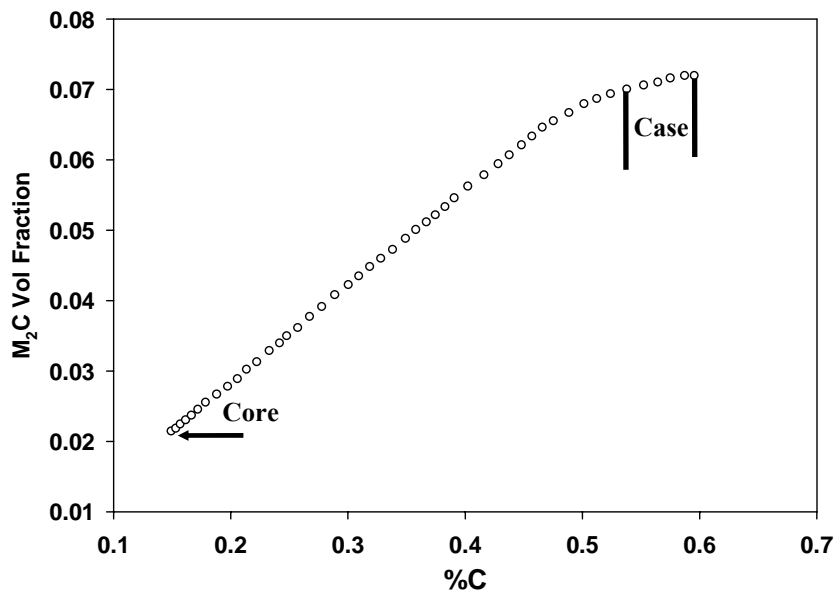
Figure 6.1. *Variation in M_2C volume fraction from the case layer to the core with carbon content in the martensitic steel [180].*

6.3. Overview of the simulation-based investigation

The objective of this work is to devise a computational framework to couple the effects of intrinsic variability and extrinsic variability on the minimum fatigue resistance

of the selected martensitic gear steel. Attention is devoted towards statistically quantifying the fatigue potency at partially debonded Al_2O_3 inclusions, a worst case scenario for fatigue crack formation (see Chapter 5). Inclusions are modeled as isotropic linear elastic. A microstructure-based constitutive model for cyclic deformation and HCF behavior of secondary hardening martensitic gear steel is developed and implemented. The strategy to model the microstructure hierarchy exhibited by BCC lath martensite at the grain scale as illustrated in Section 4.2 is employed. Each block of lath martensite with an average size of 2 μm $\left(= d_{gr}\right)$ is considered to be an effective grain with 48 potentially active slip systems. The matrix is modeled using a crystal viscoplasticity framework with dislocation density as an internal state variable. Effects on various sources of strengthening such as Orowan strengthening due to fine scale non-shearable M_2C precipitates on initial slip resistance and work hardening are implicitly incorporated in the physically based evolution laws. The model is calibrated using limited experiments available for case hardened steels in literature. Subsequently, parametric studies are conducted to assess fatigue crack formation potency at primary inclusions. The microstructure attributes of interest include the size and spacing of primary inclusions, variation in polycrystalline matrix grain orientation, precipitate size and spacing. Grain scale averaged values of the Fatemi-Socie parameter (FS) (see Section 3.7) and Mononukul and Dunne (MD) parameter [181] are used as the candidate FIPs in this study. Three-dimensional statistical volume elements (SVEs) with idealized ellipsoidal alumina particles embedded in the polycrystalline steel matrix are subjected to several fatigue cycles with $R_\varepsilon = 0$. These SVEs are too small to be regarded as statistically representative in terms of the distribution of localized plastic deformation. Hence, a

137

number of SVE realizations or instantiations are necessary to build ensemble statistics. The target microstructure response (i.e., cyclic microplasticity) varies among each SVE realizations. Here, multiple realizations of the polycrystalline matrix grain orientation distribution are considered, and the peak values of FIP from each realization are utilized to construct extreme value distributions, namely Weibull, Gumbel and Frechet distributions [182]. An Anderson-Darling [183] goodness-of-fit test is conducted to identify the most suitable distribution among the selected extreme value distributions. Consequently, an estimate of the number of fatigue cycles for crack formation and early growth corresponding to 1% probability (minimum-life) is obtained. Although the crystal plasticity model developed in this work is capable of assessing the variability arising due to variations in the size and the spacing of fine scale precipitates, we do not model such effects due to insufficient experimental data to calibrate the material model. The variability in the extreme value FIP is primarily obtained by simulating several realizations of polycrystalline matrix grain orientations.   All three-dimensional FE simulations are performed using ABAQUS.

6.4 Crystal plasticity framework

We adopt a physically-based crystal plasticity constitutive framework to model the steel matrix phase, homogenizing the effects of M_2C precipitates along the lines proposed by Wang and co-workers [184]. The kinematics of the crystal plasticity [185] are employed, with the total deformation gradient tensor multiplicatively decomposed into elastic and plastic parts, i.e., $F = F^e \cdot F^p$. The plastic deformation, produced by the collective motion of dislocations on the slip planes, does not result in lattice rotation,

138

whereas the elastic deformation leads to stretch and rigid body rotation of the lattice. The plastic velocity gradient on the αth slip system in the intermediate configuration is given by summation of the shearing rates, $\dot{\gamma}^\alpha$ on all the slip systems, i.e.,

$$L_0^p = \dot{F}^p \cdot F^{p-1} = \sum_{\alpha=1}^{N_{sys}} \dot{\gamma}^\alpha \left(s_0^\alpha \otimes m_0^\alpha \right) \tag{6.1}$$

where s_0^α and m_0^α are unit vectors in the slip direction and normal to slip plane, respectively, in the intermediate, lattice invariant configuration. The resolved shear stress on the αth slip system is given by

$$\tau^\alpha = \sigma : \left(s^\alpha \otimes m^\alpha \right) \tag{6.2}$$

where σ is the Cauchy stress tensor and s^α and m^α are unit vectors in the slip direction and normal to slip plane, respectively, in the current configuration. In a rate-dependent formulation, all slip systems are considered to be active for stresses above the threshold, and the flow rule relating the shearing rates, $\dot{\gamma}^\alpha$ to the resolved shear stress, τ^α is given by

$$\dot{\gamma}^\alpha = \dot{\gamma}_o \left\langle \frac{\left| \tau^\alpha - \chi^\alpha \right| - \kappa^\alpha}{D^\alpha} \right\rangle^m \operatorname{sgn}\left(\tau^\alpha - \chi^\alpha \right) \tag{6.3}$$

Here, χ^α represents the kinematic hardening variable or back stress on the αth slip system, D^α is the drag stress which is assumed to be a constant, m is the inverse strain-rate sensitivity exponent, and $\dot{\gamma}_o = 0.001 \text{ s}^{-1}$ is the reference shearing rate. κ^α is the scalar threshold stress that accounts for various sources of strengthening in martensitic gear steels, as given by [141]

$$\kappa^{\alpha} = \kappa_{ss} + \kappa_{p} + \kappa_{d} + \kappa_{gr} \tag{6.4}$$

where κ_{ss}, κ_{p}, κ_{d}, and κ_{gr} are terms accounting for solid solution, M_2C dispersions, dislocation, and grain boundary strengthening, respectively. A detailed discussion regarding each of these sources of strengthening in secondary hardening gear steels will be presented later. The evolution of dislocation density $\left(\rho^{\alpha}\right)$ on slip system α consists of terms related to dislocation storage and annihilation (dynamic recovery) mechanisms given by [186, 187]

$$\dot{\rho}^{\alpha} = \sum_{\beta} h^{\alpha\beta} \left\{ Z_{o} + k_1 \sqrt{\rho^{\alpha}} - k_2 \rho^{\alpha} \right\} \left| \dot{\gamma}^{\alpha} \right| \tag{6.5}$$

In Equation (6.5), we introduce a term Z_0 to model nonlocal (length scale) effects associated with the size and spacing of non-shearable M_2C precipitates (Orowan obstacles); it effectively introduces the notion that dislocation pileups are introduced at the fine scale of non-shearable precipitates. Additionally, $h^{\alpha\beta}$ is the hardening coefficient, k_1 and k_2 are the coefficients associated respectively with dislocation storage and annihilation. The term Z_0 is estimated via [184]

$$Z_{o} = \frac{\omega_1}{bS_{M_2C}} + \frac{\omega_2}{bL_{M_2C}}, \tag{6.6}$$

where S_{M_2C} and L_{M_2C} are the mean size (~3 nm) and spacing of M_2C precipitates, respectively. Nondimensional constants ω_1 and ω_2 are associated with the size and

spacing of precipitates, respectively, and b is the magnitude of Burger's vector. The term

$\sum_{\beta} h^{\alpha\beta} Z_o \left| \dot{\gamma}^{\alpha} \right|$ is Equation (6.5) is interpreted as relating to the generation of geometrically

necessary dislocations (GNDs) at the fine scale dispersions. The back stress χ^{α} accounts

for the Baushinger effect arising due to interaction of dislocations with fine scale M_2C

precipitates, evolving according to

$$\dot{\chi}^{\alpha} = \left\{ \eta G b \sqrt{\rho^{\alpha}} \operatorname{sgn}\left(\tau^{\alpha} - \chi^{\alpha}\right) - \chi^{\alpha} \right\} \left| \dot{\gamma}^{\alpha} \right| \tag{6.7}$$

Here, G is the shear modulus, and coefficient η establishes the ratio of back stress

amplitude relative to cyclic flow stress for various slip systems; its form is given by [184,

188]

$$\eta = \frac{\eta_o Z_o}{Z_o + k_1 \sqrt{\rho^{\alpha}}} \tag{6.8}$$

where η_o is a parameter describing the contribution from the GNDs, and controls the

saturation level of the back stress. Due to insufficient experimental data for the selected

secondary hardening martensitic steels, we resort to literature to estimate the model

parameters and the relevant material constants and will be described later. This is an

initial effort to devise a framework to model extreme value fatigue sensitivity to intrinsic

and extrinsic microstructure variability. In this work we do not attempt to develop a fully

nonlocal crystal plasticity model; instead, we enforce limited nonlocality by introduction

of length scale dependent terms (cf. Z_0 term in Equation (6.5) and (6.7)). This facilitates

application of an otherwise local finite element method and averts issues of higher order boundary conditions inherent in nonlocal defect field mechanics.

6.5. Modeling strength contribution from various intrinsic sources

The threshold stress is estimated through linear superposition of various strengthening sources in martensitic gear steels as shown in Equation (6.4). To estimate solid solution strengthening the model suggested by Labusch [189] is used, i.e.,

$$\kappa_{ss} = \left(0.0078G \left(\left| \varepsilon'_G \right| + 2 \left| \varepsilon_a \right| \right)^{\frac{4}{3} \varsigma^{\frac{2}{3}}} \right) M^{-1} \tag{6.9}$$

where ε'_G is the solute modulus misfit, ε_a is the solute size misfit at a specific solute atomic volume fraction denoted by ς, and $M = 2.9$ [190] is the Taylor factor for BCC martensitic steels. This approach is used to account for matrix concentration of Co, Ni, Cr, and Mo. Dislocation strengthening on the αth slip system is modeled using the Keh and Weissman [191] strength dependence relation on dislocation density ρ^{α}, i.e.,

$$\kappa_d = \alpha_d G b \sqrt{\rho^{\alpha}} \tag{6.10}$$

where $\alpha_d = 0.38$ [27] is a constant measuring the hardening efficiency of dislocations. Variable κ_d evolves with dislocation density (Equation 6.5). The strengthening due to the high density of high angle grain boundaries observed in lath martensite is modeled using classical Hall-Petch expression [141] given by

$$\kappa_{gr} = \kappa_0 + \frac{k_{HP}}{\sqrt{d_{gr}}}$$ (6.11)

where d_{gr} is the average size of the block, and k_{HP} is the Hall-Petch constant. The precipitate strengthening caused by M_2C dispersions that act as Orowan obstacles is described using the Orowan-Ashby relation with combined screw and edge dislocation effects [192, 193]

$$\kappa_p = 1.68 \frac{Gb}{2\pi\sqrt{1-\nu}\left(L_{M_2C} - 2r_{M_2C}\right)} \ln\left(\frac{2r_{M_2C}}{r_o}\right)$$ (6.12)

where $r_o = 0.5 \times 10^{-6}$ mm [194] is the dislocation core radius, $r_{M_2C} = S_{M_2C}/2$ is the average radius of M_2C dispersions, and ν is the Poisson's ratio of the matrix. It is important to clarify that except for κ_d, the remaining components of the threshold stress do not evolve during cyclic loading. They are primarily used to estimate the initial value of the total threshold stress in the crystal plasticity simulations. However, evolution of dislocation densities and back stress accounts for precipitate size and spacing as illustrated in Equations (6.5) and (6.7).

6.6 Fatigue crack formation potency at primary inclusions

A significant portion of the service life in HCF is consumed in fatigue crack formation at the scale microstructure feature (e.g. grain size) [10]. Several approaches have been formulated over the years to characterize crack formation and small crack growth as summarized in earlier chapters. In this study we utilize two parameters namely, the Mononukul and Dunne (MD) parameter shown in Equation (6.13) and the Fatemi-

Socie (FS) parameter. The aforementioned parameters are evaluated as grain scale average (nonlocal) value.

$$P_{cyc} = \int_{cyc} \sqrt{\frac{2}{3} \underset{\sim}{D}^{p*} : \underset{\sim}{D}^{p*}} \, dt \tag{6.13}$$

In Equation (6.13), $\underset{\sim}{D}^{p}$ is the plastic rate of deformation tensor. The superscript '*' denotes grain scale averaged values. Readers are referred to the review article by McDowell [10, 152] for additional information regarding various microstructure scale FIPs. In HCF, plasticity is confined to local "fatigue critical" regions such as in the vicinity of primary inclusions and the grains situated at those locations demonstrate higher potency for crack formation. The approach described in Section 5.2 is utilized to evaluate the grain scale averaged FIPs. We assert a nonlocal Coffin-Manson relation, $\Delta\Gamma = \gamma'(N_i)^q$ (see Section 5.2) to estimate the number of cycles (N_i) to form a crack of length on the order of block size (d_{gr}) in the vicinity of primary inclusion(s). The values of γ', and q are presented in Section 5.2.

6.7. Statistical framework to investigate extreme value fatigue sensitivity

An elaborate overview of extreme value statistics is presented in Section 5.3. Here, we investigate three extensively employed extreme value statistical distributions for maxima, namely Weibull, Gumbel and Frechet distributions as listed in Equations (6.14), (6.15), and (6.16), respectively. The extreme value FIP distributions obtained from numerical simulations are fit to the aforementioned distributions. Such detailed analyses of different extreme value statistical distribution functions will be useful to rank order the superiority of the distributions with regard to reflecting the extreme scenario relevant to

144

fatigue. It is noted that our intention is to present a framework to model the extreme value fatigue sensitivity to microstructure variability and detailed analyses of all possible distributions is addition to the chosen statistical distributions is beyond the scope of this work.

$$P(z) = 1 - exp\left(-\left(\frac{z}{\psi}\right)^{\lambda}\right) \quad \text{(Weibull)} \tag{6.14}$$

$$P(z) = exp\left(-exp\left(-\frac{z - \varphi}{\psi}\right)\right) \text{(Gumbell)} \tag{6.15}$$

$$P(z) = exp\left(-\left(\frac{\psi}{z}\right)^{\lambda}\right) \quad \text{(Frechet)} \tag{6.16}$$

Here, ψ is the scale parameter, λ is the shape parameter, and φ is the location parameter. It is noted that only two-parameter distributions are studied in this work. The distributions listed in Equations (6.14)-(6.16) are fit using computer software package EasyFit [195]. In this study the response variable z is the peak grain scale averaged FIP obtained from 3D FE simulations for each realization.

The most common goodness-of-fit test is conducted using the coefficient of determination, R^2 which often lacks any hypothesis testing. In this study we apply the Anderson-Darling goodness-of-fit test statistic, a quadratic test, to rank order various statistical distributions in capturing the extreme value distributions of FIPs. The aforementioned test demonstrates higher sensitivity to the tails of the distribution [174]

and it was shown by Stephens [183] to be superior to a majority of other goodness-of-fit tests for a variety of distributions. The test statistic, A^2 is defined as

$$A^2 = -n - \frac{1}{n} \sum_{i=1}^{n} (2i - 1) \left[ln\left(P(z_i)\right) + \left(ln\left(1 - P(z_{n-i+1})\right)\right) \right] \qquad (6.17)$$

where $P(z_i)$ is the cumulative probability of each data point, $i(=1...n)$. Low values of A^2 demonstrates higher confidence that data follows the distribution being tested.

6.8. Methodology

We consider idealized partially debonded ellipsoidal Al_2O_3 inclusions. Prior studies have revealed partially debonded inclusions to be most severe with regard to crack formation (discussed in Chapters 3 and 5). In addition to modeling the effects of intrinsic features such as fine scale dispersions we investigate the effects of inclusion size and spacing on fatigue crack formation and early growth. The elastic properties of Al_2O_3 are presented in Section 5.2. Table 6.1 lists the cases simulated in this parametric study. In Table 6.1, $2a_{inc}$ and $2b_{inc}$ is the major axis and minor axis dimension of the ellipsoidal inclusion, respectively. L_{inc} is the longitudinal spacing between the inclusions. It is noted that we choose a single spacing of 2 μm which is equal to the size of a single martensite block. The objective is to compare the FIP enhancement due to interaction of inclusions with that of a single isolated inclusion in fatigue. For each case listed in Table 6.1, 3D FE simulations considering several realizations of polycrystalline matrix grain orientation are conducted to build ensemble statistics; this is done for each remote loading condition. Additionally, detailed investigation of several other microstructure attributes such as

inclusion stiffness, and interfacial conditions are presented in Chapter 5. For convenience, results for all the cases presented in the subsequent sections will be identified with the 'case pointer' listed in Table 6.1.
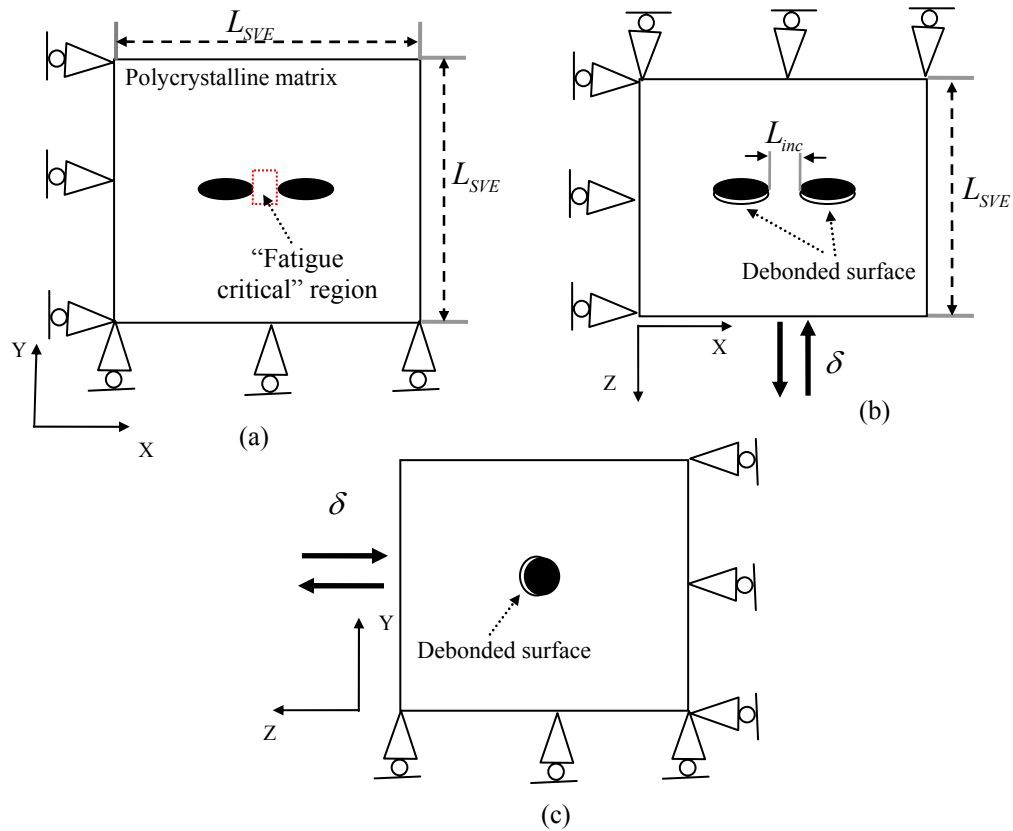
Figure 6.2. *Cross-sectional views of the 3-D section with embedded ellipsoidal inclusion elaborating on the debonded surface, boundary conditions for uniaxial loading and the direction of cyclic loading. Views across (a) XY, (b) XZ, and (c) YZ cutting planes through the center of the inclusion.*

Table 6.1. *List of cases modeled to investigate the variability in fatigue resistance.*

Case pointer	# of inclusions	Inclusion 1		Inclusion 2		
		$2a_{inc}\,(\mu m)$	$2b_{inc}\,(\mu m)$	$2a_{inc}\,(\mu m)$	$2b_{inc}\,(\mu m)$	$L_{inc}\,(\mu m)$
A	1	5	2	-	-	-
B	2	5	2	5	2	2
C	1	10	4	-	-	-
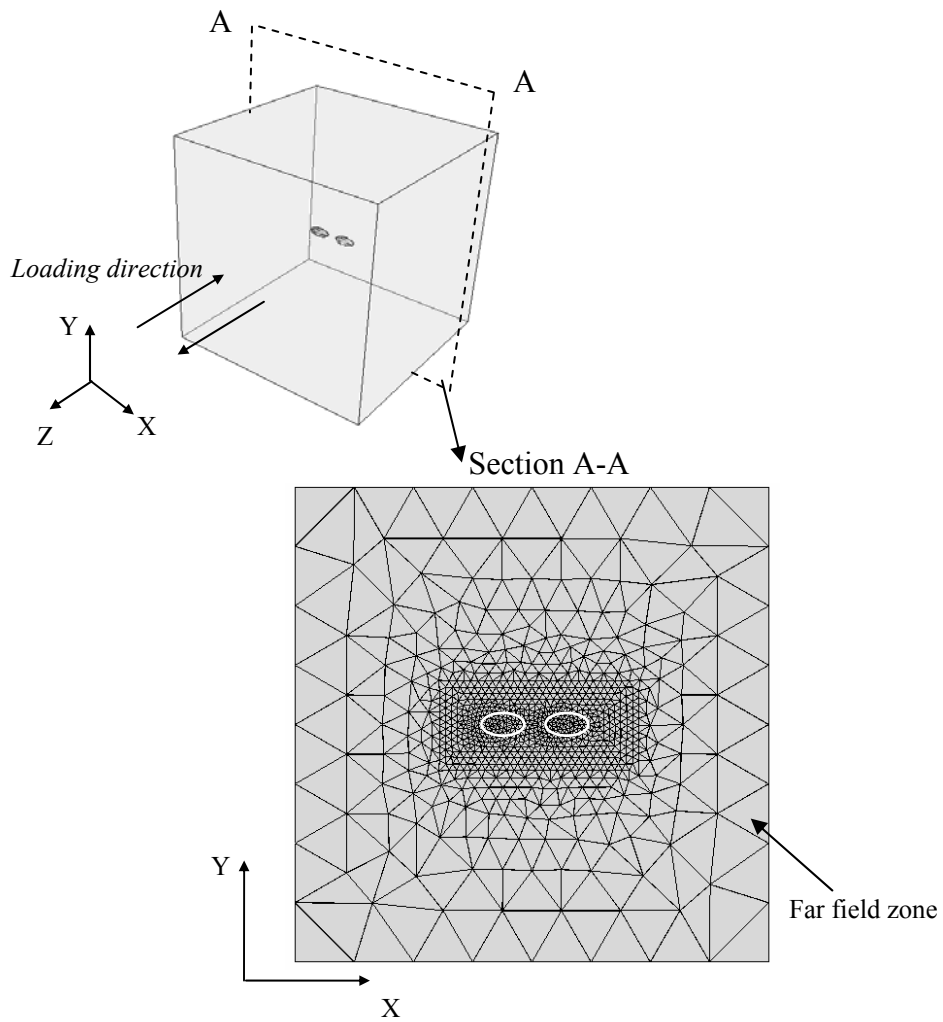
Figure 6.3. *Cross-section of the 3D FE mesh through the center of the inclusions, showing refinement close to the inclusion. Cyclic loading is in the Z direction.*

Figure 6.2 shows different cross sectional views of the 3D domain, elaborating on the boundary conditions, and uniaxial loading direction enforced in the simulations. Additionally, we impose a multipoint constraint that the nodes on the faces $x = L_{SVE}$ and $y = L_{SVE}$ have the same displacement during fatigue cycling in directions x and y, respectively. The dimensions of each SVE (L_{SVE}) are chosen to be sufficiently large that the inclusion experiences negligible boundary interaction effects. We evaluate the FIP as a volume average value over each grain within the "fatigue critical" region (see Figure 6.2a). Such an approach is followed to locate the most favorably oriented grain undergoing cyclic microplasticity under the influence of the inclusion micronotch root stress field, the most potent site for crack formation [92]. Furthermore, a consistent FIP estimation procedure is necessary while investigating the fatigue response for different remote loading conditions. Figure 6.3 shows a cross-section of a 3-D FE mesh of case B, for example. The meshing strategy discussed in Section 5.2 is employed. The "fatigue critical" (see Figure 6.2) is comprised of atleast 20 cubic lath martensite grains with each grain discretized into at least four 3D tetrahedral elements (C3D4). Reduced integration is employed. A detailed discussion on estimation of material constants relevant to the crystal plasticity model is presented in the next section.

The ratio of peak remote applied uniaxial strain (ε_{max}) to the strain at macroscopic proportional limit $(\varepsilon_y \approx 0.9\%)$ is defined by $\zeta = \dfrac{\varepsilon_{max}}{\varepsilon_y}$. FIP distributions are computed for each case listed in Table 6.1 for several values of $\zeta (= 0.5, 0.75, 1)$ with $R_\varepsilon = 0$. A SVE representing a single realization of polycrystalline matrix grain orientation is subjected to

three quasistatic strain controlled cycles $\left(\dot{\varepsilon} \sim 10^{-3} s^{-1} \right)$ for a selected ζ and R_ε to obtain a stabilized FIP response and the peak value of the FIP, $\left[\left(\Delta\Gamma_{max} \right)_i , \left(P_{cyc} \right)_i \right]$, is recorded for each of the n instantiations, $i \left(= 1, 2, ... n \right)$. A sufficiently large number of realizations are necessary to construct a statistical ensemble. The distribution of peak value of FIPs is used to construct an extreme value statistical distribution.

6.9. Model calibration and parameter estimation

The crystal plasticity framework described in Section 6.4 is implemented as a User MATerial subroutine (UMAT) in ABAQUS. The constitutive model for the steel matrix employed in this work has several material-dependent parameters. It may not be possible to determine many of the material parameters using first principles calculations since these parameters represent much higher scale phenomena. Tiemens [27] developed a design model to estimate the strength contribution (in VHN) from various intrinsic sources (described in Section 6.5) in C61 class of steels employing the approach developed by Wise [34]. Initial value of the threshold stress components κ_{gr}, κ_{ss}, and κ_d is estimated from the information provided by Tiemens [27]. He reported the contribution from solid solution, dislocation, and grain boundary strengthening to be approximately 30 VHN, 100 VHN, and 65 VHN, respectively. To estimate the threshold stress components, κ_{gr}, κ_{ss}, and κ_d at the grain scale, the values reported in VHN was converted to yield strength using the relation reported by Saha and Olson [196] for high strength steels, and subsequently, applying the Taylor factor (M), each slip system level components were determined. Furthermore, utilizing the microhardness profile (see

Figure 2.4) of C61 steel, the value of κ_p is estimated for the case layer by subtracting the contribution from the other sources. The average case layer microhardness was taken to be 680 VHN which corresponds to M$_2$C volume fraction of 0.07. Furthermore, the mean size $\left(S_{M_2C}\right)$ and spacing $\left(L_{M_2C}\right)$ of the precipitates and the initial value of the dislocation density, ρ_0^α, were obtained from [27]. The initial dislocation density does not vary between slip systems.
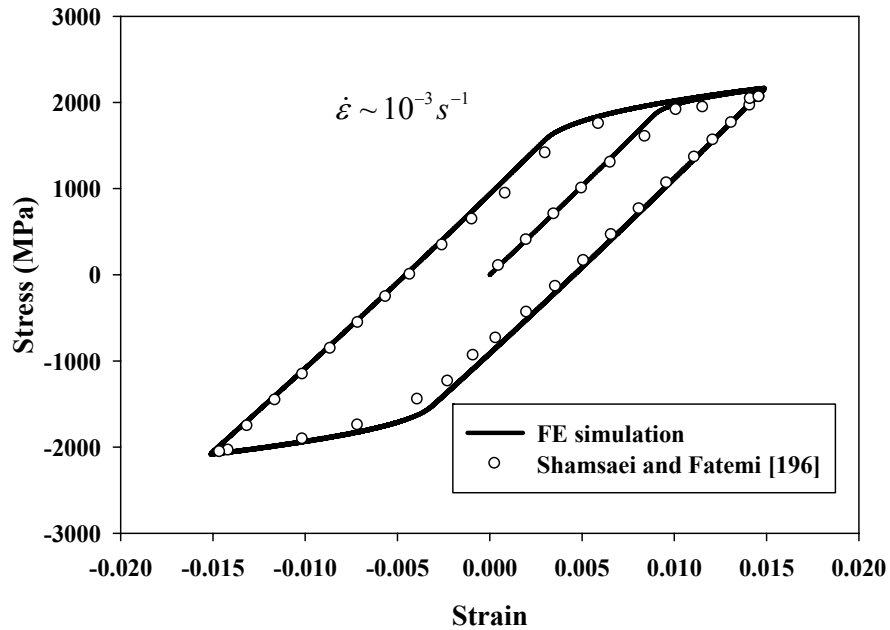
Figure 6.4. *Simulated cyclic stress-strain response of the case layer of martensitic gear steel.*

The elastic constants (C_{11}, C_{12}, C_{44}) for the martensite crystal are obtained from Ref. [150]. The magnitude of Burger's vector (b) [194], dynamic hardening and recovery coefficients (k_1, k_2) [197] are also obtained from literature for tempered martensitic steel. It is assumed that the size of the M$_2$C precipitate has minimal influence on the evolution of dislocation densities and back stress; hence, a negligibly small value is assigned to ω_1

Table 6.2. *Constants and parameters of the constitutive model at room temperature.*

Parameters	Symbol	Value	Units
Elasticity matrix component	C11	268	GPa
Elasticity matrix component	C12	110	GPa
Elasticity matrix component	C44	78	GPa
Burger's vector magnitude	b	0.25×10^{-6}	mm
inverse strain-rate sensitivity exponent	m	20	-
Shear modulus of matrix	G	78	GPa
Poisson's ratio of matrix	ν	0.29	-
Dislocation interaction coefficient	$h^{\alpha\beta} : \alpha = \beta, \alpha \neq \beta$	0.1, 0.1	-
Mean spacing between precipitates	L_{M_2C}	3×10^{-6}	mm
Coefficient for size effect of precipitates	ω_1	1×10^{-25}	-
Coefficient for spacing effect of precipitates	ω_2	2×10^{-7}	-
Drag stress	D^{α}	150	MPa
Initial dislocation density	ρ_0^{α}	1×10^9	mm^{-2}
Coefficient of back stress	η_0	7×10^5	-
Dynamic hardening/recovery coefficients	k_1, k_2	$5 \times 10^5, 15$	$mm^{-1}, -$
Initial components of the threshold stress	$\kappa_{ss}, \kappa_{gr}, \kappa_p$	30, 75, 425	MPa, MPa, MPa
Initial back stress	χ_0^{α}	0	MPa
Size of precipitates	S_{M_2C}	3×10^{-6}	mm

in Equation (6.6). Due to insufficient information, reasonable value is assigned to ω_2 in

Equation (6.6) which is on the order of that used in Ref. [184]. Experimental information

to characterize the cyclic stress-strain response of the case layer was not available for the

selected martensitic gear steel. Hence, we utilized the quasistatic cyclic stress-strain data

of the case layer of carburized and tempered martensitic steel presented in [198]; its case

hardness is comparable to the martensitic steel modeled in this study. The parameters η_0

(Equation 6.8), and $h^{\alpha\beta}$ (Equation 6.5) are obtained through fitting. A 3D periodic representative volume element (RVE) comprising of 500 randomly oriented polycrystalline lath martensite grains was used to fit the cyclic stress-strain data. The resulting constants and parameters are presented in Table 6.2 and the corresponding cyclic stress-strain response is shown in Figure 6.4.

6.10. Results

Three-dimensional crystal plasticity simulations of SVEs comprising of inclusion(s) in a polycrystalline matrix were conducted for three values of $\zeta\left(=0.5,0.75,1\right)$ and $R_{\varepsilon}=0$. Twenty different realizations $\left(n=20\right)$ of polycrystalline matrix grain orientations were considered to estimate the variability in the fatigue resistance for each case listed in Table 6.1 and to construct the corresponding extreme value distributions. Each SVE was subjected to three loading cycles and the FIPs were estimated during the third loading cycle. The strategy of subjecting the SVE to several loading cycles (more than three) in order to obtain stabilized FIP response as illustrated in Section 5.4 was followed, and the results indicated three loading cycles to be sufficient to obtain stabilized FIP response for the present material model. Two FIPs namely the FS parameter and MD parameter are estimated and the extreme value FIP was selected to be the FIP $\left(\Delta\Gamma\ and\ P_{cyc}\right)$ with highest magnitude among all the grains screened in the vicinity of the inclusion micro notch root for each realization. The grain demonstrating peak $\Delta\Gamma$ and P_{cyc} was the same for any selected realization. Furthermore, the grain demonstrating peak FIP did not change with loading cycle. Figures 6.5a-c shows the variation in extreme value FIP

(denoted as FIP_{max}) versus the cumulative probability, $P(z_i)$, estimated via mean rank statistics, i.e.,

$$P(z_i) = \frac{i}{n+1} \tag{6.18}$$

Here, $i(=1..n)$ is the rank of the data point in the ascending order. Each data point in Figures 6.5a-c represents the extreme value obtained from a single realization.
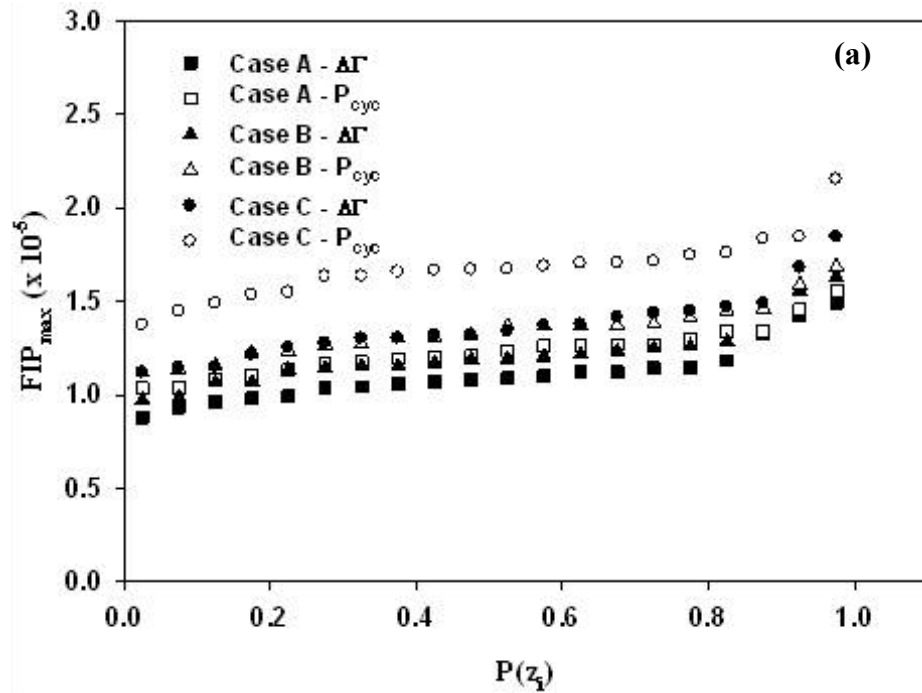
Figure 6.5. *Extreme value FIP distribution* $\left(vs.\ P(z_i) = \dfrac{i}{n+1} \right)$ *as estimated over the grain size averaging volumes for (a)* $\zeta = 0.5$, *(b)* $\zeta = 0.75$, *and (c)* $\zeta = 1$ *after 3 loading cycles. The extreme value FIP was selected to be the FIP with highest magnitude among all the grains.*
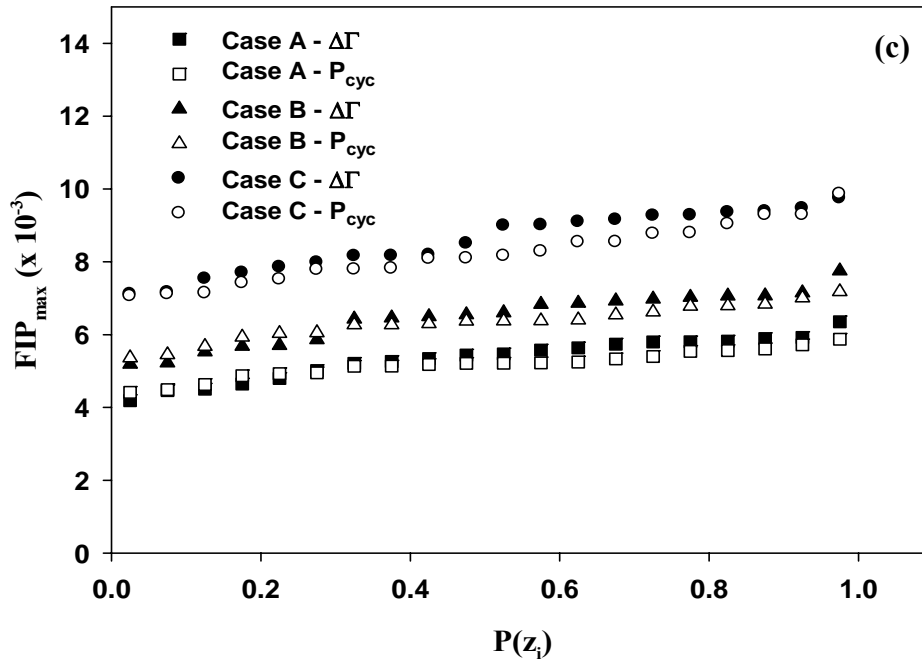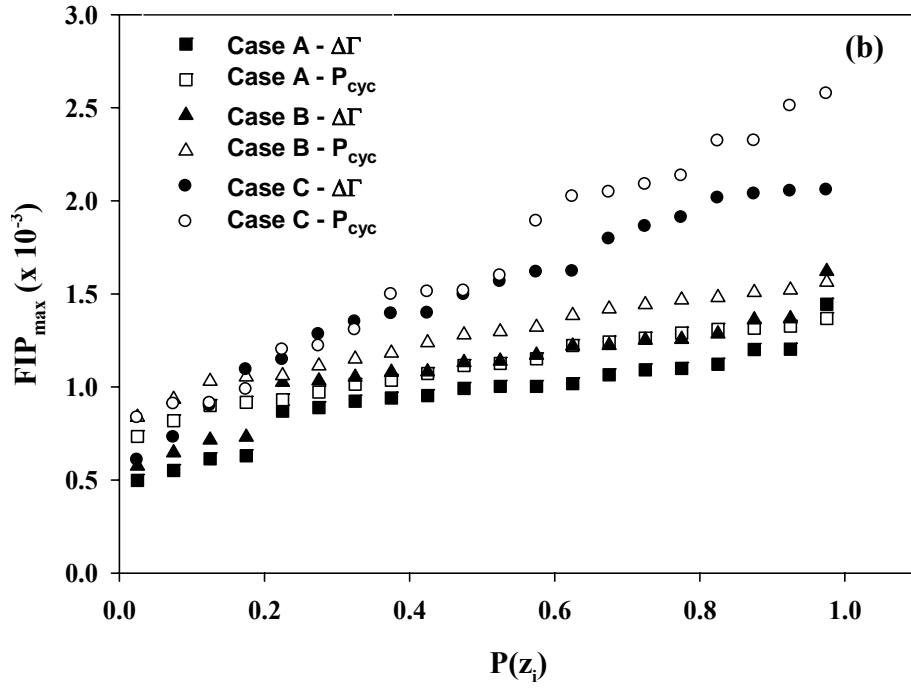
Figure 6.5. *Continued.*

As seen in Figures 6.5a-c, that significant variability is observed due to variation of microstructure attributes such as size and spatial distribution of the inclusions. Apparently, with the increase in ζ the extreme value FIP increases by several orders of magnitude. Furthermore, large isolated partially debonded inclusion (case C) demonstrated highest FIP among the cases listed in Table 6.1. The purpose of estimating two microstructure scale FIPs is to compare the extreme value statistical distribution functions that reflect the variability in fatigue resistance. The peak FIPs shown in Figures 6.5a-c are fit to the Weibull, Gumbel, and Frechet distributions. It has been shown by Castillo [182] that for the distributions of a single variable, and for large sample size, n the extreme value distributions converges to the aforementioned three types of the non-degenerated distributions. The scale, location, and shape parameters are presented in Table 6.3 (for $\Delta\Gamma$) and Table 6.4 (for P_{cyc}) for each case listed in Table 6.1. Also, shown in Tables 6.3 and 6.4 are the results of the Anderson-Darling goodness of fit statistic, A^2. The lowest value of A^2 is highlighted to illuminate the statistical function that best fits the simulated extreme value FIPs. It can be seen from Tables 6.3 and 6.4 that on an average, Weibull distribution demonstrated superior capabilities in capturing the variability in the extreme value FIPs. This is evident for the selected microstucture scale FIPs. There were few cases for which the Gumbel distribution exhibited better capabilities in capturing the statistical variability. Frechet distribution was least favored in the present study. Once the most favorable extreme value distribution function is identified, the probability for crack formation (P_i) for a given number of loading cycles can be calculated employing Equations 6.19-6.21.

Table 6.3: *Values of the fitting parameters and A^2 of various selected statistical functions obtained utilizing the extreme value FS parameter* $(\Delta\Gamma)$.

Case Pointer	ζ	Weibull			Gumbel			Frechet		
		ψ	λ	A^2	ψ	φ	A^2	ψ	λ	A^2
A	0.5	1.15E-05	8.98	1.56	1.20E-06	1.01E-05	**0.32**	1.02E-05	9.34	0.43
	0.75	1.03E-03	3.97	**0.69**	1.84E-04	8.50E-04	1.75	7.79E-04	3.52	1.90
	1	5.54E-03	10.02	**0.38**	4.51E-04	5.08E-03	1.42	4.97E-03	9.13	1.16
B	0.5	1.26E-05	8.89	1.61	1.31E-06	1.14E-05	**0.47**	1.12E-05	9.20	0.65
	0.75	1.18E-03	4.04	**0.74**	2.05E-04	9.81E-04	1.91	9.00E-04	3.57	1.96
	1	6.72E-03	9.84	**0.57**	5.52E-04	6.15E-03	1.71	6.01E-03	8.95	1.32
C	0.5	1.38E-05	12.02	**0.28**	9.95E-07	1.28E-05	0.68	1.26E-05	11.55	0.69
	0.75	1.67E-03	2.57	**0.75**	3.63E-04	1.28E-03	1.20	1.08E-03	2.24	2.04
	1	8.86E-03	11.12	**0.55**	6.39E-04	8.18E-03	1.27	8.04E-03	10.45	0.92

Table 6.4: *Values of the fitting parameters and A^2 of various selected statistical functions obtained utilizing the extreme value MD parameter* (P_{cyc}).

Case Pointer	ζ	Weibull			Gumbel			Frechet		
		ψ	λ	A^2	ψ	φ	A^2	ψ	λ	A^2
A	0.5	1.13E-05	11.85	0.88	1.02E-06	1.17E-05	**0.30**	1.16E-05	11.80	0.53
	0.75	1.17E-03	6.22	**0.32**	1.45E-04	1.02E-03	0.92	9.85E-04	5.79	0.87
	1	3.81E-03	11.51	**0.39**	2.92E-04	3.53E-03	0.76	3.47E-03	10.80	0.84
B	0.5	1.38E-05	11.72	0.84	1.11E-06	1.28E-05	**0.39**	1.26E-05	11.60	0.62
	0.75	1.34E-03	6.23	**0.30**	1.65E-04	1.17E-03	0.94	1.13E-03	5.80	0.89
	1	6.50E-03	14.49	**0.30**	3.78E-04	6.11E-03	1.14	6.14E-03	13.60	1.08
C	0.5	1.71E-05	13.95	1.40	1.28E-06	1.60E-05	**0.70**	1.58E-05	13.00	1.12
	0.75	1.82E-03	3.00	**0.38**	1.42E-03	4.40E-04	0.75	1.28E-03	2.89	0.80
	1	8.46E-03	12.06	0.47	6.18E-04	7.86E-03	**0.39**	7.76E-03	12.00	0.42

$$P_i = \exp\left(-\left(\frac{f(N_i)}{\psi}\right)^{\lambda}\right) \text{ (Weibull)} \qquad (6.19)$$

$$P_i = 1 - \exp\left(-\exp\left(-\frac{f(N_i)-\varphi}{\psi}\right)\right) \text{ (Gumbel)} \qquad (6.20)$$

$$P_i = 1 - \exp\left(-\left(\frac{\psi}{f(N_i)}\right)^\lambda\right) \quad \text{(Frechet)} \tag{6.21}$$

Here, $f(N_i) = \gamma'(N_i)^q$ is the function relating the grain scale averaged FIP to N_i. Although we compute two different grain scale averaged FIPs $(\Delta\Gamma, P_{cyc})$, $\Delta\Gamma$ parameter is used to estimate the crack formation life in the present study. It is intended to estimate the number of cycles to form a crack corresponding to 1% probability which signifies minimum life.
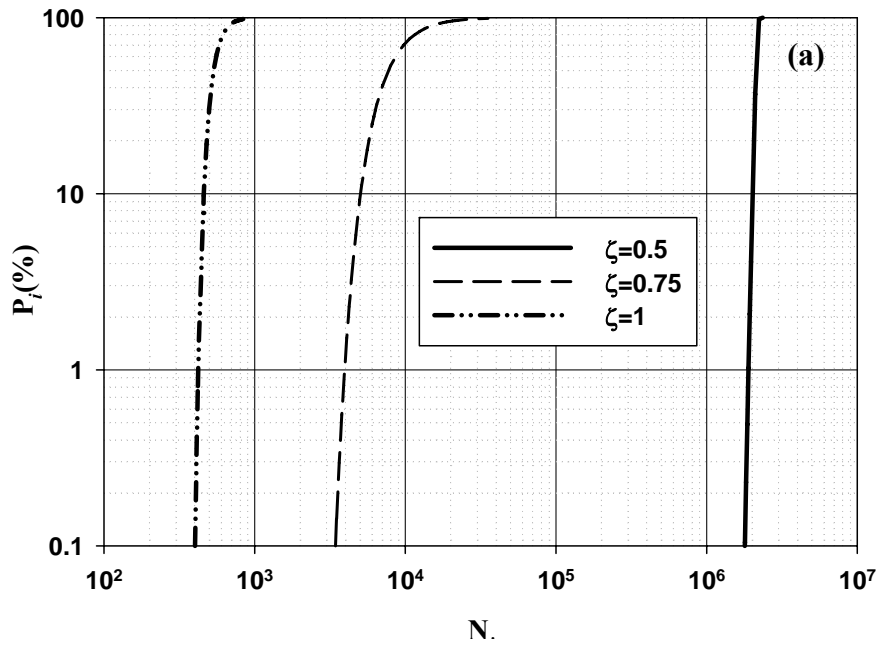
Figure 6.6. *Estimated cumulative probability P_i versus N_i for (a) Case A, (b) Case B, and (c) Case C.*
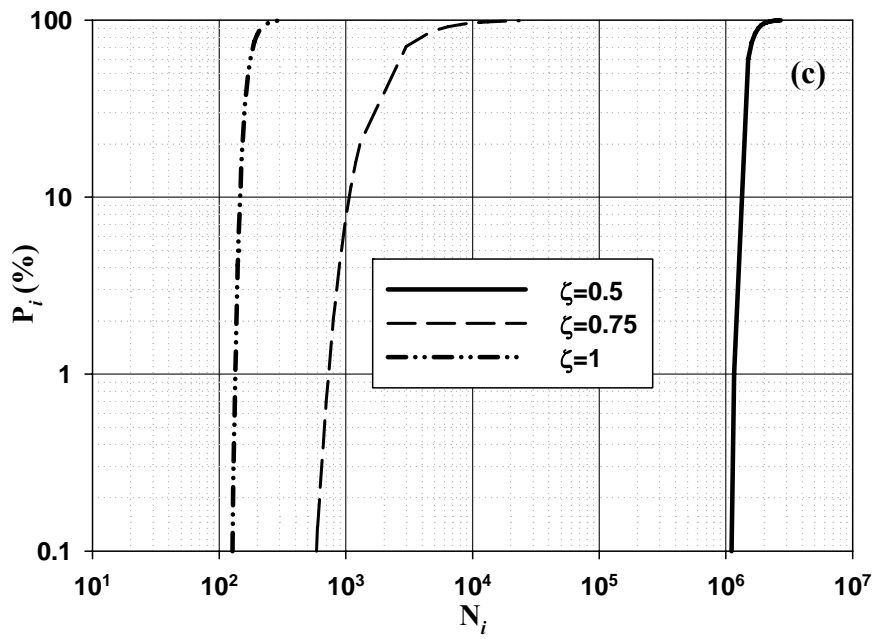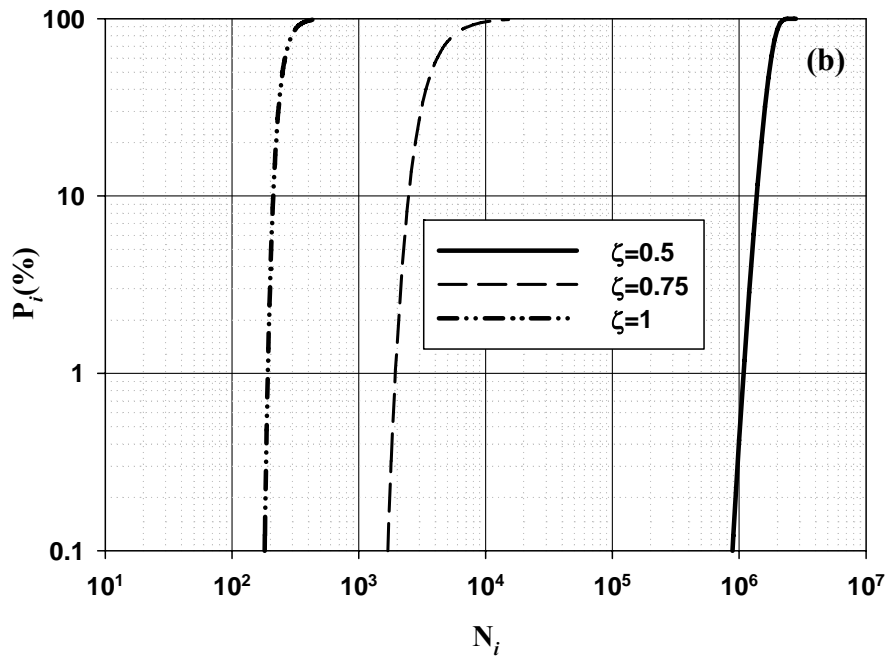
Figure 6.6. Continued.
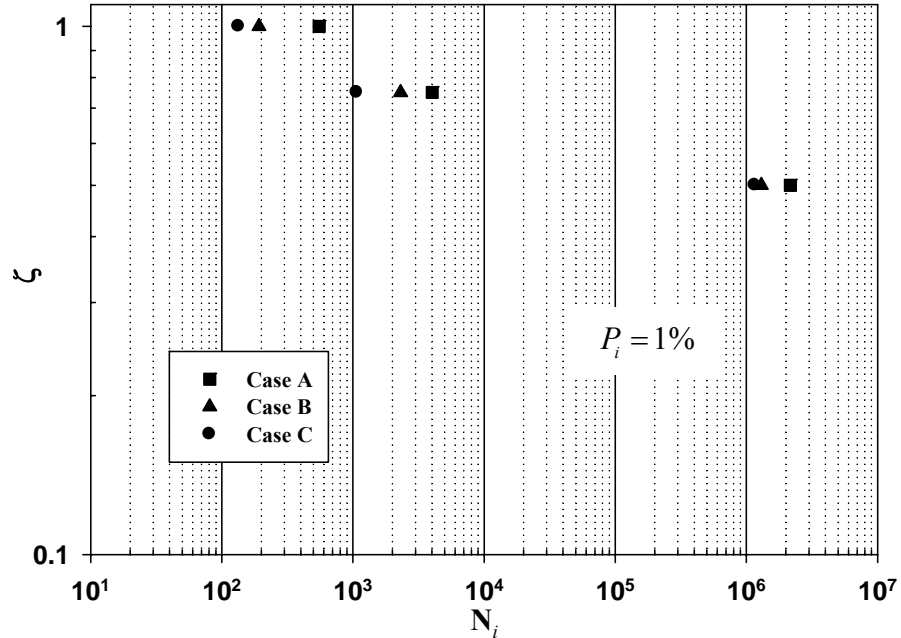
Figure 6.7. *Normalized peak applied strain (ζ) versus crack formation life for 1% probability of formation, for different cases listed in Table 6.1.*

Figure 6.6a-c illustrates the cumulative probability of crack formation versus the number of cycles to form a crack for various cases listed in Table 6.1. Such a plot would indicate the minimum life for the selected microstructure attribute. While estimating the cumulative probability for different cases, the best fit distribution shown in Table 6.3 is utilized. The purpose of estimating the crack formation lives is to qualitatively discern the effects of various microstructure attributes on the microstructure scale fatigue potency. Formation and early growth behavior of small cracks is a significant contributor to variability in HCF [169].

Based on the nonlocal FIPs estimated for each case listed in Table 6.1, a normalized applied strain (ζ) versus crack formation life can be plotted which corresponds to the 1% probability as shown in Figure 6.7. Apparently, case C demonstrates the worst case scenario for crack formation. The disparity in minimum life estimates between case A

and case C increases rapidly with increase in ζ. Such a response is attributed to the discontinuity arising due to large interfacial separation at elevated ζ coupled with the size effect of the stress raisers. Interestingly, significant reduction in fatigue life is realized due to interaction of inclusions (case B). The disparity in minimum life estimates between case A and case B also increases with increase in ζ. This observation supports the idea that a single microstructure attribute such as the size of the inclusion may be inadequate to define the minimum fatigue properties. For example, often we observe clusters of primary inclusions on the fracture surface (e.g., see Figure 2.8 in Chapter 2). Such clusters could be fractured remnants of a larger particle. Hence, the fatigue potency of a large particle could be aggravated through interaction with several smaller particles. Such local interactions will contribute to scatter in HCF. Additionally, the enhancement of FIPs due to inclusion interaction illustrates the potency of closely spaced inclusions to replicate the effect of a larger isolated inclusion.

The framework developed in this chapter is suitable to qualitatively rank order the severity of various intrinsic and extrinsic microstructure attributes in HCF. Although, only partially debonded inclusions (worst case scenario) are considered in the present study, prior studies (see Chapter 5) revealed significant difference in the minimum crack formation life between debonded and intact particles. Hence, this study reinforces the importance of modeling effects of various microstructure attributes while designing materials for a specific fatigue application. It is worth mentioning that in addition to accounting for interactions between the most favorably orientated grain and the local stress raisers, the effect of interaction among the grains is intrinsically accounted for while estimating the peak FIP. Additional constitutive degrees of freedom introduced in

the microstructure-sensitive material model permits investigation of the effects of other intrinsic variability such as variation in block size on microstructure-scale FIP response at critical life-limiting attributes.

6.11. Discussion

There are several factors that contribute to variability in HCF. In this study we have attempted to address a few of them such as inclusion size, spatial interaction, and variations in polycrystalline matrix grain orientation. The primary goal was to develop a microstructure-sensitive computation framework to couple the intrinsic variability at micron and sub-micron scales with the extrinsic attributes such as size and spacing of primary inclusions. Detailed modeling of heterogeneous cyclic plasticity (slip bands) and crack formation process is still in its very early stages. Alternatively, systematic parametric studies such as the present work can be used as guidance in framing critical experiments that investigate key microstructure attributes controlling the minimum fatigue properties. Such an approach would result in significant cost savings and also accelerate the insertion of modified and new materials to service [4]. The framework utilized in the present study affords the ability to explore the effects of variations of single features of microstructure holding other features fixed which is generally not possible in experimental study. With this approach, the effects of extreme variations of microstructure on material properties can be studied. For example, the effects of higher length scale inclusions can be neglected in the computational simulation if the aim is to isolate the effects of M_2C precipitates on the intrinsic fatigue resistance of the microstructure. However, experiments are still needed on a limited range of microstructures to calibrate and validate such frameworks.

We acknowledge that understanding and physics-based models for secondary hardening martensitic gear steels are evolving within the research community; accordingly, the levels of hierarchy are expected to improve over time. As summarized by McDowell [152] that with improvements in atomistic-to-discrete dislocation, and discrete dislocation –to-continuum descriptions, it should be possible to augment or replace lower-scale (for e.g. fine scale precipitates) continuum descriptions with suitable homogenized descriptions. But to do so requires not only the mechanics formalisms, which already exist to varying extent, but also necessary initial and boundary conditions of defects, defect source distributions, and types of dislocation reactions that occur in the vicinity of sub-micron scale precipitates and primary inclusions. Necessary supporting understanding and characterization for such a predictive quantitative framework at fine scales in by no means already established in the literature for secondary hardening steels.

6.12. Summary and conclusions

A dislocation density-based crystal plasticity model relevant to model the sub-micron scale strengthening in case hardened martensitic gear steel was developed. A simplified scheme to model the fatigue crack formation and early growth at critical life-limiting microstructure attributes was demonstrated. A statistical framework was utilized to characterize the variability in fatigue response. An Anderson-Darling goodness of fit test was conducted to identify the extreme value statistical distribution function that best fits the simulated variability in extreme value FIPs. By identifying certain key microstructure attributes such as inclusion size, spacing, polycrystalline matrix grain orientation, and remote loading conditions we have constructed an extreme value

statistical framework to estimate the minimum life for crack formation on the order of a martensite block in the case layer of secondary hardening martensitic steels. The sole purpose of correlating with life was to rank order the severity of different attributes in fatigue and it is acknowledged that experimental data are essential to obtain actual fatigue lives. Idealized cases were considered in the present study to facilitate parametric investigation. This work offers a simple yet effective framework to relate FIPs to micron and sub-micron scale microstructure features, effectively constituting a multiscale approach. Certain key findings are summarized below:-

1. For the selected material model, inclusion size, inclusion stiffness, remote loading, interfacial conditions and the selected extreme value statistical distribution functions, Weibull distribution demonstrated superior capabilities in capturing the variability in microstructure scale fatigue response. This inference is based on identifying the number of cases for which Weibull fit showed lowest A^2 compared to Gumbel and Frechet distribution.

2. Large isolated partially debonded inclusions were observed to be most severe with regard to crack formation among the simulated cases. However, significant enhancement in FIP is observed due to interaction of inclusions in cluster. Estimation of minimum life based on single microstructure attribute can be misleading due to the role played by various other microstructure attributes such as inclusion spacing, and interfacial conditions. Furthermore, intrinsic variability such as variation in polycrystalline matrix grain orientation and variation in phase fractions of fine scale dispersions contribute towards defining minimum fatigue resistance in HCF.

6.13. Limitations

a. Due to insufficient experimental data regarding cyclic stress-strain data of secondary hardening martensitic gear steels, the crystal plasticity model developed in this study is calibrated using available experimental data from literature. Due to significant number of material parameters and constants involved in the constitutive model, it is necessary to rely on future experiments. For example, fatigue tests of material whose microstructure represents the case layer of heat treated secondary hardening martensitic steels will be very useful to improve model predictions.

b. We have attempted to model the grain scale response of lath martensite respecting the microstructure hierarchy exhibited by lath martensite at that scale. However, the effects of low angle boundaries within the blocks are neglected. It is necessary to understand the effects of low angle boundaries in HCF and detailed experimental investigations are imperative to develop better tools for materials design. TEM characterization, nanoindentation, and other relevant imaging methods and studies that relate microstructure to cyclic plasticity at block or sub-block scale will certainly enhance model predictions.

c. Limited parametric studies were conducted with regard to variation in size and spacing of inclusions while computing the minimum fatigue resistance in this work. A more comprehensive study involving statistical variation of size and spacing of primary inclusions in a cluster in addition to variation in polycrystalline matrix grain orientation will be more fruitful to obtain a better estimate of the minimum fatigue resistance. The aforementioned study will require well characterized experimental data of statistical extremes of the microstructure attributes and is left to future work.

Chapter 7

MODELING EFFECTS OF COMPLIANT COATINGS ON HCF

RESISTANCE AT PRIMARY INCLUSIONS

In this Chapter, we explore the capabilities of an elastic interphase material adhered to the inclusion surface to alter the FIPs in the matrix. By varying the elastic stiffness of the encapsulating interphase, the stresses and cyclic plastic strains are examined in the matrix in the proximity of a partially debonded inclusion, a worst case scenario for crack formation. The matrix is modeled as elastic-plastic with pure kinematic hardening expressed in a hardening minus dynamic recovery format. The inclusion and interphase are modeled as isotropic linear elastic. An idealized spherical, homogeneous inclusion is considered to facilitate parametric study. A nonlocal average value of the maximum plastic shear strain amplitude was used in a modified form of the Fatemi-Socie parameter in the proximity of inclusions as a FIP to facilitate comparative parametric study of the potency for crack formation.

7.1 Introduction

Design of improved process routes and new material systems that address the increasing demand for extended fatigue performance in technologically significant structural materials is a key research focus. Nonmetallic primary inclusions are a major life-limiting feature in advanced metallic systems as described in Chapter 1. Simulation-based strategies offer a convenient platform to understand mechanisms of crack

formation and early growth from such second phase particles [10, 199], which in turn can be applied to develop understanding of possible means to suppress such phenomena.

The mechanisms of crack formation and early growth from inclusions involve either cracking of the inclusion or debonding of the inclusion/matrix interface, with the inclusion serving as a notch to concentrate cyclic plastic strain in the surrounding metal matrix [12, 18]. Of the three scenarios, decohesion of the inclusion/matrix interface, either during processing or service, has been observed to be most detrimental with regard to fatigue crack formation in metals (see Chapter 3). Gall et al. [19] reported for A356-T6 Al alloy that the FIPs near perfectly bonded inclusions are two orders of magnitude smaller than those near cracked or debonded particles, within the range of elastic stiffness contrast and yield strengths studied. Due to high stress concentration, it is improbable that a cracked inclusion would remain completely bonded to the matrix material, and the cracked inclusion might eventually debond during service. Improving the inclusion/matrix interface strength is one way to negate or delay the process of decohesion. Another remedy would be to introduce an interphase layer between inclusion and matrix either to inhibit decohesion or to reduce stresses and plastic strain localization in the matrix in the event of decohesion. In this Chapter we propose to study the effect of the latter by introducing an elastic interphase material that adheres to the inclusion surface, forming a layer between the inclusion and matrix.

The influence of such coatings on the structural response of different material systems have been studied by many researchers [200-207]. Interaction of pre-existing cracks and dislocations with coated particles (inclusions or fibers) have also been studied by many researchers [204, 208-213]   Such second phase particles have often been reported to

167

serve as crack nuclei in different grades of steel [12, 15, 214-217]. Gubenko [218] performed experiments to understand the role of interphase between an inclusion and steel matrix. Based on the experimental findings on void formation from corundum and spinel inclusions, the author suggested to create silicate and sulfide shells around such second phase particles in order to lower the susceptibility of decohesion of the inclusion/matrix interface. Miao and Knott [219] performed experiments on C-Mn steel weld metal and demonstrated that heating the steel to austenitization temperature followed by slow cooling resulted in formation of sulfide coating (MnS) on oxide inclusions with thickness ranging between 0.1-0.5 μm. Manganese sulfide is relatively less stiff than oxide inclusion and can be viewed as a soft coating layer or interphase between the steel matrix and the oxide particle. In comparison to the bulk materials, thin coatings exhibit strong anisotropy in mechanical properties [220, 221]. Additionally, the properties of the substrate can influence the mechanical behavior of coatings [222]. Although the aforementioned factors can influence the severity of plastic strain localization in the surrounding ductile matrix, detailed investigation of their effects is beyond the scope of this work.

The effect of introducing a compliant coating on fatigue crack formation at nonmetallic inclusions in metals has not been explored to date from a modeling standpoint. We examine the possible reduction of the FIP in such a case for a parametric range of relative elastic stiffnesses of the inclusion, interphase, and matrix, for given properties of matrix elasto-plastic flow that mimic high strength steel. To avoid ambiguity, the interphase material is labeled 'coating' throughout this manuscript. Specifically, we consider a lath martensitic steel matrix with hard nonmetallic inclusions.

In this work, we investigate crack formation potency of partially debonded spherical inclusions with/without coating and to support efforts to modify the inclusion/matrix interface for improved HCF performance. For simplicity, we model the coating as isotropic linear elastic.

7.2. Methodology

The elasto-plastic response of the steel matrix is modeled using J_2 type plasticity with kinematic hardening outlined in Section 3.4. Nonlocal averaged value of FS parameter $(\Delta\Gamma)$ is used in the present study as fatigue indicator parameter (see Chapter 3, Section 3.7). We may assert a nonlocal Coffin-Manson relation $\Delta\Gamma = \gamma'(2N_i)^q$ where material constant γ' is estimated to be 0.335, and material constant $q = -0.514$ [110]. N_i is the number of cycles to form a crack of size of the order of 1μm in length at the inclusion notch root. Three-dimensional FE simulations were performed to characterize the $\Delta\Gamma$ parameter for nonmetallic primary inclusions, with and without coatings, for the case of debonded matrix/inclusion or coating/inclusion interfaces. Figure 7.1 shows a schematic of an elastic inclusion with coating embedded in an elasto-plastic matrix. The coating-matrix interface is assumed initially debonded over half the interface to facilitate parametric study of effects of properties of the constituents in the three phase system. The diameter of the spherical isotropic elastic inclusion is 5 μm. Material parameters of matrix, coating and inclusion are distinguished using superscripts *m, c,* and *i,* respectively. Table 7.1 summarizes the material parameters of the elastic-plastic response of the steel matrix in Equations 7.1-7.6. These are typical values for carburized and tempered lath martensitic steels intended for HCF applications [217]. Properties assigned

for the inclusion include Young's modulus E^i = 380 GPa and Poisson's ratio v^i = 0.2 [18]. The coating is assumed to also behave as an isotropic linear elastic solid with thickness of 0.5 μm, a typical thickness for sulfide coatings on oxide particles [219], for example. In this study we vary the Young's modulus of the coating to study effects on the $\Delta\Gamma$ parameter in the matrix, assuming the coating Poisson's ratio is also v^c = 0.2 [223].

Table 7.1. *Material parameters of martensitic steel.*

E^m (GPa)	v^m	σ^m_{ys} (MPa)	c^m (GPa)	r^m
193.6	0.28	987	112.1	200

Figure 7.2 shows a cross-section of a 3-D FE mesh. A fine mesh is employed close to the inclusion (element size about 0.25 μm) to capture the details of inelastic deformation around the coating, fanning out with a coarse mesh away from the inclusion. The domain in Figure 7.2 is subjected to three different uniaxial strain ranges (ε_r = 0.3%, 0.5% and 0.6%), applied remotely with R_ε = 0 and -1 and the nonlocal average of the FS parameter, $\Delta\Gamma$, is evaluated over the third loading cycle. The averaging volume for all cases was taken to be 1 μm^3 (unit cube), selected as that particular volume at the notch root that maximizes the nonlocal FS parameter. Figure 7.3 shows different cross sectional views of the 3D domain, elaborating on the dimensions of FE domain with the boundary conditions, and loading direction enforced in the simulations. All simulations were performed using 4-node 3D (C3D4) tetrahedral elements in ABAQUS. Reduced integration is employed. Frictionless contact is assumed along debonded regions. The *Tie command in ABAQUS was used to describe connectivity of the inclusion and coating surfaces and bonded portion of coating and matrix surface.
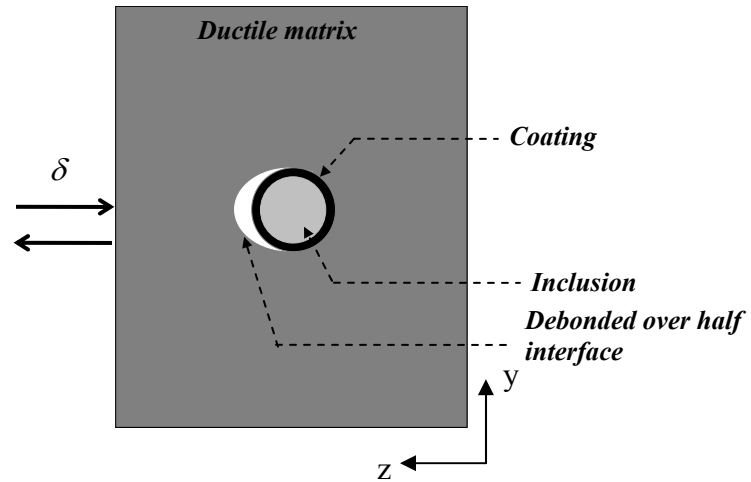
Figure 7.1. *Schematic showing a partially debonded elastic inclusion with coating embedded in an elasto-plastic matrix subjected to cyclic loading.*
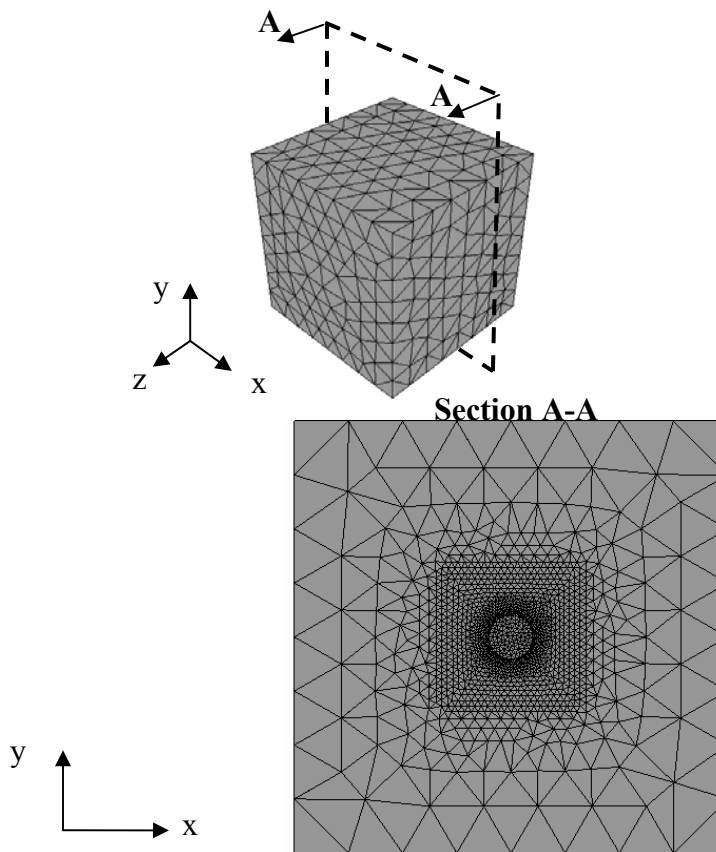
Figure 7.2. *Cross section of FE mesh through the center of the inclusion, showing refinement close to the inclusion. Cyclic loading is in the Z direction.*

171
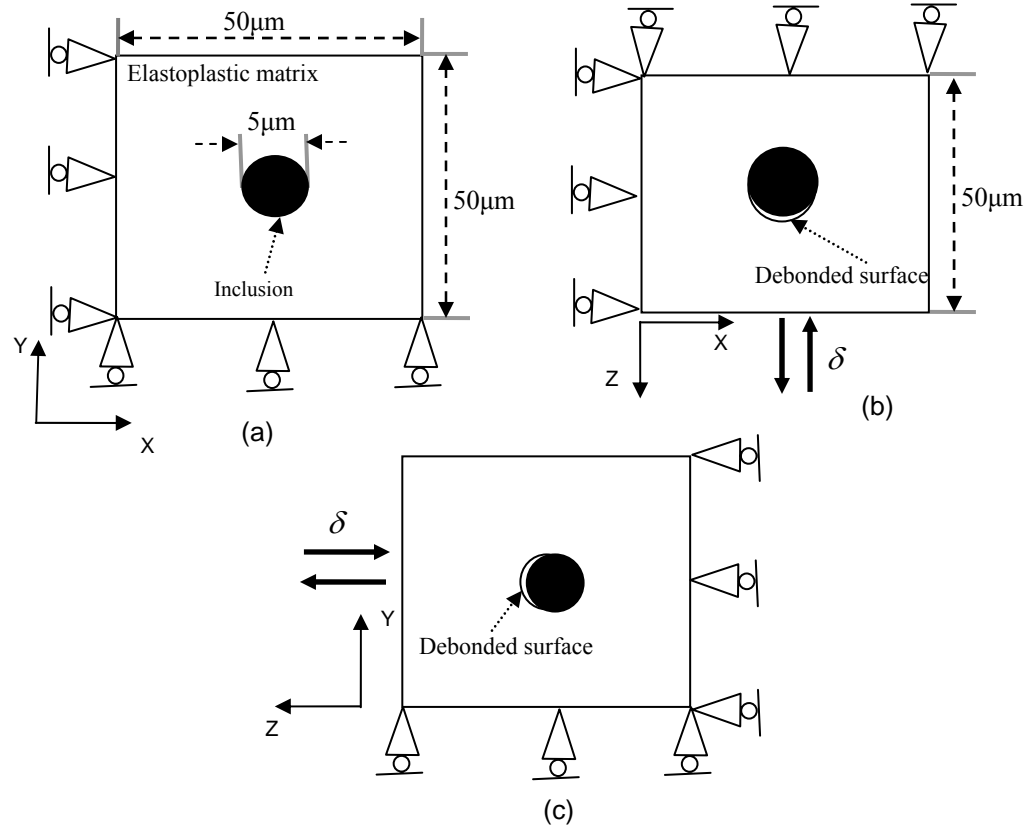
Figure 7.3. *Cross sectional views of the 3-D section with embedded inclusion elaborating on the debonded surface, boundary conditions for uniaxial loading and cyclic loading direction. Views across (a) XY, (b) XZ, and (c) YZ cutting planes through the center of the inclusion.*

7.3. **Results and Discussion**

The ratio of Young's modulus of inclusion to coating is defined by $\zeta = \dfrac{E^i}{E^c}$. Figure

7.4 shows the variation of the maximum nonlocal FS parameter, $\Delta\Gamma^{nc}$ for $\zeta = 1$ and $R_\varepsilon = 0$

and -1 loading conditions; in this case, the coating effectively increases the size of a

partially debonded inclusion without any coating in an elasto-plastic matrix. The

superscript 'nc' denotes that the FIP corresponds to an inclusion without any coating. For

clarity, the numerical values of FS parameter plotted in Figure 7.4 are also presented in Table 7.2.
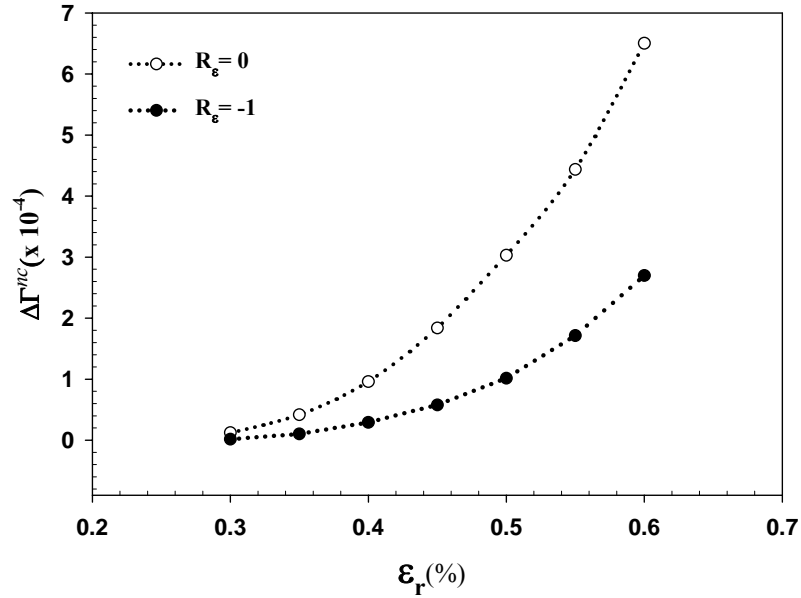
Figure 7.4. *Variation of FS parameter with applied strain range and strain ratio.*

Table 7.2. *Variation of FS parameter with applied strain range and strain ratio.*

ε_r (%)	$\Delta\Gamma^{nc}$ (R_ε=0)	$\Delta\Gamma^{nc}$ (R_ε=-1)
0.30	1.21×10^{-5}	0.14×10^{-5}
0.35	4.16×10^{-5}	1.01×10^{-5}
0.40	9.61×10^{-5}	2.91×10^{-5}
0.45	1.83×10^{-4}	5.78×10^{-5}
0.50	3.03×10^{-4}	1.03×10^{-4}
0.55	4.44×10^{-4}	1.71×10^{-4}
0.60	6.51×10^{-4}	2.69×10^{-4}

It can be seen that $\Delta\Gamma^{nc}$ increases exponentially with remote applied strain range. Comparing the results for different R_ε, we observe that the FS parameter is relatively

higher for $R_\varepsilon = 0$ for the same remote applied strain range. This is due to higher associated maximum applied stress level encountered during cycling at high R_ε ratios. Additionally, the constraints experienced during contact of inclusion with matrix manifests an R ratio effect [19]. The debonded inclusion facilitates high localized plastic strains under monotonic loading conditions, which in turn leads to high local stress states. Consequently, reversed yielding occurs more readily near the debonded inclusion. At high R_ε, the aforementioned mechanism allows for high plastic strain ranges near a debonded inclusion. However, under fully reversed loading conditions, the contact of the inclusion with the matrix inhibits reversed plasticity near the debonded inclusion in the same location as observed under maximum tensile strains. As a result, at very low R_ε ratios the values of $\Delta\gamma_{max}^p$ are relatively small for the debonded inclusion.
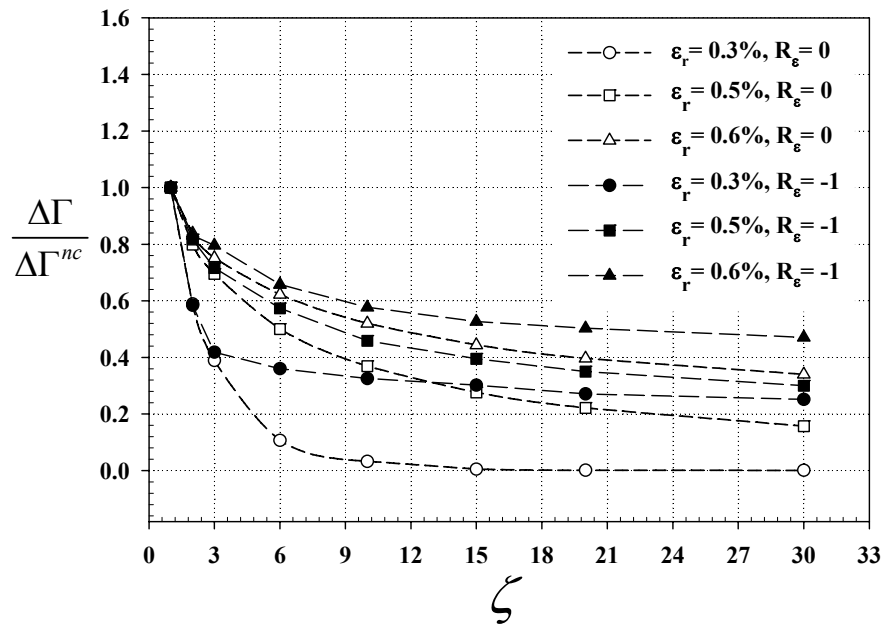
Figure 7.5. *Variation of the normalized nonlocal FS parameter with ζ (normalized by respective values at $\zeta = 1$).*

Further simulations were performed by reducing the elastic stiffness of the coating, with results shown in Figure 7.5. The stiffness ratio, ζ, was varied from 1 to 30 for each remote applied strain range and R_ε. The values of $\Delta\Gamma$ were normalized by their respective values at $\zeta = 1$ ($\Delta\Gamma^{nc}$ in Figure 7.4) to illustrate the percentage reduction in the FIP relative to $\zeta = 1$. At low applied strain ranges (0.3%) and $R_\varepsilon = 0$ and -1 loading conditions, a coating with elastic stiffness half that of the inclusion ($\zeta = 2$) leads to a reduction of $\Delta\Gamma$ by 40%. This would lead to substantial improvement in the fatigue crack formation life (~ 200% increase). Further reduction of coating stiffness ($\zeta \rightarrow 30$) leads to negligible $\Delta\Gamma$ values for an applied strain range $\varepsilon_r = 0.3\%$ and $R_\varepsilon = 0$. Equation 7.7 is used to evaluate the fatigue crack formation life over the nonlocal region of calculation of the FS parameter, as shown in Figure 7.6. For higher values of ζ, substantial enhancement of fatigue crack formation life can be realized. In Figure 7.6, the fatigue crack formation life is not plotted beyond $\zeta = 10$ for $\varepsilon_r = 0.3\%$ and $R_\varepsilon = 0$ loading condition. We assign the points for $\zeta > 10$ as 'run-outs' corresponding to negligibly small values of $\Delta\Gamma$.

In the case of $\varepsilon_r = 0.3\%$ and $R_\varepsilon = -1$ loading condition, the FS parameter ratio (Figure 7.5) does not trend to zero with increasing ζ; this is unlike the trend observed in the case of $\varepsilon_r = 0.3\%$ and $R_\varepsilon = 0$ loading condition. The presence of a compliant coating reduces the severity of the plastic strain localization and the local stress state near debonded inclusion. This is evident from the results obtained by varying the elastic stiffness of the coating. On the contrary, a compliant coating relaxes the effect of constraint experienced during the contact of matrix and coating and permits reverse plasticity under fully

reversed loading conditions. This effect is believed to be responsible for the FS parameter

ratio not trending to zero with increasing ζ under fully reversed loading conditions. The

aforementioned observation is along the lines reported by Gall et al. [19], who studied the

sensitivity of the plastic shear strain ranges near pores and debonded inclusions to the R

ratio in A356-T6 Al alloy. However, significant improvement in the fatigue resistance is

still realized by introducing compliant coating under fully reversed loading.
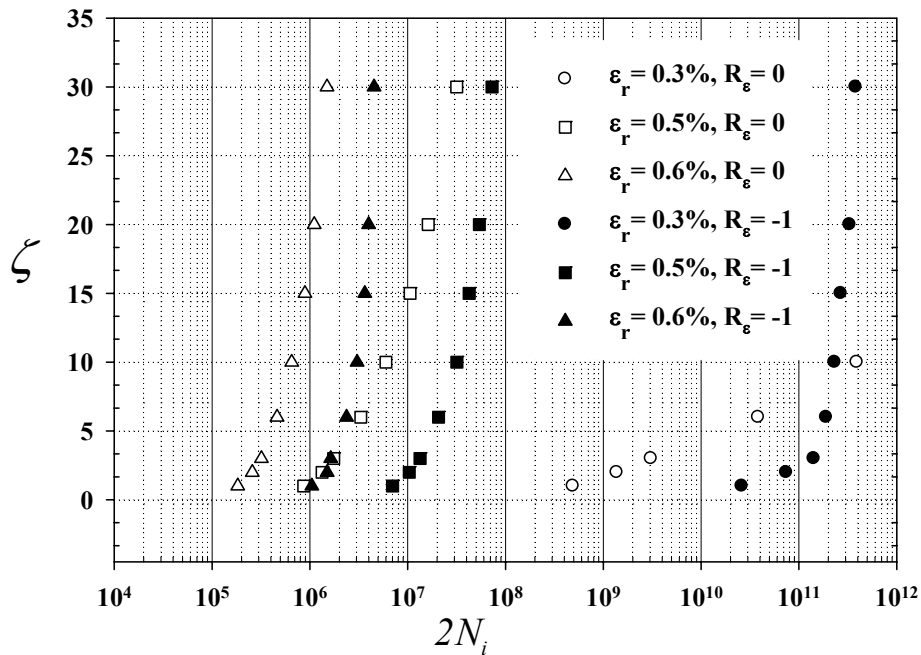
Figure 7.6. *Elastic stiffness ratio versus crack formation life for several applied strain ranges and strain ratios (R_ε =0 and -1).*

Further investigations were carried out to assess the influence of coating at higher

applied strain ranges. For a given value of ζ, the percentage reduction in $\Delta\Gamma$ decreased

with increase in the applied strain range for R_ε= 0 and -1 loading conditions.

Nevertheless, considerable increase could still be realized in fatigue resistance. We

observe from Figure 7.5 that for $\zeta = 2$, $\Delta\Gamma$ reduces by approximately 20% for the applied strain ranges of $\varepsilon_r = 0.5\%$ and $\varepsilon_r = 0.6\%$, which correlates to approximately 50% increase fatigue crack formation lives (Figure 7.6). Figure 7.5 also shows that the effectiveness of a coating is maximized at low imposed strain range. Based on this observation it can be concluded that the idea of introducing a coating at the inclusion/matrix interface is most effective in the HCF and VHCF regimes.

7.4. Summary and Conclusions

Three-dimensional FE simulations suggest the possibility of introducing an elastically compliant interphase layer between a hard inclusion and an elasto-plastic matrix to enhance HCF performance. The sensitivity of FS parameter in the presence of a compliant coating to R_ε ratio was investigated. Significant reduction in FIP after decohesion is observed for compliant coatings at $R_\varepsilon = 0$ and -1. Parametric studies of an idealized nature considered here are useful for discerning trends and potential magnitudes of effects of coatings. Of course, numerous other microstructural factors influence the fatigue response, such as inclusion clustering, inclusion size, grain size, anisotropy of coating and/or inclusion, residual stresses, and so forth.

The advent of computer-controlled processing and experimental techniques, and the extensive work available on coatings through the work of many researchers, encourages pursuit of design of fatigue resistant material systems. Nonmetallic inclusions in steels provide higher energy interfaces that can be leveraged to deposit a soft coating layer through controlled heat treatment processes, thereby producing 'duplex' inclusions [219]. This research work has been published in 2009 as a journal manuscript [224].

Chapter 8

MODELING EFFECT OF HOT ISOSTATIC PRESSING ON HCF RESISTANCE AT DEBONDED PRIMARY INCLUSIONS

In this Chapter, a three-dimensional finite element based framework is used to assess the effect of hot isostatic pressing (HIPping) on void closure at partially debonded nonmetallic primary inclusion in high strength martensitic gear steels. The effect of HIPping on fatigue crack formation potency at nonmetallic primary inclusion is evaluated. The matrix is modeled as rate-independent elasto-plastic material with pure kinematic hardening expressed in hardening minus dynamic recovery format. Idealized linear elastic spherical inclusion is considered to facilitate parametric studies. Temperature dependent material properties are used to simulate deformation at elevated temperatures, e.g. HIPping. A nonlocal average value of plastic shear strain range is used in the modified form of Fatemi-Socie parameter as the FIP. Simulation results reveal enhanced HCF resistance in HIPped steels.

8.1 Introduction

HIPping subjects materials to a combination of high pressure inert gas (e.g., argon) and elevated temperature. The process temperature is selected so that the material yields or creeps in compression under the action of the applied pressure. The result is elimination of internal voids (porosity) and full densification of the material. The isostatic nature of the pressure (i.e., uniform in all directions) means that the component being HIPped retains its shape without the need for support tooling. HIPping removes internal voids from all types of material and promotes diffusion bonding across the surfaces of the

voids. The replacement of the voids by continuous material is the basis for the improvements in mechanical properties that HIPping provides. The basics of HIPping have been summarized previously [225].

Yield strength decreases, for most metals and ceramics, with increasing temperature. The HIPping conditions are generally chosen so that the gas pressure is greater than the reduced yield strength of the material at that temperature. Plastic flow at the microscopic scale occurs under such conditions. During HIPping, creep processes such as Nabarro-Herring creep, Coble creep, and dislocation creep could occur at relatively high rates. The major effects of HIPping on microstructure are the removal of porosity and grain growth. The precipitate distribution and the segregation pattern may be altered during the process. Atkinson and Davies [226] pointed out that after HIPping a PM ferrous alloy, the material tended to fracture along the prior particle boundaries. This was due to segregation of certain alloy content such as titanium to the prior particle boundaries through enhanced diffusion during high temperature processing.

The aforementioned discussion suffices to describe the complexity of the microstructural changes that occur in steels during high temperature processing such as HIPping. Furthermore, steels in general are composed of highly complex microstructure. There are a myriad of interactions between steel chemistry and heat-treatment processing that combine to produce desirable microstructures and properties for specific applications [30, 227]. Hence, it is tedious to develop an all-inclusive model to simulate the complete microstructural response occurring during HIPping; however, there are many aspects of fatigue of microstructures that are amenable to relatively straightforward computation in

order to gain insight into structure–property relations and to build the basis for efforts to pursue modified process routes to enhance fatigue resistance.

Void formation at metal-inclusion interfaces during manufacturing and large deformation processing is a common occurrence. Furthermore, nonmetallic primary inclusions are critical life-limiting features in high strength steels [228]. The objective of this work is to model the effects of HIPping on void closure at debonded metal-inclusion interface. Furthermore, the effect of such a process on fatigue crack formation potency at isolated primary inclusion is evaluated. Several material models have been proposed to simulate HIPping as summarized by Atkinson and Davies [226]. In this work, we adopt a rate-independent elasto-plastic constitutive model to represent the stress-strain response of martensitic steels. This is acceptable since the motive of this work is to qualitatively discern the effect of HIPping on altering the local stress and plastic strain states in the vicinity of debonded primary inclusion in addition to void closure. The inclusions are assumed to be isotropic linear elastic. The two-parameter Fatemi-Socie (FS) critical plane approach discussed in Section 3.5 is used as fatigue indicator parameter. It is well known that significant portion of service life of metallic components is consumed in fatigue crack formation and small crack growth in HCF and VHCF regime [10, 229].

Partially debonded Al_2O_3 inclusions were modeled as the potential fatigue crack nuclei as observed in experiments (see Chapter 2). Simulation-based investigations have revealed partially debonded inclusions to be the worst case scenario for fatigue crack formation (see Chapter 3). Furthermore, void formation at secondary precipitates such as TiC particles during processing can be detrimental to fatigue and fracture resistance [230, 231]; however, such investigations are left to future work.

8.2. Elasto-plastic framework

The general outline of the rate-independent elasto-plastic framework is described in Section 3.4. However, in this study the total strain-rate is additively decomposed into its elastic, plastic, and thermal parts given by

$$\dot{\varepsilon} = \dot{\varepsilon}^e + \dot{\varepsilon}^p + \dot{\varepsilon}^T \qquad (8.1)$$

In the rate-independent formulation, the increments of strain are taken to be additively decomposed into elastic, plastic, and thermal parts, i.e.,

$$d\varepsilon = d\varepsilon^e + d\varepsilon^p + d\varepsilon^T \qquad (8.2)$$

where $d\varepsilon^T = \alpha_{CTE}(T)dT$. Here, $\alpha_{CTE}(T)$ is the coefficient of thermal expansion which is a function of temperature in the present study.

The elastic response is given by

$$\sigma = C : \varepsilon^e \qquad (8.3)$$

where ε^e denotes the elastic strain tensor, and C is the isotropic elastic stiffness tensor.

8.3. Methodology

Idealized spherical alumina inclusions are embedded in a steel matrix. It is assumed that HIPping is conducted prior to case hardening. Hot deformation simulations are conducted at the austenization temperature, approximately 1373 K, of the selected

181

martensitic steel. A systematic parametric investigation is conducted to assess the effect of HIPping on void closure and fatigue resistance at primary inclusion. The elasto-plastic and thermal properties of steel [232-234] and the elastic and thermal properties of alumina [235] were obtained from literature for various temperatures, as listed in Table 8.1. Yield strength could exhibit non-linear dependence on temperature. Due to insufficient data we interpolate the variation in yield strength with temperature using a polynomial relation shown in Equation (8.4) between 300K and 1100 K. The polynomial relation between yield strength and temperature is obtained by fitting the experimental data provided in [234] for AF1410 steel. Between 1100 K and 1373 K the yield strength of the steel matrix is linearly interpolated. All other properties of the steel matrix and alumina are linearly interpolated within the selected temperature range. It is noted that in addition to variation in strength and compliance of the inclusion and steel matrix, the effect of variation in CTE is also considered. The data provided in [235] for alumina and martensitic steel shows a linear interpolation of the elastic modulus and the CTE to be a reasonable approximation. Room temperature (RT) is considered to be 300 K. For simplicity, the steel matrix is assumed to be elastic-perfectly plastic at elevated temperatures (T > 1273 K).

$$\sigma_y\left(MPa\right)=1541.9-0.231T-0.0009T^2 \quad \left(300 \; K < T \leq 1100 \; K\right) \tag{8.4}$$
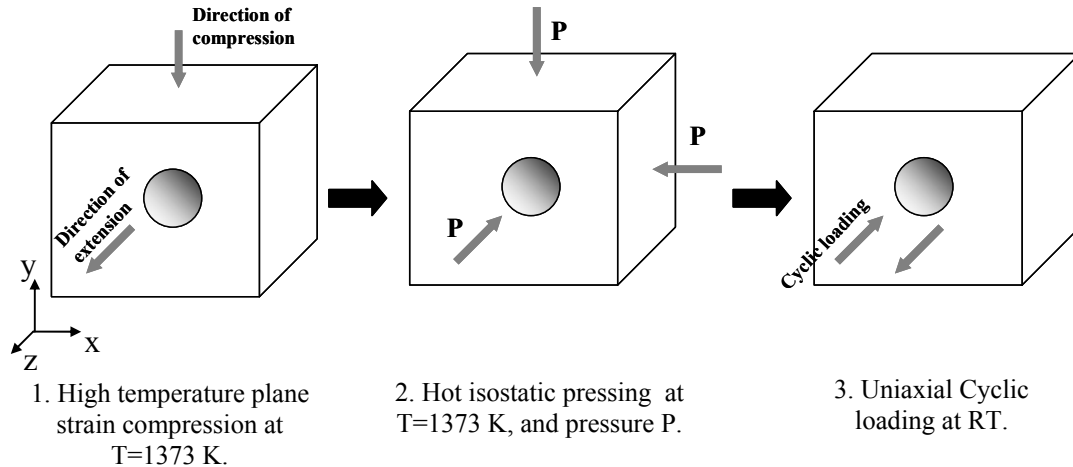
Figure 8.1. *Schematic illustrating the different steps involved in the simulation based investigation of HIPping and fatigue resistance at primary inclusion.*

Table 8.1. *Material parameters of steel and alumina at various temperatures.*

Material	T(K)	E (GPa)	ν	σ_y (MPa)	c (GPa)	r	$\alpha_{CTE}\left(\times 10^{-6} K^{-1}\right)$
Steel	300	194	0.28	1400	112	200	9.54
	1373	112	0.28	100	-	-	11.25
Alumina	300	385	0.25	-	-	-	0.0388
	1373	304	0.25	-	-	-	0.81

Figure 8.1 shows a schematic of the different stages of the simulation conducted to model the effect of HIPping on fatigue resistance. Inclusions are assumed to be partially debonded at the start of the simulation to permit interfacial decohesion during hot deformation such as plane strain compression. The simulation procedure is summarized as follows:

1. The 3D inclusion-matrix volume element (VE) is subjected to high temperature (T= 1373 K) plane strain compression to a macroscopic strain level, $\varepsilon_{yy} = -0.2$. Such

high strain deformation promotes large interfacial decohesion (void formation) at the inclusion-matrix interface. The direction convention illustrated in Figure 8.1 is followed.

2. Following the plane strain compression, the VE is cooled to RT. This allows the residual stresses to build at the inclusion matrix interface by virtue of CTE mismatch.

3. The VE is raised to 1373 K and subjected to uniform pressure P on all directions as illustrated in Figure 8.1. The magnitude of pressure is varied to investigate its effect on void closure at the inclusion-matrix interface.

4. The VE is cooled to RT and subjected to three cycles of loading at several remote loading strain range, ε_r with R_ε =0. The FIP is evaluated over the 3rd loading cycle.

Figure 7.3 shows the different cross sectional views of the 3D domain, elaborating on the dimensions of the FE domain with the boundary conditions, partially debonded interface, and cyclic loading direction enforced in the simulations. All simulations were performed using 4-node 3D tetrahedral elements (C3D4) in ABAQUS. Reduced integration is employed. Frictionless contact is assumed along debonded regions. During plane strain compression the nodes on the face X=50 μm are fixed along direction X. The inclusion diameter is 5 μm, typical of the inclusion size observed on the fracture surface of the selected martensitic steel [27].

Figure 8.2 shows a cross-section of a 3-D FE mesh. A fine mesh is employed close to the inclusion (element size about 0.25 μm) to capture the details of inelastic deformation around the inclusion, fanning out with a coarse mesh away from the inclusion. During cyclic loading, the domain in Figure 8.3 is subjected to several different uniaxial strain ranges (ε_r = 0.25%, 0.35%, 0.45%, 0.5% and 1%), applied remotely with R_ε = 0. The

184

nonlocal average of the FS parameter, $\Delta\Gamma$ is evaluated over the third loading cycle. The averaging volume for all cases was taken to be 1 μm^3 (unit cube), selected as that particular volume at the notch root that maximizes the nonlocal FS parameter.
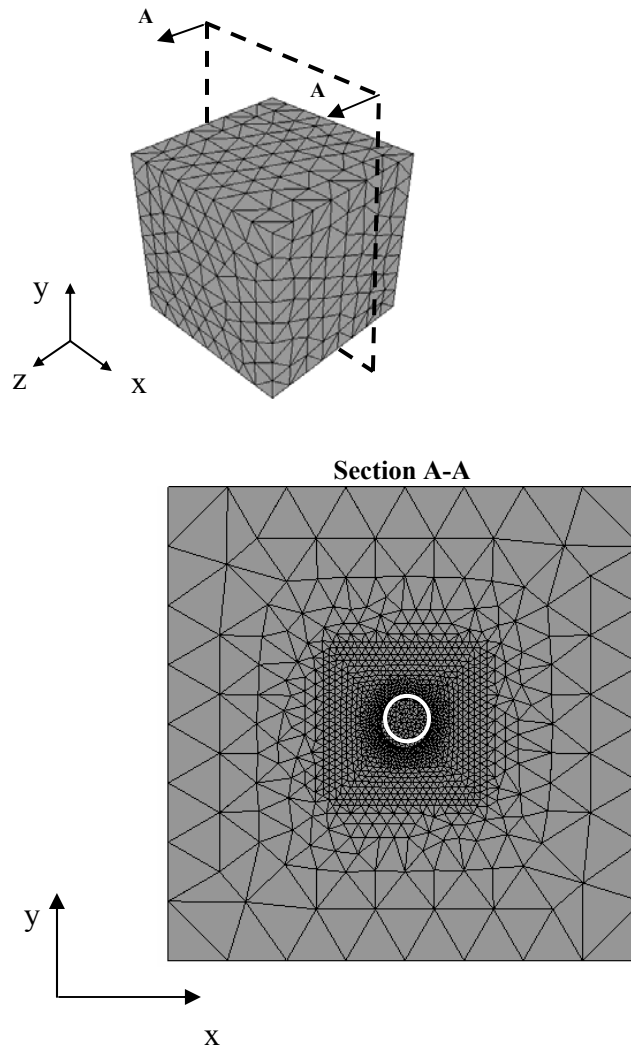
Figure 8.2. *Cross section of FE mesh through the center of the inclusion, showing refinement close to the inclusion. Cyclic loading is in the Z direction.*
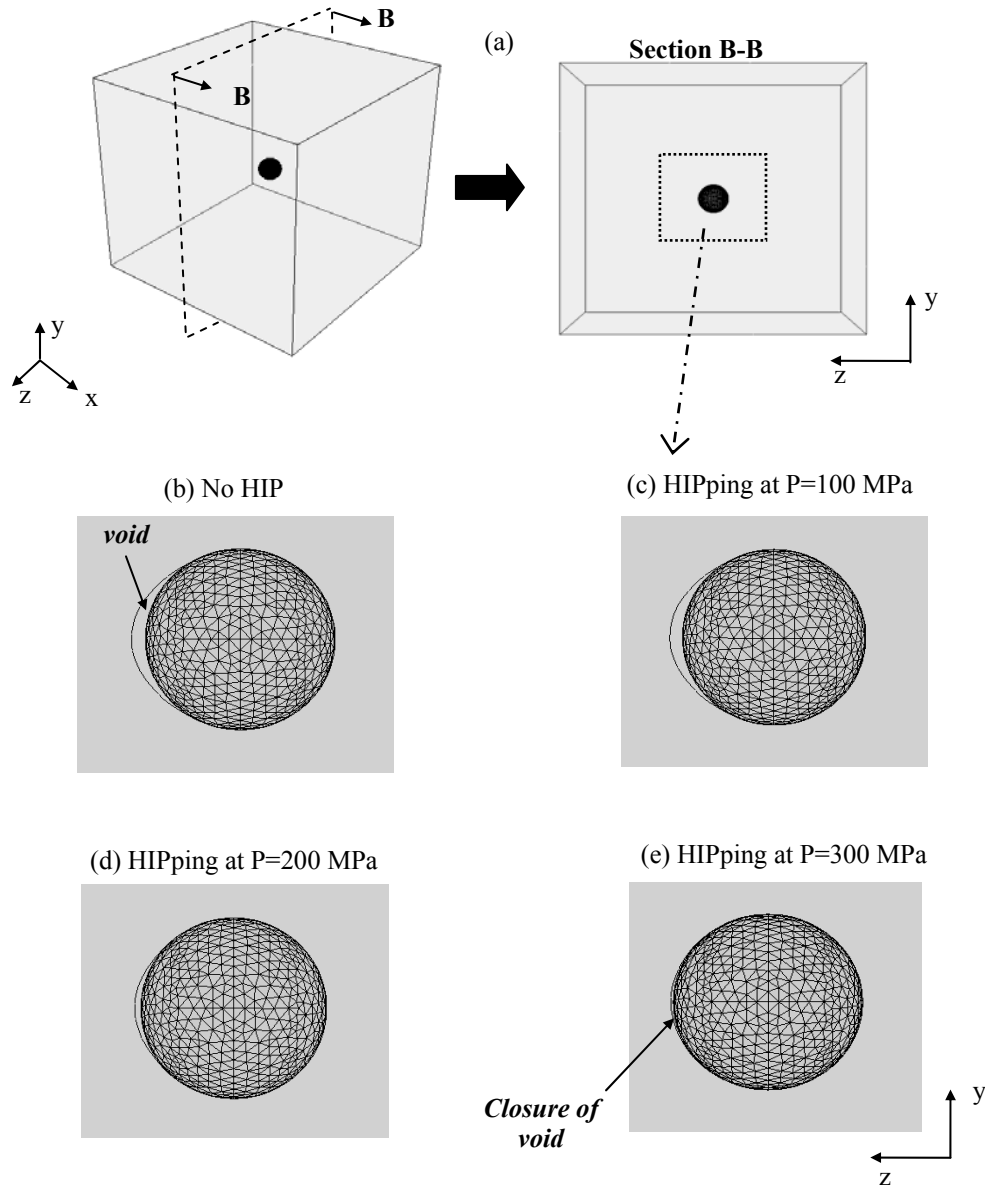
Figure 8.3. *(a) Cross section of the FE domain through the center of the inclusion, (b) Decohesion of inclusion-matrix interface (void) after high temperature plane strain compression, (c) Effect of HIPping at 100 MPa pressure on the void, (d) Effect of HIPping at pressure of 200 MPa on the void, and (e) Effect of HIPping at pressure of 300 MPa on the void- results in complete closure of the void.*

8.4. Results and Discussion

The cross section view of a 3D inclusion-matrix volume element is shown in Figure 8.3a illustrating the enlarged 2D viewing scheme that was followed to monitor the debonded region of the inclusion-matrix interface during processing, as shown in Figures

8.3b-e. The partial decohesion of inclusion-matrix interface occurs during high temperature plane strain compression, as shown in Figure 8.3b. Following plane strain compression, the VE is subjected to uniform pressure at elevated temperature (T = 1373 K) mimicking HIPping. We choose three different magnitudes of remote applied pressure, namely 100 MPa, 200 MPa, and 300 MPa. The deformation scale factor relative to the undeformed configuration for all the images in Figures 8.3 b-e is set to 1. Evidently, high pressure (P >100 MPa) tends to close the void present at inclusion-matrix interface, as illustrated in Figures 8.3c-e. At a remote applied pressure of 300 MPa, we observe complete closure of the void. It is noted that the selected magnitudes of pressure are either equal to or greater than the yield strength of the steel at the processing temperature. It was pointed out by Pagounis and co-workers [236] that optimum bonding between the metal and ceramic and full densification occurs with sufficient hold times during HIPping. The presence of fine dispersions such as grain refining precipitates increases the pressure required for full densification [237]. The selected material model is inadequate to simulate the aforementioned effects; however, the closure of the inclusion-matrix interface does provide useful insights into the advantages of such high temperature processing in suppressing the growth of voids at primary inclusions. Several macroscopic continuum based models have been proposed to simulate the process of HIPping of porous media [226, 238, 239]. However, the material investigated in this work has minimum porosity. Voids are formed at isolated sites within the material such as in the vicinity of primary inclusions; hence, the present material model used to study the effect of HIPping on fatigue potency at such critical life-limiting attributes is reasonable.

Figure 8.4 shows the variation in the nonlocal FS parameter with the applied strain range for unHIPped inclusion-matrix volume element denoted by superscript '*nh*'. It can be seen that $\Delta\Gamma^{nh}$ increases exponentially with the remote applied strain range (note: the ordinate in Figure 8.4 is in log scale). Pre-existing crack-like defects such as debonding of the inclusion-matrix interface invariably facilitates higher local stresses at the intersection of bonded and unbonded portions of the matrix. Furthermore, large interfacial separation occurring at high applied strain ranges aggravates the stresses and plastic strain localization and increases the plastic zone size in the vicinity of micronotches [19]. The aforementioned factor coupled with the constraints experienced during contact gives rise to exponential increase in the FIP with applied strain range.
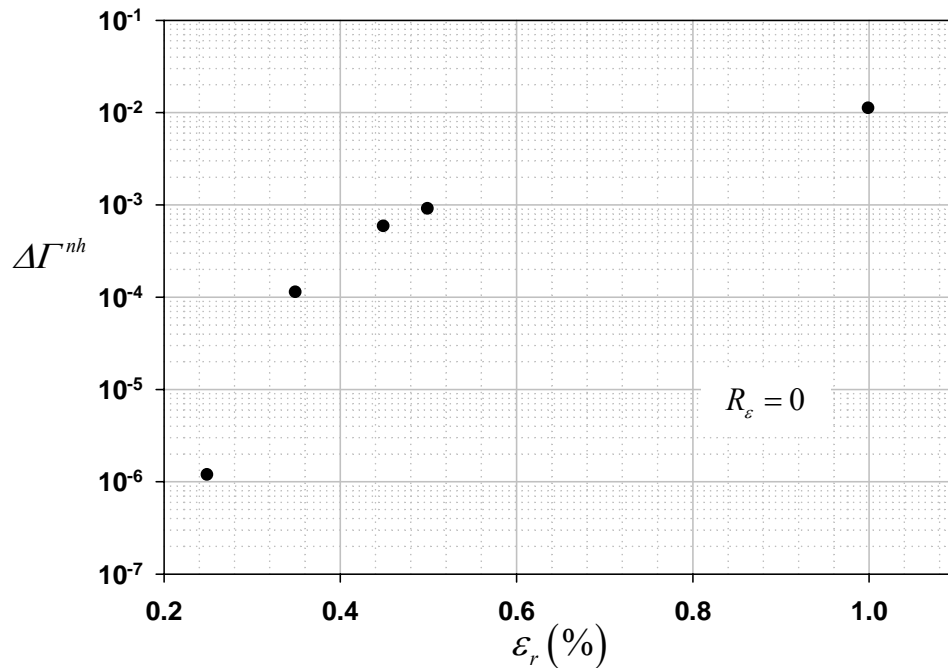
Figure 8.4. *Variation of the nonlocal FS parameter (log scale) with strain range applied remotely with $R_\varepsilon = 0$ for material subjected to fatigue cycling without HIPping.*

Figure 8.5 illustrates the variation in the nonlocal $\Delta\Gamma$ with applied strain range for HIPped steels at RT. The values of $\Delta\Gamma$ at a particular strain range are normalized by the respective values of the unHIPped material ($\Delta\Gamma^{nh}$ in Figure 8.4) to illustrate the percentage reduction in the FIP due to HIPing. At very low applied strain ranges ($\varepsilon_r = 0.25\%$) the FIP is negligibly small for HIPped steel. Compressive stresses develop in the vicinity of primary inclusions during HIPping which in turn suppress the FIP. The effect of the CTE mismatch between the inclusion and matrix is significant during cooling after high temperature processing; however, such effects are present in unHIPped material too. Hence, the results presented in Figure 8.5 can be used to qualitatively discern the effect of HIPping pressure on fatigue crack formation potency.

Significant enhancement of fatigue resistance is observed with increasing HIPping pressure. The effectiveness of a HIPping is maximized at low imposed strain range. For example, at applied strain range of 0.35% we observe approximately 40% reduction in $\Delta\Gamma$ for material HIPped at 300 MPa. This would lead to substantial improvement in fatigue crack formation life. However, the percentage improvement in fatigue resistance decreases at higher applied strain ranges ($\varepsilon_r = 1\%$). As observed in Figure 8.3, HIPping results in void closure at the debonded inclusion-matrix interface. This would reduce the interfacial separation that occurs during subsequent fatigue cycling. The aforementioned factor coupled with the compressive stresses induced during HIPping effectively alleviates the stresses and plastic strain localization in the vicinity of the stress raisers at low applied strain ranges. At higher strain ranges, the local stress states in the proximity of primary inclusions are relatively very high. This effectively negates the effect of any prior residual stresses and facilitates large interfacial separation at the inclusion-matrix

interface. Hence, the improvement in fatigue resistance at high applied strain ranges ($\varepsilon_r = 1\%$) is relatively less significant (~10%), as illustrated in Figure 8.5. Based on this observation it can be concluded that the idea of HIPping of steels containing debonded primary inclusions is most effective in the HCF and VHCF regimes.
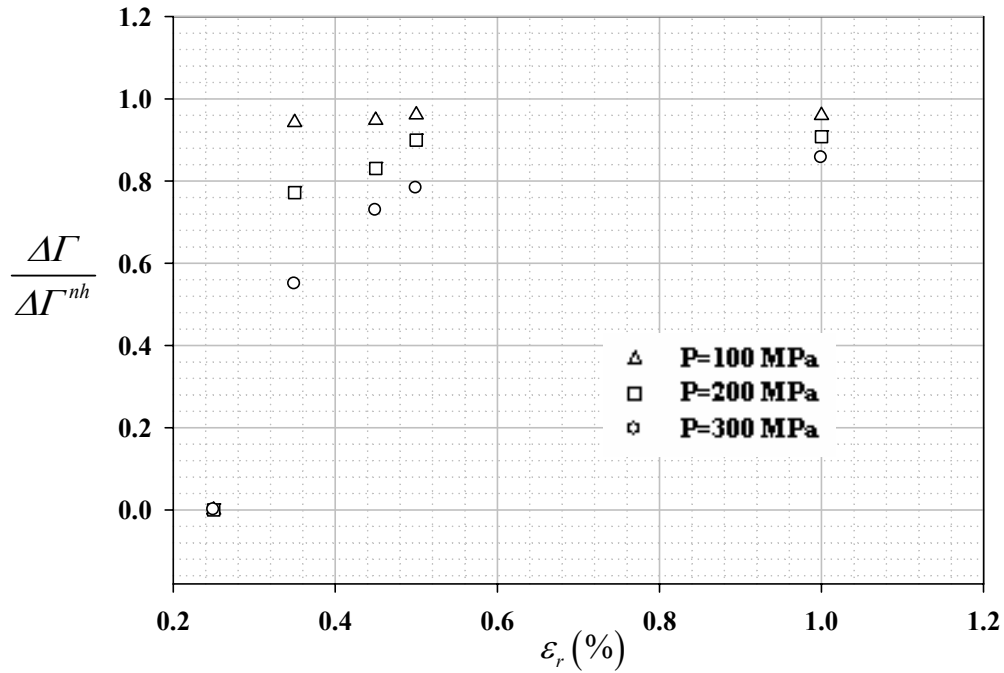
Figure 8.5. *Variation of normalized FIP with applied strain range in HIPped martensitic steel.*

Although development of interfacial bonding between inclusion and the steel matrix is not simulated in the present study, prior simulations have revealed at least two orders of magnitude difference in the $\Delta\Gamma$ between intact and partially debonded inclusion [121] with partially debonded inclusion being the most severe with regard to fatigue crack formation. Hence, in the event of bonding between inclusion and matrix during HIPping [236] the improvement in fatigue resistance would be substantial. In this work we assumed that HIPping is performed prior to case hardening such as carburization and

190

surface treatments such as shot peening. The aforementioned processing steps could drastically alter the local stress state in the proximity of primary inclusions (see Chapter 3). Furthermore, while cooling from austenization temperature to RT after HIPping, phase transformation occurs in martensitic steels. The selected material model utilized in this study does not account for such effects. It is acknowledged that the simulations conducted in this study are primarily intended to obtain qualitative trends with regard to enhancement in fatigue resistance due to HIPping. Detailed experiments and microstructure dependent material models [238] are necessary to conduct quantitative evaluation of HIPping. However, it is important to note that FE based models that are capable of combining the hot deformation process such as HIPping with fatigue are limited. Furthermore, FE based studies evaluating the effect of HIPping on fatigue potency at nonmetallic primary inclusions are very limited.

8.5. Conclusions

Three-dimensional FE simulations suggest the possibility of using HIPping to enhance HCF performance of martensitic steel. The sensitivity of the FS parameter to HIPping pressure was investigated. The simulations revealed that HIPping reduces the interfacial separation at the debonded inclusion-matrix interface. At high pressure (= 300 MPa) closure of a pre-existing void present at inclusion-matrix interface was observed. The effectiveness of HIPping is maximized at low imposed strain range. Parametric studies of idealized nature, such as those considered here, are useful for discerning trends and potential magnitudes of effects of HIPping. Of course, numerous other

191

microstructural factors influence the fatigue response, such as inclusion clustering, inclusion size, grain size, residual stresses, and so forth.

Chapter 9

SUMMARY, CONTRIBUTIONS, AND RECOMMENDATIONS FOR FUTURE WORK

9.1. Summary and contributions

A comprehensive set of 3D computational tools and algorithms for microstructure-sensitive fatigue modeling of lath martensitic steels has been developed in this research. The primary objective was to quantify the fatigue potency at critical life-limiting primary inclusions in lath martensitic steels. More emphasis was placed on the use of computational tools to compare microstructure attributes with the goal of design or specification of material microstructure. To understand the role of various microstructure attributes that affect crack formation and growth in lath martensitic steel, a hierarchical computation framework was adopted. Relevant microstructure-scale fatigue descriptors were identified. The computational tools and algorithms can support:-

1. Tailoring of microstructures to maximize fatigue resistance;

2. Comparison of candidate microstructures for a desired application;

3. Characterization of variability and scatter in fatigue;

4. Modification of process routes to enhance fatigue resistance; and

5. Rank ordering the severity of various microstructure attributes in fatigue to develop cost effective strategies to extend fatigue life.

Even though the constitutive modeling studies and the computational studies were conducted on a specific lath martensitic steel (C61 steel), the generic 3D framework

should be applicable to any processed martensitic steel with similar microstructure. The key outcomes of this research are summarized as follows:-

1. Devised simplified schemes to simulate materials processing effects on subsurface and near inclusion residual stresses in order to evaluate the potency for crack formation and early growth.

2. Developed physically based constitutive models suitable to investigate fatigue crack formation and early growth at microstructural heterogeneities (for e.g., nonmetallic primary inclusions, fine scale precipitates, etc.).

3. Devised methodologies to account for the 3D effects of inclusion size, spacing, orientation, and clustering on fatigue crack formation potency.

4. Devised crystal plasticity based methodology to model the relaxation of compressive residual stresses in HCF.

5. Developed a computational micromechanics framework to study the variability of crack formation and early growth due to material microstructure and process routes.

6. Devised strategies to explore modified process routes that enhance the fatigue resistance of martensitic steels (e.g., HIPping).

The key innovations and intellectual contributions are summarized as follows:-

1. Novel strategies were developed to couple the process route with the microstructure scale response for comprehensive fatigue analyses of critical life-limiting attributes in high strength steels. This will contribute significantly to the

development of reliable life-prediction models. Such strategies can readily feed into concurrent/hierarchical multiscale modeling schemes for materials design with the aim of understanding the sensitivity of fatigue response to microstructure and process routes. Simulation results utilizing continuum crystal plasticity with the microstructural dependence embedded in the model will provide tremendous insights into the evolution of fatigue damage at various microstructure scales.

2. Methods were developed for computational study of improved process routes such as HIPping, and coated inclusions. These methods should provide a basis for efforts to modify the actual process routes in order to achieve enhanced fatigue resistance.

3. A computational micromechanics based statistical/probabilistic framework was developed to evaluate the effect of microstructure and process variability on fatigue life variability. This framework will have significant implications in the minimum-life design approach followed in industry.

9.2 Recommendations for future research

Extensive computational studies have been performed in this thesis to characterize the fatigue crack formation and early growth in lath martensitic gear steels. Several aspects of this research are relatively new and may not be practical to classify this work as complete in all respects. There are many avenues for future research as listed below:-

1. Experiments

- *Characterizing the cyclic stress-strain response of the case layer*

It is evident that the primary inclusions present at the case layer serve as highly potent site for crack formation. Furthermore, significant strength gradient is induced during case hardening from the surface to the core. Hence, detailed experimental study is imperative in order to characterize the cyclic stress-strain response of the case layer of high strength steels. Furthermore, such studies should provide information regarding the degree of cyclic hardening that occurs during the initial stages of fatigue cycling. This can be achieved by machining fatigue specimens (e.g. dog bone specimens) with varying degrees of out of plane thickness. Such samples when subjected to similar heat treatment will develop different strength characteristics by virtue of varying case and core depth along the thickness. Subsequent fatigue tests will provide qualitative information regarding the fatigue response of the case layer. Furthermore, the experiments will be useful to discern the effect of variation in volume fraction of fine scale size precipitates (M_2C) on cyclic hardening characteristics. The experimentally obtained stress-strain response can be used to calibrate the material-dependent parameters and constants in fatigue models.

- I*nvestigation of fatigue crack formation at the grain scale*

Although much work in this research has focused on characterizing the fatigue crack formation potency at the grain scale, several experimental studies can be conducted to support and improve model predictions. For example, the effects of prior austenite grain boundaries on crack formation and early growth are still unclear. In this work, a single

block of lath martensite is considered to be an effective grain; however, crack formation potency of a block situated close to a prior austenite grain boundary could differ from that situated in the interior. Atomic force microscopy techniques can be utilized to study such crack formation mechanisms at the nanoscale. Transmission electron microscopy (TEM) could be conducted to better characterize complex dislocation interactions and other deformation mechanisms in secondary hardening martensitic steels that contain several microstructure inhomogenieties (e.g., primary inclusions, precipitates) in fatigue. The aforementioned information would certainly assist in improving the existing microstructure-sensitive fatigue models.

- *Experimental measurement of residual stress relaxation*

One factor that is not well understood in the present material is the evolution of the compressive residual stresses in fatigue. Attempts have been made in this research to investigate the residual stress relaxation utilizing a computational crystal plasticity model. However, validating the model predictions with experiments is critical. Interrupted residual stress measurements or non-destructive high energy x-ray diffraction methods could be utilized to gain insight into residual stress profile evolution during cyclic loading. Such detailed investigation will certainly improve model predictions and also help guide selection and tailoring of microstructures to better resist residual stress relaxation and improve fatigue resistance.

2. Computational modeling

- *Multiresolution Models*

Limited attempts have been made as a part of the collaborative research to evaluate fatigue potency at primary inclusions by constructing 3D FE meshes from measured (realistic) microstructures containing about 8 nonmetallic inclusions [105]. A simple J_2 type macroscopic elasto-plastic model was utilized to simulate the cyclic stress-strain response of the steel matrix for simulations involving realistic particle distribution. However, conducting crystal plasticity simulations of similar 3D FE domains can be computationally prohibitive. Although such computationally intensive simulations can provide useful insight into the effects of cluster morphology on fatigue potency, the HCF crack formation life could be dependent on a few critical "hot spots" such as the largest inclusion within the cluster. Multiscale modeling such as the schemes developed by Liu and co-workers [240, 241] can be utilized to identify the fatigue critical "hot spots". Such multiresolution strategies have demonstrated superior capabilities in capturing the localization of stresses and plastic strains at various microstructure scales under monotonic loading conditions [242]. Furthermore, the aforementioned schemes can be utilized to rank order the severity of various microstructure attributes in fatigue. Once the fatigue critical "hot spots" are identified, detailed crystal plasticity simulations can be conducted locally to characterize the variability in HCF. It is noted that crystal plasticity calculations are imperative to understand variability in fatigue crack formation and small crack growth potency in HCF.

- *Modeling effects of retained austenite on fatigue crack formation potency*

The heat treatment of the selected martensitic steels assures complete transformation of the case layer microstructure to lath martensite prior to surface treatment and service. However, it will be interesting to investigate the effect on the fatigue performance of having limited retained austenite (RA) in the case layer. There is a possibility that during fatigue cycling, the RA present in the vicinity of primary inclusions could undergo phase transformation by virtue of stress localization. RA is relatively softer than lath martensite and will deform more readily in fatigue. A portion of the fatigue load could be consumed in phase transformation, thereby reducing the degree of plastic strain localization in the proximity of the stress raisers. The aforementioned phenomenon could potentially improve the fatigue life of the steel component. Such investigations are possible using computational models such as the FE model developed by Alley and Neu [118].

- **Transition from single particle-dominated fatigue to that dominated by inclusion cluster (interaction effects)**

The simulation-based studies performed in this work showed that for the selected inclusion size, interfacial conditions (debonded and cracked particles), inclusion stiffness, and remote loading conditions, a single microstructure attribute such as the size of the inclusion may be inadequate to characterize the minimum fatigue resistance of the selected martensitic gear steel. In Chapter 6, we showed that interaction of relatively smaller size inclusions in a cluster demonstrated the potential to replicate the effect of a larger isolated particle in HCF. However, with the increase in the size of the inclusion there exists a critical inclusion size above which the second order effects such as the interaction of inclusions may become less prominent. It is important to estimate the

aforementioned transition from a single large particle-dominated fatigue response to that dictated by interaction of inclusions in a cluster. Such a study would require simulation over a range of inclusion sizes and spacing to correlate the fatigue potency with the aforementioned microstructure attributes. Furthermore, it is important to introduce suitable MSC growth law at the scale of single inclusion and inclusion clusters. Estimating the life consumed in crack formation and small crack growth to length of the order of cluster size and comparing the crack formation and MSC growth life at single isolated particle of varying size would provide a better indication of the critical inclusion size. Also, the aforementioned study will be useful to estimate the minimum fatigue resistance of the material for a desired fatigue application provided statistical extremes of the microstructure attributes (e.g., inclusion size, cluster size, inclusion spacing) are well characterized.

References

[1] Gear Industry Vision. Gear Industry Vision Workshop, Detroit, MI, Organizers: U. S. Army, Publisher: Energetics Inc, March 10, 2004.

[2] Olson GB. Computational Design of Hierarchically Structured Materials. Science 1997;277(5330):1237-1242.

[3] Smith CS. A Search for Structure. Cambridge: The MIT Press, 1981.

[4] McDowell DL, Olson GB. Concurrent design of hierarchical materials and structures. Scientific Modeling and Simulation 2008;15(1):207-240.

[5] McDowell DL, Gall K, Horstemeyer MF, Fan J. Microstructure-based fatigue modeling of cast A356-T6 alloy. Engineering Fracture Mechanics 2003;70(1):49-80.

[6] McDowell DL. Multiaxial Small Fatigue Crack Growth in Metals. International Journal of Fatigue 1997;19(1):127-135.

[7] Lankford J, Kusenberger FN. Initiation of fatigue cracks in 4340 steel. Metallurgical Transactions A (Physical Metallurgy and Materials Science) 1973;4(2):553-559.

[8] Bennett V, McDowell DL. Polycrystal orientation effects on microslip and mixed-mode behavior of microstructurally small cracks. ASTM Special Technical Publication 1999(1359):203-228.

[9] Xue Y, McDowell DL, Horstemeyer MF, Dale MH, Jordon JB. Microstructure-based multistage fatigue modeling of aluminum alloy 7075-T651. Engineering Fracture Mechanics 2007;74(17):2810-2823.

[10] McDowell DL. Simulation-based strategies for microstructure-sensitive fatigue modeling. Materials Science and Engineering A 2007;468-470:4-14.

[11] Simonovski I, Nilsson KF, Cizelj L. The influence of crystallographic orientation on crack tip displacements of microstructurally small, kinked crack crossing the grain boundary. Computational Materials Science 2007;39(4):817-828.

[12] Kunio T, Shimizu M, Yamada K, Sakura K, Yamamoto T. Early Stage of Fatigue Crack Growth in Martensitic Steel. International Journal of Fracture 1981;17(2):111-119.

[13] Toyoda T, Matsui T, Murakami Y. A Study of Inclusions Causing Fatigue Cracks in Steels for Carburized and Shot Peened Gears. JSAE Review 1990;11:50-54.

[14] Murakami Y, Endo T. Effects of small defects on fatigue strength of metals. Int J Fatigue 1980;2(1):23-30.

[15] Lankford J. Inclusion-matrix debonding and fatigue crack initiation in low alloy steel. Int J Fract 1976;12(1):155-156.

[16] Lankford J. Initiation and early growth of fatigue cracks in high strength steel. Engineering Fracture Mechanics 1977;9(3):617-624.

[17] Yin F, Fatemi A. Fatigue behaviour and life predictions of case-hardened steels. Fatigue and Fracture of Engineering Materials and Structures 2009;32(3):197-213.

[18] Melander A. A finite element study of short cracks with different inclusion types under rolling contact fatigue load. International Journal of Fatigue 1997;19(1):13-24.

[19] Gall K, Horstemeyer MF, Degner BW, McDowell DL, Fan J. On the driving force for fatigue crack formation from inclusion and voids in a cast A356 aluminum alloy. International Journal of Fracture 2001;108(3):207-233.

[20] Norstrom LA. On the Yield Strength of Quenched Low-Carbon Lath Martensite. Scandinavian Journal of Metallurgy 1976;5(4):159-165.

[21] James MN, Hughes DJ, Chen Z, Lombard H, Hattingh DG, Asquith D, Yates JR, Webster PJ. Residual stresses and fatigue performance. Engineering Failure Analysis 2007;14(2):384-395.

[22] Krauss G. Deformation and fracture in martensitic carbon steels tempered at low temperatures. Metallurgical and Materials Transactions A: Physical Metallurgy and Materials Science 2001;32(4):861-877.

[23] Krauss G. Martensite in steel: strength and structure. Vol. A273-275 San Carlos de Bariloche, Argentina: Elsevier, 1999, pp. 40-57.

[24] Krauss G. Microstructure and performance of carburized steel. Part I: martensite. Advanced Materials and Processes 1995;147(5):40-40.

[25] Shin J-C, Lee S, Ryu JH. Correlation of microstructure and fatigue properties of two high-strength spring steels. International Journal of Fatigue 1999;21(6):571-579.

[26] Zaccone MA, Kelley JB, Krauss G. Strain hardening and fatigue of simulated case microstructures of carburized steels. Industrial Heating 1989;56(9):7.

[27] Tiemens BL. Performance Optimization and Computational Design of Ultra-High Strength Gear Steels. In: Department of Materials Science and Engineering, PhD Thesis, Evanston, IL: Northwestern University, 2006.

[28] Wang L, Liu L, Ao C, Liu X, Chen C, Kang M. Investigation of transformation for ultrahigh strength steel Aermet 100. Journal of Materials Science and Technology 2000;16(5):491-494.

[29] Carinci GM, Hetherington MG, Olson GB. M_2C carbide precipitation in AF1410 steel. Journal de Physique Colloque 1988;49:311-316.

[30] Olson GB, Cohen M. Principles of Martensitic Transformation. In: Front in Mater Technol, Vol. 26 Amsterdam, Neth: Elsevier Science Publ BV, 1985, pp. 43-87.

[31] Hildebrandt U, Dickenscheid W. Plasticity and alloy- softening in iron- nickel-alloys. Acta Metallurgica 1971;19(1):49-55.

[32] Leslie WC, Sober RJ, Babcock SG, Green SJ. Plastic flow in binary substitutional alloys of BCC iron- Effects of strain rate, temperature and alloy content. 1969;62(3):690-710.

[33] Vernerey FJ, McVeigh C, Liu WK, Moran B, Tewari D, Parks DM, Olson GB. The 3-D computational modeling of shear-dominated ductile failure in steel. Journal of Materials 2006;58(12):45-51.

[34] Wise JP. Systems Design of Advanced Gear Steels. PhD Thesis, Northwestern University 1998.

[35] Lee HM, Allen SM. Coarsening resistance of M2C carbides in secondary hardening steels: part III. Comparison of theory and experiment. Metallurgical transactions A, Physical metallurgy and materials science 1991;22 A(12):2877-2888.

[36] Kuehmann CJ, Olson GB. Gear steels designed by computer. Advanced Materials and Processes 1998;153(5):40-43.

[37] McClung RC. A literature survey on the stability and significance of residual stresses during fatigue. Fatigue and Fracture of Engineering Materials and Structures 2007;30(3):173-205.

[38] Ceschini L, Minak G. Fatigue behaviour of low temperature carburised AISI 316L austenitic stainless steel. Surface and Coatings Technology 2008;202(9):1778-1784.

[39] Tokaji K, Akita M. Effect of carburizing on notch fatigue behaviour in AISI 316 austenitic stainless steel. Surface and Coatings Technology 2006;200(20-21):6073-6078.

[40] Farfan S, Rubio-Gonzalez C, Cervantes-Hernandez T, Mesmacque G. High cycle fatigue, low cycle fatigue and failure modes of a carburized steel. International Journal of Fatigue 2004;26(6):673-678.

[41] Kawagoishi N, Nagano T, Moriyama M. Effect of shot peening on fatigue strength of maraging steel. Sixth International Conference on Computer Methods and Experimental Measurements for Surface Treatment Effects Vol. 7 Crete, Greece: WITPress, Southampton, United Kingdom, 2003, pp. 99-108.

[42] Iwata N, Tomota Y, Katahira K, Suzuki H. Effect of shot peening on fatigue fracture for an as quenched martensitic steel. Materials Science and Technology 2002;18(6):629-632.

[43] Brown J. Shot peening increases gear life. Power Transmission Design 1996;38(5):61-64.

[44] Benedetti M, Fontanari V, Hohn BR, Oster P, Tobie T. Influence of shot peening on bending tooth fatigue limit of case hardened gears. Int J Fatigue 2002;24(11):1127-1136.

[45] Almen JO. Fatigue weakness of surfaces. Product Engineering 1950;21(11):117-140.

[46] Sieber R. Bending fatigue performance of carburized gear steels. Detroit, MI, USA: Publ by SAE, Warrendale, PA, USA, 1992, pp. 1-18.

[47] Freborg AM, Ferguson BL, Li Z, Schwam DX, Smith BJ. Bending fatigue strength improvement of carburized aerospace gears. Vol. III Phoenix, AZ, United States: American Helicopter Society, Alexandria, VA 22314-2538, United States, 2006, pp. 2092-2102.

[48] Krug T, Lang KH, Fett T, Lohe D. Influence of residual stresses and mean load on the fatigue strength of case-hardened notched specimens. Materials Science and Engineering A 2007;468-470:158-163.

[49] Inoue K, Kato M. Estimation of fatigue strength enhancement for carburized and shot-peened gears. Journal of Propulsion and Power 1994;10(3):362-368.

[50] Farrahi GH, Ghadbeigi H. An investigation into the effect of various surface treatments on fatigue life of a tool steel. Journal of Materials Processing Technology 2006;174(1-3):318-324.

[51] Masuyama T, Kato M, Inoue K, Yamashita T. Evaluation of bending strength of carburized gears based on a quantification of defect size in the surface layer. Journal of Mechanical Design, Transactions of the ASME 2002;124(3):533-538.

[52] Norstrom LA, Johansson B. Surface Yield Strength and Flow Stress in High-Strength Martensitic Steels. Scandinavian Journal of Metallurgy 1983;12(1):37-39.

[53] Murakami Y, Endo M. Quantitative evaluation of fatigue strength of metals containing various small defects or cracks. Engineering Fracture Mechanics 1983;17(1):1-15.

[54] Umezawa O, Nagai K. Deformation structure and subsurface fatigue crack generation in austenitic steels at low temperature. Metall Mater Trans A 1998;29A(3):809-822.

[55] Wang QY, Bathias C, Kawagoishi N, Chen Q. Effect of inclusion on subsurface crack initiation and gigacycle fatigue strength. Int J Fatigue 2002;24(12):1269-1274.

[56] Torres MAS, Voorwald HJC. An evaluation of shot peening, residual stress and stress relaxation on the fatigue life of AISI 4340 steel. Int J Fatigue 2002;24(8):877-886.

[57] Shaw BA, Aylott C, O'Hara P, Brimble K. The role of residual stress on the fatigue strength of high performance gearing. Vol. 25 Hyannis, MA, United States: Elsevier Ltd, 2003, pp. 1279-1283.

[58] Nishijima S, Kanazawa K. Stepwise S-N curve and fish-eye failure in gigacycle fatigue. Fatigue and Fracture of Engineering Materials and Structures 1999;22(7):601-607.

[59] Shiozawa K, Lu L. Very high-cycle fatigue behaviour of shot-peened high-carbon-chromium bearing steel. Fatigue and Fracture of Engineering Materials and Structures 2002;25(8-9):813-822.

[60] Meurling F, Melander A, Tidesten M, Westin L. Influence of carbide and inclusion contents on the fatigue properties of high speed steels and tool steels. International Journal of Fatigue 2001;23(3):215-224.

[61] Larsson M, Melander A, Blom R, Preston S. Effects of shot peening on bending fatigue strength of spring steel SS 2090. Materials Science and Technology 1991;7(11):998-1004.

[62] Li JK, Zhang R, Yao M, Wang R. Experimental study on the compressive residual stress field introduced by shot-peening. Vol. 1-2 Tokushima, Jpn: Publ by Elsevier Science Publ Ltd, Barking, Engl, 1991, p. 750.

[63] Wang S, Li Y, Yao M, Wang R. Compressive residual stress introduced by shot peening. Journal of materials Processing Technology 1998;73(1-3):64-73.

[64] Shaw MC, De Salvo G. On the Plastic Flow Beneath a Blunt Axisymmetric Indentor. Transactions of the ASME Journal of Engineering for Industry 1970;92:480-494.

[65] Meguid SA, Klair MS. Elasto-plastic co-indentation analysis of a bounded solid using finite element method. International Journal of Mechanical Sciences 1985;27(3):157-168.

[66] Khabou MT, Castex L. The effect of material behaviour law on the theoretical shot peening results. European Journal of Mechanics, A/Solids 1990;9(6):537-549.

[67] Johnson W. Impact strength of materials. London: Edward Arnold, 1972.

[68] Iida K. Dent and Affected Layer Produced by Shot Peening. Vol. 2: Pergamon Press, Oxford, Engl, 1986, pp. 217-227.

[69] Meguid SA, Shagal G, Stranart JC. Development and validation of novel FE models for 3D analysis of peening of strain-rate sensitive materials. Journal of Engineering Materials and Technology, Transactions of the ASME 2007;129(2):271-283.

[70] Meguid SA, Shagal G, Stranart JC. Finite element modelling of shot-peening residual stresses. Journal of materials Processing Technology 1999;92-93:401-404.

[71] Meguid SA, Shagal G, Stranart JC, Daly J. Three-dimensional dynamic finite element analysis of shot-peening induced residual stresses. Finite Elements in Analysis and Design 1999;31(3):179-191.

[72] Eltobgy MS, Ng E, Elbestawi MA. Three-dimensional elastoplastic finite element model for residual stresses in the shot peening process. Proceedings of the Institution of Mechanical Engineers, Part B (Journal of Engineering Manufacture) 2004;218(B11):1471-1481.

[73] Hong T, Ooi JY, Shaw B. A numerical simulation to relate the shot peening parameters to the induced residual stresses. Engineering Failure Analysis 2008;15(8):1097-1110.

[74] Hong T, Ooi JY, Shaw BA. A three-dimensional finite element analysis of two/multiple shots impacting on a metallic component. Structural Engineering and Mechanics 2008;29(6):709-729.

[75] Fathallah R, Frija M, Hassine T, Bouraoui C, Dogui A, Mecanique LG. Finite element modelling of shot peening process: Prediction of the compressive residual stresses, the plastic deformations and the surface integrity. Materials Science and Engineering A (Structural Materials: Properties, Microstructure and Processing) 2006;426(1-2):173-180.

[76] Suresh S. Fatigue of materials. Cambridge University Press, 2nd Edition 1998.

[77] Kim C, Diesburg DE, Eldis GT. Effect of Residual Stress on Fatigue Behavior of Carburized Steels- An Analytical Model. In: ASTM STP 776, Residual Stress Effect in Fatigue, 1982, pp. 224-234.

[78] Sharma VK, Walter GH, Breen DH. Factors Influencing Fracture toughness of High Carbon Martensitic Steels. Gear Technology 1989:7-18.

[79] Lin H, Fett GA, Binoniemi RR. Bending Fatigue Life Analysis of Carburized Components using Strain Life and Fracture Mechanics Approaches. Journal of Materials and Manufacturing 2004;112:154-164.

[80] MackAldener M, Olsson M. Tooth Interior Fatigue Fracture - computational and material aspects. Int J Fatigue 2001;23(4):329-340.

[81] McDiarmid DL. General criterion for high cycle multiaxial fatigue failure. Fatigue and Fracture of Engineering Materials and Structures 1991;14(4):429-453.

[82] Borbely A, Mughrabi H, Eisenmeier G, Hoppel HW. A finite element modelling study of strain localization in the vicinity of near-surface cavities as a cause of subsurface fatigue crack initiation. Int J Fract 2002;115(3):227-232.

[83] Ogawa K, Asano T. Theoretical prediction of residual stress produced by shot peening and experimental verification for carburized steel. Materials Science Research International 2000;6(1):55-62.

[84] Inoue K, Kato M. Crack growth resistance due to shot peening in carburized gears. Journal of Propulsion and Power 1995;11(5):973-979.

[85] Blarasin A, Guagliano M, Vergani L. Fatigue crack growth prediction in specimens similar to spur gear teeth. Fatigue and Fracture of Engineering Materials & Structures 1997;20(8):1171-1182.

[86] Chaboche JL, Jung O. Application of a kinematic hardening viscoplasticity model with thresholds to the residual stress relaxation. Int J Plasticity 1997;13(10):785-807.

[87] Li JK, Yao M, Wang D. Mechanical approach to the residual stress field induced by shot peening. Materials Science and Engineering A (Structural Materials: Properties, Microstructure and Processing) 1991;A147(2):167-173.

[88] Meguid SA, Shagal G, Stranart JC, Liew KM, Ong LS. Relaxation of peening residual stresses due to cyclic thermo-mechanical overload. Journal of Engineering Materials and Technology, Transactions of the ASME 2005;127(2):170-178.

[89] Fathallah R, Laamouri A, Sidhom H, Braham C. High cycle fatigue behavior prediction of shot-peened parts. International Journal of Fatigue 2004;26(10):1053-1067.

[90] Yanhuai L, Jian L, Kewei X. Calculation of relaxation of residual stress and change of yield strength in shot peened layer. Materials Science Forum 2005;490-491:396-403.

[91] Gall K, Yang N, Horstemeyer M, McDowell DL, Jinghong F. The debonding and fracture of Si particles during the fatigue of a cast Al-Si alloy. Metallurgical and

Materials Transactions A (Physical Metallurgy and Materials Science) 1999;30A(12):3079-3088.

[92] Shenoy MM, Kumar RS, McDowell DL. Modeling effects of nonmetallic inclusions on LCF in DS nickel-base superalloys. International Journal of Fatigue 2005;27(2):113-127.

[93] Fan J, McDowell DL, Horstemeyer MF, Gall K. Cyclic plasticity at pores and inclusions in cast Al-Si alloys. Engineering Fracture Mechanics 2003;70(10):1281-1302.

[94] Fatemi A, Socie DF. A critical plane approach to multiaxial fatigue damage including out-of-phase loading. Fatigue and Fracture of Engineering Materials and Structures 1988;11(3):149-165.

[95] ABAQUS. Simulia, Providence, Rhode Island 2006;Ver 6.6.

[96] Donzella G, Pola A, Solazzi L, Marconi GP. Effect of shot peening on carburized surfaces. International Journal of Materials and Product Technology 2000;15(1-2):117-130.

[97] Pedersen R, Rice SL. "Case crushing" of carburized and hardened gears. Society of Automotive Engineers (SAE), New York, NY, United States, 1960, p. 12.

[98] Elghazal H, Lormand G, Hamel A, Girodin D, Vincent A. Microplasticity characteristics obtained through nano-indentation measurements: Application to surface hardened steels. Materials Science and Engineering A (Structural Materials: Properties, Microstructure and Processing) 2001;A303(1-2):110-119.

[99] Vincent A, Lormand G, Girodin D, Elghazal H, Hamnel A. Local elasto-plastic properties of bearing steels determined by nano-indentation measurements. American Society for Testing and Materials, 2002, pp. 427-442.

[100]   Boller C, Seeger T. Materials Data for Cyclic Loading, Part B: Low Alloy Steels. New York: Elsevier, 1987).

[101]   ABAQUS/ standard reference manual, Simulia, RI, Ver 6.6. 2006.

[102]   Kobayashi M, Ohno N. Implementation of cyclic plasticity models based on a general form of kinematic hardening. International Journal for Numerical Methods in Engineering 2002;53(9):2217-2238.

[103]   Xiao H, Chen Q, Shao E, Wu D, Chen Z, Wang Z. The effect of shot peening on rolling contact fatigue behaviour and its crack initiation and propagation in carburized steel. Wear 1991;151(1):77-86.

[104]   Kobayashi M, Matsui T, Murakami Y. Mechanism of creation of compressive residual stress by shot peening. Int J Fatigue 1998;20(5):351-357.

[105]   Zhang J, Prasannavenkatesan R, Shenoy MM, McDowell DL. Modeling fatigue crack nucleation at primary inclusions in carburized and shot-peened martensitic steel. Engineering Fracture Mechanics 2009;76(3):315-334.

[106]   McDowell DL, Berard J-Y. Δ J-based approach to biaxial fatigue. Fatigue and Fracture of Engineering Materials and Structures 1992;15(8):719-741.

[107]   McDowell DL. Multiaxial Fatigue Strength. ASM Handbook 1996:263-273.

[108]   Shenoy M, Zhang J, McDowell DL. Estimating fatigue sensitivity to polycrystalline Ni-base superalloy microstructures using a computational approach. Fatigue and Fracture of Engineering Materials and Structures 2007;30(10):889-904.

[109]   Jiang Y, Hertel O, Vormwald M. An experimental evaluation of three critical plane multiaxial fatigue criteria. International Journal of Fatigue 2007;29(8):1490-1502.

[110]   Kim KS, Park JC. Shear strain based multiaxial fatigue parameters applied to variable amplitude loading. International Journal of Fatigue 1999;21(5):475-483.

[111]   Findley KO, Saxena A. Low cycle fatigue in Rene 88DT at 650 C: crack nucleation mechanisms and modeling. Metallurgical and Materials Transactions A (Physical Metallurgy and Materials Science) 2006;37A(5):1469-1475.

[112]   Chen X, Gao Q, Sun XF. Damage analysis of low-cycle fatigue under non-proportional loading. International Journal of Fatigue 1994;16(3):221-225.

[113]   Kwon JD, Park JC. Multiaxial fatigue life prediction of duplex stainless steels with thermal aging at 430 °C under axial-torsional load. Vol. 270-273 Jeju Island, South Korea: Trans Tech Publications Ltd, Zurich-Ueticon, CH-8707, Switzerland, 2004, pp. 1183-1188.

[114]   Reis L, De Freitas M. Analytical and experimental studies on fatigue crack path under complex multi-axial loading. Fatigue and Fracture of Engineering Material and Structures 2006;29(4):281-289.

[115]   Shamsaei N, Fatemi A. Effect of hardness on multiaxial fatigue behaviour and some simple approximations for steels. Fatigue and Fracture of Engineering Materials and Structures 2009;32(8):631-646.

[116]   Gall K, Horstemeyer M, McDowell DL, Fan J. Finite element analysis of the stress distributions near damaged Si particle clusters in cast Al-Si alloys. Mechanics of Materials 2000;32(5):277-301.

[117]   Ott M, Mughrabi H. Dependence of the high-temperature low-cycle fatigue behaviour of the monocrystalline nickel-base superalloys CMSX-4 and CMSX-6 on the γ/γ '-morphology. Materials Science and Engineering A-Structural Materials Properties Microstructure and Processing 1999;272(1):24-30.

[118]   Alley ES, Neu RW. Microstructure-sensitive modeling of rolling contact fatigue. International Journal of Fatigue 2009;In Press.

[119]   Knight MG, de Lacerda LA, Henshall JL, Wrobel LC. A parametric study of inclusion interaction in particulate- and fibre-reinforced materials using the boundary element technique. Journal of Strain Analysis for Engineering Design 2002;37(1):47-58.

[120]   Mughrabi H, Ott M, Tetzlaff U. New microstructural concepts to optimize the high-temperature strength of γ'-hardened monocrystalline nickel-based superalloys. Materials Science and Engineering A 1997;234-236:434-437.

[121]   Prasannavenkatesan R, Zhang J, McDowell DL, Olson GB, Jou H-J. 3D modeling of subsurface fatigue crack nucleation potency of primary inclusions in heat treated and shot peened martensitic gear steels. International Journal of Fatigue 2009;31(7):1176-1189.

[122]   Guagliano M, Vergani L. An approach for prediction of fatigue strength of shot peened components. Vol. 71 Milan, Italy: Elsevier, 2004, pp. 501-512.

[123]   Sidhom N, Laamouri A, Fathallah R, Braham C, Lieurade HP. Fatigue strength improvement of 5083 H11 Al-alloy T-welded joints by shot peening: Experimental characterization and predictive approach. International Journal of Fatigue 2005;27(7):729-745.

[124]   Holzapfel H, Schulze V, Voehringer O, Macherauch E. Residual stress relaxation in an AISI 4140 steel due to quasistatic and cyclic loading at higher temperatures. Materials Science & Engineering A: Structural Materials: Properties, Microstructure and Processing 1998;A248(1-2):9-18.

[125]   Capello E, Davoli P, Filippini M, Foletti S. Relaxation of residual stresses induced by turning and shot peening on steels. Journal of Strain Analysis for Engineering Design 2004;39(3):285-290.

[126]   Teodosio JR, Cindra FM, Pedrosa PD. Relaxation of residual stresses during fatigue cycles in steels. Vol. 426-432 Madrid, Spain: Trans Tech Publications Ltd, 2003, pp. 3981-3986.

[127]   Zhuang WZ, Halford GR. Investigation of residual stress relaxation under cyclic load. International Journal of Fatigue 2001;23(SUPPL 1):31-37.

[128]   Qin M, Ji V, Ma SY, Li JB. A study on residual stress relaxation under quasi-static load. Vol. 490-491 Xi'an, China: Trans Tech Publications, 2005, pp. 430-435.

[129]   Webster GA, Ezeilo AN. Residual stress distributions and their influence on fatigue lifetimes. International Journal of Fatigue 2001;23(SUPPL 1):375-383.

[130]   Almer JD, Cohen JB, Moran B. Effects of residual macrostresses and microstresses on fatigue crack initiation. Materials Science and Engineering A: Structural Materials: Properties, Microstructure and Processing 2000;284(1-2):268-279.

[131]   Jhansale HR, Topper TH. Engineering Analysis of the Inelastic Stress Response of a Structural Metal Under Variable Cyclic Strains. ASTM Special Technical Publication 1971:246-227.

[132]   Iida K, Yamamoto S, Takanashi M. Residual stress relaxation by reversed loading. Welding in the World, Le Soudage Dans Le Monde 1997;39(3):138-144.

[133]   Smith DJ, Farrahi GH, Zhu WX, McMahon CA. Experimental measurement and finite element simulation of the interaction between residual stresses and mechanical loading. International Journal of Fatigue 2001;23(4):293-302.

[134]   Marder AR, Krauss G. Formation of Low Carbon Martensite in FE-C Alloys. ASM Trans Quart 1969;62(4):957-964.

[135]   Marder AR, Krauss G. Morphology of martensite in iron-carbon alloys. American Society of Metals -- Trans 1967;60(4):651-660.

[136]   Morito S, Saito H, Ogawa T, Furuhara T, Maki T. Effect of austenite grain size on the morphology and crystallography of lath martensite in low carbon steels. ISIJ International 2005;45(1):91-94.

[137]   Kitahara H, Ueji R, Tsuji N, Minamino Y. Crystallographic features of lath martensite in low-carbon steel. Acta Materialia 2006;54(5):1279-1288.

[138]   Hayakawa M, Matsuoka S, Furuya Y. Nanoscopic measurement of local plastic deformation for a tempered martensitic steel by atomic force microscopy. Materials Letters 2003;57(20):3037-3042.

[139]   Ohmori Y, Sugisawa S. Carbide Precipitation in Tempered Martensite. Sumitomo Search 1973(9):31-45.

[140]   Norstrom LA. The relation between microstructure and yield strength in tempered low-carbon lath martensite with 5% nickel. Metal Science 1976;10(12):429-436.

[141]   Morito S, Yoshida H, Maki T, Huang X. Effect of block size on the strength of lath martensite in low carbon steels. Materials Science and Engineering A 2006;438-440(SPEC ISS):237-240.

[142]   Schastlivtsev VM, Rodionov DP, Khlebnikova YV, Yakovleva IL. Peculiarity of structure and crystallography of plastic deformation of lath martensite in structural steels. Materials Science and Engineering A: Structural Materials: Properties, Microstructure and Processing 1999;A273-275:437-442.

[143]   McGinty R. Multiscale representation of polycrystalline inelasticity. PhD Thesis, Georgia Institute of Technology 2001.

[144]   McGinty RD, McDowell DL. Multiscale polycrystal plasticity. Journal of Engineering Materials and Technology, Transactions of the ASME 1999;121(2):203-209.
[145]   Cuitino AM, Ortiz M. Computational modelling of single crystals. Modelling and Simulation in Materials Science and Engineering 1993;1(3):225-263.

[146]   Asaro RJ. Micromechanics of Crystals and Polycrystals. Advances in Applied Mechanics 1983;23:1-115.

[147]   Horstemeyer MF, McDowell DL, McGinty RD. Design of experiments for constitutive model selection: Application to polycrystal elastoviscoplasticity. Modelling and Simulation in Materials Science and Engineering 1999;7(2):253-273.

[148]   Bennett VP, McDowell DL. Polycrystal orientation distribution effects on microslip in high cycle fatigue. International Journal of Fatigue 2003;25(1):27-39.

[149]   Xie CL, Ghosh S, Groeber M. Modeling cyclic deformation of HSLA steels using Crystal plasticity. Transactions of the ASME Journal of Engineering Materials and Technology 2004;126(4):339-352.

[150]   Kim SA, Johnson WL. Elastic constants and internal friction of martensitic steel, ferritic-pearlitic steel, and α-iron. Materials Science and Engineering A 2007;452-453:633-639.

[151]   Qian Y, Almer J, Lienert U, Tiemens BL, Olson GB. Nondestructive Residual Stress Distribution Measurements in Nanostructured Ultrhigh-Strength Gear Steels. In: 5th International Conference on Synchrotron Radiation in Materials Science Chicago, 2006.

[152]   McDowell DL. Viscoplasticity of heterogeneous metallic materials. Materials Science and Engineering: R Reports 2008;62(3):67-123.

[153]   Kumar RS, Wang AJ, McDowell DL. Effects of microstructure variability on intrinsic fatigue resistance of nickel-base superalloys - a computational micromechanics approach. International Journal of Fracture 2006;137(1-4):173-210.

[154]   Shiozawa K, Lu L. Very high-cycle fatigue behaviour of shot-peened high-carbon-chromium bearing steel. Fatigue and Fracture of Engineering Material and Structures 2002;25(8-9):813-822.

[155]   Prasannavenkatesan R, Mcdowell DL. Polycrystal Plasticity Modeling of Cyclic Residual Stress Relaxation in Shot Peened Martensitic Gear Steel. International Journal of Solids and Structures 2009;(In review).

[156]   Morrissey R, Goh C-H, McDowell D. Microstructure-Scale Modeling of HCF Deformation. Mechanics of Materials 2003;35(3-6):295-311.

[157]   Przybyla CP, McDowell DL. Microstructure-Sensitive Extreme Value Probabilities for High Cycle Fatigue of Ni-Base Superalloy IN100. International Journal of Plasticity 2009;(in review).

[158]   Ortiz M. Computational micromechanics. Computational Mechanics 1996;18(5):321-338.

[159]   McDowell DL. Modeling and experiments in plasticity. International Journal of Solids and Structures 2000;37(1-2):293-309.

[160]   Chai G. The formation of subsurface non-defect fatigue crack origins. International Journal of Fatigue 2006;28(11):1533-1539.

[161]   Wang D, Hua H, Fine ME, Cheng HS. Fatigue crack initiation and fracture in 52100 steel. Materials Science & Engineering A: Structural Materials: Properties, Microstructure and Processing 1989;A118(1-2):113-120.

[162]   Atkinson HV, Shi G. Characterization of inclusions in clean steels: a review including the statistics of extremes methods. Progress in Materials Science 2003;48(5):457-520.

[163]   Yates JR, Shi G, Atkinson HV, Sellars CM, Anderson CW. Fatigue tolerant design of steel components based on the size of large inclusions. Fatigue and Fracture of Engineering Materials and Structures 2002;25(7):667-676.

[164]   Sharpe PS, Hillberry BM, Craig BA. Fatigue life variability prediction based on crack forming inclusions in a high strength alloy steel. ASTM Special Technical Publication 2004(1450):150-163.

[165]   Murakami Y. Effects of small defects and nonmetallic inclusions on the fatigue strength of metals. Key Engineering Materials 1991;51-52:37-42.

[166]   Ochi Y, Ishii A, Sasaki SK. An experimental and statistical investigation of surface fatigue crack initiation and growth. Fatigue and Fracture of Engineering Materials and Structures 1985;8(4):327-339.

[167]   Ballard P, Dang Van K, Deperrois A, Papadopoulos YV. High cycle fatigue and a finite element analysis. Fatigue and Fracture of Engineering Materials and Structures 1995;18(3):397-411.

[168]   Gumbel EJ. Statistics of Extremes New York: Columbia University Press, 1958.

[169]   Sasaki SK, Ochi Y, Ishii A, Abe H. Effects of material structures on statistical scatter in initiation and growth lives of surface cracks and failure life in fatigue. JSME International Journal, Series 1: Solid Mechanics, Strength of Materials 1989;32(1):155-161.

[170]   Przybyla C, Prasannavenkatesan R, Salajegheh N, McDowell DL. Microstructure-sensitive modeling of high cycle fatigue. International Journal of Fatigue;In Press, Accepted Manuscript.

[171]   Vali R. Electronic, dynamical, and dielectric properties of lanthanum oxysulfide. Computational Materials Science 2006;37(3):300-305.

[172]   Sobon LE, Wickersheim KA, Buchanan RA, Alves RV. Growth and properties of lanthanum oxysulfide crystals. Journal of Applied Physics 1971;42(8):3049-3053.

[173]   Beretta S, Murakami Y. Statistical analysis of defects for fatigue strength prediction and quality control of materials. Fatigue and Fracture of Engineering Materials and Structures 1998;21(9):1049-1065.

[174]   Tiryakioglu M. Statistical distributions for the size of fatigue-initiating defects in Al-7%Si-0.3%Mg alloy castings: a comparative study. Materials Science and Engineering: A (Structural Materials: Properties, Microstructure and Processing) 2008;497(1-2):119-125.

[175]   McVeigh C, Vernerey F, Liu WK, Moran B, Olson G. An interactive micro-void shear localization mechanism in high strength steels. Journal of the Mechanics and Physics of Solids 2007;55(2):225-244.

[176]   Garrison Jr WM. Controlling inclusion distributions to achieve high toughness in steels. Iron and Steel Technology 2007;4(6):132-139.

[177]   Prasannavenkatesan R, Pryzbyla CP, Salajegheh N, McDowell DL. Simulated extreme value fatigue sensitivity to inclusions and pores in martensitic gear steels. Modelling and Simulation in Materials Science and Engineering 2009;(in review).

[178]   Iorio LE, Garrison WM, Jr. The effects of titanium additions on AF1410 ultra-high-strength steel. Metallurgical and Materials Transactions A (Physical Metallurgy and Materials Science) 2006;37A(4):1165-1173.

[179]   Garrison WM, Jr., Moody NR. The influence of inclusion spacing and microstructure on the fracture toughness of the secondary hardening steel AF1410. Metallurgical Transactions A (Physical Metallurgy and Materials Science) 1987;18A(7):1257-1263.

[180]   Jou H-J. Questek Innovations LLC. Unpublished Research 2009.

[181]   Manonukul A, Dunne FPE. High- and low-cycle fatigue crack initiation using polycrystal plasticity. Proceedings of the Royal Society of London, Series A (Mathematical, Physical and Engineering Sciences) 2004;460(2047):1881-1903.

[182]   Castillo E. Extreme value theory in engineering. New York: Academic Press, Inc., 1988.

[183]   Stephens MA. EDF Statistics for Goodness of Fit and Some Comparisons. Journal of the American Statistical Association 1974;69:730-737.

[184]   Wang AJ, Kumar RS, Shenoy MM, McDowell DL. Microstructure-based multiscale constitutive modeling of γ -γ' nickel-base superalloys. International Journal for Multiscale Computational Engineering 2006;4(5-6):663-692.

[185]   Asaro RJ. Crystal plasticity. Transactions of the ASME Journal of Applied Mechanics 1983;50(4B):921-934.

[186]   Estrin Y, Mecking H. A unified phenomenological description of work hardening and creep based on one-parameter models. Acta Metallurgica 1984;32:57-70.

[187]   Mecking H, Kocks U. Kinetics of flow and strain-hardening. Acta Metallurgica 1981;29:1865-1875.

[188]   Shenoy M, Tjiptowidjojo Y, McDowell D. Microstructure-sensitive modeling of polycrystalline IN 100. International Journal of Plasticity 2008;24(10):1694-1730.

[189]   Labusch R. A statistical theory of solid solution hardening. Physica Status Solidi A 1970;41(2):659-669.

[190]   Sauzay M, Brillet H, Monnet I, Mottot M, Barcelo F, Fournier B, Pineau A. Cyclically induced softening due to low-angle boundary annihilation in a martensitic steel. Materials Science and Engineering A (Structural Materials: Properties, Microstructure and Processing) 2005;400-401:241-244.

[191]   Keh AS, Weissmann S. Electron Microscopy and Strength of Crystals. Thomas G, Washburn J, editors. New York: Interscience Publishers, 1963, pp. 231-300.

[192]   Ashby MF. On the Orowan Stress. Cambridge, MA: M.I.T. Press, 1969.

[193]   Hirsch PB, Humphreys FJ. Plastic Deformation of Two-Phase Alloys Containing Small Nondeformable Particles. Cambridge, MA: M.I.T. Press, 1969.

[194]   Abe F. Precipitate design for creep strengthening of 9% Cr tempered martensitic steel for ultra-supercritical power plants. Science and Technology of Advanced Materials 2008;9(1).

[195]   Mense A. www.mathwave.com. 2009.

[196]   Saha A, Olson GB. Computer-aided design of transformation toughened blast resistant naval hull steels: Part I. Journal of Computer-Aided Materials Design 2007;14(2):177-200.

[197]   Bonade R, Spatig P. On the strain-hardening of tempered martensitic alloys. Materials Science and Engineering A 2005;400-401(1-2 SUPPL):234-240.

[198]   Shamsaei N, Fatemi A. Deformation and fatigue behaviors of case-hardened steels in torsion: Experiments and predictions. International Journal of Fatigue 2009;31(8-9):1386-1396.

[199]   McDowell DL. Engineering model for propagation of small cracks in fatigue. Engg Frac Mech 1997;56(3):357-377.

[200]   Al-Ostaz A, Jasiuk I. Influence of interface and arrangement of inclusions on local stresses in composite materials. Acta Mater 1997;45(10):4131-4143.

[201]   Tursun G, Weber U, Soppa E, Schmauder S. The influence of transition phases on the damage behaviour of an Al/10vol.%SiC composite. Computational Materials Science 2006;37(1-2):119-133.

[202]   Sevostianov I, Kachanov M. Effect of interphase layers on the overall elastic and conductive properties of matrix composites. Applications to nanosize inclusion. Int J Solid Struct 2007;44(3-4):1304-1315.

[203]   Hughes JDH. Carbon fibre/epoxy interface. A review. Composites Science and Technology 1991;41(1):13-45.

[204]   Kim K, Sudak LS. A three-phase circular inclusion with a sliding interface and a radial matrix crack. Vol. 7 Ancona, Italy: WIT Press, Southampton, SO40 7AA, United Kingdom, 2004, pp. 147-156.

[205]   Lombardo N. Effect of an inhomogeneous interphase on the thermal expansion coefficient of a particulate composite. Composites Science and Technology 2005;65(14):2118-2128.

[206]   Benveniste Y, Dvorak GJ, Chen T. Stress fields in composites with coated inclusions. Mechanics of Materials 1989;7(4):305-317.

[207]   Wu Y, Dong Z. Three-dimensional finite element analysis of composites with coated spherical inclusions. Materials Science and Engineering A: Structural Materials: Properties, Microstructure and Processing 1995;A203(1-2):314-323.

[208]   Kim K, Sudak LJ. Interaction between a radial matrix crack and a three-phase circular inclusion with imperfect interface in plane elasticity. International Journal of Fracture 2005;131(2):155-172.

[209]   Cheeseman BA, Santare MH. The effect of the interphase on crack-inclusion interactions. International Journal of Fracture 2001;109(3):303-323.

[210]   Liu YW, Fang QH, Jiang CP. A piezoelectric screw dislocation interacting with an interphase layer between a circular inclusion and the matrix. International Journal of Solids and Structures 2004;41(11-12):3255-3274.

[211]   Cheeseman BA, Santare MH. Thermal residual stress and interphase effects on crack-inclusion interactions. Journal of Composite Materials 2002;36(5):553-569.

[212]   Xiao ZM, Chen BJ. Stress intensity factor for a Griffith crack interacting with a coated inclusion. International Journal of Fracture 2001;108(3):193-205.

[213]   Wang X, Shen YP. An edge dislocation in a three-phase composite cylinder model with a sliding interface. Journal of Applied Mechanics, Transactions ASME 2002;69(4):527-538.

[214]   Shiozawa K, Morii Y, Nishino S, Lu L. Subsurface crack initiation and propagation mechanism in high-strength steel in a very high cycle fatigue regime. Int J Fatigue 2006;28(11):1521-1532.

[215]   Kuhlmann-Wilsdorf D, Thomason PF. Role of Vacant Lattice Sites in the Low-Amplitude Fatigue Failure at Inclusions in Steel. Acta Metall 1982;30(6):1243-1245.

[216]   Murakami Y, Kodama S, Konuma S. Quantitative evaluation of effects of non-metallic inclusions on fatigue strength of high strength steels. I. Basic fatigue mechanism and evaluation of correlation between the fatigue fracture stress and the size and location of non-metallic inclusions. Int J Fatigue 1989;11(5):291-298.

[217]   Tiemens BL. Performance Optimization and Computational Design of Ultra-High Strength Gear Steels. PhD Thesis 2006:Northwestern University, IL.

[218]   Gubenko SI. Effect of "nonmetallic inclusion - Matrix" phase boundaries on the cohesive resistance of steel. Metal Science and Heat Treatment 2006;48(1-2):13-18.

[219]   Miao P, Knott JF. Formation of sulphide 'patches' on inclusions in C-Mn steel weld metal. Materials Science and Technology 2004;20(11):1440-1446.

[220]   Freund LB, Suresh S. Thin Film Materials: Stress, Defect Formation and Surface Evolution. London: Cambridge University Press, 2003.

[221]   Pei YT, Song GM, Sloof WG, De Hosson JTM. A methodology to determine anisotropy effects in non-cubic coatings. Surface and Coatings Technology 2007;201(16-17):6911-6916.

[222]   Luo F, Gao K, Pang X, Yang H, Qiao L, Wang Y. Characterization of the mechanical properties and failure modes of hard coatings deposited by RF magnetron sputtering. Surface and Coatings Technology 2008;202(14):3354-3359.

[223]   Hsin-Chang T, Weileun F. Determining the Poisson's ratio of thin film materials using resonant method. Sensors and Actuators A (Physical) 2003;A103(3):377-383.

[224]   Prasannavenkatesan R, McDowell DL, Olson GB, Jou HJ. Modeling Effects of Compliant Coatings on HCF Resistance of Primary Inclusions in High Strength Steels. Journal of Engineering Materials and Technology-Transactions of the Asme 2009;131(1).

[225]   Atkinson HV, Rickinson BA. Hot Isostatic Processing. Bristol: Adam Hilger, 1991.

[226]   Atkinson HV, Davies S. Fundamental aspects of hot isostatic pressing: An overview. Metallurgical and Materials Transactions A: Physical Metallurgy and Materials Science 2000;31(12):2981-3000.

[227]   Olson GB. Advances in theory: Martensite by design. Materials Science and Engineering A (Structural Materials: Properties, Microstructure and Processing) 2006;438-440:48-54.

[228]   Weijun H, Yihong N, Han D, Yuqing W, Chunxu W. High-cycle fatigue fracture behavior of ultrahigh strength steels. Journal of Materials Science and Technology 2008;24(5):787-792.

[229]   McDowell DL. Microstructure-Sensitive Computational Fatigue Analysis. In: Handbook of Materials Modeling. Sidney Y, Horstemeyer MF, editors.: Springer Netherlands, 2005, pp. 1193-1214.

[230]   Cowie JG, Azrin M, Olson GB. Microvoid formation during shear deformation of ultrahigh strength steels. Metallurgical Transactions A (Physical Metallurgy and Materials Science) 1989;20A(1):143-153.

[231]   Liu WK, McVeigh C, Vernerey F, Moran B, Olson G. An interactive micro-void shear localization mechanism in high strength steels. Journal of the Mechanics and Physics of Solids 2007;55(2):225-244.

[232]   http://www.questek.com/PDF/ferriumc61.pdf. 2008.

[233]   Tomita Y, Shibutani Y. Estimation of deformation behavior of TRIP steels - smooth/ringed-notched specimens under monotonic and cyclic loading. International Journal of Plasticity 2000;16(7-8):769-789.

[234]   Troiano E. Applications of advanced materials for cannon production- Technical report ARCCB-TR-92049.   Watervliet, NY-12189: US Army Armament Research - Development and Engineering Center and Bennet Labs, 1992.

[235]   Karditsas PJ, Baptiste M-J. http://www-ferp.ucsd.edu/LIB/PROPS/. 2009.

[236]   Pagounis E, Talvitie M, Lindroos VK. Microstructure and mechanical properties of hot work tool steel matrix composites produced by hot isostatic pressing. Powder Metallurgy 1997;40(1):55-61.

[237]   Pagounis E, Talvitie M, Lindroos VK. Consolidation behavior of a particle reinforced metal matrix composite during HIPing. Materials Research Bulletin 1996;31(10):1277-1285.

[238]   Li WB, Haggblad HA. Constitutive laws for hot isostatic pressing of powder compact. Powder Metallurgy 1997;40(4):279-281.

[239]   Ramakrishnan N, Balakrishna Bhat T, Arunachalam VS. An analysis of pressure sintering by computer simulation. Acta Metallurgica 1984;32(3):357-370.

[240]   McVeigh C, Liu WK. Linking microstructure and properties through a predictive multiresolution continuum. Computer Methods in Applied Mechanics and Engineering 2008;197(41-42):3268-3290.

[241]   Vernerey F, Liu WK, Moran B. Multi-scale micro morphic theory for hierarchical materials. Journal of the Mechanics and Physics of Solids 2007;55(12):2603-2651.

[242]   Liu WK, McVeigh C. Predictive multiscale theory for design of heterogeneous materials. Computational Mechanics 2008;42(2):147-170.